Understanding the Aqueous-Phase Adsorption and Hydrogenation of Model Bio-Oil Molecules on Metals and Alloys

by

Isaiah Barth

A dissertation submitted in partial fulfillment
of the requirements for the degree of
Doctor of Philosophy
(Chemical Engineering)
in the University of Michigan
2023

Doctoral Committee:

Professor Bryan R. Goldsmith, Chair
Professor Johannes Schwank
Professor Nirala Singh
Professor Paul Zimmerman

Isaiah Barth

ibarth@umich.edu

ORCID iD: 0000-0002-3052-0467

Dedication

To my friends and family.

I would not be here without your support.

Acknowledgements

I would like to acknowledge my committee members who have given me guidance while I have worked to complete this dissertation. Foremost, I would like to thank my advisor, Professor Bryan Goldsmith, who taught me the basics of computational modeling and whose insight and guidance helped me succeed as my time as a Ph.D. student. I would also like to thank Professor Nirala Singh who has given me invaluable feedback during our five-year collaboration and has helped me ensure that my conceptual work remains closely tied with experimentally measurable phenomena. I would also like to thank Professor Paul Zimmerman and Professor Johannes Schwank whose thought-provoking questions have helped me see how my project fits into the broader field of computational chemistry and catalysis. I would also like to acknowledge James Akinola, my collaborator. Over the past five years, we both grown as researchers. I would also like to thank my lab members who I have worked alongside throughout my time at the University of Michigan. Frank Doherty, Jacques Esterhuizen, Zixuan Wang, Sam Young, Ankit Mathanker, Oluwatosin Ohiro, Cameron Gruich, and Chenggong Jiang have helped me develop my research skills and have provided valuable feedback on my work. I would also like to acknowledge the many undergraduate students in the lab who I have met over the years, particularly Jonathan Lee, who I had the pleasure of mentoring for two years. Finally, I would like to thank my friends and family who have all supported me and encouraged me along this journey.

I would like to acknowledge the funding sources that have made this work possible. The work in Chapter 2 relied on resources from the National Energy Research Scientific Computing

Center (NERSC), a U.S. Department of Energy Office of Science User Facility operated under Contract No. DE-AC02-05CH11231. The work in Chapter 3 was supported by the National Science Foundation under grant no. #1919444. Computing resources were generously provided by NERSC. Kinetic measurements for the particle size dependence of Rh/C were taken as part of the Chemical Transformation Initiative at Pacific Northwest National Laboratory (PNNL), conducted under the Laboratory Directed Research and Development Program at PNNL, a multiprogram national laboratory operated by Battelle for the U.S. Department of Energy. The authors would also like to acknowledge the financial support by the U.S. Department of Energy (DOE), Office of Basic Energy Sciences, Division of Chemical Sciences, Geosciences, and Biosciences (FWP 47319). Finally, the work in Chapter 4 was supported by the National Science Foundation under grant no. #1919444 and grant #2116646. Computing resources were provided by NERSC. This research used resources of the Advanced Photon Source Sector 20, a U.S. Department of Energy (DOE) Office of Science User Facility operated for the DOE Office of Science by Argonne National Laboratory under Contract No. DE-AC02-06CH11357, and the Canadian Light Source and its funding partners. The authors thank and acknowledge Chengjun Sun for help with X-ray absorption. The authors acknowledge the University of Michigan College of Engineering for financial support and the Michigan Center for Materials Characterization for use of the instruments and staff assistance.

Table of Contents

List of Tables

List of Figures

List of Appendices

Abstract

Valorization of biomass-derived molecules via aqueous-phase catalytic hydrogenation is a promising strategy for producing CO_2-neutral fuels and chemicals to reduce our reliance on fossil fuels and lower our greenhouse gas emissions. However, the high cost and low activity of current catalysts prevent the economical implementation of the technology. The work herein focuses on gaining a fundamental understanding of the processes that govern aqueous-phase hydrogenation of biomass-derived compounds to inform the design of efficient materials for the production of sustainable chemicals.

In Chapter 2, we measure the aqueous-phase adsorption enthalpies and free energies of phenol, benzaldehyde, furfural, benzyl alcohol, and cyclohexanol on polycrystalline Pt and Rh via experimental isotherm fitting and density functional theory modeling. We find that the experimental aqueous-phase adsorption enthalpies are between 50 to 250 kJ mol^{-1} less exothermic than calculated gas-phase enthalpies. We also find that there is a larger difference between the gas-phase and aqueous-phase enthalpies for Rh than there is for Pt. Aromatics adsorb with similar strength on Pt and Rh in the aqueous-phase, despite Rh binding compounds more strongly in the gas phase. A widely used implicit solvent model overpredicts the heats of adsorption for all organics compared with experimental measurements. However, accounting for the enthalpic penalty of displacing surface-adsorbed water molecules upon organic adsorption using a bond-additivity model explains the greatly reduced heats of adsorption and rationalizes the similar binding strength on Pt and Rh in the aqueous phase.

In Chapter 3, we identify the active facet of Pt and Rh catalysts for aqueous-phase hydrogenation of phenol and explain the origin of size-dependent activity trends observed on Pt and Rh nanoparticles. We extract phenol adsorption energies on the active sites of Pt and Rh by fitting kinetic data, and we show that the active sites adsorb phenol weakly. We predict turnover frequencies (TOF) on the (111) terraces and (221) steps of Pt and Rh with density functional theory modeling and mean-field microkinetic simulations and find that the (111) terraces are more active than the step sites. The higher activities of the (111) terraces are due to lower activation energies and weaker phenol adsorption, which prevents high coverages of adsorbed phenol from inhibiting hydrogen adsorption. Finally, we measure the TOF for phenol hydrogenation on Rh nanoparticles as a function of particle diameter and find that the TOF increases as a function of particle size, which is caused by larger particles having higher fraction of (111) terrace sites.

Lastly, in Chapter 4, we investigate platinum-cobalt alloys for the hydrogen evolution reaction (HER) and the electrocatalytic hydrogenation (ECH) of phenol, and we evaluate the adequacy of the hydrogen adsorption energy as a descriptor the catalytic activity for both reactions. Through a combination of electrochemical measurements, DFT calculations, and kinetic modeling, we show that while that the hydrogen adsorption energy is a useful descriptor for HER, it is an insufficient descriptor for ECH of phenol. Structural characterization reveals that the Pt_xCo_y catalysts have a surface containing both Co and Pt. DFT calculations paired with kinetic modeling of the Pt_xCo_y surface corroborates our experimental finding that the ECH is not enhanced by weakening hydrogen adsorption. However, kinetic modeling predicts that platinum-cobalt catalysts with a core-shell may have enhanced ECH performance, warranting future consideration.

Chapter 1 Introduction & Background

1.1 Motivation

Producing transportation fuels and chemicals through the valorization of biomass-derived molecules is a promising strategy to decrease our reliance on fossil fuels and reduce our greenhouse gas emissions in favor of a CO_2-neural resource. Biomass waste produced through agricultural, municipal, and industrial sources is typically disposed of,[1] but as access to renewable electricity becomes more widespread, there is growing interest in converting this abundant and underutilized resource into useful fuels and chemicals. Current biomass wastes can be converted to product specialty and commodity fuels and chemicals that can be used for a variety of applications including transportation and energy storage.[2] **Figure 1-1** highlights how emerging technologies can leverage renewable electricity to convert current waste streams into useful products.

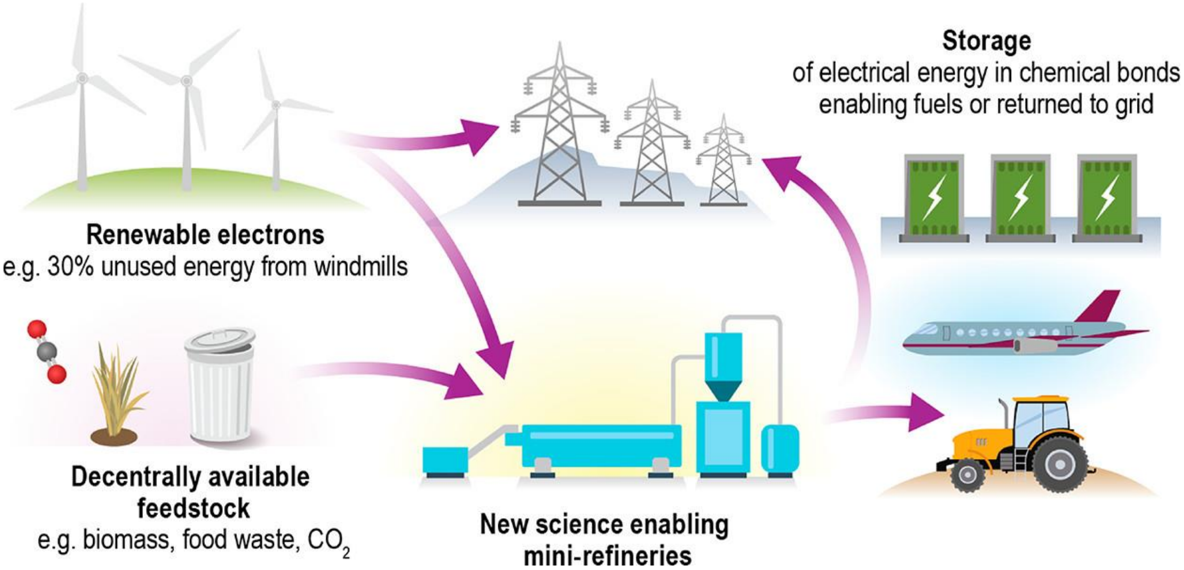

Figure 1-1 Schematic of biomass conversion into fuels and chemicals. Simplified scheme for the conversion of current biomass wastes into useful fuels and chemical using renewable electricity. Adapted from ref [2].

Lignocellulosic biomass, produced as waste in the agriculture and forestry industries,[1] is an abundant and inexpensive carbon resource that can be broken down into a mixture of organic compounds through established processes such as hydrothermal liquefaction or pyrolysis.[3,4] These processes are used to depolymerize and decompose lignin, cellulose, and hemicellulose that make up the biomass to produce an aqueous mixture of organic compounds referred to as bio-oil. Bio-oil contains hundreds of different components including various phenols, aldehydes, furans, and acids.[3,5–8] **Figure 1-2** shows some of the prototypical organic compounds found in a bio-oil mixture produced from the pyrolysis of lignocellulosic biomass. Unfortunately, the mixtures' high oxygen content, high acidity, and low heating value make it unsuitable for direct use as a fuel.[9,10] However, the stability and energy density of biomass-derived organics can be improved through catalytic hydrogenation and deoxygenation.

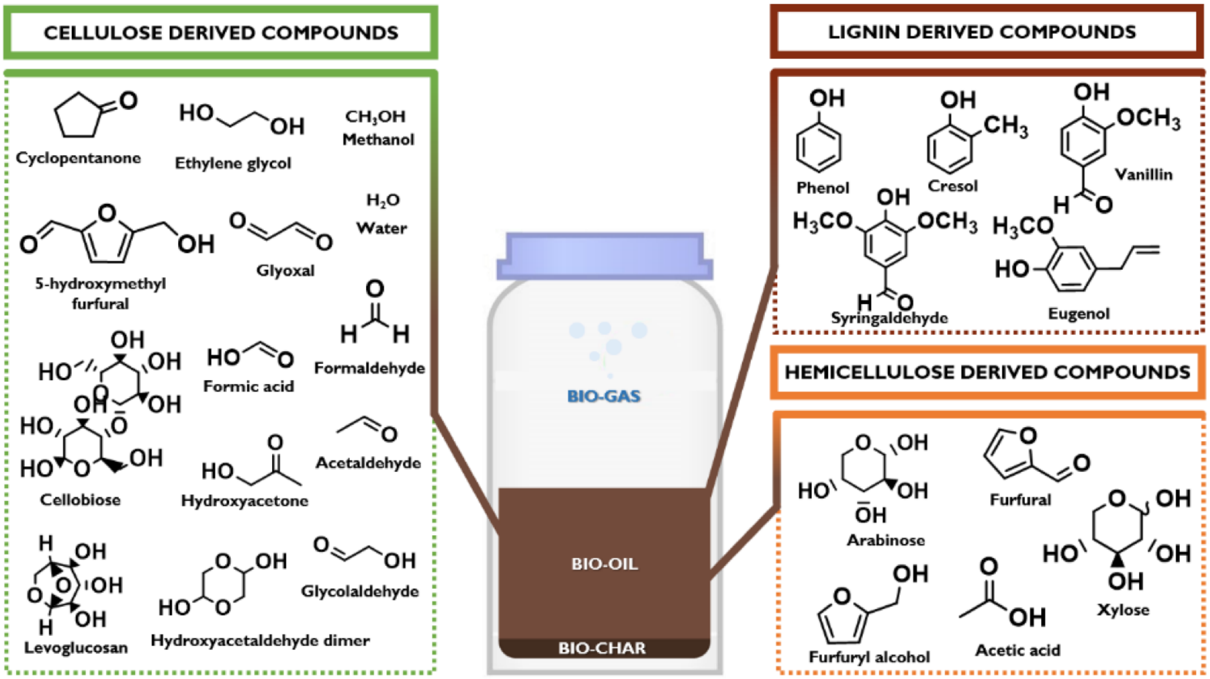

Figure 1-2 Example bio-oil mixture. Some of the representative compounds present in a typical bio-oil mixture produced through the thermal treatment of cellulose, hemicellulose, and lignin. Adapted from ref. [8].

Thermocatalytic hydrogenation (TCH) and electrocatalytic hydrogenation (ECH) are two promising strategies for upgrading the compounds in bio-oil to produce stable, high-energy density transportation fuels and other value-added chemical products. TCH uses high pressure H_2 and a thermal driving force to promote hydrogenation reactions, whereas ECH uses an applied electric potential to produce hydrogen equivalents in situ by reducing protons from the solution phase.[11] Hydrogenation of organics via TCH and ECH typically follow the same reaction mechanism,[11] thus the main difference between the two processes is the source of hydrogen. Although in principle both processes can be driven renewably, the H_2 in TCH is typically produced through the energy-intensive steam-methane reforming process, which produces large amounts of CO_2. In ECH, hydrogen is produced electrochemically at mild temperatures and pressures,[12] thus opening a route for the production of CO_2-neutral fuels and chemicals from a sustainable biomass feedstock. **Figure 1-3** shows a simplified electrochemical cell for the ECH of guaiacol, which is representative of molecules found in a bio-oil mixture. In the electrochemical cell, hydrogen equivalents are produced via the oxidation of water at the anode, and hydrogenation (reduction) of the organic molecule occurs at the cathode, thus eliminating the need for an external H_2 source.

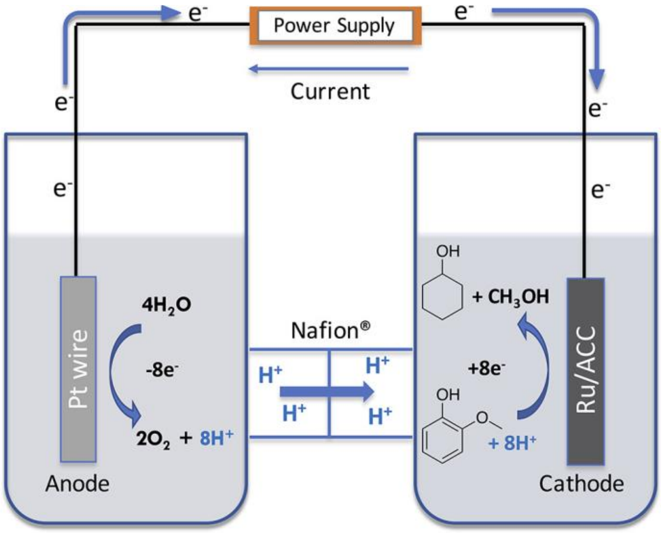

Figure 1-3 Example electrochemical cell for ECH of bio-oils. Electrochemical cell for the electrocatalytic hydrogenation of guaiacol, a model bio-oil compound. Pt acts as the anode and Ru acts as the cathode for the two half-cell reactions. Adapted from ref. [13].

Unfortunately, chemicals produced through biomass conversion are not cost-competitive alternatives to petrochemicals. Techno-economic analysis reveals that bio-oil hydrogenation is the most capital and energy-intensive part of the process, which is in part due to the high cost and low activity of current catalysts.[14–16] The development of novel high-activity and low-cost catalysts is required for the efficient hydrogenation of biomass-derived organic molecules.

1.2 Background

The work herein investigates thermocatalytic and electrocatalytic hydrogenation of phenol, furfural, and benzaldehyde on Pt, Rh, and Pt-based alloys. These molecules were chosen because they are representative of the oxygenated aromatic molecules that are present in an aqueous bio-oil mixture, and they are recognized by the US Department of Energy for their potential to be upgraded into value-added fuels and chemical products.[17,18] **Figure 1-4** shows phenol, benzaldehyde, and furfural as well as their hydrogenated products. Pt and Rh were selected because they are among the most active pure metals for bio-oil hydrogenation, and the reaction mechanism on Pt and Rh is well understood.[19] Platinum-based alloys are promising catalysts for a variety of applications,[20] however the use of alloys for the aqueous-phase catalytic upgrading of biomass-based organic compounds is underexplored.

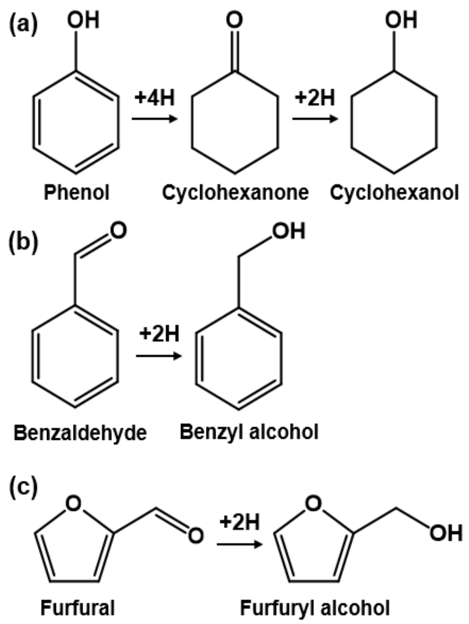

Figure 1-4 Representative bio-oil molecules. **(a)** Phenol, cyclohexanone, and cyclohexanol. Cyclohexanone and cyclohexanol are formed as products from phenol hydrogenation. **(b)** Benzaldehyde and benzyl alcohol, which is a product of benzaldehyde hydrogenation. **(c)** Furfural and furfuryl alcohol, which is a product of furfural hydrogenation.

The work included in this dissertation aims to study the structure-property relationships that govern aqueous-phase hydrogenation of bio-oil compounds to help establish a set of design principles that may be used to guide future development of active, selective, and low-cost materials for the catalytic hydrogenation of aromatics. Both computational and experimental research is required to elucidate catalytically relevant thermodynamic properties such as aqueous-phase adsorption strengths and kinetic properties such as activation energies and reaction rates for TCH and ECH. Computational modeling is a powerful technique that can be used to provide mechanistic insight into which properties of a material are responsible for its catalytic activity and can be used to rationalize experimental observations and inform further catalyst design. Density functional theory (DFT) is a popular quantum mechanical modeling approach that is used to gain an atomistic understanding of the structure-property relationships of a wide range of materials in the field of catalysis. DFT allows for important catalytic properties to be predicted, which can be used to rationalize experimentally observed phenomena and to guide catalyst discovery. The following sections highlight the relevant thermodynamic and kinetic phenomena that govern aqueous-phase hydrogenation of aromatics.

1.2.1 Reaction Mechanism Governing Bio-Oil Hydrogenation

Developing an accurate kinetic model for bio-oil hydrogenation helps us understand how relevant thermodynamic and kinetic phenomena affect a catalyst's performance. Aqueous-phase ECH and TCH of phenol,[19,21–25] benzaldehyde,[11,19,21] and furfural[19] has been studied experimentally on Pt and Rh. ECH and TCH of aromatics often follow a Langmuir-Hinshelwood reaction mechanism at moderate pH,[25] in which the reaction is rate-limited by a surface reaction between the adsorbed organic molecule and adsorbed hydrogen. A simple schematic of a Langmuir-Hinshelwood reaction mechanism is shown in **Figure 1-5**. In this reaction mechanism, first, both reactant species must adsorb on the catalyst surface. Next, the adsorbed molecules react on the catalyst surface to form the product. Finally, the product molecule desorbs from the catalyst surface. In the case of bio-oil hydrogenation, multiple sequential surface reactions between the adsorbed organic and adsorbed hydrogen occur before the hydrogenated product desorbs. The Langmuir-Hinshelwood model for phenol hydrogenation is discussed in depth in Chapter 3.

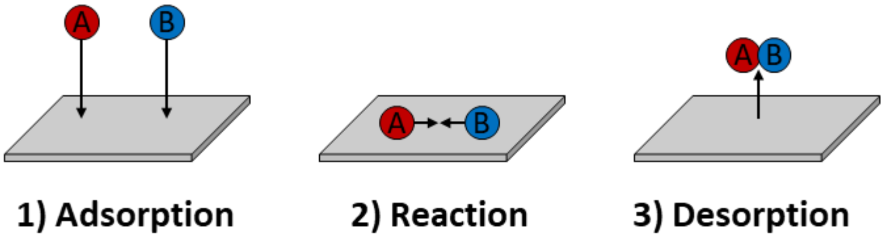

Figure 1-5 Langmuir-Hinshelwood reaction mechanism. A simplified schematic depicting a Langmuir-Hinshelwood reaction mechanism where reactant molecules adsorb on the catalyst surface, react to form a product, and desorb.

The rate of the example reaction between species A and species B depicted in **Figure 1-6** is described by **Eq. 1-1**. In this expression, k is the rate constant, K_A and K_B are the adsorption equilibrium constants of species A and B, and C_A and C_B are the concentrations of species A and B.

$$\text{rate} = k\frac{K_\mathrm{A}C_\mathrm{A}K_\mathrm{B}C_\mathrm{B}}{(1+K_\mathrm{A}C_\mathrm{A}+K_\mathrm{B}C_\mathrm{B})^2} \qquad \textbf{Eq. 1-1}$$

asThe rate constant k is related to the related to the reaction kinetics, and the adsorption equilibrium constants (K_A and K_B) are related to the adsorption thermodynamics of the species. The adsorption equilibrium constant K_A is related to the adsorption free energy of species A (ΔG_A) through **Eq. 1-2**. K_B follows a similar relationship. In this expression R is the ideal gas constant and T is temperature.

$$K_A = \exp\left(\frac{-\Delta G_\mathrm{A}}{RT}\right) \qquad \textbf{Eq. 1-2}$$

Because the reaction rate is closely related to the adsorption energies of the reactant species, it is essential to be able to accurately predict adsorption properties to construct an accurate kinetic model. For bio-oil hydrogenation, the rate depends on the properties of the bio-oil molecule and hydrogen, instead of the representative species A and B used in the model above. Therefore, understanding how bio-oil molecules adsorb onto a catalyst surface in the aqueous-phase is critical in order to understand catalyst performance for TCH and ECH. However, accurately predicting aqueous-phase adsorption energies is challenging due to the complexity of the solvent environment. Computational approaches for predicting aqueous-phase adsorption energies of model bio-oils are discussed in Section 1.2.2.

1.2.2 Predicting Aqueous-Phase Adsorption Energies

Accurately predicting adsorption energies of aromatic and organic molecules on metal and alloy catalysts in the aqueous phase is challenging despite its relevance to many catalytic reactions such as biomass hydrogenation. Adsorption is a fundamental process in which an atom or molecule binds to the surface of a material. The energetics, stability, and reactivity of a molecule changes upon binding to a catalyst surface; therefore, knowledge of adsorption is often the first step in understanding a range of other properties. Although adsorption energies are generally well understood in the gas phase, much less is known about adsorption in the aqueous phase. This lack of understanding of aqueous-phase adsorption leads to inaccurate predictions of aqueous-phase catalytic behavior. Specifically, the adsorption energies of bio-oils dictate their surface coverages and are closely linked to reaction kinetics. Therefore, accurately predicting aqueous-phase adsorption energies is necessary to make valid predictions of reaction kinetics from first principles. To this end, numerous computational and experimental studies have investigated gas-phase and aqueous-phase adsorption on metals.

The gas-phase heat of adsorption of phenol on Pt(111) from calorimetry measurements (220 kJ mol^{-1}) is similarly reproduced from gas-phase DFT calculations.[26,27] However in the aqueous-phase, the heat of adsorption is much less exothermic than what is measured in the gas-phase. Experimentally, the aqueous-phase heat of adsorption of phenol on Pt(111) was found to be 71 kJ mol^{-1} relative a gas-phase phenol molecule, which is approximately 150 kJ mol^{-1} more endothermic than in the gas phase.[28] Similar differences between the gas-phase and aqueous-phase adsorption energies were observed for other bio-oil compounds such as benzaldehyde.[11,29] The large difference between gas-phase and aqueous-phase adsorption is caused, in part, by the solvation of reactant molecules and the catalyst surface as well as the competition between solvent molecules and the organic for adsorption sites.[30–33] Solvent effects must be accurately described by DFT models in order for aqueous-phase adsorption energy predictions to agree with experimentally measured values.[34] **Figure 1-6** highlights the difference between adsorption in the gas-phase and adsorption in the aqueous phase, where the organic molecule must interact with solvent the solvent environment. Adsorption in the solution phase is more complex than in the gas phase due to solvation of the adsorbate, displacement of solvent molecules from the metal surface, and additional effects such as hydrogen bonding between water and the adsorbate.

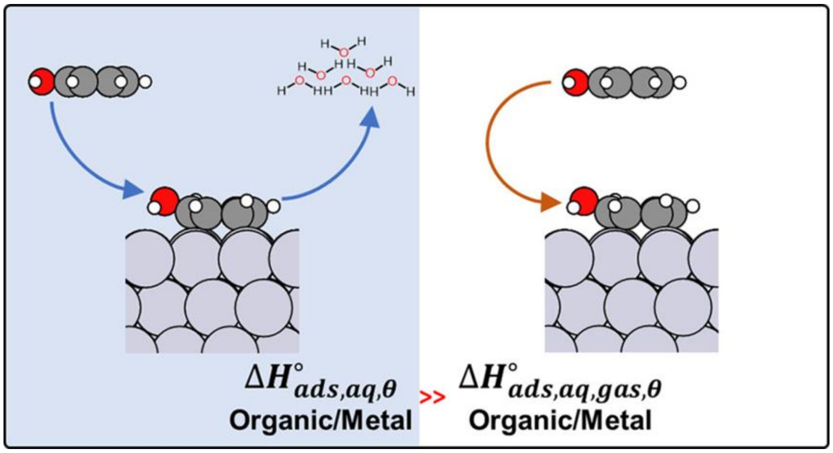

Figure 1-6 Gas-phase and aqueous-phase adsorption. The aqueous phase adsorption enthalpy of phenol ($\Delta H^{\circ}_{ads,aq,\theta}$) is less exothermic (more positive in energy) than the gas-phase adsorption enthalpy of phenol ($\Delta H^{\circ}_{ads,aq,gas,\theta}$) because of complex solvent effects. Adapted from ref [35].

There are various computational strategies to describe solvent effects including implicit solvation models, explicit solvation models, and hybrid approaches.[34,36–38] **Figure 1-7** illustrates implicit, explicit, and hybrid approaches for the solvation of methanol. Implicit solvation models treat solvent as a polarizable continuum and describe electrostatic solvent effects, although they fail to capture effects such as hydrogen bonding which can only be captured through explicit modeling of water.[34,39] Previously, the adsorption of phenol and benzaldehyde on Pt(111) in the aqueous-phase was studied using VASPsol,[40,41] a popular implicit solvation model implemented in the Vienna Ab initio Simulation Package (VASP) code.[42,43] Iyemperumal and Deskins found that adsorption of gas-phase phenol and benzaldehyde in the aqueous phase is more exothermic than gas-phase adsorption on Pt(111).[44] This finding contradicts the experimental observation that adsorption of bio-oils is much less exothermic in aqueous phase compared to gas phase, highlighting the limitations of implicit solvation models for predicting adsorption energies of large organics, especially if the free energy for cavitation is not carefully parameterized in these implicit models.[34] Implicit solvation models tend to perform better for small organic molecules, and their accuracy for larger molecules can be improved through proper parameterization of the solvation model.[45]

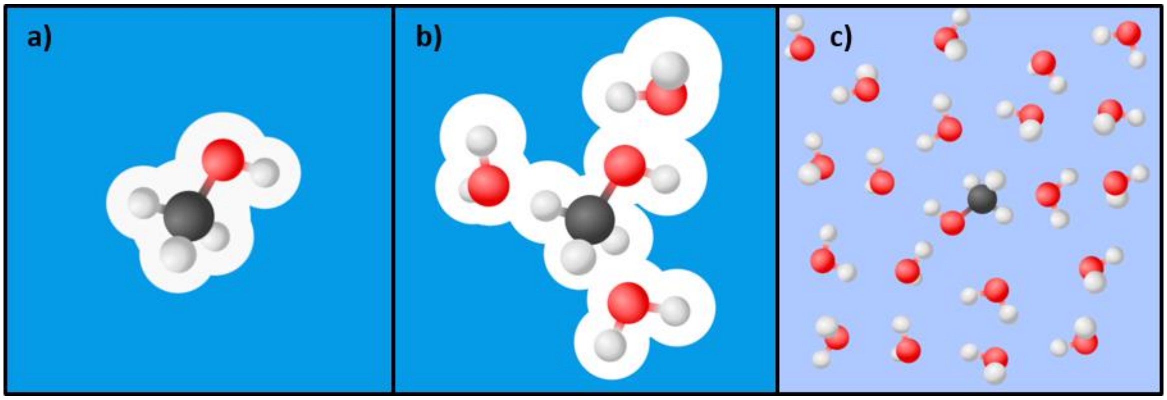

Figure 1-7 Implicit solvation, microsolvation, and explicit solvation approaches. **a)** The solvation of methanol using an implicit solvation approach where all solvent is treated using a dielectric continuum model. **b)** The solvation of methanol using a microsolvation model where the local solvent environment around methanol is modeled using explicit water molecules and the long-range solvent environment is modeled using an implicit model. **c)** The solvation of methanol where all solvent molecules are explicitly modeled. Adapted from ref [36].

Aqueous-phase adsorption can be evaluated more rigorously using explicit solvent modeling techniques such as molecular dynamics paired with enhanced sampling techniques such as umbrella sampling,[46–48] thermodynamic integration,[49,50] or metadynamics.[36,51–53] In these approaches, solvent−solvent, solvent−organic, solvent−metal, and organic−metal interactions can either be described classically through the use of empirical force fields, through first-principles electronic structure calculations, or through a combination of the two (referred to as quantum mechanics/molecular mechanics (QM/MM)).[34,54–58] One of the challenges in classical molecular dynamics is the lack of force fields parameterized to accurately describe the interactions present in many aqueous-phase catalytic systems involving aqueous solvent, organics, and metals.[59,60] First-principles based molecular dynamics simulations do not need to be parameterized, however, they are computationally expensive, which limits the system size and time scales that may be explored.[34,44] A QM/MM approach, where interactions in the local environment around the molecule of interest are treated quantum mechanically and long range solvent effects are treated classically, can speed up simulation times, but these calculations still rely on properly parameterized force fields.[54–57] The aqueous-phase adsorption energy of phenol on Pt(111) was calculated with QM/MM with close agreement to experimental measurements.[55] However, the force field used for these calculations is currently only parameterized for interactions between water and the (111) and (100) facets of Au, Ag, Cu, Pt, and Pd.[61,62] Without the development of additional force fields, classical molecular dynamics and QM/MM approaches are currently limited to a small catalyst design space.

Singh and Campbell developed a bond-additivity model to explicitly account for formation of water−organic bonds and organic−metal bonds as well as the breaking of water−water and water−metal bonds in order to predict aqueous-phase adsorption energies based on experimental gas-phase measurements or DFT calculations.[63] Using this model the aqueous-phase adsorption energy of organics on surfaces can be quickly predicted using tabulated thermodynamic properties like the surface energy, enthalpy of vaporization of liquid water, and solvation energy of the organic in addition to the adsorption enthalpies of water and the organic from gas-phase calorimetry measurements or DFT calculations.[64,65] **Figure 1-8** shows the individual steps involved in estimating the aqueous-phase adsorption energy using the bond-additivity model. In the first step, water−water bonds are broken to separate the bulk water from the water adsorbed on the metal surface. The energy for this step is accounted for using the surface energy of liquid water. In the second step, the adsorbed layer of water is displaced in the gas phase to expose the bare metal surface. The gas-phase enthalpy of adsorption of water on is used to account for the energy of this step. In the third step, water is condensed back into the liquid phase, and the enthalpy of vaporization of water is implemented to account for this step. In the fourth step, the gas-phase adsorption enthalpy of the organic on the surface from calorimetry or DFT calculations can be used to account for the energy of phenol adsorption on the surface. Finally, water−organic interactions are accounted for using a combination of the water surface energy and the solvation enthalpy of the organic. Additional details about the derivation of this model and its application for phenol adsorption on Pt(111) are reported in ref [63]. The application of this model for predicting aqueous-phase adsorption energies of model bio-oils is discussed in detail in Chapter 2.

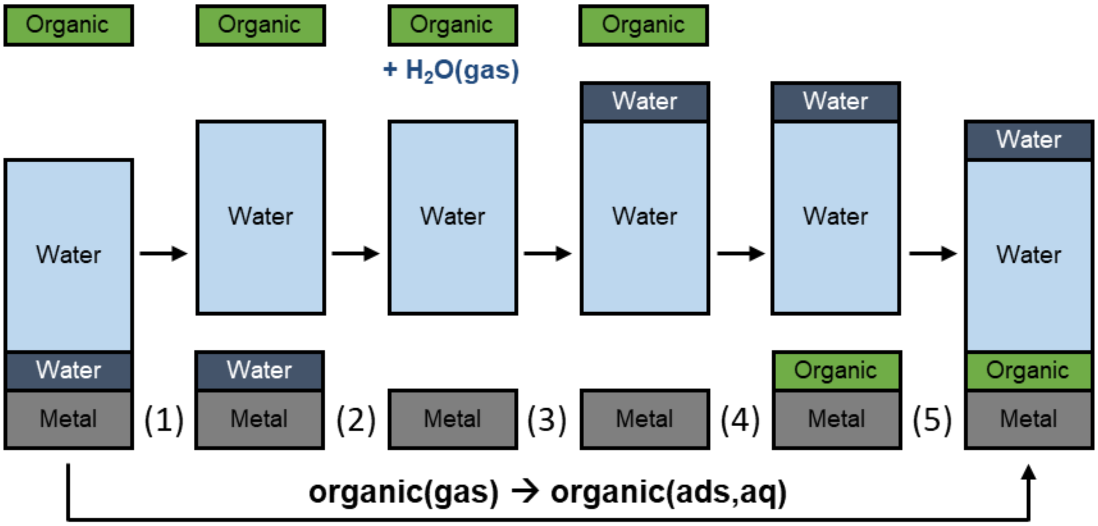

Figure 1-8 Bond-additivity model used to predict aqueous-phase adsorption energies of organics. Bond-additivity model which accounts for (1) the breaking of water−water bonds, (2) the displacement of solvent from the surface, (3) the condensation of water into the liquid phase, (4) the formation of organic−metal bonds, and (5) the formation of water−organic bonds. Adapted from the figures in ref [63].

This bond-additivity model is a powerful tool that allows for the rapid prediction of aqueous-phase adsorption properties of molecules when adequate gas-phase data is available. Because this model relies on measured or calculated adsorption energies (or adhesion energies) of organics and solvents on the specific surface in question, the model is limited to systems with existing adsorption data. Density functional theory calculations allow for the model to be applied to new organics, because predictions of gas-phase adsorption behavior of organics can be obtained much more quickly than they can be with experimental calorimetry measurements. Unfortunately, accurate solvent adsorption or adhesion energies are difficult to obtain both computationally and experimentally, which limits the extension of the model to new surfaces and facets. Adhesion energies of methanol, acetic acid, water, benzene, and phenol were measured on Pt(111) and Ni(111), allowing the bond-additivity model to be applied to Ni(111) and Pt(111) for a variety of solvents.[66] The adhesion energy of a solvent on a surface is the adsorption energy per unit area. Despite the model's generalizability for a variety of solvents and surfaces, the lack of solvent adsorption or adhesion data limits the ability of this model to be rapidly applied to novel systems. Despite the myriad computational models for describing solvent effects and predicting aqueous-phase adsorption behavior of molecules, balancing the accuracy of a model with its computational cost is a remaining challenge in the domain.

1.2.3 Understanding Bio-Oil Hydrogenation through Computational Modeling

A fundamental understanding of the elementary reaction steps of bio-oil hydrogenation on metals and alloys is important to build accurate kinetic models from first-principles modeling and rationalize catalytic activity. The reaction rate described by the Langmuir-Hinshelwood model (**Eq. 1-1**) is dependent on both the adsorption thermodynamic properties as well as the reaction rate constant, k, which is dependent on the activation barriers for hydrogenation. Reactions with lower activation barriers have faster intrinsic kinetics than reactions with higher activation barriers. Activation barriers for hydrogenation can be readily calculated with DFT. Modeling the elementary reaction steps for bio-oil hydrogenation allows us to compare possible reaction pathways, determine the rate-determining step in a given reaction mechanism, and gain insight about the relative rates of reactions on different surfaces.

The hydrogenation of phenol has been studied computationally on Pt(111), and the reaction mechanism was elucidated.[67,68] In the aqueous-phase, phenol is first hydrogenated to form cyclohexanone, which can be further hydrogenated for form cyclohexanol.[12,69,70] Two reaction mechanisms for the formation of cyclohexanone and cyclohexanol were modeled by using DFT to calculate the energetics of the elementary reaction steps.[68] **Figure 1-9** shows two possible reaction pathways in which phenol is hydrogenated to form cyclohexanone and cyclohexanol. In one pathway, phenol is hydrogenated to form 1-cyclohexenol, which undergoes a tautomerization reaction to form cyclohexanone. In the other pathway, phenol dissociates to form an adsorbed phenoxy intermediate, which is sequentially hydrogenated to form cyclohexanone. DFT analysis shows that on Pt(111), the dissociation of phenol to phenoxy was not thermodynamically or kinetically favorable and that the hydrogenation on Pt(111) would likely proceed through the first pathway.[68] However, the dissociation of phenol on metals like Pd and Rh is thermodynamically favorable,[26,68] highlighting the necessity of mechanistic modeling when exploring bio-oil hydrogenation on new materials. The construction of detailed mechanistic models using DFT can provide critical insight into reactions and the calculated energies can provide a basis to rationalize plausible reaction mechanisms and compare the performance of various catalysts for a given reaction.

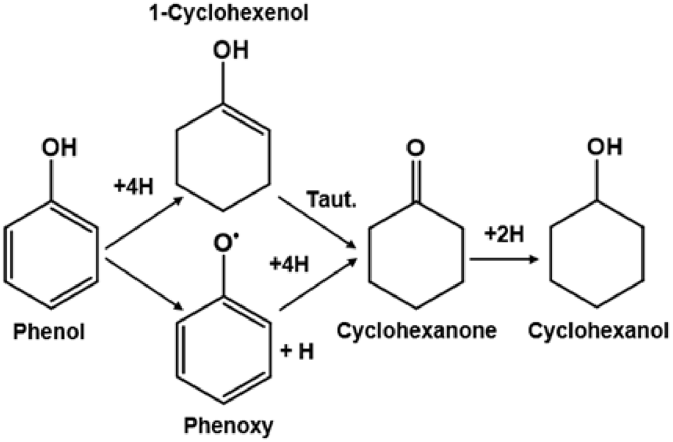

Figure 1-9 Comparison of mechanisms for phenol hydrogenation. (Top) Hydrogenation of phenol to cyclohexanone and cyclohexanol via tautomerization (taut.). (Bottom) Hydrogenation of phenol via a phenoxy intermediate.

Solvent influences the adsorption thermodynamics of bio-oil molecules and can influence hydrogenation barriers by solvating transition states and by participating in the reaction mechanism.[33] Multiple studies have compared the mechanisms for gas-phase and aqueous-phase hydrogenation of bio-oils.[71–74] The presence of an aqueous solvent environment reduces the activation barriers for the cleavage of O−H bonds and hydrogenation of C=O bonds because of their strong interactions with water, which can facilitate the reaction between surface-adsorbed hydrogen or H^+ in solution and the O–H and C=O groups.[71–73] However, water has a negligible effect on the barriers for hydrogenation of C=C bonds, which are hydrophobic in nature.[73] The hydrogenation of C=C bonds primarily proceeds through a surface-mediated pathway between the adsorbed organic and adsorbed H* rather than through a solution-mediated pathway.[73] The hydrogenation of many bio-oil compounds are rate-limited by the surface hydrogenation of C=C bonds,[11,75,76] but some elementary reaction steps, particularly those containing polar groups, require rigorous evaluation of solvation effects to properly capture reaction kinetics. Implicit solvation models do not describe hydrogen bonding, and cannot be used to accurately model elementary steps where water participates directly in the reaction mechanism.[71] Therefore, when modeling bio-oil hydrogenation, it is important to understand the reaction mechanism, particularly the steps that contribute the most to the overall rate, to determine which modeling approaches are most appropriate to calculate reaction energetics.

Chapter 2 Adsorption Energies of Organics on Pt and Rh in the Aqueous Phase

This chapter was adapted from Akinola, J.; Barth, I.; Goldsmith, B. R.; Singh, N. Adsorption Energies of Oxygenated Aromatics and Organics on Rhodium and Platinum in Aqueous Phase. *ACS Catal.* **2020**, *10* (9), 4929–4941. My contribution to this work is the density functional theory modeling. James Akinola performed the experimental work.

2.1 Introduction

Over 143 billion gallons of motor gasoline are consumed annually within the USA to power transportation, emitting huge amounts of greenhouse gases like CO_2.[77] The need to supply energy for transportation in a sustainable manner has spurred efforts to replace fossil fuels with renewable and CO_2-neutral transportation fuels. One promising strategy is to produce transportation fuels from lignin biomass waste.[5,78–80] Converting the oxygenated aromatic compounds in water that come from fast pyrolysis of lignin (i.e., bio-oil) to transportation fuels or chemical precursors requires aqueous-phase catalytic or electrocatalytic hydrogenation and hydrodeoxygenation,[81] typically rate-limited on metals by surface reactions. To improve the kinetics of these and other aqueous-phase catalytic reactions, an understanding of the effect of water (or solvent) on organic adsorption is critical, because adsorption energies can determine coverages and alter activation barriers.

Although adsorption energies on metals are generally well understood in the gas phase, much less is known about adsorption in the aqueous phase. This lack of knowledge about adsorption in the aqueous phase is problematic for catalyst design because gas-phase adsorption energies often cannot be used to explain aqueous-phase catalytic activity trends. For example, the experimental gas-phase adsorption of phenol on Pt(111) is so strong (-220 kJ mol^{-1})[65] that room-temperature hydrogenation would seem unlikely to occur because of site poisoning by phenol, yet phenol hydrogenation on Pt occurs in the aqueous phase at room temperature.[12,23,75,82,83] Also, Pt(111) and Rh(111) are predicted by density functional theory (DFT) modeling to have a ~50 kJ mol^{-1} difference in their adsorption energy of phenol in the gas phase,[26] but have similar aqueous-phase hydrogenation turnover frequencies (TOFs) and apparent activation barriers.[22,23] Recent work shows that the aqueous-phase heat of adsorption of phenol on a Pt(111)-like surface is much smaller than in the gas phase,[28] which was attributed to the enthalpy associated with the displacement of multiple water molecules from the Pt surface upon adsorption of phenol and described by a bond-additivity model.[63] This more moderate adsorption energy of phenol is consistent with the aqueous hydrogenation activity observed at room temperature. Here we specifically: (1) extend the bond-additivity model to four new molecules on Pt(111) terraces and also to three new surfaces, Rh(111) terraces, Rh(110) steps, and Pt(110) steps; (2) confirm the adsorption of these molecules is reversible, which is a requirement for extracting adsorption energies using adsorption isotherms; and (3) perform a DFT analysis for all studied molecules to compare quantitatively with our measurements. To our knowledge, this is the first direct comparison of DFT-computed adsorption energies with experimentally extracted values for these molecules and surfaces in the aqueous phase. Each of these aspects improves upon previous studies and taken together provide a more advanced study of molecule adsorption in the aqueous phase than prior work.[28,63,84]

In this work, we report adsorption enthalpies and free energies on Pt and Rh for select US Department of Energy platform chemicals that serve as bio-oil model compounds. Specifically phenol, benzaldehyde, and furfural,[17] as well as two hydrogenated products—benzyl alcohol and cyclohexanol—in aqueous phase on polycrystalline Rh and Pt wires are studied using cyclic voltammetry (CV) and DFT modeling. We use CV to measure the charge from reversible hydrogen underpotential deposition (H_{upd}) and desorption ($H^+ + e^- + * (\mathrm{Metal}) \rightleftarrows H^*$)[85–87] on polycrystalline Rh and Pt without organics present and with increasing organic concentration. The decrease in H_{upd} charge due to adsorbed organics[75,88–90] is used to estimate the organic coverage as a function of organic concentration and construct adsorption isotherms.[28] Aqueous-phase adsorption equilibrium constants are extracted using a Temkin adsorption model to fit the adsorption isotherms. Enthalpies are determined from the Gibbs free energies of adsorption as previously described.[28] Adsorption enthalpies and free energies of these organics on Pt and Rh surfaces are also predicted using DFT modeling and a bond-additivity model to compare with experimental values.

Ultimately, our work finds that the heats of adsorption of organics in the aqueous phase are reduced by 50–250 kJ mol^{-1} compared with their gas-phase values because of the enthalpic penalty of displacing several water molecules upon adsorption. This weaker adsorption explains why surface reactions of organics that bind too strongly to react in the gas phase can occur at room temperature in water. Additionally, we show that unlike in gas phase, Rh and Pt have similar adsorption energies in aqueous phase for phenol, benzaldehyde, and their reaction intermediates. This similar adsorption energy in aqueous phase could be responsible for the comparable aqueous hydrogenation activity of these molecules observed on Pt and Rh. We also show that using DFT modeling with only implicit solvation overestimates adsorption energies and does not capture observed experimental trends, which prevents accurate predictions of coverages. Using a bond-additivity model combined with gas-phase DFT calculations enables more accurate predictions of aqueous adsorption energies of C5/C6 organics. These results highlight the necessity of properly accounting for the effect of solvent displacement at the metal interface when modeling adsorption of organic molecules, particularly those with large adsorption footprints such as aromatics.

2.2 Experimental & Computational Methods

2.2.1 Cyclic Voltammetry

The working electrode for the CV measurements was either a polycrystalline Pt wire (0.5 mm diameter, 99.997% Alfa Aesar) or Rh wire (0.5 mm diameter, 99.8% Alfa Aesar) and the counter electrode was a graphite rod. A two-compartment electrochemical cell with a working and reference electrode compartment and a counter electrode compartment separated by a N117® Nafion membrane was used. The working electrodes were first exposed to a flame for cleaning any adventitious organic, followed by rinsing with Milli-Q water. Before each use, the cell was cleaned with Milli-Q water and oven dried at 80 °C three times. This cleaning procedure removes trace impurities of organics that would otherwise result in inconsistent measurements from run to run. An Ag/AgCl reference electrode was calibrated to 0 V vs. reversible hydrogen electrode (RHE) in the supporting electrolyte and all potentials are reported vs. RHE based on this calibration. Acetate buffer (pH 5) containing 100 mM acetic acid (Sigma Aldrich, 99.995%) and 100 mM sodium acetate (Sigma Aldrich 99.999%) was used as the supporting electrolyte. Acetic acid is used in this work to mimic a bio-oil environment containing carboxylic acids[91] and has negligible adsorption on Pt and Rh in the H_{upd} region.[92] The working electrode compartment was filled with 130 mL of acetate buffer and sparged with N_2 (99.999%) to remove dissolved oxygen. The working electrode was further cleaned under voltammetric conditions in the potential window of −0.2 V to 1.8 V vs. RHE for 60 cycles at a scan rate of 100 mV s^{-1}. After voltammetric cleaning, CV was carried out at a 100 mV s^{-1} scan rate in the potential window of 0.05 V to 1.1 V for Rh wire and 0.05 V to 1.3 V for Pt wire. Within these potential windows the cyclic voltammograms were repeatable and reversible. There was no scan rate dependence (between 20–100 mV s^{-1}) of the H_{upd} charge on Pt[28] and less than 7% change in H_{upd} charge with scan rate on Rh (**Appendix Figure A-1** and **Appendix Table A-1**).

Organics dissolved in acetate buffer solution were introduced to the cell to increase the concentration of organics from 1 µM up to 500 mM. The organics used for adsorption studies were phenol (Sigma Aldrich, >99%), benzaldehyde (Sigma Aldrich >99%), furfural (Sigma Aldrich 99%), benzyl alcohol (Sigma Aldrich 99.8%), and cyclohexanol (Sigma Aldrich 99%). At the lowest organic concentration (1 µM), the bulk organic concentration would decrease by at most 0.2% upon adsorption of a complete monolayer of the organic onto the metal electrode, thus we assumed the bulk concentration was unchanged by adsorption (see Appendix **A.2** for calculation details). The electrolyte was stirred and re-sparged with N_2 to remove oxygen prior to CV measurements for each organic concentration. The working electrode was continuously cycled in the same potential window between each CV measurement (0.05 V to 1.1 V for Rh and 0.05 V to 1.3 V for Pt). The CV measurements were repeated under the conditions specified at each organic concentration until steady state was reached. The charge from chemisorbed hydrogen in the H_{upd} region (0.05 V–0.35 V) was obtained by integrating the area under the desorption peaks in the CV, dividing by the scan rate, and then subtracting the baseline capacitive charge calculated from the double layer charging region of the CV. With phenol present, the H_{upd} charge from H* adsorption and desorption match closely on Pt (**Appendix Figure A-2a**). On Rh, the H adsorption region had a contribution from the Rh_2O_3 reduction peak,[85] causing the apparent adsorption charge to be larger than the desorption charge (**Appendix Figure A-2b**), hence the H_{upd} desorption peak was used instead to estimate the amount of chemisorbed hydrogen on both Rh and Pt.

2.2.2 Dilution of Organic Concentration to Determine Reversibility

To test whether organic adsorption was reversible, after taking a cyclic voltammogram at a given organic concentration the organic concentration was diluted by removing a given volume of the existing solution and replacing with the same volume of acetate buffer supporting electrolyte while the working electrode containing the adsorbed organic was kept in place under a continuous blanket of N_2. After dilution, the working electrode was cycled at the normal potential window used for H_{upd} measurements until the adsorbed organic reached equilibrium with the diluted cell solution concentration (indicated by a stable CV). This stable CV at the diluted concentration was compared to measurements done at the same concentration, but without previously going to higher organic concentrations.

2.2.3 Adsorption Isotherm Fitting

Each isotherm was fit by a one site or two site model using the same procedure from ref [28]. Briefly, the equilibrium constant of adsorption $K_{eq,ads,\theta}^{aq}$ for each site was obtained by fitting the fraction of H_{upd} inhibited at different organic concentrations to a Temkin isotherm (**Eq. 2-1**), where the saturation coverage for site 1 was the coverage (θ) where the first plateau is seen, and the saturation coverage of site 2 was the second plateau. $\Delta G_{ads,aq,\theta=0}^{0}$ is the adsorption free energy of the aqueous organic at zero coverage, R is the ideal gas constant, and T is the temperature. Several models can be used to fit the adsorption isotherm, such as the Langmuir-Hinshelwood (LH) model where metal surface sites can either be unoccupied, have adsorbed hydrogen, or have adsorbed organic. Instead of a LH model, we used a modified Langmuir model where the organic adsorption energy varies linearly with the coverage because of adsorbate-adsorbate interactions (also known as the Temkin model).[93,94] The Temkin model assumes that the coverage of organic does not depend on adsorbed H in the reversible H_{upd} region but depends only on the bulk organic concentration and the organic equilibrium adsorption constant. This model is used because of its simplicity compared to the LH model. Recently, a LH model was used to fit kinetics for Pt/C for aqueous-phase phenol hydrogenation over a range of phenol concentrations, resulting in an equilibrium constant for phenol of 33 (standard-state concentration of 1 M phenol, as used here).[21] This value is similar to the adsorption equilibrium constant of 38 measured for phenol/Pt(111) using the Temkin model,[28] supporting the accuracy of the Temkin model used for this work. Additional discussion about the isotherm derivation and fitting is provided in Appendix **A.6**.

$$K_{eq,ads,\theta}^{aq} = \exp\left(\frac{-\Delta G_{ads,aq,\theta=0}^{0} + \alpha\theta}{RT}\right) \qquad \textbf{Eq. 2-1}$$

Ideally the measurements would be done as a function of surface charge on both Pt and Rh to determine the influence of the surface charge of the metal electrode on the water layer and organic adsorption[95,96] or at a potential where maximum organic adsorption is reached, often slightly cathodic to the potential of zero charge.[97] However, the H_{upd} technique inherently cannot be done at a single potential but requires cycling over a range of potentials. Hence, our reported values may be underpredictions of the organic adsorption strength relative to the adsorption on an uncharged surface. Despite this, there is still general agreement between the adsorption energies extracted through this method and solution calorimetry, as well as gas-phase calorimetry once the effects of the water layer on the metal surface have been accounted for.[63]

2.2.4 Computational Methods

Density functional theory (DFT) calculations were done using the Vienna Ab Initio Simulation Package (VASP).[42,43] All DFT calculations were non-spin polarized because spin polarization was found to have 0.14% and 0.43% average change in the organic and water adsorption energies, respectively, on Pt and Rh in gas phase. The Perdew-Burke-Ernzerhof functional with the semi-empirical D3 dispersion correction (PBE-D3) was used because of its good trade-off between computational cost and accuracy, although PBE-D3 has been shown to overestimate adsorption strengths of aromatics.[98–101] Projector-Augmented Wave pseudopotentials[102] were used with a kinetic energy cutoff at 400 eV. The convergence criteria for electronic and ionic forces were set to 10^{-5} eV and 0.01 eV Å^{-1}. Atomic structures were geometry optimized using either the conjugate-gradient algorithm or the quasi-Newton algorithm. Lattice parameters of bulk Pt and Rh were determined by relaxing a four-atom face-centered cubic cell of each metal. A 15×15×15 Monkhorst-Pack *k*-point grid was used for bulk relaxations. The calculated lattice parameters were 3.925 Å and 3.792 Å for Pt and Rh and are within 1.2% and 0.1%, respectively, of the experimentally determined values.[103,104]

The adsorption enthalpies of phenol, benzaldehyde, furfural, benzyl alcohol, and cyclohexanol were predicted on (111) terraces and the (110)-like and (100)-like steps of the (553) and (533) surfaces, respectively. Throughout this text we refer to the steps of the (553) and (533) surfaces simply as (110) and (100). The surface slab models of Pt and Rh were modeled using 4×4 supercells that were four layers thick. For all considered surfaces, the top two layers could relax during geometry optimization, whereas the bottom two layers were fixed in their bulk coordinates. Metal slabs were separated by a 20 Å vacuum in the direction perpendicular to the surface. A 3×3×1 Monkhorst-Pack *k*-point grid was used for adsorption energy calculations of organics on 4×4 slabs corresponding to a 1/16 monolayer (ML) coverage. A 5×5×1 Monkhorst-Pack *k*-point grid was used for adsorption energy calculations of organics on 3×3 slabs corresponding to a 1/9 ML coverage. Spurious dipole interactions between periodic images were corrected in VASP (IDIPOL = 3, LDIPOL = True).

A variety of implicit and explicit modeling approaches have been used to treat the water-adsorbate-metal interface to enable prediction of thermodynamic and kinetic parameters for aqueous-phase reactions.[30,34] Explicit treatment of water through classical,[105] ab initio,[72] and hybrid[54] molecular dynamics calculations has been employed to describe water-adsorbate-metal interactions at the interface, although these approaches are computationally demanding because they require sampling over long time scales. Alternatively, simple ice-like layers have been used to explicitly model water, although this approach is too crude to accurately describe the water-adsorbate-metal interactions at standard electrochemical conditions.[105] In place of explicit solvent modeling, adsorption energies may be calculated using computationally inexpensive implicit solvent models.[44,106]

Two approaches—an implicit solvent model using the VASPsol model[40,107] and a bond-additivity model recently published by Singh and Campbell[63]—were used in this study to model solvation effects. VASPsol, which was developed to treat solvated molecules and nanocrystal surfaces, models the interactions between solvent and solute by using DFT to describe the solute explicitly and the linear Poisson-Boltzmann equation to describe the solvent as a continuum dielectric. In this work the water solvent was implicitly treated using the default VASPsol parameters (see **A.7** for gas-phase, implicit solvent, and thermodynamic calculations). The bond-additivity model, which accounts for the formation of water-organic bonds as well as the breaking of water-water and water-metal bonds, was originally developed to estimate the aqueous-phase adsorption energy of phenol on Pt(111) based on the experimental gas-phase adsorption energy.[63]

Here, the bond-additivity model (**Eq. 2-2**)[63] was used to estimate the aqueous-phase adsorption enthalpies of all organic molecules considered at 298.15 K and 1 atm.

$$
\begin{aligned}
-\Delta H^0_{ads,aq,gas,R/M} & \\
&= -\Delta H^0_{ads,gas,R/M} + n\left(\Delta H^0_{ads,gas,water/M} + \Delta H^0_{vap}\right) \qquad \textbf{Eq. 2-2} \\
&- 2\gamma_{water(liq)}\sigma_R + (water\text{-}R)
\end{aligned}
$$

$\Delta H^0_{ads,aq,gas,R/M}$ is the adsorption enthalpy of gas-phase organic R onto metal M in the aqueous phase, $\Delta H^0_{ads,gas,R/M}$ is the adsorption enthalpy of gas-phase organic R onto metal M in the gas phase, n is the number of water molecules displaced from metal M upon organic adsorption, $\Delta H^0_{ads,gas,water/M}$ is the adsorption enthalpy of a water molecule onto metal M in the gas phase, ΔH^0_{vap} is the vaporization enthalpy of water, $\gamma_{water(liq)}$ is the surface energy of liquid water, σ_R is the area of an adsorbed organic molecule, and $water\text{-}R$ is $-1/2\Delta H_{Solv,R} + \gamma_{water(liq)}\sigma_R$, where $\Delta H_{Solv,R}$ is the solvation enthalpy of the organic in water. For simplicity, in the subsequent text we omit R or R/M when it is clear which metal and organic are being referred to (e.g., we refer to $\Delta H^0_{ads,aq,gas,R/M}$ as $\Delta H^0_{ads,aq,gas}$). A similar equation using experimental adhesion energies (rather than our calculated values) of aqueous and non-aqueous solvents is presented in ref [66], but as the adhesion energy of water on Rh is not experimentally available we use **Eq. 2-2** here. Conceptually these equations are the same bond-additivity model.

The number of water molecules displaced upon organic adsorption, *n*, was calculated for each molecule on each surface by studying the heat of adsorption as a function of organic coverage using the bond-additivity model (details provided in Appendix **A.11**). Treating each modeled coverage as saturation, n was calculated over a range of organic coverages. In subsequent applications of the bond-additivity model, we choose the *n* that corresponds to the coverage at which the heat of adsorption reaches a maximum. Using this method, we find that phenol adsorbs on Pt(111) at 1/9 ML coverage (9 Pt atoms per phenol molecule) and displaces 6.5 water molecules assuming a water coverage of 0.72 ML.[64] This phenol coverage on Pt(111) matches the coverage in aqueous phase determined from quantitative Auger electron spectroscopy measurements,[108] and the value of 6.5 water molecules is the same as used in our previous bond-additivity model for phenol on Pt(111) using experimental values.[63] Therefore, we believe our computational approach is reasonable for estimating the number of water molecules displaced from the Pt(111) terrace upon adsorption of phenol, and we apply it to the other organics on Pt(111) and Rh(111) terraces. Because it is difficult to vary organic coverage on stepped surfaces, we calculate *n* on (110) and (100) terraces and assume that *n* is the same on the respective steps. Although, the value of *n* on stepped surfaces may be evaluated more rigorously using ab initio molecular dynamics, this computationally demanding approach was not employed in this current work. Since *n* is not calculated explicitly on (110) and (100) steps, predicted heats of adsorption on the stepped surfaces are not as accurate as the heats of adsorption on the (111) terrace.

2.3 Results & Discussion

2.3.1 Impact of Phenol on the Underpotential Deposition of Hydrogen on Pt and Rh

The data in **Figure 2-1** shows that H_{upd} on a Pt wire and a Rh wire is inhibited by phenol adsorption, which implies competitive adsorption between H* and phenol* on the surfaces of both metals in the aqueous phase. The cyclic voltammograms with phenol for the Pt wire (**Figure 2-1a**) match those measured previously, where the difference in H_{upd} charge on Pt with and without phenol was used to quantify the coverage of adsorbed phenol.[28,75] On Rh, the H_{upd} charge, proportional to the H* desorption peak area in the potential range 0.05–0.35 V, also decreases with increasing phenol concentration (H_{upd} charge values are shown in **Appendix Figure A-2**). Similar to Pt, we attribute the decreasing H_{upd} charge to blocking of Rh sites by adsorbed phenol, resulting in fewer sites available for hydrogen to adsorb. Hydrogen underpotential deposition on Rh in acetate buffer without phenol is kinetically fast and reversible within the potential window used in this work, shown by the symmetry of the reduction and oxidation peaks associated with H_{upd} and the H_{upd} charge independence on scan rate (**Appendix Figure A-1** and **Appendix Table A-1**). The H_{upd} on Rh and Pt is also reversible when phenol is present (**Appendix Figure A-2**), indicating that H* does not react with adsorbed phenol during these scans. The change in H_{upd} charge with phenol concentration is reproducible (**Appendix Figure A-3** and **Appendix Table A-2**).

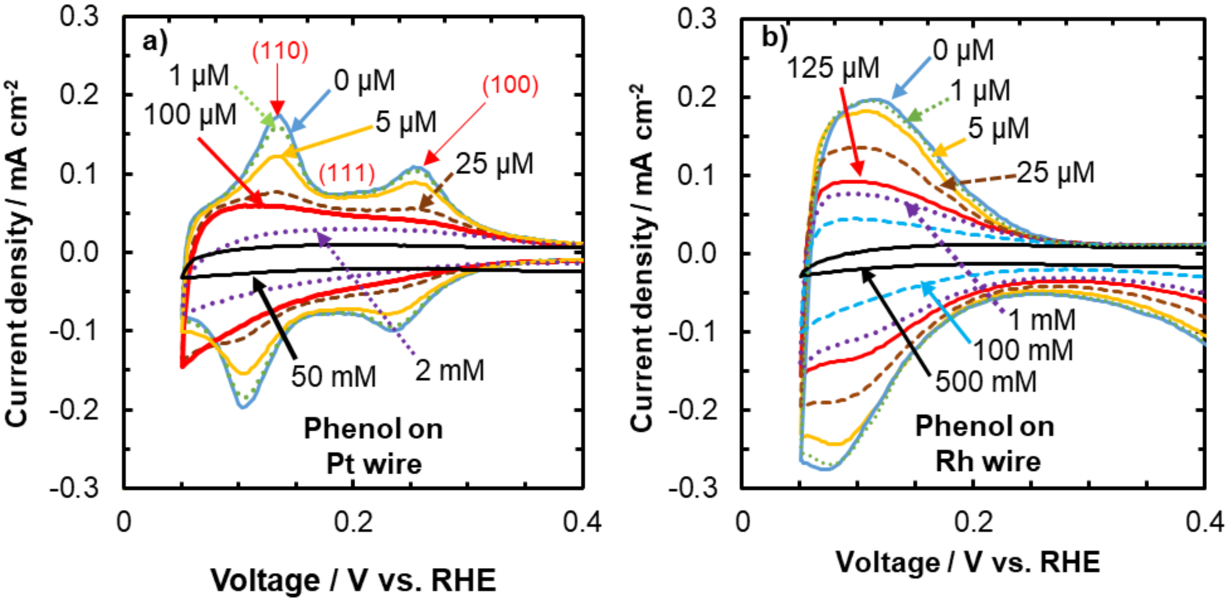

Figure 2-1 Cyclic voltammograms on Pt and Rh wire. Cyclic voltammograms showing the H_{upd} region at different bulk phenol concentrations on **a)** platinum wire and **b)** rhodium wire. The H_{upd} current peaks attributed to Pt(110) steps and Pt(100) steps and the broad region corresponding to Pt(111) terraces are labeled. The H_{upd} peaks corresponding to different Rh facets overlap with one another. The cyclic voltammograms were taken in 100 mM acetate buffer supporting electrolyte (pH 5) at 298 K and using 100 mV s^{-1} scan rate. Phenol competes with H* adatoms for metal sites, hence the drop in area under the H_{upd} adsorption and desorption peaks as phenol concentration increases.

The polycrystalline Pt and Rh wires have different H_{upd} peak shapes, based on how H* interacts with the different surface facets. The peak voltages for Pt in **Figure 2-1a** are consistent with prior polycrystalline Pt studies,[28,75] and individual H_{upd} peaks have been identified on Pt single crystals in 0.1 M H_2SO_4 and $HClO_4$.[90,109] These studies indicate the peak located at ~0.10–0.15 V is from Pt(110) steps, the peak at ~0.23–0.3 V is from Pt(100) steps, and the broad feature that underlies the two peaks from ~0.05–0.35 V is from Pt(111) terraces. Contributions from H_{upd} on (111) steps, (110) terraces, and (100) terraces on Pt are at CV peak locations that overlap with those of (111) terraces, (110) steps, and (100) steps.[110–114] Unlike on Pt, the H_{upd} peaks all overlap for the facets of polycrystalline Rh[85] (i.e., Rh(110),[115] Rh(100),[116] and Rh(111)[116–118]). Consequently, a single adsorption/desorption peak is observed for H_{upd} on Rh wire in 0.1 M acetate buffer, **Figure 2-1b**. This overlap of H_{upd} peaks from the different facets of Rh, attributed to the similar hydrogen adsorption free energies on the different facets, makes deconvolution of organic adsorption on the different facets from H_{upd} alone difficult.

Adsorbed phenol blocks H_{upd} across the Pt facets to different extents, with the Pt(110) peak decreasing more than the Pt(100) peak for the same phenol concentrations, whereas the broad Pt(111) feature drops the least at concentrations between 1 μM and 100 μM (**Figure 2-1a**). Therefore, the Pt(110) and Pt(100) steps adsorb phenol stronger than the Pt(111) terrace, in agreement with a prior report.[28] In **Figure 2-1b**, any differences in phenol adsorption on the different facets of Rh wire are not immediately evident since the H_{upd} peaks of Rh(110), Rh(100), and Rh(111) cannot be distinguished. Nonetheless, we will show below based on the shape of the adsorption isotherm that there are also two distinct types of adsorption sites on Rh.

First, the inhibition of H_{upd} charge as a function of phenol concentration (**Figure 2-1**) can be used to extract adsorption energies using an adsorption isotherm, so long as the H_{upd} process remains reversible in the presence of phenol and phenol adsorption is an equilibrated, reversible process. We show that the H_{upd} oxidation and reduction charges match both in the absence of phenol and with phenol present (**Appendix Figure A-2**), proving reversible H^+ reduction and H* oxidation. This observation matches the report that phenol is reduced on Pt and Rh only at lower potentials (< 0 V vs. RHE) than applied in this work.[12] To test whether the adsorption of organics on Pt and Rh is reversible we measure the H_{upd} charge at a certain bulk organic concentration, then dilute the bulk concentration to see if the H_{upd} charge recovers to that associated with the new (lower) bulk organic concentration (**Appendix Figure A-4**). The observation that H_{upd} charge and thus phenol coverage is recovered (**Appendix Table A-3**), i.e., there is no hysteresis in the adsorption isotherms, implies phenol adsorption is an equilibrated, reversible process. The data in **Appendix Figure A-4** show that other organics also adsorb/desorb reversibly on both Pt and Rh.

2.3.2 Extracted Adsorption Energies of Phenol on Platinum and Rhodium

Having fulfilled both criteria for reversibility as discussed above, the adsorption isotherms of phenol on Pt and Rh shown in **Figure 2-2** were constructed by plotting the fraction of H_{upd} inhibited by phenol from the cyclic voltammograms (**Figure 2-1**) against the bulk concentration of phenol. The fraction of H_{upd} inhibited, which we assume was caused by the reversible adsorption of phenol on the metal surface, was obtained from the difference in the H_{upd} charge with and without phenol in solution (details in **A.5** of the appendix). The fraction of H_{upd} inhibited by phenol on Pt at different concentrations determined using the CV technique matches a report using a radiotracer method.[119] The dilution points are shown in **Figure 2-2** as open triangles to indicate the reversibility of phenol adsorption and the lack of hysteresis using this technique. For example, diluting from 100 µM (filled triangle) to 10 µM (open triangle) is shown in the isotherm in **Figure 2-2a** for phenol on Pt wire, where the diluted point matches the measurement at 10 µM without dilution. The variation between the data points after dilution compared to without dilution at the same bulk phenol concentration is within the small run-to-run variation from multiple measurements (see **Appendix Figure A-3** for run-to-run variations).

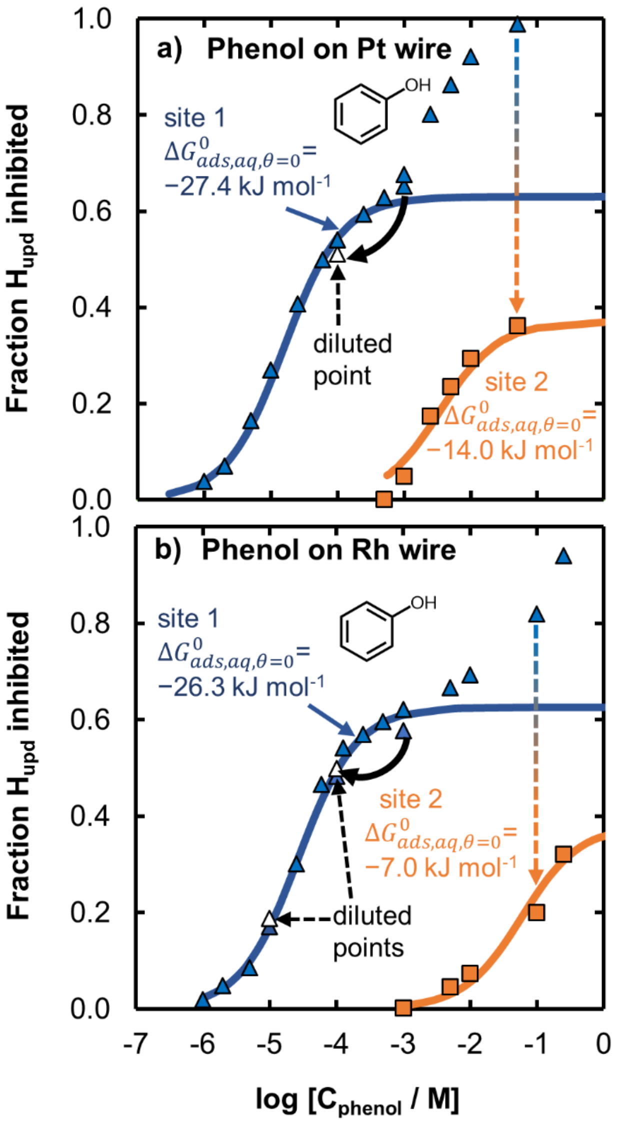

Figure 2-2 Adsorption isotherms of phenol on Pt and Rh. Adsorption isotherms of phenol on **a)** Pt and **b)** Rh wires constructed by plotting the fraction of H_{upd} inhibited by phenol vs. the bulk phenol concentration. Each data point (blue triangle) is obtained from the drop in H_{upd} charge with phenol in **Figure 2-1**. Fits are from a two-site Temkin adsorption model with $\alpha = 0$ kJ mol^{-1} giving the best fit. The orange squares (site 2) correspond to the fraction of H_{upd} inhibited that is greater than the saturation amount of site 1. Thus, site 2 data points are adjusted by subtracting the saturation fraction of site 1 at the higher phenol concentration. Diluted points are shown by open triangles (solid black arrow indicates dilution by a factor of 10). The agreement of the diluted points with points directly taken by adding phenol without first reaching a higher concentration shows that phenol adsorption under these conditions is reversible.

The isotherm shapes in **Figure 2-2** indicate the presence of two distinct adsorption sites on both Pt and Rh, based on the initial increase in coverage with concentration, followed by a plateau with increasing concentration (saturation of the first site), then by a second region of increasing coverage corresponding to adsorption on the second set of sites. Thus, we divide the phenol adsorption isotherm into two sites for both Pt and Rh, where site 1 corresponds to the stronger binding site and site 2 corresponds to the weaker binding sites. The H_{upd} peaks for Pt(110) and Pt(100) in **Figure 2-1a** decrease at lower phenol concentrations, whereas the Pt(111) H_{upd} peak only decreases at higher concentrations. Thus, site 1 in **Figure 2-2a** is attributed to a combination of stepped facets of Pt(110) and Pt(100), and site 2 is attributed to Pt(111) terraces.[28] The adsorption free energy extracted in this way on site 2 matches those from a kinetic model for phenol hydrogenation, as discussed in the Experimental & Computational Methods section. The fraction of site 2 corresponding to the Pt(111) terrace-like sites (0.37 from the isotherm for Pt in **Figure 2-2** and 0.4 from Ref 15) is similar to predictions from electrochemical Wulff construction of the fraction of (111) sites (~0.4 in the 0 V to 0.4 V vs. RHE range for Pt),[120] supporting this assignment. Our DFT calculations using the bond-additivity model for Pt also predict stronger phenol adsorption on the (110) steps compared with the (111) terraces, consistent with our assignment. The model, however, predicts weaker phenol adsorption on the (100) steps than (111) terrace despite stronger adsorption in the gas phase. This discrepancy from the experimental results may be a result of an inaccurate (too strong) water adsorption energy on the (100) step or an inaccurate number of water molecules displaced upon organic adsorption as discussed in the methods.

Although from the CV of Rh (**Figure 2-1b**) we cannot distinguish between facets, from **Figure 2-2b** it is apparent that there are two adsorption sites, where site 1 reaches saturation coverage at 1 mM phenol, followed by continued adsorption on site 2 at higher concentration. We attribute site 1 to a combination of (110) and (100) steps facets and site 2 to (111) terraces, the same as the assignment on Pt. Our assignment is supported by the similar fraction of site 1 on Pt and Rh (0.63 and 0.62 respectively). The bond-additivity calculations for Rh predict that phenol adsorbs on (110) steps the strongest, followed by (111) terraces, then (100) steps the weakest, the same order as predicted for Pt. It is possible that site 1 of Rh is only the (110) step and not the (100) step, although the weak adsorption predicted on the (100) steps may be a result of an erroneous treatment of water on the (100) steps in the model as described above for Pt.

The values of experimental adsorption free energies ($\Delta G^0_{ads,aq,\theta}$) from isotherm fitting using the procedure outlined in **A.6** are compiled in **Table 2-1**, along with the free energy of gas-phase organic adsorption in aqueous phase ($\Delta G^0_{ads,aq,gas,\theta}$), calculated from $\Delta G^0_{ads,aq,\theta}$ using Henry's law constant in **Appendix Table A-5**. The adsorption values are also converted to enthalpies of gas-phase organic adsorption in aqueous phase ($\Delta H^0_{ads,aq,gas,\theta}$) and aqueous organic adsorption enthalpies ($\Delta H^0_{ads,aq,\theta}$) following the method discussed in detail in **A.9** and outlined in **Scheme A-1**. Briefly, the standard entropy of each gas-phase organic molecule is used to estimate the entropy of adsorption using a known correlation for many gas-phase molecules,[121] allowing us to convert from $\Delta G^0_{ads,aq,gas,\theta}$ to $\Delta H^0_{ads,aq,gas,\theta}$. Although this accounts for the loss in entropy from the gas-phase organic adsorption, we assume that the displaced water layer has the same entropy, i.e., that the water layer on top of the adsorbed organic has the same structural order as the water layer on top of the metal surface. This assumption of invariant entropy from water is supported by the close agreement between aqueous-phase calorimetry of benzaldehyde on both Pt/C and Rh/C compared to the enthalpies extracted here using this method. The assumption that the water layer maintains the same entropy could be tested by measuring $\Delta G^0_{ads,aq,\theta}$ as a function of temperature and constructing a van't Hoff plot, so that this approximation is not required. If there was an increase in entropy from the water being displaced (i.e., water on the adsorbed organic has higher entropy than water adsorbed on metal), the enthalpies of adsorption would be more positive than reported here, but the effect is estimated to not be more than 11 kJ mol^{-1}.[63]

2.3.3 Difference in Gas-Phase and Aqueous-Phase Adsorption Energies of Phenol

Here we compare our experimentally measured aqueous-phase heats of adsorption ($-\Delta H^0_{ads,aq,gas,\theta}$) of phenol on both Pt(111)[28,63] and Rh(111) with DFT-computed values in the gas phase and aqueous phase. The data in **Figure 2-3** shows computed gas-phase heats of adsorption ($-\Delta H^0_{ads,gas,\theta}$) and aqueous-phase heats of adsorption ($-\Delta H^0_{ads,aq,gas,\theta}$) calculated using implicit solvation, the bond-additivity approach, and experimental isotherm fitting. Our gas-phase DFT calculations for phenol heat of adsorption on Pt(111) agrees with low-coverage values measured by ultrahigh vacuum calorimetry.[65] Phenol is calculated to adsorb ~50 kJ mol^{-1} stronger on Rh(111) compared with Pt(111) in the gas phase, but the experimental measurements show that Rh(111) and Pt(111) both adsorb phenol with similar and weaker strength in the aqueous phase.

Heats of adsorption computed using implicit solvation predict that phenol should adsorb stronger than in the gas phase on Pt and Rh and overpredict adsorption strengths by at least 100 kJ mol^{-1} compared with experiment. Here, calculations using only implicit solvation predict that phenol binds 29 kJ mol^{-1} stronger on Pt(111) in the aqueous phase compared with the gas phase, which is consistent with the 25 kJ mol^{-1} increase in phenol binding strength previously reported using an implicit solvation model.[44] Past work that treated water explicitly reported the aqueous-phase adsorption enthalpy of a gas-phase phenol molecule to be 37 kJ mol^{-1} more exothermic than in the gas phase.[72] Implicit and explicit solvent calculations that model water surrounding the organic but not displaced from the surface yield far more exothermic adsorption enthalpies than our equilibrated adsorption measurements and even calorimetry values. Also, DFT calculated adsorption energies that account for displacement of adsorbed water from a metal surface[84] have not been compared directly with experimental values. The consequence of these significantly stronger adsorption energies would be a many orders of magnitude error in adsorption equilibrium constants, which are used for catalysis in trying to predict or understand surface coverages (e.g., through a LH reaction or other microkinetic model).

The bond-additivity model (**Eq. 2-2**) corrects the DFT-predicted gas-phase adsorption enthalpies for solvation and water displacement at the metal interface upon organic adsorption, bringing the predictions into much closer agreement with experiment for phenol adsorption on Pt(111) and Rh(111). The bond-additivity model here does not account for the differences in the potential of zero charge (PZC) between Pt(111) and Rh(111), which could affect the metal surface charge and thus the water adsorption layer. The PZC of the (111) facets of Pt and Rh in 0.1 M H_2SO_4 are much different (0.3 V on Pt(111)[122,123] and 0.1 V on Rh(111) vs. RHE).[124] Accounting for this effect would further improve the accuracy of this model.

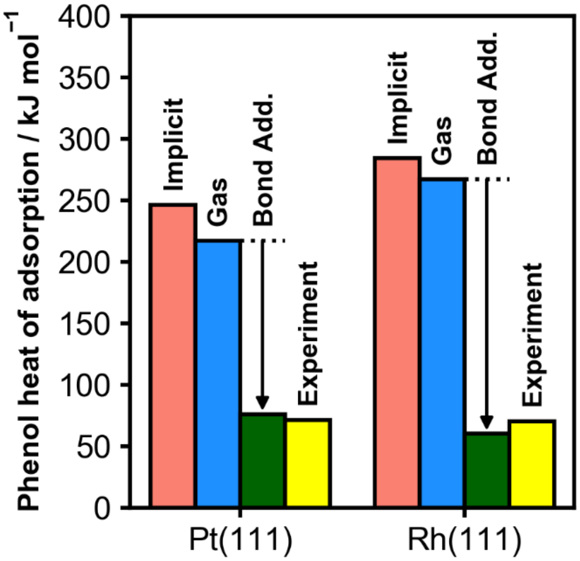

Figure 2-3 Computed heats of adsorption. DFT-computed heats of adsorption in implicit solvent (orange), gas phase (blue), and aqueous phase using a bond-additivity model to correct the gas-phase calculation for solvation and water displacement at the metal interface (green). Experimentally derived heats of adsorption for gas-phase phenol on the metal in the aqueous phase for site 2, attributed to Pt(111) and Rh(111) terraces, are shown in yellow. Abbreviations: Bond Additivity = Bond Add.

As previously discussed for Pt,[63] the difference in gas-phase and aqueous-phase adsorption is mainly attributed to the fact that in aqueous phase, organics must displace water adsorbed to the metal surface. This has been described qualitatively by Gileadi[125] and Bockris,[119] but used quantitatively in recent work since we now know the number of water molecules displaced by phenol and the enthalpy associated with those adsorbed waters. For example, a phenol molecule adsorbing on Pt(111) surface in aqueous phase displaces approximately 6.5 water molecules, based on the footprint of adsorbed phenol on Pt[108] and saturation coverage of water on Pt.[64] Since Pt(111) has been recently shown to be the active facet for phenol hydrogenation,[82] it is important to understand how the presence of solvent/water impact the effective adsorption strength of phenol on this facet.

The similarity between phenol adsorption on Rh and Pt in the aqueous phase is primarily caused by the stronger water adsorption on Rh than on Pt as calculated here and in ref [126]. Our DFT calculated water/Rh(111) adsorption energy (-52 kJ mol^{-1}) is stronger than water/Pt(111) (-39 kJ mol^{-1}) in the gas phase, consistent with temperature programmed desorption experiments where water desorption on Rh(111) is observed at higher temperatures than on Pt(111).[127] Water adsorption energies on other surfaces are included in **Appendix Table A-4**. We assume the phenol "footprint" is similar on Rh and Pt[108] and that n from **Eq. 2-2** is the same for the two metals. This assumption is supported by the similar adsorption geometries (**Appendix Figure A-5** and **Appendix Figure A-6**) and metal surface area covered by phenol on Rh and Pt (0.60 nm^2 for Pt and 0.56 nm^2 for Rh) from our calculations. Thus, the stronger water adsorption on Rh offsets the stronger gas-phase phenol adsorption energy, resulting in comparable aqueous-phase adsorption energies.

2.3.4 Impact of other Oxygenated Aromatics and Organics on the Underpotential Deposition of Hydrogen on Rh

Besides phenol, other oxygenated aromatics and organics (i.e., benzaldehyde, furfural, benzyl alcohol, cyclohexanol) tested here also compete with hydrogen for adsorption sites on Rh, as seen in **Figure 2-4**. Consequently we can broadly apply the CV technique to extract adsorption energies of organics in the aqueous phase provided that in the H_{upd} potential window the adsorbed organic and H* adsorb and desorb reversibly. The drop in the H_{upd} peaks with individual organic concentration varies in the order of furfural > benzaldehyde > phenol > benzyl alcohol >> cyclohexanol. Cyclohexanol in particular has much lower impact on the H_{upd} than the other organics, even at 200 mM.

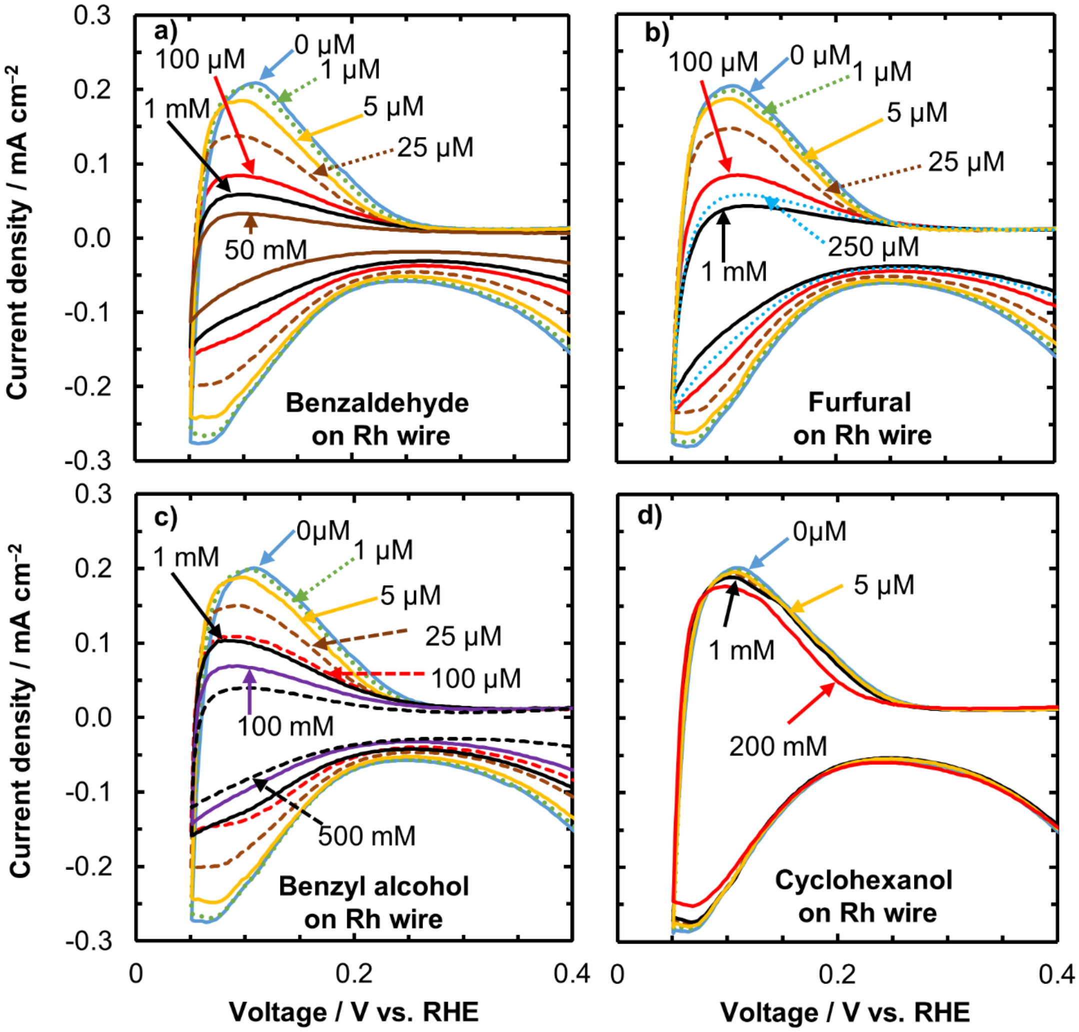

Figure 2-4 Cyclic voltammograms of benzaldehyde, furfural, benzyl alcohol, and cyclohexanol. Cyclic voltammograms in the H_{upd} region with increasing bulk organic concentration on a Rh wire for **a)** benzaldehyde, **b)** furfural, **c)** benzyl alcohol, and **d)** cyclohexanol. Experiments were carried out in 100 mM acetate buffer supporting electrolyte (pH 5) at 298 K and using a 100 mV s^{-1} scan rate. The adsorbed organic competes with H* for sites hence the drop in H_{upd} charge indicated by the reduced current density with increasing organic concentration.

Similar to the reversibility of H_{upd} discussed above for phenol, the H_{upd} charges in the cathodic and anodic direction in the presence of benzaldehyde, benzyl alcohol, and cyclohexanol are the same, implying reversible H_{upd}, however, furfural H_{upd} (**Figure 2-4b**) became less reversible with increasing furfural concentration on Pt and Rh (**Appendix Figure A-7** and **Appendix Figure A-8**). With increasing furfural concentration, a larger portion of the adsorbed hydrogen is not desorbed in the H_{upd} region (i.e., the difference in H_{upd} adsorption and desorption charge increases). This irreversible reduction current is also seen at higher furfural concentrations.[128] This behavior does not seem to be due to a catalytic reaction, because the difference in H_{upd} adsorption and desorption charge was independent of scan rate (**Appendix Figure A-8c** and **Appendix Figure A-8d**). Thus, one possibility for the irreversible H_{upd} reduction in the presence of furfural may be that H* partially hydrogenates the adsorbed furfural species, but complete furfural hydrogenation and desorption does not occur in this potential region. Recent studies have shown that furfural may also decarbonylate at potentials just positive of the H_{upd} region, forming strongly adsorbed CO, adsorbed furyl fragments, and adsorbed H.[128,129] In this case, the irreversible reduction current we observe here may be related to the reduction or reaction of adsorbed furyl to furan, but without furan desorption that would allow catalytic turnover.

2.3.5 Adsorption Energies of Furfural, Benzaldehyde, Benzyl Alcohol, and Cyclohexanol on Rh

Using the data in **Figure 2-4**, the fraction of H_{upd} inhibited by the organics is shown in **Figure 2-5**, with specified points testing the reversibility of the adsorption process indicated by open symbols. The data in **Appendix Figure A-4** contains CVs used to test the reversibility of all organics tested here, except for cyclohexanol which did not adsorb at appreciable coverages. The adsorption free energies of these organics were extracted the same way as was done for phenol. The two-site behavior seen for phenol on Rh is not observed for furfural and cyclohexanol. We deduce that furfural does not adsorb differently on the individual Rh facets as opposed to phenol, benzyl alcohol and benzaldehyde, which adsorb on distinct Rh sites (attributed to stronger adsorption on steps and weaker adsorption on terraces). This may also be a result of furfural decarbonylating upon adsorption, as discussed earlier. Thus, the extracted adsorption energies of furfural without a two-site adsorption behavior are an average over the different sites. For cyclohexanol, the adsorption is not strong enough to reach sufficiently high coverages where adsorption on a second site may be seen. Further coverage increases were limited by the solubility of cyclohexanol. The fraction of H_{upd} inhibited at 1 mM cyclohexanol concentration, shown in **Figure 2-5d** is less than 5% whereas for other organics (**Figure 2-5**), greater than 50% organic coverage was achieved at 1 mM. Our DFT calculations also indicate that cyclohexanol adsorption is weaker on Pt and Rh than aromatic adsorption. As the main difference between the phenol and cyclohexanol is the aromatic ring, the weaker adsorption of cyclohexanol (**Figure 2-5d**) is consistent with the idea that the adsorption of aromatics on a transition metal arises from the interaction between the aromatic π electron system and the metal *d*-band.[130] The measured adsorption energies of the model compounds are included in **Table 2-1**, converted between free energies and enthalpies as discussed in **A.9** of the appendix. **Table 2-1** also includes the adsorption energies from calculations using DFT and adjusting using the bond-additivity model.

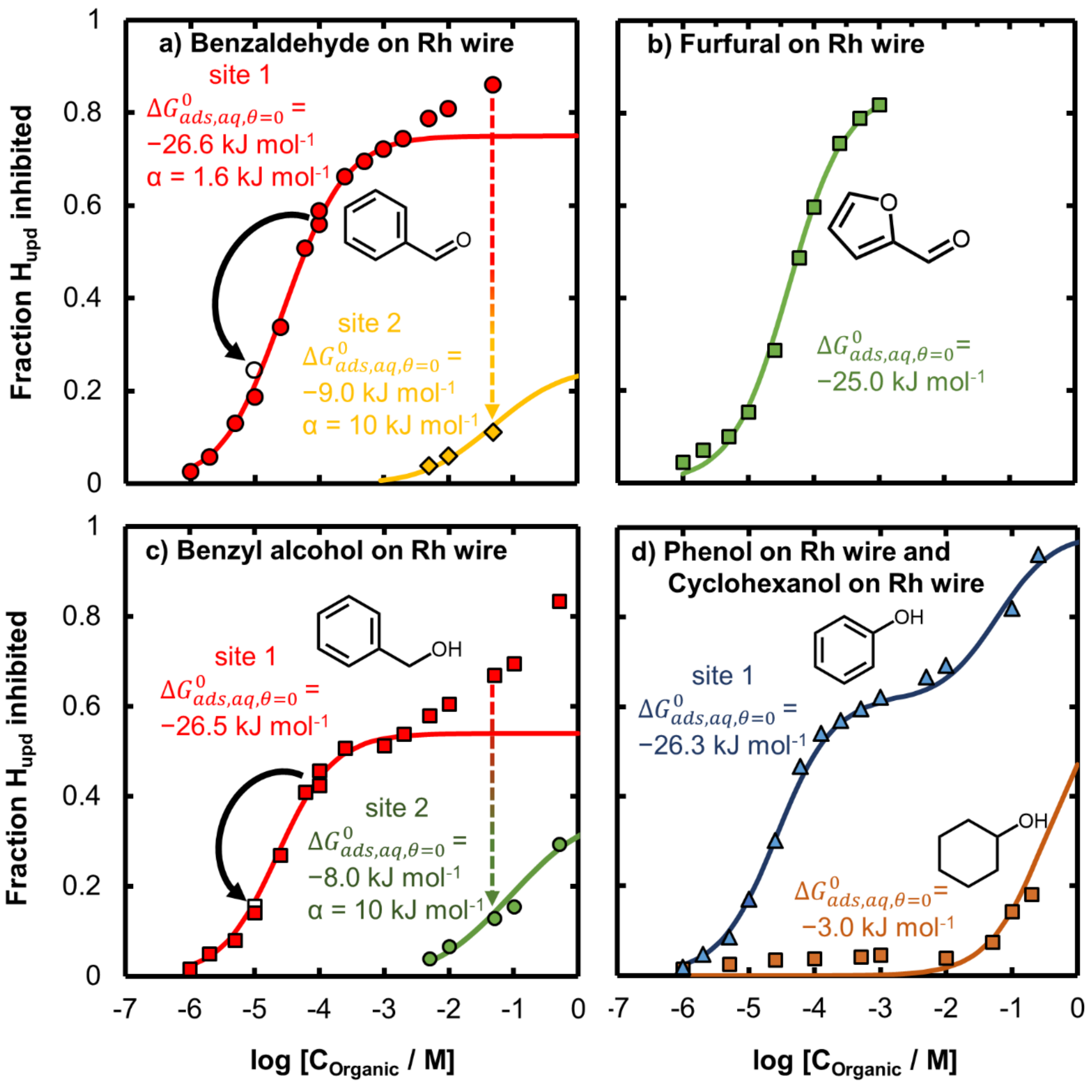

Figure 2-5 Adsorption isotherms of benzaldehyde, furfural, benzyl alcohol, and cyclohexanol. Adsorption isotherms of **a)** benzaldehyde, **b)** furfural, **c)** benzyl alcohol, and **d)** phenol on Rh wire and cyclohexanol on Rh wire. The data points were obtained from the fraction of H$_{upd}$ inhibited on Rh by the different organics from **Figure 2-4** at various organic concentrations. The values for phenol in d) are from **Figure 2-2b** and are compared directly to the non-aromatic cyclohexanol values taken in a separate experiment to show the effect of the aromatic ring. A Temkin isotherm model was used to fit the data and extract the adsorption free energies. Benzaldehyde, phenol, and benzyl alcohol isotherms are divided into two sites for fitting. Furfural do not show a two-site adsorption behavior as seen for phenol. Dilution is shown by the solid arrows to test the reversibility of organic adsorption. New measurements after dilution are denoted by open symbols.

Table 2-1 Adsorption free energies and enthalpies. Measured adsorption free energies and enthalpies of organic compounds on Rh and Pt wires at 298 K in aqueous phase from hydrogen site blocking experiments. DFT calculated values adjusted using the bond-additivity model are also included.

Molecule	$\Delta G_{ads,aq,\theta=0}$ kJ mol^{-1} [a]	α kJ mol^{-1}	Sat. frac.	$-\Delta H^0_{ads,aq,\theta}$ kJ mol^{-1} [a]	$-\Delta H^0_{ads,aq,gas,\theta}$ kJ mol^{-1} [a]	$-\Delta H^0_{ads,aq,gas,\theta}$ kJ mol^{-1} DFT + Bond Add. [b]
Pt from ref [28] and measured here for furfural						

Phenol (site 1)	−29	4	0.53	41	91	130
Phenol (site 2)	−9	0	0.40	21	71	76
Benzaldehyde	−30.5	4.5	0.80	43 [c]	83	121/94
Furfural	−26.1	0	0.89	26	84	95/92
Benzyl alcohol	−33	5	0.86	32	99	159/128
Cyclohexanol [d]	−17	0	0.66	−2	69	24/ −3
Rh						
Phenol (site 1)	−26.3	0	0.62	39	89	86
Phenol (site 2)	−7	0	0.38	20	70	60
Benzaldehyde (site 1)	−26.6	1.6	0.75	39 [c]	81	124
Benzaldehyde (site 2)	−9	10	0.25	20 [c]	62	112
Furfural	−25	0	0.82	25	83	88/66
Benzyl alcohol (site 1)	−26.5	0	0.54	28	95	114
Benzyl alcohol (site 2)	−8	10	0.36	9	76	104
Cyclohexanol [d]	−3	0	0.63	−7	63	−34/−65

a. The adsorption free energies are extracted from **Figure 2-2** and **Figure 2-5**. Heats of adsorption at standard coverage $\theta^0 = 0.054$ are also listed based on conversions using the methodology described in the appendix (**A.9**). $-\Delta H^0_{ads,aq,\theta}$ refers to the heat of adsorption of solvated phenol and $-\Delta H^0_{ads,aq,gas,\theta}$ refers to the aqueous-phase heat of adsorption of gas-phase phenol. *b*. $-\Delta H^0_{ads,aq,gas,\theta}$ is reported here from the values in **Appendix Table A-4** using the bond-additivity model. “Step” site values (site 1) correspond to (110) step calculations and the “terrace” sites (site 2) corresponding to (111) terraces. For molecules where two distinct adsorption sites were not found experimentally, (110) calculated values are listed first, followed by (111). *c*. Heats of adsorption measured by solution calorimetry from ref [11] on Pt/C and Rh/C were 44 kJ mol^{-1} and 39 kJ mol^{-1}, respectively. *d*. Cyclohexanol coverages did not reach saturation, so these values are estimated by using the same saturation coverage of phenol on site 1 for Rh (0.63 ML).

2.3.6 Comparing Experiments with Implicit Solvent and Bond-additivity Calculations

The aqueous-phase heats of adsorption from experiments increase in the order of benzaldehyde > phenol > benzyl alcohol > furfural >> cyclohexanol, which has the same trend as Pt in aqueous phase.[28] Furfural adsorption on Pt was not previously measured in ref [28] but is reported here (H_{upd} and adsorption isotherm are in **Appendix Figure A-9**). The heat of adsorption for benzaldehyde on site 1 of Rh (39 kJ mol^{-1}) obtained here from the isotherm fitting is the same as the value determined from solution calorimetry of benzaldehyde on Rh/C (39 kJ mol^{-1}),[11] supporting the accuracy of this technique for estimating adsorption energies on metal surfaces. The exact order of the heats of adsorption for the aromatics differs between experiment and our computationally predicted energies (**Table 2-1**), yet this is unsurprising given the small variation in heats of adsorption on a given site, which is well within the expected accuracy of DFT-based predictions, and the assumptions/estimates of the number of waters displaced and its impact on the predicted adsorption energies. Nevertheless, the much stronger adsorption of the aromatic molecules compared with the more weakly adsorbing cyclohexanol is captured by our computational results.

The differences between experimental and predicted heats of adsorption for all five organics studied here are shown in **Figure 2-6**. Heats of adsorption were also predicted using the optB88-vdw functional,[131,132] which has been used to predict accurate gas-phase adsorption energies of phenol on Pt(111),[133] though we find no qualitative differences between using the optB88-vdw functional and PBE-D3 (see **Appendix Figure A-12** of SI for comparison). The heat of adsorption of each molecule on the (110) step and the (111) terrace is calculated in the gas phase and in the aqueous phase using either DFT with implicit solvent or the bond-additivity model. Here we use the (110) step to compare to the experimental site 1 and the (111) terrace to compare to site 2. The triangles for phenol in **Figure 2-6** correspond to the difference between the values shown in **Figure 2-3**. Generally, the energy of solvating organics and the penalty of displacing adsorbed water, which is explicitly accounted for in the bond-additivity model, results in a drastic reduction in the apparent adsorption energy of the organics in the aqueous phase compared with the gas phase.

For all organics, a large difference between gas-phase and experimental heats of adsorption is observed, indicating that gas-phase DFT predicts adsorption to be much stronger than what is observed experimentally in the aqueous phase. Similarly, DFT with implicit solvent predicts adsorption of the organics to be much stronger than what is experimentally measured. The heats of adsorption predicted using the bond-additivity model, however, are much closer to experimental values for all organics, with cyclohexanol as an exception. Since cyclohexanol adsorbs so weakly, we are unable to get a saturation coverage, hence the isotherm fit is poor and the extracted aqueous values may not be accurate. Furthermore, because cyclohexanol already binds weakly in the gas phase compared with the aromatics, it may have insufficient driving force to displace as many water molecules as the aromatics.

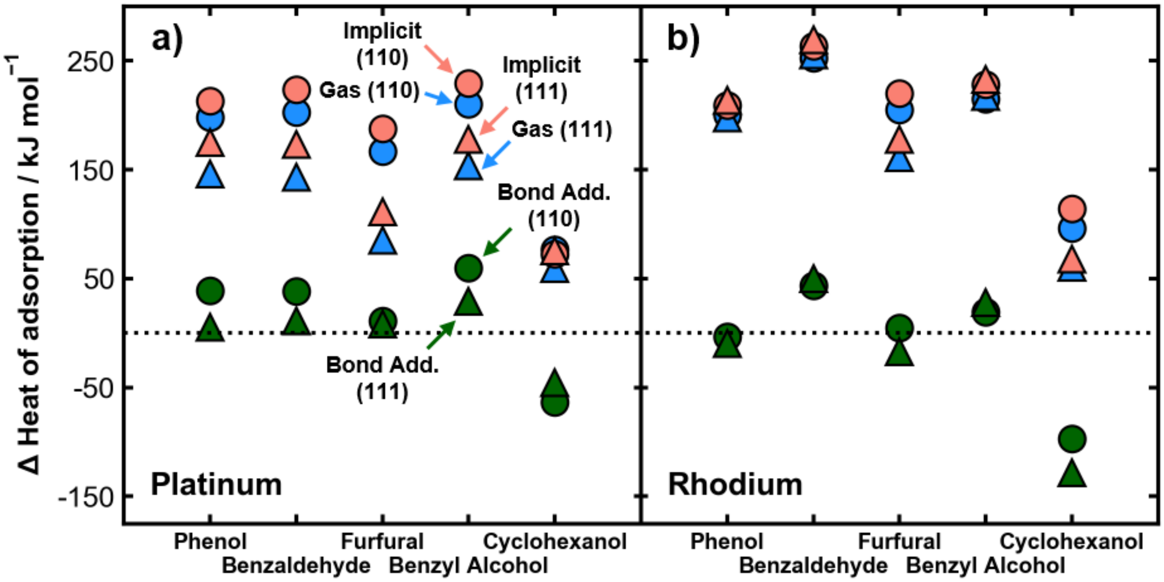

Figure 2-6 DFT-calculated heats of adsorption of phenol, benzaldehyde, furfural, benzyl alcohol, cyclohexanol. Calculated heats of adsorption using the PBE-D3 functional referenced to experimental heats of adsorption for organics using different methods. Calculations on (110) steps are compared to site 1 and (111) facets are compared to site 2. **a)** Pt(110) step and Pt(111) terrace differences between theory and experiment; **b)** Rh(110) step and Rh(111) terrace differences. Heats of adsorption are calculated in the gas phase and in the aqueous phase using an implicit solvent model or a bond-additivity model (Bond Add.). Calculated enthalpies on the (111) terrace and (110) step were referenced to the same experimental enthalpy when two distinct adsorption sites were not extracted from the isotherms. Values greater than zero indicate that adsorption is predicted by DFT to be stronger than experiment, whereas values less than zero indicate that adsorption is predicted by DFT to be weaker. Experimental values and Bond Add. values are shown in **Table 2-1** and all computational values are shown in **Appendix Table A-4**.

The number of water molecules displaced by each organic molecule (used for bond additivity) from each surface was chosen based on an estimated saturation coverage of each organic and an approximate coverage of water (**Appendix Figure A-10** and **Appendix Table A-6**). Unsurprisingly, the closest agreement between bond-additivity calculations and the experimental values are for (111) terraces, where UHV work has given a more accurate understanding of the footprint of the adsorbed organic and hence number of displaced waters. Ultimately, the data in **Table 2-1** and **Figure 2-6** show that the adsorption enthalpies of the organics in aqueous phase are greatly reduced by the presence of water compared with gas-phase adsorption enthalpies, and that closer agreement with experimental measurements in aqueous phase is obtained with the bond-additivity model.

2.3.7 Consequences of Weaker Effective Organic Adsorption on Pt and Rh on Hydrogenation Rates

The comparable free energies of adsorption of phenol and benzaldehyde on Rh and Pt wires in aqueous phase may explain why there is considerable similarity in the Rh/C and Pt/C activity for both aqueous-phase thermal and electrocatalytic hydrogenation of those molecules. Aqueous-phase hydrogenation of phenol and benzaldehyde on Pt/C and Rh/C can be described using a Langmuir-Hinshelwood mechanism with a surface reaction rate-determining step,[11,12] so the adsorption energies of the organic and of hydrogen should play a key role in the observed kinetics. In particular, the adsorption energies of the reactants and intermediates will dictate the surface coverages when adsorption/desorption is fast compared to the surface reaction, thus these adsorption energies will control the reaction orders. The adsorption energies will also impact the TOF, both through the surface coverages and the activation energies. Phenol has similar TOFs and reaction orders for hydrogenation of the aromatic ring on Pt/C and Rh/C.[22,23] Benzaldehyde also shows comparable hydrogenation TOFs and reaction orders for the aldehyde group on Pt/C and Rh/C.[11] Pt and Rh have similar effective activation energies for phenol[12,23] and benzaldehyde,[11] with Rh having a slightly lower (~4 to 6 kJ mol^{-1}) effective activation energy for both reactions.

The similar hydrogen adsorption energies of Pt and Rh,[134] combined with the above evidence for aqueous-phase hydrogenation implies that there are not major differences in the organic adsorption energy on Pt and Rh. This observation is inconsistent with the different organic adsorption strengths in gas phase (e.g., phenol adsorbs 50 kJ mol^{-1} more strongly on Rh(111) than Pt(111)). However, the similar aqueous adsorption strengths for Pt and Rh in this work agree qualitatively with the observed catalytic activity for phenol and benzaldehyde hydrogenation. In addition, the much lower adsorption energy for phenol and benzaldehyde in the aqueous phase explains why these reactions can proceed at room temperature, whereas in gas phase the adsorption energy would be too strong for appreciable reaction, and desorption may be rate limiting, as opposed to the surface reaction being rate-limiting in aqueous phase. The adsorption equilibrium constant for phenol on Pt(111) using the bond-additivity model[63] in fact matches closely to the adsorption equilibrium constant for phenol hydrogenation on Pt/C,[21] whereas the adsorption constant from gas-phase or implicit solvent calculations is more than 30 orders of magnitude too large. The large difference in gas-phase and aqueous-phase adsorption energies highlights the importance of understanding adsorption in aqueous phase for catalysis, which we show can be approximated using gas-phase calculations coupled with the bond-additivity model. Although this method would enable more accurate estimates of coverage and adsorption/desorption, it would not account for solvent effects in preferentially stabilizing the transition state or identifying new reaction mechanisms that require interaction with the solvent.

2.4 Conclusions

Generally, we find that organics bind weaker in the aqueous phase compared to gas phase on Pt and Rh. This observation is well explained by a bond-additivity model that accounts for the large enthalpic penalty for displacement of multiple water molecules by the organics from the water/metal interface. Using this model, we predicted adsorption energies in aqueous phase from gas-phase calculations which match qualitatively with experiments. As a result of this water displacement enthalpy, phenol and other organics adsorb with similar strength on Pt and Rh in aqueous phase despite the considerable difference in their gas-phase adsorption enthalpies.

Although for surface reactions this weaker adsorption in aqueous phase may apply to the energies of adsorbed products, intermediates and transition states equally relative to the adsorbed reactant species and thus may not greatly change catalytic barriers, the weakening of adsorption energies has important consequences in understanding adsorption/desorption, coverages, and TOFs. These results help explain how aromatics such as furfural, benzaldehyde, and phenol, which bind so strongly to metals in the gas phase (200–250 kJ mol^{-1}) can be hydrogenated even at room temperature in the presence of water. Additionally, these findings show how computational techniques can be used to predict and rationalize how solvents tune adsorption on metal surfaces. Understanding how solvents impact adsorption can enable the control of condensed-phase catalytic rates through selection of the solvent environment.

Chapter 3 Explaining the Structure Sensitivity of Pt and Rh for Aqueous-Phase Hydrogenation of Phenol

This chapter was adapted from Barth, I.; Akinola, J.; Lee, J.; Gutiérrez, O. Y.; Sanyal, U.; Singh, N.; Goldsmith, B. R. Explaining the Structure Sensitivity of Pt and Rh for Aqueous-Phase Hydrogenation of Phenol. *J. Chem. Phys.* **2022**, *156* (10), 104703. My contribution to this work is the density functional theory modeling. James Akinola performed the experimental work.

3.1 Introduction

Upgrading bio-oils derived from waste biomass is a route to sustainably produce fuels and chemicals and reduce our dependency on petrochemicals.[135–137] Currently, the aqueous-phase hydrogenation step in biomass conversion is too capital- and energy-intensive to compete economically with fossil fuels.[14,16] Many studies have explored electrocatalytic hydrogenation (ECH) and thermocatalytic hydrogenation (TCH) to understand the reaction mechanism and improve the efficiency of bio-oil conversion.[2,13,138,139] The most active ECH and TCH catalysts are platinum group metals,[2,12,21–23,75,82,140] typically dispersed as nanoparticles onto supports to increase fractional exposure and improve catalyst utilization. However, the surfaces of these nanoparticles have multiple exposed facets, not all of which are active for hydrogenation.[21,82] Thus, decreasing the particle size to increase the catalyst surface area may actually decrease the catalyst performance and utilization because a lower fraction of active sites may be exposed at small particle sizes. A better understanding of why certain catalyst sites are active for hydrogenation is required to effectively upgrade the many compounds present in bio-oil. We hypothesize that the adsorption energies of the bio-oil compound and hydrogen on the active site largely affect the catalytic activity, as expected from the Sabatier principle;[141] however, it may not be the sole predictor (i.e., intrinsic differences in kinetics between surfaces may also affect the rate). Ideally, the aqueous-phase hydrogenation activity of a given molecule on a catalyst surface could be qualitatively estimated based on simple adsorption energy calculations,[35,63] which would accelerate the computational screening of active catalysts for aqueous-phase reactions on metal surfaces. Thus, it is important to know if adsorption energies alone are sufficiently accurate as descriptors to predict trends in hydrogenation kinetics.

In this work, we use computational and experimental methods to identify the active sites of Pt and Rh for ECH and TCH of phenol, a model bio-oil compound, and explain why these sites are active. We study phenol because it is representative of phenolic compounds within many bio-oil mixtures,[8,137,142] and Pt[21,75,82] and Rh[12,21–23] are among the most well-studied catalysts for ECH and TCH of phenol. Phenol hydrogenation is structure sensitive on Pt and the Pt(111)-like sites (i.e., (111) terraces) have been shown to be the active facet for ECH and TCH;[21,82] however, the reason why only this Pt facet is active for phenol ECH and TCH is unclear. In addition, it is unclear if phenol ECH and TCH are also structure sensitive on Rh or what the active site is for Rh. One hypothesis is that certain facets are active due to weaker adsorption of phenol, which prevents phenol from poisoning the catalyst surface and blocking hydrogen adsorption under typical operating conditions.[12,21–23,75,82]

Herein, we show that ECH and TCH of phenol is structure sensitive on Rh, similar to what has been shown for Pt. We test the hypothesis that certain Pt or Rh facets are active due to weaker phenol adsorption. Computational and experimental data for phenol ECH and TCH on Pt and Rh corroborate our hypothesis that the adsorption energy of phenol influences the reaction rate on the active site, but other factors, namely the activation energies, also contribute to the activity. We emphasize that although the adsorption energy of the reacting compound influences the reaction rate, it is not the sole descriptor of a catalyst's activity.

The electrocatalytic and thermocatalytic hydrogenation of phenol on both Pt/C and Rh/C have been reported to follow a Langmuir-Hinshelwood (LH) mechanism. This LH mechanism involves the competitive adsorption of phenol and hydrogen followed by sequential surface reactions of adsorbed hydrogen (H*) and the adsorbed organic to form cyclohexanone and cyclohexanol.[12,21] The major difference between ECH and TCH of phenol is the source of adsorbed hydrogen. For ECH, hydrogen equivalents are produced on the catalyst surface by reducing protons from aqueous solution using an applied cathodic potential. For TCH, the H* is derived from dissociative adsorption of H_2. ECH and TCH of phenol have similar apparent activation energies and product distributions at applied potentials where the ECH rate is comparable to that of TCH at 1 bar H_2, implying the same rate-determining step (RDS).[12,22,23] The surface reaction between adsorbed phenol and H* has been proposed as the RDS for ECH and TCH on Pt/C, indicating the turnover frequency (TOF) is controlled by the rate constant (k) and equilibrium coverages of phenol (θ_P) and hydrogen (θ_H), according to the LH model described by **Eq. 3-1**.

$$\mathrm{TOF} = k\theta_P\theta_H \qquad \textbf{Eq. 3-1}$$

Because the surface reaction is rate-determining, θ_P and θ_H are assumed to be quasi-equilibrated and controlled by the aqueous equilibrium adsorption constants on the active site (K_P and K_H, where P = phenol and H = hydrogen). The TOF can be written in terms of the bulk concentration of phenol divided by the standard concentration of 1 M (C_P) and the aqueous hydrogen concentration (C_H) in **Eq. 3-2**.

$$\mathrm{TOF} = k\frac{K_P C_P K_H C_H}{(1 + K_P C_P + K_H C_H)^2} \qquad \textbf{Eq. 3-2}$$

The C_H is equivalent to $[P_{H_2} / (1\ \mathrm{bar})]^{1/2}$ for TCH, where P_{H_2} is the pressure of hydrogen in equilibrium with the solution. For ECH, C_H is the concentration of H^+ divided by 1 M.[21] For TCH, K_H is the equilibrium adsorption constant of H* from ½ H_2. For ECH, K_H is also the equilibrium adsorption constant of H*, but from H^+ and e^-, thus K_H increases with more negative applied potential due to the increased thermodynamic driving force to form H*. The potential dependence of phenol ECH TOFs on Pt/C and Rh/C are qualitatively explained by **Eq. 3-2** by considering this change in K_H.[21] Briefly, the TOF increases with more negative applied potential at low hydrogen coverages and decreases with more negative applied potential at high hydrogen coverages due to competitive adsorption with phenol.[21]

Solvent can influence the hydrogenation rate of organic molecules by changing their adsorption thermodynamics and hydrogenation barriers of elementary steps. Upon adsorption, organic molecules with large footprints, such as aromatics, must displace solvent molecules at the solvent/metal interface. The aqueous-phase adsorption energies of aromatic compounds are weaker than those measured in the gas phase because of the energetic penalty of solvent displacement.[63,125] For example, the adsorption free energies of phenol on Pt and Rh are over 150 kJ mol^{-1} weaker in the aqueous phase compared to the gas phase due to the displacement of multiple water molecules upon adsorption.[35,55,63] At room temperature, the weaker adsorption energy of phenol in the aqueous phase increases reaction rates compared to the gas phase because of more balanced coverages of phenol and hydrogen. Water solvent can lower barriers through two ways: first, water solvation can reduce the energy of transition states more than reactant species, and second, water can directly participate in transition states to facilitate bond breaking and formation. In aqueous-phase hydrogenation reactions on metals, water is predicted to lower the barriers for the hydrogenation of C=C bonds by less than 10 kJ mol^{-1} through solvation.[57,71,73] In contrast, water is predicted to lower the barriers of O-H bond breaking by >35 kJ mol^{-1} through direct participation in transition states.[32,57,71–73,143]

The LH model (**Eq. 3-2**) has been shown to approximate the rates of ECH and TCH of phenol on platinum group metals.[21,23,83] **Eq. 3-2** has been used to fit the TOF measured over a range of phenol concentrations for TCH of phenol on Pt/C.[21] The extracted K_P value on the active site was compared with K_P values of stepped facets and Pt(111)-like sites extracted independently from adsorption isotherms on polycrystalline Pt.[21,28] The active facet for phenol hydrogenation was attributed to Pt(111)-like sites due to similar K_P values. However, whether the activity of Pt(111) is due to fast intrinsic hydrogenation kinetics (larger k) or optimal coverages of the adsorbed reactants (higher $\theta_P \theta_H$) is unknown. In the case of Rh, even the active site and reason for its activity are unknown, despite Rh/C being a commonly studied metal for phenol hydrogenation.[12,21–23]

Here we elucidate which Rh facet is active for phenol hydrogenation and explain the origin of the high TOF on the active sites of Pt/C and Rh/C. Using DFT modeling, microkinetic simulations, and experimental kinetics measurements, we address whether the active site for phenol hydrogenation is a step or terrace facet and how intrinsic kinetics (i.e., transition state energies) and the phenol adsorption energy govern the phenol hydrogenation activity of Pt/C and Rh/C. We predict that (111) terraces of Pt/C and Rh/C are the active sites for phenol hydrogenation due to faster intrinsic kinetics and weaker adsorption of phenol compared to (221) stepped facets. We report that the TOF on Rh/C for ECH of phenol increases with particle size, similar to what has been shown previously on Pt/C, consistent with the active sites for phenol hydrogenation being the (111) terraces. These results indicate that synthesis techniques to preferentially expose (111) terraces on supported nanoparticles should be used to optimize the utilization of metals, increase bio-oil hydrogenation rates, and reduce the cost of bio-oil valorization.

3.2 Methods

3.2.1 Atomistic Modeling Details

The Vienna Ab initio Simulation Package (VASP) was used for all DFT calculations[42,43,144,145] along with the Atomic Simulation Environment (ASE) interface.[146] The Perdew-Burke-Ernzerhof functional[101] with the semi-empirical D3 dispersion correction[100] was chosen because of its reasonable accuracy and tractable computational expense.[147] The projector augmented wave method and a plane wave kinetic energy cutoff of 400 eV were used for all calculations.[148,149] The first-order Methfessel-Paxton smearing scheme with a 0.2 eV smearing width was used.[150]

The Pt(111), Pt(221), Rh(111), and Rh(221) surfaces were modeled using 3×3×4 slabs consisting of 36 metal atoms. The bottom two layers of each surface were fixed in their bulk lattice coordinates and the top two layers could relax during geometry optimization. Metal slabs were separated by a 20 Å vacuum. The bulk lattice parameters of Pt (3.925 Å) and Rh (3.972 Å) were determined by relaxing four-atom face centered cubic unit cells of both metals. A 16×16×16 Monkhorst-Pack *k*-point grid was used when determining the bulk lattice parameters.[151] For surface calculations, a 5×5×1 Monkhorst–Pack *k*-point grid was used. All DFT calculations were non-spin polarized. Spin polarization was found to have a negligible effect on the adsorption energy of phenol on Pt and Rh. Geometries were optimized until the electronic energy and ionic forces were converged to within 10^{-5} eV and 0.01 eV $Å^{-1}$. The climbing-image nudged elastic band (CI-NEB) method was used to find transition states of the hydrogenation reaction.[152] CI-NEB images were optimized until the electronic energies and ionic forces were within 10^{-5} eV and 0.05

eV $Å^{-1}$. The free energies for phenol and all reaction intermediates were evaluated in the harmonic limit at 300 K (including translation, rotational, and vibrational free energy contributions). The free energies of gas-phase species were evaluated using ideal gas thermodynamic corrections at 300 K and 1 bar.

Co-adsorbed hydrogen is typically present on the catalyst surface in acidic solution.[153–156] The Gibbs free energies of adsorbed phenol with co-adsorbed hydrogen on the (111) terraces and (221) steps of Pt and Rh were calculated as a function of hydrogen coverage at 300 K and 1 bar H_2. The system with the lowest free energy on each surface was chosen to model the phenol hydrogenation reaction. On the (111) surfaces, hydrogen was placed in the same configurations used previously to model benzene hydrogenation with co-adsorbed hydrogen.[157] The lowest energy configuration on Pt(111) and Rh(111) consisted of phenol adsorbed in the bridge-30 configuration with 4/9 monolayer (ML) coverage of co-adsorbed hydrogen (**Appendix Figure B-1 & Appendix Figure B-2**). On Pt(221) and Rh(221), phenol adsorbed at the step edge with 4/9 ML of hydrogen co-adsorbed on Pt(111) and 6/9 ML of hydrogen co-adsorbed on Rh(111) (**Appendix Figure B-3 & Appendix Figure B-4**). The relative free energy of adsorbed phenol with co-adsorbed hydrogen as a function of hydrogen coverage is shown in **Appendix Figure B-5**.

Mean-field microkinetic simulations were performed using the MKMCXX software[158] to predict TOFs of phenol hydrogenation on Pt and Rh. Here we assume adsorption of all species require a single site in the microkinetic model. In reality, phenol adsorbs to multiple atoms and thus it would be more appropriate to require phenol to adsorb on an ensemble of surface atoms. Nonetheless, as we show below, the single site microkinetic model gives predictions that are qualitatively consistent with experimental observations on Pt. Forward and reverse reaction rate constants were calculated using harmonic transition state theory and DFT-computed activation free energies. Thermochemistry corrections were included for all reaction intermediates and transition states using the harmonic approximation. A constant pre-exponential factor of 6.25×10^{12} s^{-1} calculated using $\frac{k_BT}{h}$ at 300 K was used. Adsorption and desorption of phenol, hydrogen, and cyclohexanone were also treated using an Arrhenius model. Adsorption and desorption were assumed to be barrierless. In the microkinetic model we use partial pressures of phenol and hydrogen at the same ratio as what is in solution experimentally.[159,160] The concentration of phenol was 20 mM and the concentration of hydrogen in solution (0.78 mM) was estimated using Henry's law for hydrogen in equilibrium with 1 bar H_2. The total system pressure was 1 bar.

Although solvent affects the hydrogenation kinetics of aromatic molecules, we found that implicit solvation using VASPsol[40,41] for phenol hydrogenation had a negligible effect on the reaction energies and transition states and thus was not considered further (**Appendix Figure B-6**). Experimental aqueous-phase adsorption free energies of phenol on Pt and Rh were used in place of DFT-computed free energies as inputs into the microkinetic model to capture the effects of solvation, solvent displacement, and changes in entropy upon adsorption of phenol. Due to challenges in explicitly treating solvation of reactants and intermediates along each step in the reaction mechanisms, we assume all species have solvation energies similar to phenol. The desorption energy of cyclohexanone was chosen to maintain thermodynamic consistency in the overall reaction free energy. The reaction free energy (–44 kJ mol^{-1}) was calculated using the reaction $P_{(aq)} + 2H_{2(g)} \rightleftharpoons CHO_{(aq)}$, where the aqueous-phase free energies of phenol (P) and cyclohexanone (CHO) are from gas-phase free energies calculated from DFT that were shifted for solvation using the Henry's law constants of the species.[161] The average adsorption free energy of H* along the reaction energy diagram was used for the microkinetic model. Cyclohexanone was modeled as the sole product of phenol hydrogenation because the formation of cyclohexanone dominates the product distribution under experimental conditions with low phenol conversion (< 10% conversion).[22]

3.2.2 Experimental Details

3.2.2.1 Chemicals and Catalytic Materials

Chemicals were obtained from Sigma-Aldrich and used as received. Aqueous sodium acetate buffer solution (3 M, pH = 5.2 ± 0.1) was used as the supporting electrolyte for ECH of phenol (≥99.0%). Ethyl acetate (≥99.8%) was used as solvent for extraction and dimethoxybenzene (99%) was used as the internal standard for gas chromatography. N_2 (>99.99%, Cryogenic Gases) was used to remove dissolved oxygen from the reactor. H_2 (ultra-high purity grade, Cryogenic Gases) was used for TCH. All water was purified with a Milli-Q system up to a resistivity of 18.2 MΩcm. Rh/C purchased from Sigma Aldrich (1, 3, 5, and 10 wt%) was used for all ECH studies at a phenol concentration of 20 mM. For the TCH studies as a function of phenol concentration, the rates at low (10 mM) and high (900 mM) phenol concentrations were low enough that product quantification was difficult with the low total amount of metal for these catalysts. Therefore, a higher Rh metal loading, 20 wt% Rh/C from Fuel Cell Store, was used for all TCH studies.

3.2.2.2 Catalyst Characterization and Surface Area Measurements

X-Ray Diffraction (XRD) analysis was done on the 20 wt% Rh/C using a Rigaku Miniflex X-Ray diffractometer with Cu Kα radiation ($\lambda = 1.5418$ Å) and a Ni filter. Samples were scanned between the 2θ range of $10° < 2\theta < 90°$ at a rate of 5°/min. The Scherrer equation was used to calculate the average crystallite size of the 20 wt% Rh/C as 2.9 nm using the full width at half maximum of the Rh(111), Rh(220) and Rh(311) diffraction peaks in **Appendix Figure B-7**. The XRD instrument line broadening was negligible compared to the estimated particle size and was thus ignored for calculating the particle size. For the TCH studies using this same 20 wt% Rh/C, the number of surface metal atoms used to normalize TOF was estimated from the particle size obtained by XRD (see SI). The particle diameters of Rh/C used to determine the particle size dependence for ECH of phenol were estimated to be 2, 5, 7, and 10 nm for the 1, 3, 5, and 10 wt% loading, respectively, from transmission electron microscopy (TEM). Ground catalyst samples were suspended in ethanol, and microliters of the catalyst suspension were applied on a copper grid coated with carbon and dried before a TEM measurement was performed with a JEOL JEM-2011 electron microscope operating at 120 keV accelerating voltage. For further detail and sample images see ref. [11]. The number of surface metal atoms for the 1, 3, 5, and 10 wt% Rh/C catalysts used for the particle size studies was determined from H_2 chemisorption as described previously.[11,22] The metal dispersions, or moles of surface Rh per total moles of Rh, of the 1, 3, 5, and 10 wt% Rh/C samples were 0.43, 0.2, 0.135, and 0.1, respectively. Details on weight loading of Rh supported on carbon, commercial source of the catalyst, reaction for which each catalyst was used, average particle sizes from TEM, XRD, and H_2 chemisorption and dispersion from H_2 chemisorption and XRD are shown in **Appendix Table B-1**.

3.2.2.3 Thermocatalytic Hydrogenation

A 125 mL jacketed glass batch reactor was used to perform TCH of phenol. 10 mg of 20 wt% Rh/C catalyst was added to Millipore water in the cell and then sparged with a flow of N_2 for 30 min at 100 mL min^{-1} under continuous stirring at 500 rpm to remove oxygen and disperse the nanoparticles. A flow of H_2 at 70 mL min^{-1} into the cell for 30 minutes was used to activate the catalyst, saturate the solution with H_2, and bring the headspace pressure to 1 bar H_2. Before introducing phenol, the H_2 flow was reduced to 25 mL min^{-1} and kept constant throughout the reaction to maintain the reactor pressure at 1 bar H_2 and prevent air from entering the reactor. The temperature was kept at 25 °C using a refrigerated/heated bath circulator (Fisher Scientific). To attain a desired phenol concentration in the cell, a particular concentration of phenol in water, already sparged with N_2 to remove dissolved O_2, was introduced into the cell. A syringe connected to PEEK tubing was used to avoid possible contamination from a metal needle. The pH of the solution with phenol was 5.2–5.4, which is the same as the pH of phenol in acetate buffer used for ECH. Previous studies of TCH of phenol on Pt/C show that at this pH, the phenol TCH activity is essentially independent of the presence of acetate.[23] The reactor mixture was stirred using a stir bar at 500 rpm for the duration of the reaction. At this stir rate, limitations on the measured rate due to mass transfer were eliminated (**Appendix Figure B-8**). The reaction start time was recorded immediately after the phenol was introduced in the cell. All measurements were done under differential conditions (<10% conversion of phenol).

3.2.2.4 Electrocatalytic Hydrogenation

A two-compartment batch electrolysis cell was used for ECH studies.[11] The cathodic and anodic compartments were separated by a Nafion 117 membrane. The carbon felt (Alfa Aesar, >99.0%, 3 cm×1.5 cm with 3.2 mm thickness) used as the working electrode was first presoaked in water and connected to a 3 mm diameter graphite rod (Sigma Aldrich, 99.99%). For each of the 1, 3, 5, and 10 wt% Rh/C catalysts, 10 mg catalyst were added to the acetate buffer supporting electrolyte in the cathodic compartment. The carbon felt connected to a graphite rod was inserted into the cell and the catalyst was loaded into the felt by stirring the catalyst/acetate buffer mixture for 30 min at 500 rpm until the catalyst infiltrated the carbon felt.[22] The effectiveness factor of 0.97 for the carbon felt (3.2 mm thick) used in this work indicates the felt was thin enough to avoid internal mass transfer limitations.[82] The reference electrode was a Ag/AgCl double junction electrode and the counter electrode was a high-surface area Pt mesh. Acetate anions are reported to have negligible adsorption on Pt and Rh at the cathodic potential used in this work (i.e., −0.1 V vs. RHE).[92] Hence we assume ECH is not impacted by competitive adsorption between the reactants and acetate. Before ECH, the supporting electrolyte was sparged with N_2, which was also used as a blanket to prevent O_2 from entering the cell. A current of −40 mA was applied for 30 min to the working electrode to polarize the catalyst.

To measure the ECH rate, phenol solution already sparged with N_2 was added to the cell to make a final concentration of 20 mM and the reaction was performed at a fixed potential using a Bio-Logic VSP-300. The solution resistance was measured using impedance spectroscopy based on the real part of the impedance at a frequency of 200 kHz. During the ECH measurements, only 85% of the solution resistance was compensated automatically, because a higher fraction of compensation results in instability in the applied voltage due to the limitations of the potentiostat controller.[162] The remaining 15% of the solution resistance was manually corrected following the measurement and used to calculate the final iR-compensated applied potential of −0.1 V vs. RHE that is reported. The pH of acetate buffer and phenol solution in the cathodic compartment was measured before and after the reaction for each catalyst metal weight loading and no change was observed.

3.2.2.5 Product Analysis

The TCH and ECH reactions were monitored by removing 0.5 mL aliquots every 3 min from the batch reactor. Three sequential liquid-liquid extractions were performed to transfer phenol and its associated hydrogenation products from the aqueous phase to an organic phase. In each extraction step, the aqueous phase was mixed with 1 mL of pure ethyl acetate to transfer phenol and its associated hydrogenation products from the aqueous phase to the organic phase, and then the two liquids were separated. Three extractions were sufficient to transfer all organics from the aqueous-phase aliquot to the organic phase because no phenol or product was detected upon additional extraction. Remaining water was removed from the organic phase with anhydrous Na_2SO_4 (Sigma Aldrich 99%). 20 µL of pure dimethoxybenzene was added as internal standard to 1 mL of the dried organic phase. 1 µL of the resulting solution was injected to an Agilent Varian 450 gas chromatograph equipped with a flame ionization detector. Carbon balances were greater than 90% for all reported data. Rates were calculated using the moles of cyclohexanone and cyclohexanol detected to determine the moles of phenol converted. At least four time points were used to determine the rate. TOFs were calculated based on the rate of cyclohexanol and cyclohexanone formed per surface metal atom as described in ref. [22]. Additional details on TOF calculations are given in **B.2**.

3.2.2.6 Fitting TCH Rate Data to a Langmuir-Hinshelwood Model

The experimental TCH rate data was fitted by minimizing the sum of the squared errors between the experimental TOF at different phenol concentrations and the TOF predicted from the reaction model in **Eq. 3-2**, in the same way as described in ref. 10. To minimize the difference, the values of k, K_P, and K_HC_H were optimized, and these are the values reported. For simplicity in fitting the kinetic model, the values of k, K_P, and K_HC_H were assumed to be constant with phenol concentration (i.e., Langmuir adsorption). We have previously shown that equilibrium adsorption isotherms on Rh were best fit assuming an adsorbate interaction term of zero (i.e., Langmuir model)[35] supporting our assumption of Langmuir adsorption when fitting the kinetic data here.

3.3 Results & Discussion

3.3.1 Adsorption Energies of Phenol on the Active Sites of Pt and Rh

By fitting phenol hydrogenation rate data to a LH model, K_P of the active site can be extracted and compared with known K_P values on different facets to determine the identity of the active site. This approach has been used on Pt/C to determine that Pt(111) is the active site for phenol hydrogenation,[21] but similar analysis has not yet been performed on Rh. Here we measure phenol hydrogenation rates on Rh/C under the same TCH conditions as performed for Pt/C (i.e., 1 bar H_2)[21] and extract K_P on Rh/C by fitting kinetic data to **Eq. 3-2**. We compare the extracted K_P on the active site with K_P values previously extracted from an aqueous-phase phenol adsorption isotherm on Rh wire at the same temperature and pH as our kinetic measurements here.[35]

The TOF in **Figure 3-1** shows a phenol concentration dependence typical of a competitive LH mechanism, where at low concentrations of phenol the reaction order in phenol is positive due to the phenol coverage being low, and at high concentrations of phenol the reaction order is negative due to the phenol coverage being too high and poisoning the metal surface. By minimizing the error between the experimental TOF values and the predicted TOF values from **Eq. 3-2**, we determine k, K_P, and K_HC_H.

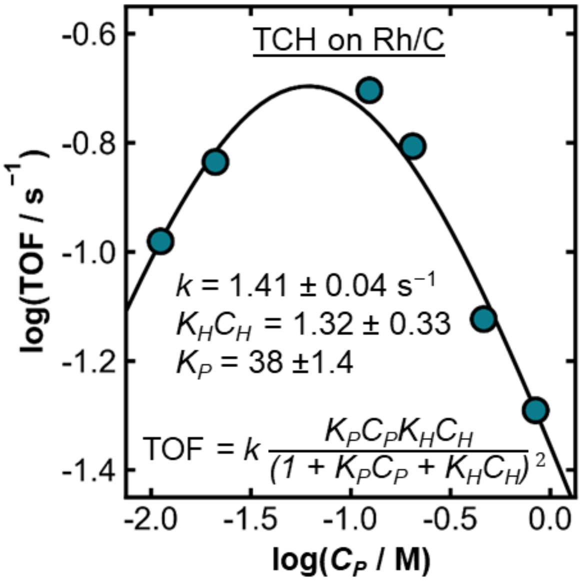

Figure 3-1 Thermocatalytic hydrogenation of phenol on Rh. Log(TOF) for thermocatalytic hydrogenation (TCH) of phenol on 10 mg of 20 wt% Rh/C as a function of log(phenol concentration) for phenol concentrations (C_P) from

0.01 M to 1 M. The TOF data points (circles) were fit to the Langmuir-Hinshelwood rate law (solid black line) assuming competitive adsorption between phenol and hydrogen. TCH of phenol in water (pH 5.2–5.4) was performed under 1 bar H_2 at 298 K with a stir bar at 500 rpm. The values of k, K_P, and K_HC_H on the active site were extracted by minimizing the sum of the squared errors between the experimental TOF and the theoretical TOF obtained using **Eq. 3-2**. The standard error of each parameter was estimated using the "jackknife" procedure.[163,164]

We compare the phenol adsorption equilibrium constant, K_P, on the active site from TCH rate measurements to the K_P values extracted independently from adsorption isotherm fitting to understand the active site on Pt and Rh (**Table 3-1**). K_P on the active site of Pt/C was measured previously to be 33, which corresponds to a Gibbs free energy of adsorption (ΔG_P) of –8.7 kJ mol^{-1}, by fitting kinetic data using **Eq. 3-2**.[21] K_P values of 38 and 120000 have been measured previously for two distinct adsorption sites on polycrystalline Pt by fitting to a phenol adsorption isotherm constructed by measuring the fraction of hydrogen underpotential deposition (H_{UPD}) sites inhibited by phenol adsorption as a function of phenol concentration.[28] Phenol adsorption sites with the lower K_P values adsorb phenol more weakly and sites with the higher K_P values adsorb phenol more strongly. We refer to the adsorption equilibrium constants of the weak and strong adsorption sites as $K_{P,weak}$ and $K_{P,strong}$, respectively. We refer to the corresponding Gibbs free energies as $\Delta G_{P,weak}$ and $\Delta G_{P,strong}$. The weaker phenol adsorption site of Pt is attributed to the (111) terraces, and the stronger phenol adsorption site is attributed to (110)-like, (100)-like, and step sites based on the measured cyclic voltammograms (CVs).[21,28] As discussed in ref. [21], the similarity between the K_P value on the active site of Pt/C from kinetic measurements (K_P = 33) and $K_{P,weak}$ from adsorption isotherm fitting ($K_{P,weak}$ = 38) implies that the active facet for phenol hydrogenation on Pt/C is a Pt(111)-like terrace, which adsorbs phenol more weakly than stepped facets.

Table 3-1 Measured adsorption energies on Pt and Rh. Experimental equilibrium adsorption constants of phenol and corresponding adsorption free energies (ΔG_P) extracted from TCH rate measurements and CV adsorption isotherm fitting at 298 K and pH = 5.2. TCH rates are measured on Pt/C and Rh/C and adsorption isotherms are on a Pt or Rh wire. Standard concentration of phenol is defined as 1 M. ΔG_P values have units of kJ mol^{-1}.

Metal	Technique used to extract phenol adsorption equilibrium constant

	Fitting TCH rates to rate law		*Adsorption isotherm fitting to CV+H_{UPD} measurements*			
			Weak adsorption site		*Strong adsorption site*	
	K_P	ΔG_P	$K_{P,weak}$	$\Delta G_{P,weak}$	$K_{P,strong}$	$\Delta G_{P.strong}$
Pt	33 from ref. [21]	−8.7	38 from ref. [28] (attributed to (111) terraces).	−9.0	120000 from ref. [28] (attributed to step sites).	−29
Rh	38 (this work)	−9.0	17 from ref. [35]	−7.0	41000 from ref. [35]	−26

ΔG_P values for Pt are from a Temkin adsorption isotherm and have lateral interaction energy values of 0 and 4 kJ mol^{-1} for the weak and strong binding sites. Rh values were found to have a best fit using a Langmuir adsorption isotherm i.e., the adsorption energies were not a function of phenol coverage.

Similar to Pt, polycrystalline Rh has two distinct adsorption sites with different equilibrium constants for phenol—the values of $K_{P,weak}$ and $K_{P,strong}$ on Rh wire were measured previously from adsorption isotherm fitting to be 17 and 41000, respectively (**Table 3-1**).[35] The comparable K_P value on the active site of Rh from **Figure 3-1** (K_P = 38) and $K_{P,weak}$ from adsorption isotherm measurements ($K_{P,weak}$ = 17) suggests that the facet which adsorbs phenol more weakly is active for phenol TCH on Rh/C. The three order of magnitude difference between $K_{P,strong}$ and K_P of the active site of Rh indicate that this stronger adsorption site does not contribute significantly to catalytic turnover. Unlike on Pt, where the H_{UPD} peaks of (111) terraces and step sites are distinguishable, the CVs on Rh do not indicate whether (111) terraces or steps are weak or strong adsorption sites. Therefore, we cannot determine from CVs alone whether the active site of Rh is the (111) terrace or if stepped facets (e.g., Rh(221) steps) are responsible for TCH activity. In Section 3.3.3, we describe our first principles calculations and microkinetic modeling to determine the active Rh facet.

3.3.2 Explaining the Activity of Pt(111) from First Principles Modeling

It is unclear whether Pt(111) is intrinsically more active than the stepped facets (i.e., larger *k*) or whether the activity of Pt(111) is from differences in adsorption energies between the weak and strong adsorption sites. To clarify the origin of the activity of the Pt(111) facet, we study the phenol hydrogenation reaction on the Pt(111) terrace and Pt(221) step at 0 V vs. RHE (i.e., 1 bar H_2 at 300 K) using DFT modeling and mean-field microkinetic simulations. This is identical to the methodology for calculating the TCH rate at 1 bar H_2 from a computational perspective. Our calculations of phenol hydrogenation on Pt(100) in the gas phase show that Pt(100) is over four orders of magnitude less active than Pt(111) and thus is not considered further (**Appendix Figure B-9**). As discussed earlier, the surface reaction for TCH and ECH is hypothesized to be the same,[12,22,23] so we assume ECH and TCH share the same active site.

On both Pt(111) and Pt(221), the first hydrogenation step was modeled to occur on the *ortho* carbon followed by hydrogenation of the *meta* carbon to form 1,3-cyclohexadienol, in accord with a prior study of phenol on Pt.[72] We predict the third and fourth hydrogenation steps occur at the *para* carbon and *meta* carbons, respectively, to form 1-cyclohexenol. We model the tautomerization of 1-cyclohexenol to form cyclohexanone; however, tautomerization can occur at an earlier point along the reaction pathway. DFT-predicted geometries of this hydrogenation mechanism on Pt(111) are shown in **Figure 3-2a**, and the geometries on Pt(221) are shown in **Appendix Figure B-10**. The corresponding energetics of the surface reactions relative to aqueous-phase phenol and gas-phase hydrogen, with a surface hydrogen coverage of 4/9 ML are given in **Figure 3-2b**. Because of the difficulties in accurately predicting aqueous-phase organic adsorption energies computationally, we instead use the experimental values for phenol adsorption from **Table 3-1** as a calibration (i.e., to determine the relative energy of (ii)). The dotted lines refer to the assumption that the modeled Pt site is 'weak' adsorption ($\Delta G_{P,weak}$) and the solid lines refer to the assumption that the modeled Pt site is ‘strong’ adsorption ($\Delta G_{P,strong}$). Although, as discussed above, we know that Pt(111) corresponds to the ‘weak’ adsorption ($\Delta G_{P,weak}$), and thus the dotted black line is the ‘correct’ pathway for Pt(111), and the solid blue line in **Figure 3-2b** is the ‘correct’ pathway for Pt(221), we show both cases here to understand the effect of this initial adsorption step on the overall rate. All subsequent energies (i.e., (iii) through (xvi)) are plotted based on the calculations relative to the adsorbed phenol, using the assumption that any solvation effects on phenol adsorption are the same as for the adsorbed intermediates and transition states. The final energy of (xvii) is from the thermodynamic value of the difference in energy of phenol and cyclohexanone in the aqueous phase, to maintain thermodynamic consistency for all plotted pathways. The surface-adsorbed H* consumed was replenished after each hydrogenation step to maintain the initial hydrogen coverage over the course of the reaction.

Hydrogen co-adsorption has been found to reduce hydrogenation barriers for various organic compounds on platinum group metals,[157,165,166] but has not yet been studied for phenol hydrogenation on Pt. On average, we find that co-adsorption of hydrogen decreases the activation energies of hydrogenation and tautomerization on Pt(111) by 20 kJ mol^{-1} (**Appendix Figure B-9**). However, we find that the Pt(111) terrace is more active than the Pt step regardless of the presence or absence of co-adsorbed hydrogen (**Appendix Figure B-9**). Although co-adsorbed hydrogen does not change the activity ordering of Pt terraces and steps, this may not always be the case for other catalysts (**Appendix Figure B-9** shows that hydrogen co-adsorption may change the predicted active site for Rh).

When looking at the reaction energy diagram for phenol hydrogenation on Pt(111) and Pt(221) (**Figure 3-2b**), there are differences beyond the phenol adsorption energy that contribute to the kinetics. Even if the phenol adsorption energy were the same (i.e., comparing the solid blue and black lines in **Figure 3-2b** to one another and the dotted lines to each other), the transition state barriers are often higher on Pt(221) than on Pt(111). These correspond to intrinsic kinetic differences on the two surfaces, rather than solely coverage effects.

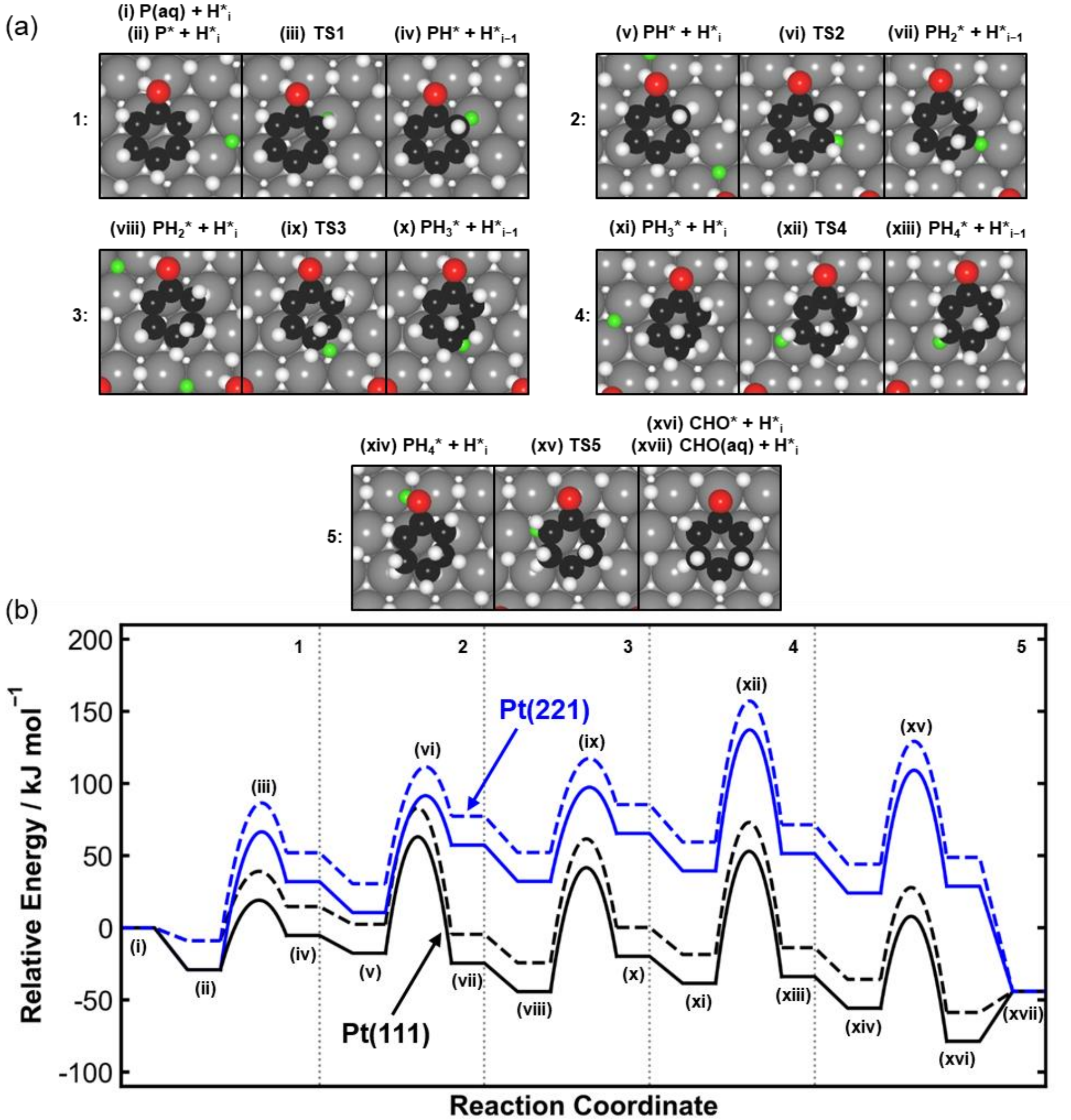

Figure 3-2 Free energy diagram for phenol hydrogenation on Pt. **(a)** DFT-predicted geometries corresponding to the initial, transition, and final states for the hydrogenation of phenol ($P_{(aq)}$) to cyclohexanone ($CHO_{(aq)}$) on Pt(111) with 4/9 ML of co-adsorbed hydrogen. Products of the first, second, third, and fourth hydrogenation additions are denoted as PH*, PH_2*, PH_3*, and PH_4*, respectively. H^*_i corresponds to adsorbed hydrogen at 4/9 ML hydrogen coverage, and H^*_{i-1} corresponds to adsorbed hydrogen after one hydrogen has reacted with the organic. TS1, TS2, TS3, and TS4 denote hydrogenation transition states and TS5 denotes the tautomerization transition state. Color legend: Pt = grey, O = red, C = black, and H = white. The H* atom participating in each elementary reaction step is colored green (cases where more than one hydrogen is colored green are due to periodic boundary conditions). **(b)** Reaction free energy profiles for the electrocatalytic hydrogenation of phenol to cyclohexanone on Pt(111) and Pt(221) at hydrogen coverages of θ_H = 4/9 ML on Pt(111) and Pt(221) at 0 V vs. RHE. Dotted lines refer to the adsorption energy of phenol matching the experimental adsorption energy corresponding to $\Delta G_{P,weak}$, while the solid lines

correspond to the adsorption energy of phenol matching the experimental adsorption energy of $\Delta G_{P,strong}$ in **Table 3-1** for Pt. All subsequent adsorption energies are referenced to this value, with the overall reaction energy of phenol to cyclohexanone plotted according to calculated reaction energies. Thermal corrections to the free energies of adsorbed species and transition states are included within the harmonic approximation at 300 K.

To predict whether Pt(221) or Pt(111) is more active, we construct a mean-field microkinetic model to predict TOFs for phenol hydrogenation on Pt(111) and Pt(221) based on the reaction energetics in **Figure 3-2b**. The energies used for each adsorption and elementary reaction step in the microkinetic model of each facet are given in the Appendix (**Appendix Table B-3**). The calculated TOFs between 290 and 310 K from the microkinetic simulations of phenol hydrogenation on Pt(111) and Pt(221) in **Figure 3-3** show that Pt(111) is the active site. The reaction on both facets is modeled using both the weak and strong phenol adsorption free energies to clarify how differences in phenol adsorption on the two facets affect phenol hydrogenation kinetics. Pt(111) is more active than Pt(221) regardless of whether the reaction is modeled with $\Delta G_{P,weak,}$ or $\Delta G_{P,strong}$. Considering that $\Delta G_{P,weak}$ is attributed to Pt(111)-like terraces and $\Delta G_{P,strong}$ is attributed to stepped facets,[28] our computational results predict that Pt(111) is over thirteen orders of magnitude more active than Pt(221) at 300 K and 0 V vs. RHE. Even when the reaction is modeled with $\Delta G_{P,weak}$ on both facets, Pt(111) is still over thirteen orders of magnitude more active than Pt(221), highlighting that the activity differences between Pt(111) terraces and steps are largely due to intrinsic kinetic differences and not only due to differences in phenol adsorption on Pt(111) and step sites. Our predicted TOFs based on the microkinetic modeling support previous experimental results that Pt(111) is the active facet for phenol hydrogenation.[21] The joint factors of adsorption energy and intrinsic kinetic activity contributing to the activity of a catalyst site helps to explain why Pd/C is less active than Pt/C for phenol hydrogenation despite their similar adsorption energies.[21]

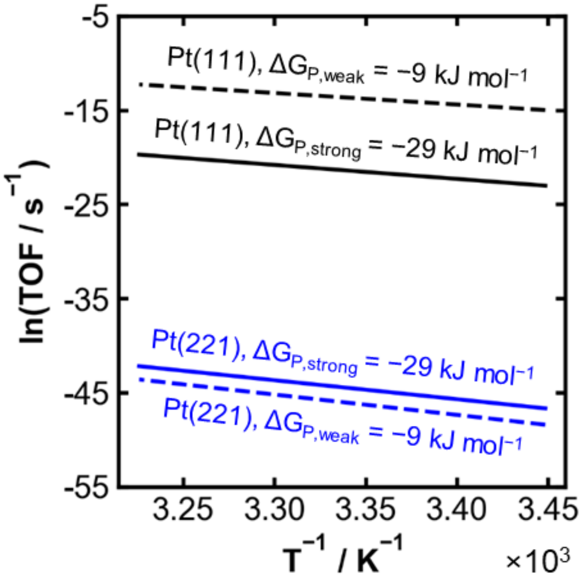

Figure 3-3 Arrhenius plot of phenol hydrogenation on Pt. Arrhenius plot for the hydrogenation of phenol between 290 K and 310 K at 0 V vs. RHE based on microkinetic modeling of all elementary steps (i.e., without assumption of RDS). Concentration of phenol is 20 mM (see methods). Values corresponding to Pt(111) are shown with blacklines and values corresponding to Pt(221) are shown with blue lines. Both facets are modeled using $\Delta G_{P,weak}$ (dashed lines) and $\Delta G_{P,strong}$ (solid lines) from **Table 3-1**. Elementary rate constants are calculated from the activation energies of the steps shown in **Figure 3-2b**.

The predicted apparent activation energies of the reactions are extracted from the slopes of the Arrhenius plots in **Figure 3-3**. The predicted activation energy of 102 kJ mol^{-1} on Pt(111) ($\Delta G_{P,weak}$ = −9 kJ mol^{-1}) and 168 kJ mol^{-1} on Pt(221) ($\Delta G_{P,strong}$ = −29 kJ mol^{-1}) are much higher than the experimental apparent activation energy of 29 kJ mol^{-1} on Pt/C at 300 K.[12] Besides the commonly attributed error in predicted energetics due to using an approximate exchange-correlation functional, the high computed apparent activation energy relative to the experimental value may arise from the exclusion of explicit solvation effects in our atomistic model.

Although the microkinetic modeling simulations reveal that the higher activity of Pt(111) compared to stepped facets is due to Pt(111) having both faster intrinsic kinetics and weaker phenol adsorption, there are some discrepancies between our predicted RDS and that in our LH model (**Eq. 3-2**). Microkinetic simulations predict that the fourth hydrogenation step on Pt(111) has the highest degree of rate control (**Appendix Figure B-11**).[167] This prediction supports that a surface hydrogenation step, not adsorption or desorption, is the RDS for phenol hydrogenation, but is different than our assumption in **Eq. 3-1 & Eq. 3-2** that the first hydrogenation step is the RDS. Explicit treatment of solvent effects along the reaction coordinate would lead to a more accurate prediction of the RDS. Recent experimental and computational work has suggested that the second hydrogen addition to phenol on Pt is the RDS at temperatures of 433 to 473 K, because H/D exchange of phenol was found to be fast compared to the hydrogenation rate, implying a quasi-equilibrated first hydrogenation step.[25] Because of the uncertainty in which hydrogenation step (1-4 in **Figure 3-2a**) is the RDS, a more general interpretation of **Eq. 3-2** is to describe a surface reaction between hydrogen and either phenol or a partially hydrogenated phenol intermediate, as postulated in ref. [21].

3.3.3 Discerning the Active Facet of Rh from First Principles Modeling

Comparing K_P from our experimental TCH kinetic measurements with the $K_{P,weak}$ and $K_{P,strong}$ values extracted from adsorption isotherms indicates that the active facet for phenol hydrogenation on Rh is the facet that adsorbs phenol more weakly (**Table 3-1**). However, experimental CV adsorption isotherms do not reveal whether $K_{P,weak}$ (and hence the active facet) may be attributed to the Rh(111) terraces or stepped facets.[35] To identify the active facet of Rh and explain the origin of the activity, we computationally model the hydrogenation of phenol to cyclohexanone on Rh(111) and Rh(221) with co-adsorbed hydrogen using the same mechanism considered for Pt. Similar to the observation on Pt, hydrogen co-adsorption reduces activation energies on Rh(111) by 8 kJ mol^{-1} on average (**Appendix Figure B-9**). The geometries on Rh(111) are shown in **Figure 3-4a** and the geometries on Rh(221) are shown in **Appendix Figure B-12**. On Rh, it has been proposed that phenol may be hydrogenated through a mechanism that involves the conversion of phenol (C_6H_5OH) to phenoxy (C_6H_5O) followed by sequential hydrogenation to form cyclohexanone (**Scheme B-1**).[68] We model this mechanism (**Appendix Figure B-13**) and predict it to be slow compared to the mechanism in **Figure 3-4a**, which involves phenol hydrogenation to 1-cyclohexenol followed by tautomerization to form cyclohexanone. We use the same methodology as described for **Figure 3-2b** to plot the reaction energy diagram on Rh in **Figure 3-4b**, again using the experimentally measured adsorption energies of phenol. Unlike for phenol, here we do not know already whether Rh(111) or Rh(221) correspond to ‘weak’ or ‘strong’ adsorption. Like on Pt, the data in **Figure 3-4b** shows that there are differences in the reaction energy profile between Rh(111) and Rh(221) apart from the phenol adsorption energy, despite the same mechanism being investigated on both surfaces.

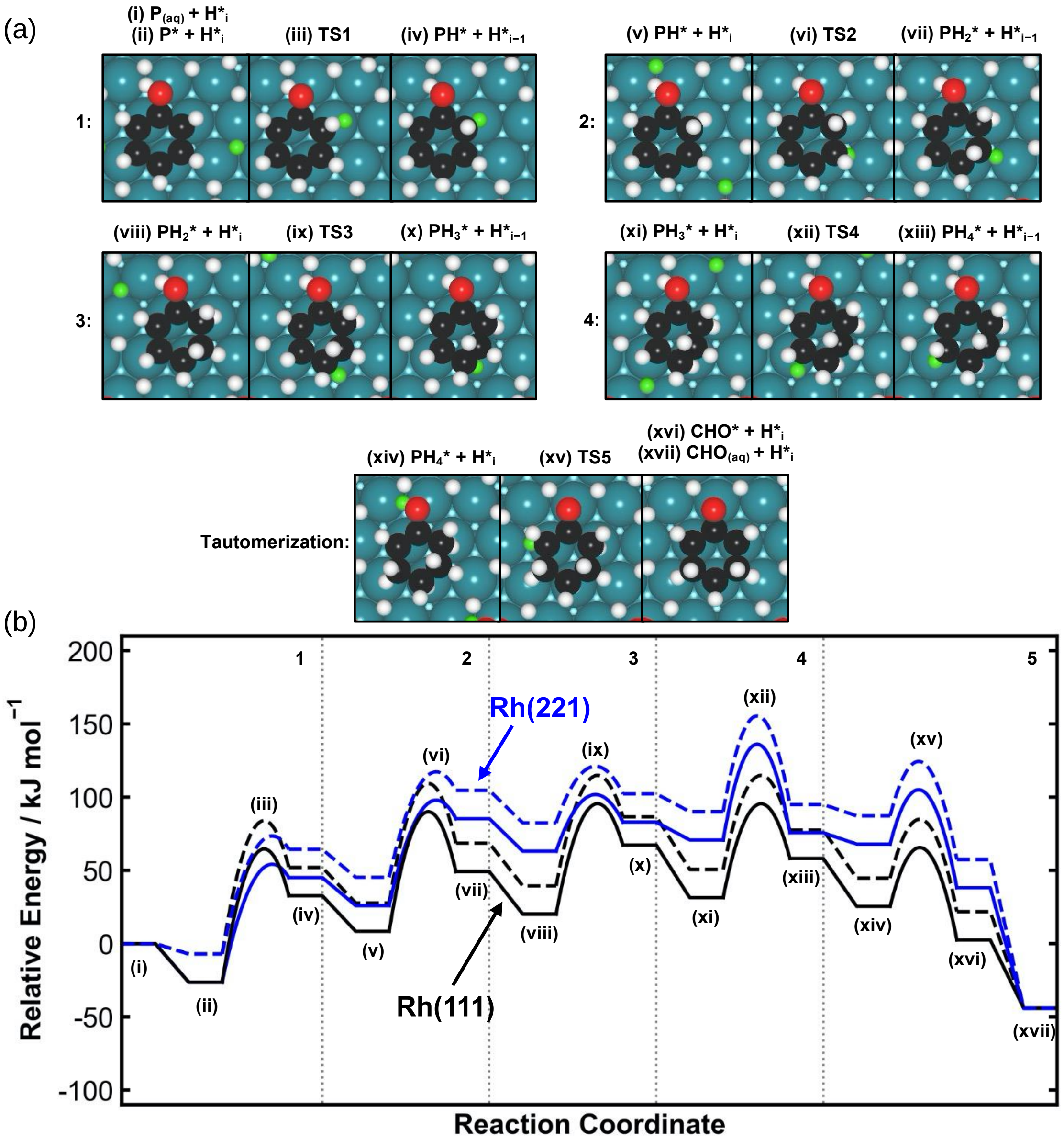

Figure 3-4 Free energy diagram for phenol hydrogenation on Rh. **(a)** DFT-predicted geometries corresponding to the initial, transition, and final states for the hydrogenation of phenol ($P_{(aq)}$) to cyclohexanone ($CHO_{(aq)}$) on Rh(111) with 4/9 ML of co-adsorbed hydrogen. Products of the first, second, third, and fourth hydrogenation additions are denoted as PH*, PH_2*, PH_3*, and PH_4*, respectively. H^*_i corresponds to adsorbed hydrogen at 4/9 ML hydrogen coverage, and H^*_{i-1} corresponds to adsorbed hydrogen after one hydrogen has reacted with the organic. TS1, TS2, TS3, and TS4 denote hydrogenation transition states and TS5 denotes the tautomerization transition state. Color legend: Rh = teal, O = red, C = black, and H = white. The H* atom participating in each elementary reaction step is colored green (cases where more than one hydrogen is colored green are due to periodic boundary conditions). **(b)** Reaction free energy profiles for the electrocatalytic hydrogenation of phenol on Rh(111) and Rh(221) at hydrogen coverages of $\theta_H = 4/9$ ML on Rh(111) and $\theta_H = 6/9$ ML on Rh(221) at 0 V vs. RHE. Dotted lines refer to the adsorption energy of phenol matching the weak experimental adsorption energy of Rh ($\Delta G_{P,weak}$ in **Table 3-1**) while the solid lines correspond to the adsorption energy of phenol matching the experimental adsorption energy $\Delta G_{P,strong}$ in **Table 3-1**. All subsequent adsorption energies are referenced to this value, with the overall reaction energy of phenol to cyclohexanone plotted according to calculated reaction energies. Thermal corrections to the free energies of adsorbed species and transition states are included within the harmonic approximation at 300 K.

We construct a mean-field microkinetic model to predict TOFs for phenol hydrogenation on Rh(111) and Rh(221) based on the energetics in **Figure 3-4b** and predict that Rh(111) is the active site for phenol hydrogenation. The energies used for each adsorption and elementary reaction step are given in the Appendix (**Appendix Table B-4**). By analyzing the predicted TOFs as a theoretical Arrhenius plot (**Figure 3-5**), we show that Rh(111) is more active than Rh(221) for phenol hydrogenation at temperatures between 290 K and 310 K. The Rh(111) is more active than Rh(221) regardless of whether the reaction on Rh(111) is modeled using $\Delta G_{P,weak}$ or $\Delta G_{P,strong}$. Our experimental data (**Table 3-1**) indicate that the active site for phenol hydrogenation on Rh is the site that adsorbs phenol more weakly. When modeling phenol ECH using the weak phenol adsorption energy on both facets, we predict that Rh(111) is over six orders of magnitude more active than Rh(221). These results demonstrate that Rh(111) must be the weak adsorption site of Rh due to the relative inactivity of Rh(221). Although the microkinetic model predicts Rh(111) with $\Delta G_{P,strong}$ to have the highest activity due to the more balanced coverages of hydrogen and phenol, the stronger adsorption site being the active facet is inconsistent with experimental measurements. Modeling the effect of solvation on the adsorption energy of hydrogen would improve the predicted activity ordering between $\Delta G_{P,weak}$ and $\Delta \mathrm{G}_{P,strong}$ on Rh(111).

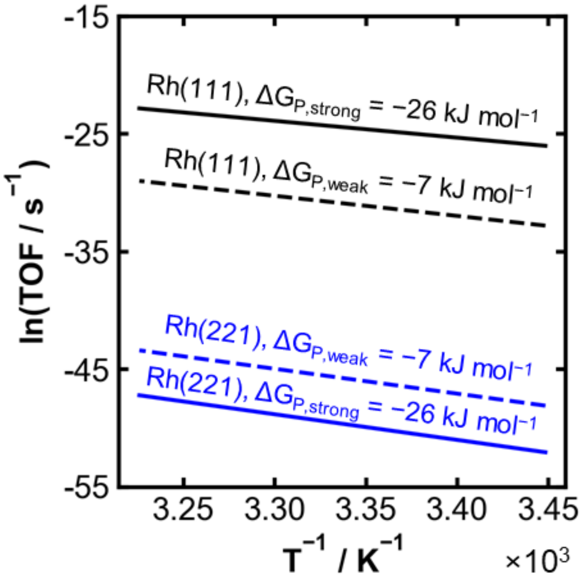

Figure 3-5 Arrhenius plot for phenol hydrogenation on Rh. Arrhenius plot for the hydrogenation of phenol between 290 K and 310 K at 0 V vs. RHE based on microkinetic modeling. Concentration of phenol is 20 mM (see methods). Values corresponding to Rh(111) are shown with black lines and values corresponding to Rh(221) are shown with blue lines. Both facets are modeled using $\Delta G_{P,weak}$ (dashed lines) and $\Delta G_{P,strong}$ (solid lines) from **Table 3-1**. Elementary rate constants are calculated from the activation energies of the steps shown in **Figure 3-4b**.

Based on **Figure 3-5**, the apparent activation energy for ECH of phenol on Rh(111) ($\Delta G_{P,weak}$ = –7 kJ mol^{-1}) is 142 kJ mol^{-1} and for Rh(221) ($\Delta G_{P,strong}$ = –26 kJ mol^{-1}) is 181 kJ mol^{-1}. Similar to Pt, the apparent activation energies from the DFT-based mean field microkinetic models are significantly larger than the experimentally measured value of 23 kJ mol^{-1} in the absence of mass transport limitations on Rh/C.[12] Similar to Pt, the fourth hydrogenation step is predicted to have the highest degree of rate control on Rh(111) and Rh(221) (**Appendix Figure B-11**).

3.3.4 Intrinsic Activity of Phenol Hydrogenation vs. Fraction of (111) Terraces

To corroborate our predictions that Pt(111) and Rh(111) are the active sites for phenol TCH and ECH, we measured the particle size dependence of the ECH TOF and Faradaic efficiency on Rh/C particles with diameters between 2 and 10 nm (**Figure 3-6a**). The TOFs for ECH of phenol on Pt/C over a similar particle size range from ref. [82] are reproduced in **Figure 3-6a**. On both Pt/C and Rh/C, larger particles are predicted to have a higher fraction of (111) sites from the cuboctahedron model,[82,168,169] while smaller particles have a higher fraction of step-like features.[170,171] These larger particles have higher TOFs and higher Faradaic efficiencies than smaller particles. At small enough particle sizes (~2 nm), we observe practically no catalytic activity, indicating that the step sites are inactive for electrocatalytic hydrogenation of phenol, consistent with our modeling predictions. Although the fraction of (100) terraces will also increase with particle size according to the cuboctahedron model, the (100) sites of Pt and Rh adsorb phenol stronger than (111) terraces.[28,35] Because our combined kinetic and adsorption measurements show that the active site should adsorb phenol weakly, the (100) sites are not the active sites. Additionally, we predict (100) sites to have lower gas-phase hydrogenation activity compared to (111) sites (**Appendix Figure B-9**). Therefore, we attribute the increase in activity and Faradaic efficiency with particle size to the increasing fraction of the active (111) terraces that dominate the catalytic turnover.

Decreasing particle size to reduce the mass of expensive metals required (i.e., Pt and Rh) is desired only down to a certain particle size, below which the decrease in fraction of active sites counteracts the benefit from a higher fractional exposure. The catalyst utilization, the phenol hydrogenation rate per gram of catalyst, is shown in **Figure 3-6b**. The smallest particles of Pt (~3 nm) have lower utilizations compared to larger particles; however, the catalyst utilization plateaus at further increasing particle sizes. We expect there to be a maximum in catalyst utilization for Pt within the 3−10 nm particle diameter range and hypothesize that increasing the particle diameter beyond 10 nm, while possibly increasing the TOF, would decrease the catalyst utilization, and thus be undesired for practical applications. The utilization of Rh increases monotonically in the 3−10 nm particle diameter range, which is unexpected as we would assume a plateau or maximum to occur, similar to what is seen for Pt, if a cuboctahedron model of the particle size-facet distribution is correct.[172] This lack of a matching catalyst utilization maximum on Pt and Rh in **Figure 3-6b** implies that the distribution of terrace sites with particle size may differ between Pt and Rh, and that higher utilizations of Rh may be achieved on nanoparticles sizes >10 nm. However, we do hypothesize a maximum in catalyst utilization will occur on Rh at large enough particle sizes.

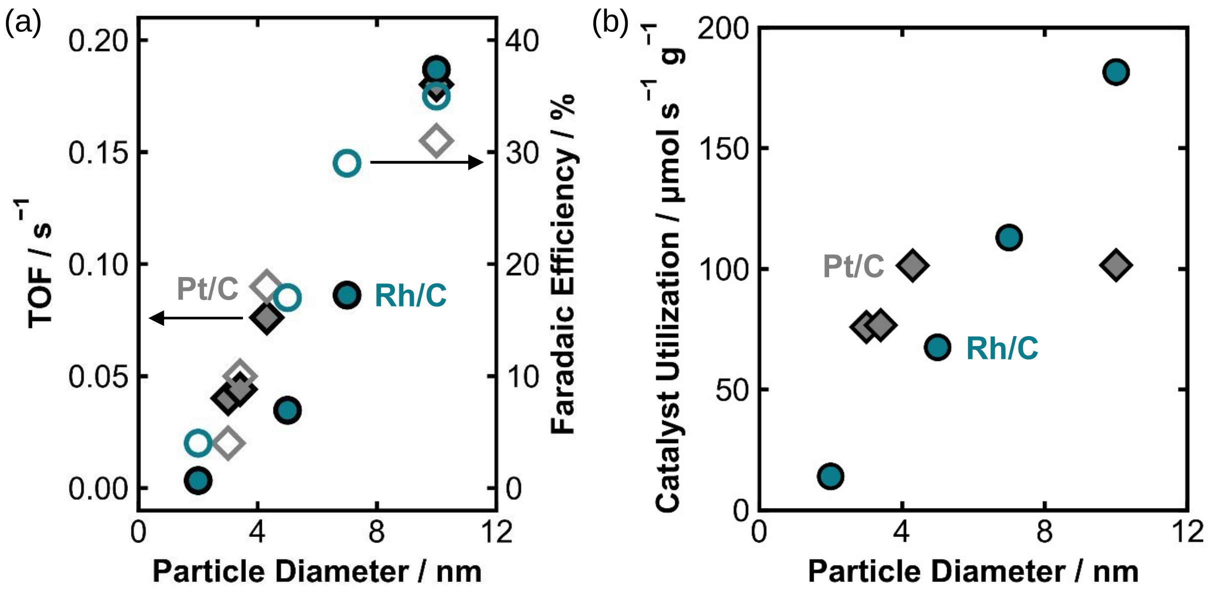

Figure 3-6 Experimental structure sensitivity of phenol hydrogenation on Pt and Rh. **(a)** The turnover frequency (TOF) and Faradaic efficiency for electrocatalytic hydrogenation (ECH) of 20 mM phenol at 298 K as a function of particle size for Pt/C and Rh/C nanoparticles. The average nanoparticle size was estimated using TEM. 10 mg of Pt/C and Rh/C were infiltrated into a carbon felt and used as the working electrode and the supporting electrolyte was 3 M acetate buffer (pH 5.2). The applied potential was −0.1 V vs. RHE for Rh/C and was corrected for solution resistance. The TOFs and Faradaic efficiencies for Pt/C are from ref. [82] measured at approximately −0.47 vs. Ag/AgCl and corrected for solution resistance. TOF is the total moles of cyclohexanol and cyclohexanone molecules produced per second normalized to the total moles of surface Pt or Rh atoms obtained from H_2 chemisorption. Open points refer to Faradaic Efficiencies and solid points refer to TOF. **(b)** Experimental catalyst utilization in rate of phenol conversion per second per gram of Pt or Rh as a function of particle size.

Synthesizing shape-specific catalysts to preferentially expose (111) sites is a potential route to improve the TOF of the structure-sensitive phenol hydrogenation reaction and improve catalyst utilization.[173–175] The insights here for phenol hydrogenation extend to structure-sensitive hydrogenation of other oxygenated aromatics relevant to bio-oils, such as benzaldehyde. The TOF of benzaldehyde ECH on Pt/C increases with particle size,[82] and the (111) terraces are predicted to adsorb benzaldehyde weaker than step sites.[35] Thus, the particle size dependence for benzaldehyde is explained by the increase in the fraction of (111) terraces with particle size, as is the case with phenol.

3.4 Conclusions

Both Pt and Rh are structure sensitive for TCH and ECH of phenol with the active site being (111) terraces. Although (111) terraces are the weaker phenol adsorption sites, which enables higher coverages of phenol and hydrogen reactants, those surfaces are also intrinsically more active, i.e., they have lower hydrogenation barriers. This finding shows that although the adsorption energy of phenol is important for predicting kinetics, it is not the sole predictor, potentially explaining why other metals that adsorb phenol similarly to Pt and Rh (e.g., Pd) have different kinetics. It is unknown whether weaker adsorption to the active site is a general phenomenon for hydrogenation of oxygenated aromatics, but other catalytic reactions, such as benzaldehyde hydrogenation, also show a similar structure sensitivity. Further work is needed to identify if (111) terraces, which adsorb a wide range of organics more weakly than step sites, are also more intrinsically active for a range of bio-oil model compounds.

Chapter 4 Electrocatalytic Hydrogenation of Phenol on Platinum-Cobalt Alloys

This chapter was adapted from Barth, I.; Akinola, J.; Singh, N.; Goldsmith, B. R. Electrocatalytic Hydrogenation of Phenol on Platinum-Cobalt Alloys. *Submitted*, **2023**. My contribution to this work is the density functional theory modeling. James Akinola performed the experimental work.

4.1 Introduction

The search for sustainable energy and chemicals has led to a growing interest in hydrogen-related processes, such as the hydrogen evolution reaction (HER) and electrocatalytic hydrogenation (ECH) of bio-oil. Electrocatalytic hydrogenation offers a sustainable pathway to stabilize lignin-derived bio-oil on the route to producing specialty chemicals and transportation fuels.[2,135–137,176–178] Understanding the mechanism and catalyst structure-activity relations for ECH of components of bio-oil may aid the transition to sustainable chemical and fuel production. In this study, we investigate phenol in aqueous acetate buffer as a representative lignin-derived phenolic compound in bio-oil,[179] and we study ECH on Pt alloyed with Co (Pt_xCo_y) to understand the mechanism and alloy nanoparticle catalyst design rules.

Electrocatalytic hydrogenation of phenol on Pt follows a Langmuir-Hinshelwood mechanism, such that the reaction rate is governed, in part, by the adsorption energies of hydrogen and phenol.[12,21] Surface-adsorbed hydrogen can either hydrogenate the phenol or combine via HER to form H_2 as a side reaction. There are multiple examples of controlling the adsorption energies of reactants through alloying for thermocatalytic hydrogenation (TCH).[20,180–186] Gas-phase TCH of cyclohexene on Pt alloyed with Fe, Co, Ni, or Cu reached a maximum activity at moderate cyclohexene and hydrogen adsorption energies.[187] The catalytic activity of Ni_xFe_y alloys for hydrogenation of C=C, C=O, and C-N bonds positively correlate with weakening hydrogen adsorption, and Ni_2Fe sites had the weakest hydrogen adsorption energy and highest hydrogenation activity.[188] Hydrogen adsorption energy (ΔG_H) is also an effective descriptor for the HER activity of metals and alloys.[189–195] There are much fewer studies using alloys for ECH of organics,[196–198] and the use of organic adsorption energy and ΔG_H as ECH descriptors is underexplored. Generally, there is limited understanding of how alloying affects adsorption energies and reaction barriers of organics in the aqueous phase and whether ΔG_H is a useful descriptor for ECH activity.

Whether a simple descriptor for ECH exists may depend on the structure of the alloy surface under reaction conditions. The activity of alloys is highly dependent on the composition of the surface and subsurface as well as nanostructure through strain,[199–201] ligand,[202,203] and ensemble effects.[204,205] The possibility of enrichment of certain elements in the catalyst surface is particularly important under reaction conditions where catalyst restructuring is possible and difficult to detect.[206] For example, Oezaslan *et al.* report that Pt_xCo_y forms a Pt skin in 0.1 M $HClO_4$,[207] whereas others report that the surface in 0.1 M $HClO_4$ or 1 M HNO_3 consists of a mixture of Pt and Co atoms rather than a pure Pt skin.[208–210] The activity of a surface consisting only of Pt atoms may differ considerably from a catalyst surface consisting of both Pt and Co atoms in close proximity, even if the subsurface composition is similar.

In this work, we synthesize and characterize Pt_xCo_y alloys of different Co compositions to understand how the catalyst structure and hydrogen adsorption energy are related to ECH activity and current efficiency. We select these Pt_xCo_y alloys because Pt is an active metal for ECH and subsurface alloying of Co is reported to weaken the hydrogen adsorption energy as a result of compressive strain and ligand effects.[199,201,202] We postulate that weakening the hydrogen adsorption energy will enhance HER activity, but ECH activity will depend more strongly on the nanostructure and presence of surface Co in the Pt_xCo_y. Our X-ray absorption spectroscopy (XAS) and scanning transmission electron microscopy (STEM) characterization of the Pt_xCo_y alloy nanoparticles show that although the surface is enriched in Pt rather than Co relative to the bulk, the surfaces are still a mixture of Pt and Co atoms (as opposed to a pure Pt skin over a Pt_xCo_y core). On our Pt_xCo_y alloys, the ECH activity does not simply trend with the hydrogen adsorption energy. Our density functional theory (DFT) calculations indicate that the ECH activities of these alloys cannot be described by the ΔG_H alone because hydrogenation barriers tend to follow a Brønsted-Evans-Polanyi relationship with respect to the reaction energies of phenol hydrogenation, and surfaces with weaker hydrogen adsorption energies do not necessarily have lower hydrogenation barriers. We demonstrate how kinetic modeling is able to qualitatively describe the experimental activity of these alloys by incorporating not only the ΔG_H but also computed transition state energies on the mixed Pt and Co surfaces.

4.2 Experimental & Computational Methods

4.2.1 Chemicals & Materials

All chemicals purchased were used as received. Chloroplatinic acid hexahydrate, $H_2PtCl_6 \cdot 6H_2O$ (38–40% Pt, Sigma Aldrich) and cobalt hydroxide, $Co(OH)_2$ (95%, Sigma Aldrich) were used as metal precursors for catalyst synthesis. 37% HCl (Sigma Aldrich) was used to neutralize alkaline $Co(OH)_2$. Sodium borohydride, $NaBH_4$ (≥96%, Sigma Aldrich) was used as the chemical reductant. Carbon felt (6.35 mm thick, 99.0%, Alfa Aesar) was used as the conductive porous support for ECH measurements. A graphite rod (3.05 mm diameter, 99.9995%, Alfa Aesar) connected to carbon felt was used as the working electrode. Sodium acetate buffer solution (Sigma

Aldrich, 3 M, pH 5.2) was used as supporting electrolyte for ECH and HER. Metal catalysts on Vulcan carbon, that is, 30 wt% Pt/C, 40 wt% Pt_3Co/C, and 40 wt% PtCo/C were purchased from the Fuel Cell store. A 5% Nafion 117 solution (Sigma Aldrich) was used as the binder for preparing catalyst inks for HER measurements. Boron nitride (99.5%, Alfa Aesar) was used to pelletize the metal catalysts for ex-situ X-ray absorption spectroscopy measurements.

4.2.2 Catalyst Preparation

Two sets of Pt_xCo_y alloys were prepared. Pt_xCo_y/C refers to purchased nanoparticles of Pt_xCo_y supported on Vulcan carbon. Pt_xCo_y/C were used to measure HER activity on a rotating disk electrode (RDE). Pt_xCo_y/felt denotes Pt_xCo_y nanoparticles synthesized on a conductive porous carbon felt. Pt_xCo_y/felt were used for ECH activity measurements because higher surface area catalysts were needed for product quantification and because of difficulties in loading the Pt_xCo_y/C onto a porous support without mechanical loss of catalyst at the negative potentials explored in this work. Both sets of samples were electrochemically cycled prior to testing for activity to avoid any leaching during activity measurements. This pretreatment process is described below.

4.2.2.1 Preparation of Platinum-Cobalt Alloy Nanoparticles on Vulcan Carbon for Rotating Disk Electrode

To perform HER measurements using a RDE, catalysts inks were prepared by adding 3 mg of the supported catalyst (i.e., 30 wt% Pt/C, 40 wt% Pt_3Co/C, or 40 wt% PtCo/C) into a mixture of 2.5 mL Millipore water and 2.5 mL isopropyl alcohol and 17.5 µL of 5 wt% Nafion solution as the binding agent. The mixture was sonicated for 2 hr to disperse the catalyst in the solution. A glassy carbon disk substrate for the inks was thoroughly polished using a 0.05 µm alumina suspension and rinsed three times with Millipore water and then sonicated in water for 30 min. 8 µL of the freshly sonicated catalyst ink was deposited on the clean glassy carbon disk substrate assembled in a Teflon rotating disk holder in two separate depositions (16 µL total) performed 30 minutes apart to achieve a catalyst loading of 9.6 µg. The deposited catalysts were air dried in a closed compartment for at least 1 hr to form a catalyst film before experiments.

4.2.2.2 Synthesis of Platinum-Cobalt Alloy Nanoparticles on Porous Carbon Felt Support

Pieces of carbon felt (1.5 cm × 1.5 cm × 6.35 mm thick) were first thermally pretreated in air at 400 °C for 16 hr to increase their surface area. Pt_xCo_y was directly synthesized on carbon felts by chemical reduction using a sodium borohydride method.[211] The target compositions of Pt and Co were adjusted to synthesize Pt/felt, Pt_3Co/felt, PtCo/felt, and $PtCo_3$/felt. An amount of $Co(OH)_2$ to achieve the desired Co metal loading and metal atomic ratio was dissolved in 20 mL mixture of 1:1 volume ratio of methanol to Millipore water. After, 37% HCl was added dropwise with a precision pipette to bring the solution to pH 2. Similarly, the desired amount of $H_2PtCl_6 \cdot 6H_2O$ was used to prepare a separate 20 mL aqueous solution of chloroplatinic acid. The two solutions were mixed, and the wetted carbon felt was sonicated in the solution for 2 hr. $NaBH_4$ was added to 5 mL of water in a separate vial to achieve $NaBH_4$:metal molar ratio of 12:1. Sodium borohydride solution was added dropwise to the precursor solution containing the felt in a water bath and sonicated for 3 hr. The felt was afterwards removed from the solution, rinsed three times with Millipore water, and left to dry in a vacuum oven set at 80 °C for 15 hr. Before use for ECH measurements, the felt was thoroughly rinsed with Millipore water.

4.2.3 Catalyst Characterization & Surface Area Measurements

4.2.3.1 Pretreatment of Platinum-Cobalt Alloys Before Use

To minimize dissolution of Co during activity testing, the Pt_xCo_y catalysts were first subjected to cyclic voltammetry by applying 1500 potential sweeps between 0.05 and 1.5 V vs. RHE at 500 mV/s in acetate buffer. The same procedure was used for the Pt_xCo_y/C and Pt_xCo_y/felt samples and is based on a protocol that is known to both remove any residual unalloyed Co in the catalyst and leach Co from the Pt_xCo_y/C surface. This process is reported to result in either a Pt shell with a Pt_xCo_y core or to form an enriched Pt surface although with surface Co present (i.e., a mixed alloy surface).[208–210] Our results here indicate that we form a mixed alloy surface that contains both Pt and Co as described in the Results and Discussion. The pretreated catalysts following cyclic voltammetry were used for all HER and ECH activity measurements and all characterization except where specified otherwise.

4.2.3.2 Bulk Elemental Analysis

The Pt and Co loadings of the as prepared Pt_xCo_y and pretreated Pt_xCo_y catalysts (i.e., following cyclic voltammetry) were measured using a PerkinElmer NexION 2000 ICP-MS. 1 mg of the catalyst was digested in 2 mL aqua regia solution (3:1 molar $HCl:HNO_3$). This solution was further diluted with Millipore water by a factor of 10000 to about 10–20 ppb. 20 ppb bismuth and 20 ppb scandium were co-fed as internal standard in the instrument to normalize Pt and Co intensities, respectively. The concentrations of Pt and Co were extracted by comparing to calibration standards of Pt and Co. The composition of the pretreated catalysts based on inductively coupled plasma-mass spectrometry (ICP-MS) is used for the catalyst naming convention.

4.2.3.3 X-ray Absorption Spectroscopy

The pretreated Pt_xCo_y/C and Pt_xCo_y/felt catalysts were crushed to powder and mixed with calculated amounts of boron nitride as a pelletizer to obtain desired edge steps and X-ray transmission through the samples. The catalysts and boron nitride were made into pellets (13 mm diameter and 1–2 mm thick) and probed at the Pt L_3-edge (11564 eV) and Co K-edge (7709 eV). These samples were also analyzed in our custom made in-situ XAS cell under negative cathodic potential with and without phenol in the supporting electrolyte to understand the catalyst structure during ECH.[24] Samples were analyzed in transmission mode or fluorescence mode depending on the quality of the data. In-situ XAS measurements were performed only in fluorescence mode because of hydrogen bubble formation that interfered with transmission signal. A minimum of three scans were taken for each sample at either edge. Pre-processing and linear combination fitting of the X-ray absorption near edge (XANES) region was performed using Athena while extended X-ray absorption fine structure (EXAFS) fitting was performed using Artemis.[212] Pt and Co foils were used as standards for either edge and used as reference in data alignment and fitting.

4.2.3.4 X-ray Diffraction

X-ray diffraction (XRD) was performed on the Pt_xCo_y/C and Pt_xCo_y/felt catalysts using a Rigaku Miniflex X-ray diffractometer with Cu Kα radiation and a Ni filter that has an X-ray wavelength of 1.5406 Å. For the Pt_xCo_y/felt samples, 10 mg of the catalyst on felt was crushed to powder and put into a transparent sample holder before setting the voltage and current to 40 kV and 15 mA, respectively. For the Pt_xCo_y/C samples, the powder was directly used. Scanning was carried out at 3°/min with a 0.02° step in the range of $10° < 2\theta < 90°$. The Scherrer equation was used to estimate the average crystallite size as discussed in the Appendix.

4.2.3.5 Transmission Electron Microscopy & Scanning Transmission Electron Microscopy Measurements

A Thermo Fisher Scientific Talos F200X G2 electron microscope equipped with a Super-X EDX detector and operating at an accelerating voltage of 200 keV was used for the scanning transmission electron microscopy (STEM) and transmission electron microscopy (TEM) imaging and analysis. A portion of the catalyst on carbon felt was ground before dissolving 1 mg of the ground catalyst in 1 mL of isopropanol. A drop of the suspension was deposited on a clean Cu grid. The Cu grid was left to dry overnight before imaging was performed. The average size and distribution of particles were acquired with the ImageJ software.

4.2.3.6 Hydrogen Underpotential Deposition

The electrochemically active surface area (ECSA) of exposed Pt surface metal atoms on the Pt_xCo_y/felt and Pt_xCo_y/C catalysts was measured using hydrogen underpotential deposition (H_{UPD}). The catalysts were electrochemically cleaned using cyclic voltammetry (CV) at 100 mV/s for 50 cycles at potentials –0.2 to 1.5 V vs. RHE. After electrochemical cleaning, CV was done at a 20 mV s^{-1} scan rate in the potential window of 0.05 V to 1.2 V and the H_{UPD} charge from the oxidative region after subtracting the baseline capacitive charge was used to estimate the ECSA of the Pt sites using a charge density of 210 μC cm^{-2}.

4.2.4 Hydrogen Evolution Reaction

The hydrogen evolution reaction (HER) was performed in a 3 M acetate buffer solution in a three-electrode single compartment batch electrolysis cell at room temperature. The working electrode was a glassy carbon disk with the deposited catalysts assembly used in an RDE setup (Pine Instruments). A Ag/AgCl double junction electrode was used as the reference electrode and a Pt wire loop was used as the counter electrode. The catalysts were first pretreated as discussed above, and the ECSA was measured by H_{UPD} before performing linear scan voltammetry at 10 mV s^{-1} between −0.2 V and 1.1 V vs. RHE at rotation rates of 400, 900, 1600, and 2500 rpm. The applied potential was corrected for potential loss due to series resistance as measured by the real part of the impedance measured at high frequency. The measured current was normalized to ECSA to obtain the current density. Based on the measurements, 1600 rpm was sufficiently high that mass transport artifacts were not observed (**Appendix Figure C-1a–c**), thus the current densities at 1600 rpm were used to evaluate intrinsic kinetics (kinetic current density). Tafel plots were constructed by plotting the log of the current density at 1600 rpm against the overvoltage for the HER rates (**Appendix Figure C-1d**). The Tafel slope and exchange current density were determined by fitting the log of current density vs. overvoltage to a linear line ($\log i = \eta/b + \log i_0$), where i is the kinetic current density, b is the Tafel slope, η is the overvoltage, and i_0 is the exchange current density. Only overvoltage values ≥100 mV were used in the fit to the Tafel equation to extract the exchange current density.

4.2.5 Electrocatalytic Hydrogenation of Phenol

4.2.5.1 ECH Measurement

ECH was performed on the Pt_xCo_y/felt catalysts using a two-compartment batch electrolysis cell where the cathodic and anodic compartments were separated with a Nafion 117 membrane. The Pt_xCo_y/felt catalysts were attached to a 3 mm diameter graphite rod (Sigma Aldrich, 99.99%) and used as the working electrode in the 140 mL cathodic compartment. Acetate buffer (3M, pH 5.2) sparged with N_2 was used as the supporting electrolyte in both cathodic and anodic compartments. A Ag/AgCl double junction electrode was used as the reference electrode and the counter electrode was a 3 mm diameter graphite rod (Sigma Aldrich, 99.99%). To perform ECH, the target negative potential was first applied for 1 hr to the working electrode to reduce the metal nanoparticles and saturate the solution with hydrogen. Phenol sparged with N_2 was added to the cathodic compartment to achieve 20 mM phenol concentration before performing ECH at a fixed potential of either −0.1, −0.15, or −0.2 V vs. RHE using a Bio-Logic VSP-300. The series resistance was automatically compensated at 85% using impedance spectroscopy at a frequency of 200 kHz and the remaining 15% was manually corrected to give ±10 mV of the reported iR-free applied potentials. No change in the pH of acetate buffer plus phenol solution before and after performing ECH for 2 hr was observed, indicating sufficient buffering capacity.

4.2.5.2 Product Quantification During ECH of Phenol

A 1 mL aliquot was taken from the cathodic compartment every 30 min to monitor ECH reaction progress. ECH products (i.e., cyclohexanone and cyclohexanol) and the phenol reactant were extracted from the aqueous supporting electrolyte into an organic phase using through three sequential liquid-liquid extractions with ethyl acetate as the solvent. For every extraction step, about 5 mg of sodium chloride was added to the aliquot before mixing with 1 mL of pure ethyl acetate to aid separation of the organic and aqueous phase. Any water present in the organic phase was removed using anhydrous Na_2SO_4 (Sigma Aldrich 99%). Dimethoxybenzene (DMB) was used as an external standard, where 10 µL DMB was mixed with 1 mL of the dried organic phase before injecting 1 µL of the mixture to an Agilent Varian 450 gas chromatograph equipped with a flame ionization detector. ECH was performed at less than 10% conversion and carbon balances were greater than 90%. The turnover frequency (TOF) for each Pt_xCo_y/felt catalyst was calculated from the rate of cyclohexanol and cyclohexanone formed per surface Pt atom estimated from the hydrogen underpotential deposition.

4.2.6 Density Functional Theory Modeling

The Vienna Ab initio Simulation Package (VASP) was used for Kohn-Sham DFT calculations.[42,43,144,145] The exchange-correlation energy was calculated using the Perdew-Burke-Ernzerhof functional[101] with the semi-empirical D3 dispersion correction.[100] The projector augmented wave method and a plane wave kinetic energy cutoff of 400 eV were used for all calculations.[148,149] The first-order Methfessel-Paxton smearing scheme with a 0.2 eV smearing width was used.[150] All calculations performed on slabs containing Co were spin-polarized. Spin polarization had a negligible effect on the pure Pt surface.

We modeled Pt and Pt_xCo_y intermetallics (i.e., Pt, Pt_3Co, PtCo, and $PtCo_3$) and Pt/Pt_xCo_y (i.e., a monolayer of pure Pt over a Pt_xCo_y subsurface) systems to investigate how Pt enrichment in the alloy surface affects adsorption of phenol and hydrogen and the catalytic performance for HER and ECH. Four-atom bulk face-centered cubic (FCC) unit cells of Pt, Pt_3Co, PtCo, and $PtCo_3$ were optimized in VASP with a 21 × 21 × 21 Monkhorst-Pack *k*-point grid.[151] We modeled only the FCC crystal structure because it is the crystal structure observed experimentally in our purchased and synthesized catalysts from XRD. The expected change in lattice constant with Co fraction (i.e., from Vegard's law) from the FCC lattice constants matches the change in lattice constant from our powder XRD data for Pt_xCo_y/C for their expected Co fraction (**Appendix Figure C-2**), indicating alloys are formed. Previous work found that the (111) facet of Pt and other metals like Rh are the active facet for hydrogenation of aromatics.[82,213] Therefore, we constructed the (111) facets of Pt, Pt_3Co, PtCo, and $PtCo_3$ from the bulk unit cells. The Pt/Pt_xCo_y slabs were modeled by replacing all Co atoms in the top layer of the slabs with Pt to achieve a pure Pt surface layer. The Pt_xCo_y and Pt/Pt_xCo_y systems were modeled using 4 × 4 × 4 slabs, where the bottom two layers were fixed in their bulk lattice coordinates and the top two layers were relaxed during geometry optimization. A 3 × 3 × 1 Mokhorst-Pack *k*-point grid was used for all slab calculations. The climbing-image nudged elastic band method was used to find the transition states for the hydrogenation reactions.[152] The enthalpies and free energies of adsorbed phenol, hydrogen, and reaction intermediates were evaluated in the harmonic limit without solvation corrections, and the free energies of non-adsorbed species were evaluated using ideal gas thermodynamic corrections at 300 K. The configurations of phenol and hydrogen with the lowest computed energies were used in the subsequent work. Implicit solvation was not used to model adsorption or hydrogenation because it was found to improperly describe solvent effects for phenol adsorption and had little effect on the adsorption energies of hydrogen or the hydrogenation barriers using default parameters.[35,213]

4.3 Results & Discussion

4.3.1 Comparing Hydrogen Evolution Activity to Hydrogen Adsorption Energy on Pt_xCo_y/C

In **Figure 4-1a** we show the HER exchange current densities on Pt_xCo_y/C catalysts as a function of Co fraction. Pt_3Co/C is the most active for HER, followed by PtCo/C and Pt/C. The exchange current density of Pt/C in acetate buffer (pH 5.2) obtained here (4.1 mA cm^{-2}) matches that reported by Zheng and coworkers (4.0 mA cm^{-2}) in the same electrolyte and pH.[190] The HER activity trend between Pt/C and Pt_3Co/C is consistent with studies that reported Pt_3Co to be superior to Pt,[210,214] although the structure of the Pt_3Co surface impacts the HER performance. Specifically, a Pt_3Co catalyst with both Pt and Co present on the surface and a Pt_3Co catalyst with a pure Pt surface layer were reported to increase the current density by two and five times compared to pure Pt, respectively.[210]

Exposing Pt_xCo_y catalysts to acidic conditions can form a Pt-enriched surface (i.e., a surface with both Pt and Co) or a Pt-skin structure on a Pt_xCo_y core. However, the structure of Pt_xCo_y alloys in our supporting electrolyte (3 M acetate buffer, pH 5) has never been reported. The enhancement we observe in **Figure 4-1a** for Pt_3Co/C compared to Pt/C (a factor of 2.25) is close to the reported enhancement for a Pt_3Co catalyst with both Pt and Co present on the surface. Although there are reports of sub-nanometer PtCo clusters with enhanced HER activity relative to pure Pt,[215] our PtCo/C, with a diameter of approximately 5 nm (characterization provided below), is less active than Pt_3Co/C and more similar to Pt/C.

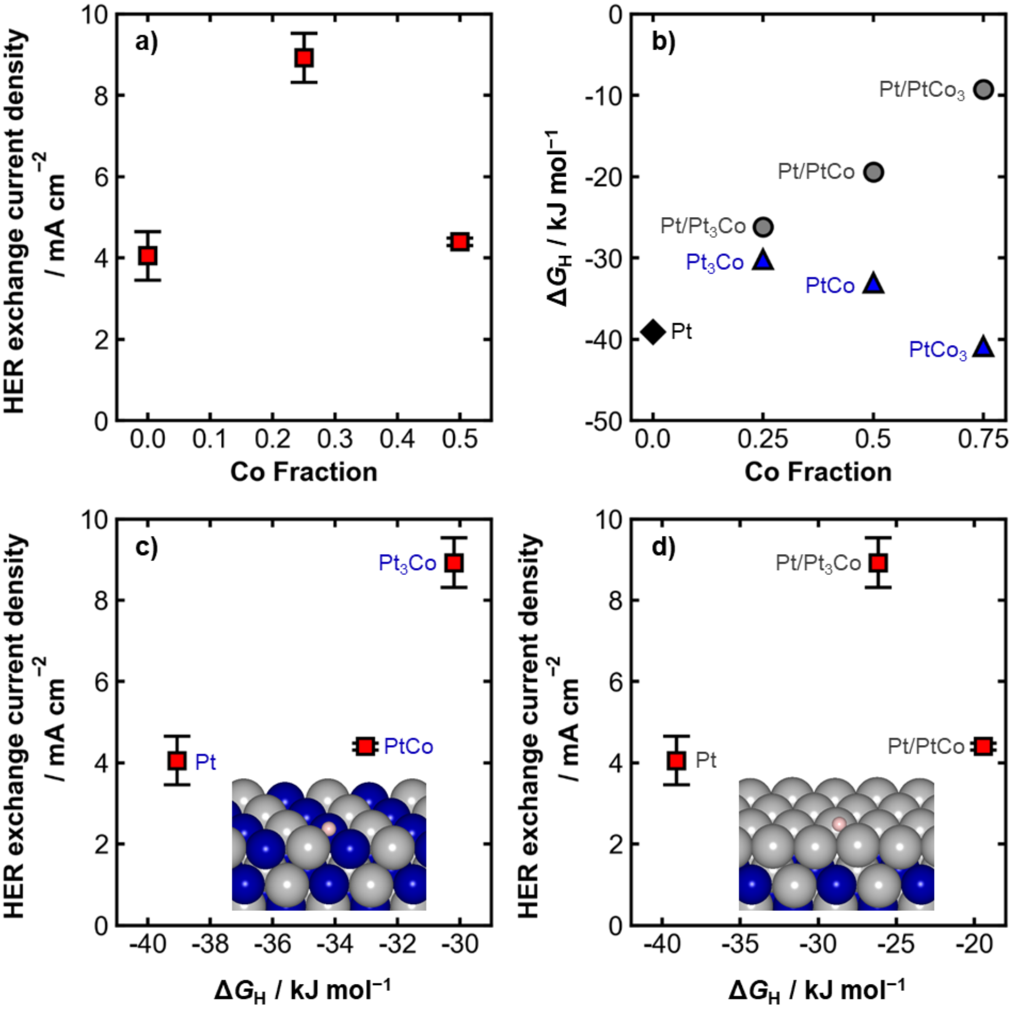

Figure 4-1 Hydrogen evolution activity related to the hydrogen adsorption energy on different Pt_xCo_y structures. **a)** HER measured exchange current densities at 23.3°C as a function of Co fraction for the Pt_xCo_y/C catalysts. Exchange current densities were extracted from Tafel plots shown in the Appendix for the Pt_xCo_y/C catalysts deposited on glassy carbon in 3 M acetate buffer supporting electrolyte (pH 5.2) sparged with H_2. **b)** DFT-calculated hydrogen adsorption free energies on Pt_xCo_y and Pt/Pt_xCo_y alloys as a function of Co content at 300 K. **c)** Measured HER exchange current densities as a function of the calculated hydrogen adsorption free energies on Pt_xCo_y alloys. **d)** HER measured exchange current densities as a function of the calculated hydrogen adsorption free energies on Pt/Pt_xCo_y alloys. Images of hydrogen adsorbed on PtCo and Pt/PtCo alloy slabs are inset in c) and d), respectively. Hydrogen is colored peach, Pt is colored gray, and Co is colored blue. Error bars for a), c) and d) denote the standard deviation from the average of two separate experiments.

To better understand the trends in HER exchange current densities on the Pt_xCo_y/C catalysts, we use DFT to model hydrogen adsorption on Pt_xCo_y for two possible types of structures: 1) both Pt and Co present in the surface and 2) a pure Pt surface covering a Pt_xCo_y core (Pt/Pt_xCo_y). In **Figure 4-1b** we show that an increasing Co fraction in Pt/Pt_xCo_y alloys causes the surface Pt to adsorb H weaker, but high fractions of Co in the surface of Pt_xCo_y alloys cause the surface to behave more like Co and bind H more strongly (ΔG_H on Co(0001) is computed to be −42 kJ mol^{-1}). For Pt/Pt$_x$Co$_y$ the presence of Co in the alloy subsurface interacts with the Pt overlayer through a combination of strain and ligand effects[216–218] to cause a monotonic weakening of the computed hydrogen adsorption energy as Co increases. For the mixed Pt$_x$Co$_y$ surfaces, the hydrogen adsorption energy weakens initially in the Pt$_3$Co case but then strengthens with increasing Co in the PtCo and PtCo$_3$ cases because of the strong Co-H interactions that are possible when high fractions of Co are on the surface. In fact, the three-fold Co sites on PtCo$_3$ are predicted to adsorb hydrogen only ~1 kJ mol^{-1} weaker than a pure Co(0001) surface.

By comparing the experimental HER exchange current density to the computed ΔG_H, we hypothesize that our experimental catalysts form a mixed Pt and Co surface rather than a Pt skin on a Pt$_x$Co$_y$ core. We show the experimental HER exchange current density for the Pt$_x$Co$_y$/C catalysts against the computed ΔG_H assuming a mixture of Pt and Co on the surface in **Figure 4-1c**. We do the same for a Pt/Pt$_x$Co$_y$ structure in **Figure 4-1d**. For the mixed Co and Pt surface, the HER exchange current density increases with weakening hydrogen adsorption (**Figure 4-1c**). The HER exchange current density does not increase with weakening of the predicted hydrogen adsorption on the Pt/Pt$_x$Co$_y$ models (**Figure 4-1d**). Because generally HER activity for Pt group metals is expected to increase with weakening hydrogen adsorption,[190,195] the results in **Figure 4-1c** compared to **Figure 4-1d** indicate that the Pt$_x$Co$_y$/C catalysts pretreated in 3 M acetate buffer (pH 5.2) do not form a Pt skin, but instead have both Pt and Co present on the catalyst surface.

Using DFT, we calculate the energy to substitute subsurface Co with surface Pt in a Pt/Pt$_x$Co$_y$ slab with and without adsorbed hydrogen to predict the preferred structure of the slabs. Our calculations suggest that the presence of H*, which interacts more strongly with Co than with Pt, has the potential to stabilize Co in the catalyst (**Appendix Figure C-3**). This modeling prediction corroborates our observation of the enhancement of Pt_3Co/C compared to Pt/C matching what is expected for a surface with both Pt and Co present. The dependence of ΔG_H on the Pt_xCo_y structure highlights the importance of identifying the surface composition for electrocatalysis, because a Pt/Pt_xCo_y catalyst may have considerably different activity than a Pt_xCo_y catalyst.

4.3.2 Synthesis and Characterization of Pt_xCo_y Alloys Supported on Conductive Carbon Felt

To measure ECH activity for Pt_xCo_y alloys, we synthesize Pt_xCo_y nanoparticles with varying compositions of Co directly on a conductive carbon felt support (Pt_xCo_y/felt) to achieve sufficiently high catalyst loading to detect the products of ECH of phenol (cyclohexanol and cyclohexanone). We cycle these catalysts from 0.05−1.5 V vs. RHE prior to use for ECH and do not detect any remaining unalloyed Co (**Appendix Figure C-4**, **Appendix Figure C-5**, and **Appendix Figure C-6**), implying alloys are formed rather than mixtures of bulk Co and Pt.[209] Although these catalysts are supported on carbon felt as opposed to the catalysts shown in **Figure 4-1** (Pt_xCo_y/C, supported on Vulcan carbon), we show below that they form similar structures.

We show Pt L_3-edge EXAFS of the Pt_xCo_y/felt samples in **Figure 4-2a** that confirms local coordination of Co with Pt. The Pt-Pt bond length of the Pt_{100}/felt matches that of a Pt foil. This Pt-Pt bond length decreases with increasing bulk Co content as measured by ICP-MS. The peak between 2.4−2.6 Å indicates scattering between two nearest neighbor Pt atoms in the first shell. Pt atoms are replaced by smaller Co atoms with increasing Co content, which leads to smaller interatomic distances. The fits of the EXAFS data of the Pt foil and the Pt_xCo_y/felt are shown in **Appendix Figure C-7, Appendix Figure C-8,** and **Appendix Figure C-9** and the Pt-Pt and Pt-Co coordination number and bond lengths extracted from the fits to a first and second shell are shown in **Appendix Table B-1**. With increasing Co content, we also see an increase in the Pt-Co coordination numbers, further indicating the formation of alloys.

Our measured lattice constant of the alloys from XRD also corroborates the formation of Pt_xCo_y alloys. We show the XRD patterns for the Pt_xCo_y/felt catalysts in **Figure 4-2b** with the Pt FCC lattice peak highlighted. There is no evidence of pure Co phases in the XRD. The Pt FCC peak shifts to higher 2θ values compared to Pt, shown in the inset image in **Figure 4-2b**. We calculate the Co fraction from the shift of the 2θ values of the (111) plane using Vegard's law (**Appendix Figure C-2**) and plot this Co fraction from XRD in **Figure 4-2c** along with the fraction of Co in the lattice based on the fitted EXAFS data using the Pt-Pt and Pt-Co coordination numbers. The Co fraction from EXAFS and XRD are similar to one another, but they differ quantitatively from the Co fraction measured using ICP-MS, although they follow the same qualitative trend. Although the higher Co content measured from ICP-MS following complete dissolution of the catalyst may indicate some unalloyed Co in the catalyst, we do not see any indication of pure Co or Co oxide redox reactions based on the cyclic voltammetry following our pretreatment (**Appendix Figure C-5**). One possibility is that excess cobalt may arise from unalloyed Co in the catalyst core that is not in contact with the electrolyte. Thus, this excess bulk Co should not influence the surface reaction.

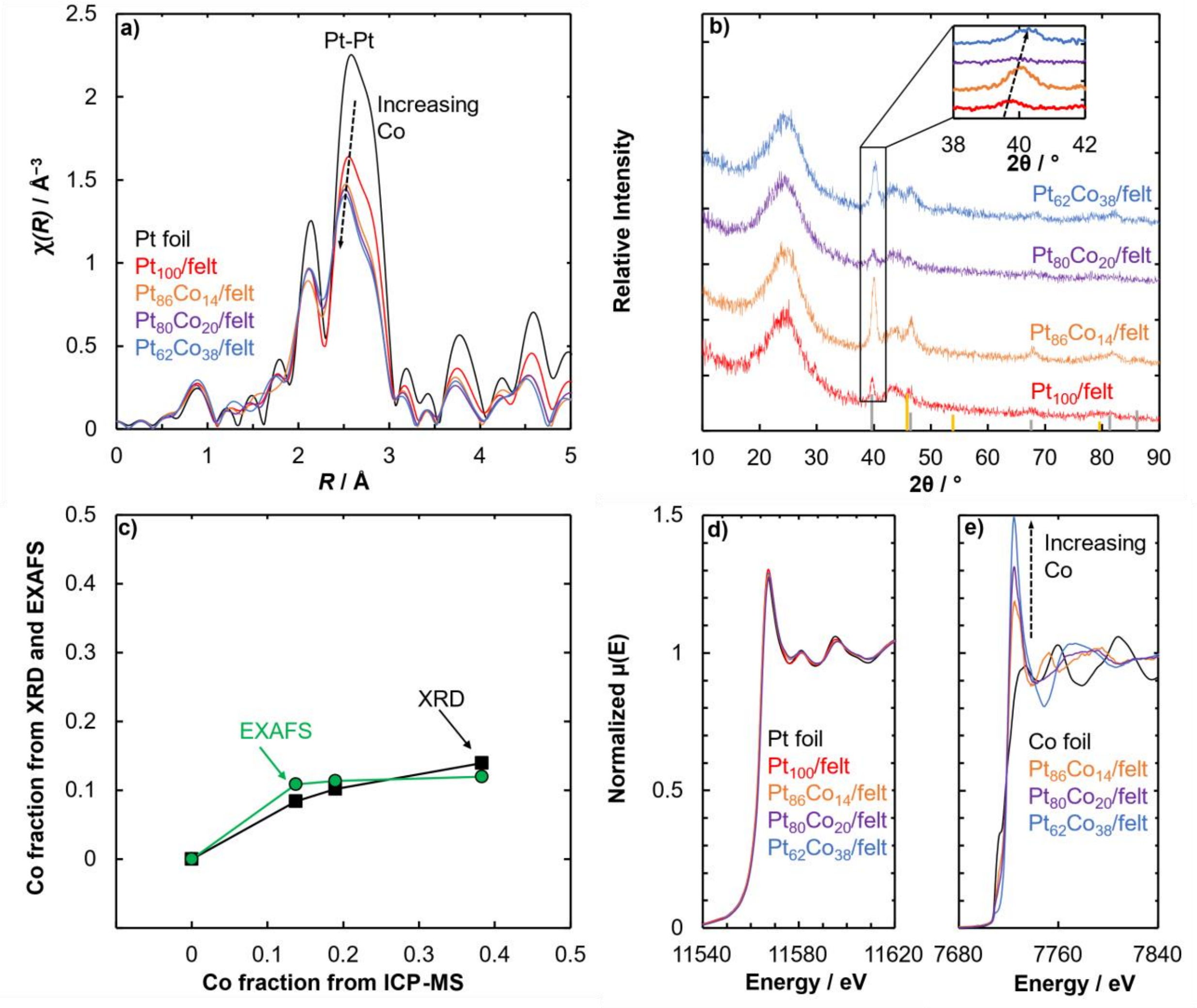

Figure 4-2 Ex-situ XAS and XRD for Pt_xCo_y/felt catalysts. **a)** Unadjusted k-weighted EXAFS spectra of Pt foil and Pt_xCo_y/felt in real space collected at the Pt L_3-edge. **b)** XRD spectra of Pt_xCo_y/felt with Pt #04–0802 and Co #15–0806 standards indicated by ash and gold vertical lines, respectively. Inset corresponds to region attributed to (111). **c)** Co fraction from XRD and EXAFS as a function of the Co fraction measured from ICP-MS. The x and y in Pt_xCo_y are the bulk atomic ratio of Pt and Co measured from ICP-MS after pretreatment. Normalized XANES spectra of metal foils and Pt_xCo_y/felt catalysts at the **d)** Pt L_3-edge and **e)** Co K-edge.

The Pt_xCo_y/felt catalysts are only slightly oxidized ex-situ and mostly metallic under applied cathodic potential. We show in **Figure 4-2d** and **Figure 4-2e** the ex-situ XANES of the catalysts on felt at the Pt L_3-edge and Co K-edge. The shape and intensity of the white line for the metallic Pt foil is similar to that of the Pt_xCo_y/felt samples, indicating Pt is mainly in the metallic phase. Using linear combination analysis of the XANES data in **Figure 4-2d** compared to Pt foil and PtO_2 (**Appendix Table C-2**) we show that less than 2% of Pt forms PtO_2. We expect 20% of all bulk Pt to be on the surface based on an average particle size of 5 nm, thus only a small fraction of the surface Pt seems to be oxidized. Under applied cathodic potential (−0.05 V vs. RHE), the XANES of Pt_{100}/felt in **Appendix Figure C-10** show a white line similar to that of the metallic Pt foil except for the broad shoulder indicating the formation of adsorbed H on Pt at negative potentials.[24] Thus, we do not expect significant differences in the electronic structure of Pt during operating conditions. Contrary to the Pt L_3-edge, the white line at the Co K-edge in **Figure 4-2e** increases with Co content which could indicate the formation of oxidized Co species. These oxidized Co species are likely from surface Co since subsurface Co would not be exposed to air. This observation of surface oxidized Co is similar to reports of surface oxidized Ni in PtNi alloys, which was interpreted as being due to Ni being present in the surface.[219,220] The presence of oxidized surface Co indicates that Pt_xCo_y does not form a Pt skin, but rather there is Co present on the surface. We were unable to evaluate the Co K-edge under operating conditions because of the noise in the XANES signal from H_2 bubble formation, but we hypothesize Co may reduce under the potentials relevant for ECH.

The Pt_xCo_y/felt nanoparticles have similar particle sizes despite the variation in bulk Co fraction, so that differences in their ECH performance can be attributed to varying the Co content, rather than structure sensitivity effects.[82,213] We have previously shown that phenol ECH on Pt and Rh is a structure sensitive reaction,[213] with larger particles with a higher fraction of terrace sites showing higher turnover frequencies. The TEM images and distribution in **Figure 4-3a**, **Figure 4-3b**, and **Figure 4-3d** show that Pt_{100}/felt, $Pt_{86}Co_{14}$/felt and $Pt_{80}Co_{20}$/felt have similar average nanoparticle sizes (5.8 ± 1.3 nm, 5.8 ± 1.8 nm and 5.5 ± 1.2 nm, respectively) and are well dispersed on the treated carbon felt (additional images are shown in **Appendix Figure C-11**). Although the average particle size and distribution is larger for the $Pt_{62}Co_{38}$/felt catalyst in **Figure**

4-3e (13.6 ± 3.2 nm), the expected increase in activity because of a higher fraction of the active terraces was not observed as we will discuss in the subsequent section. We give the average nanoparticle sizes from TEM, XRD crystallite sizes calculated from the Scherrer equation, and the EXAFS first shell total coordination number in **Appendix Table C-3**. The trend in particle sizes from these different methods in **Appendix Table C-3** are qualitatively in agreement.

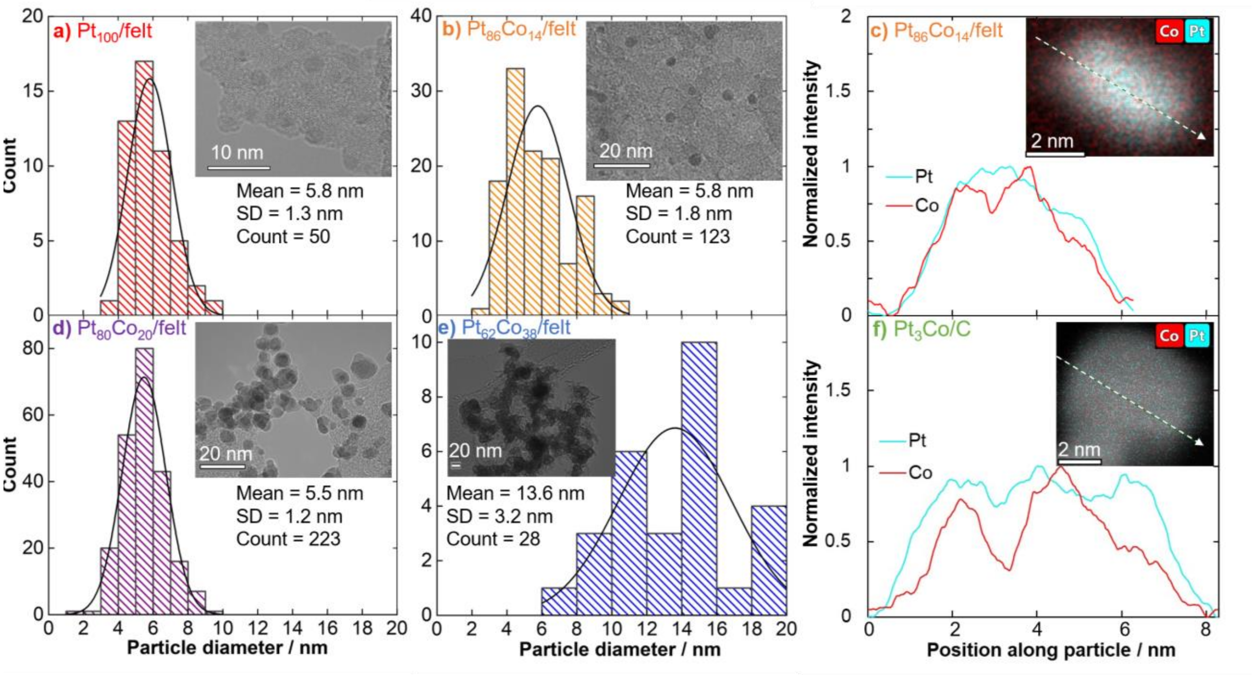

Figure 4-3 TEM histogram distribution of particle diameters and representative micrograph (inset image) of the Pt_xCo_y catalysts. **a)** Pt_{100}/felt, **b)** $Pt_{86}Co_{14}$/felt, **d)** $Pt_{80}Co_{20}$/felt, and **e)** $Pt_{62}Co_{38}$. A STEM-EDS line profile analysis across a single nanoparticle of the catalysts for **c)** $Pt_{86}Co_{14}$/felt, and **f)** Pt_3Co/C catalyst. Inset image in **b)** and **c)** shows a 2D elemental mapping of Pt (teal) and Co (red) across the nanoparticle for which the line scan was performed.

We show by STEM line scans for $Pt_{86}Co_{14}$/felt in **Figure 4-3c** and Pt_3Co/C in **Figure 4-3e** that both the carbon felt and Vulcan carbon supported catalysts do not form a Pt skin but instead form a surface with both Pt and Co present. The Co and Pt line scan across a single nanoparticle shows a similar ratio of the Pt and Co intensity at the edges of the particles as in the core of the particle, indicating no visible Pt shell is formed. This further corroborates our evidence that both the Pt_xCo_y supported on carbon felt (Pt_xCo_y/felt) and Pt_xCo_y supported on Vulcan carbon (Pt_xCo_y/C) have a surface containing both Pt and Co atoms.

4.3.3 Electrocatalytic Hydrogenation of Phenol on Pt_xCo_y Alloys

Unlike our observation that the hydrogen adsorption energy shows a clear trend with the HER activity (**Figure 4-1**), the more complex ECH performance in **Figure 4-4** prevents us from using a simple descriptor to understand the Pt_xCo_y/felt catalysts. For example, the catalyst with the highest TOF at −0.1 V vs. RHE ($Pt_{86}Co_{14}$/felt) is not the most active at more negative potentials. The more negative potentials may result in lower ECH TOFs on the Pt_{100}/felt and $Pt_{86}Co_{14}$/felt due to increased hydrogen coverage that blocks adsorption of phenol.[21] The more negative potential and hydrogen site-blocking also results in a lower current efficiency to ECH for those catalysts (**Figure 4-4b**). Although $Pt_{86}Co_{14}$/felt has the highest TOF of the catalysts for the conditions tested, it has a low current efficiency (**Figure 4-4b**) due to high HER activity. The ECH TOF for $Pt_{62}Co_{38}$/felt instead increases with more negative potential along with a corresponding increase in current efficiency. This opposite behavior on $Pt_{62}Co_{38}$/felt may arise because the hydrogen coverage is lower compared to Pt_{100}/felt and $Pt_{86}Co_{14}$/felt, such that more negative potentials enhance ECH. The complicated trend in activity and current efficiency on the alloys suggests a more complicated model than a single adsorption energy descriptor is needed to understand phenol ECH on platinum cobalt alloys. To understand the multiple effects of adsorption energies and coverage, applied potential, and activation barriers, we use a kinetic model based on a Langmuir-Hinshelwood mechanism to capture the experimental trends. To construct this model, we first investigate the effects of Co fraction on phenol adsorption and the barrier for hydrogenation in the next section.

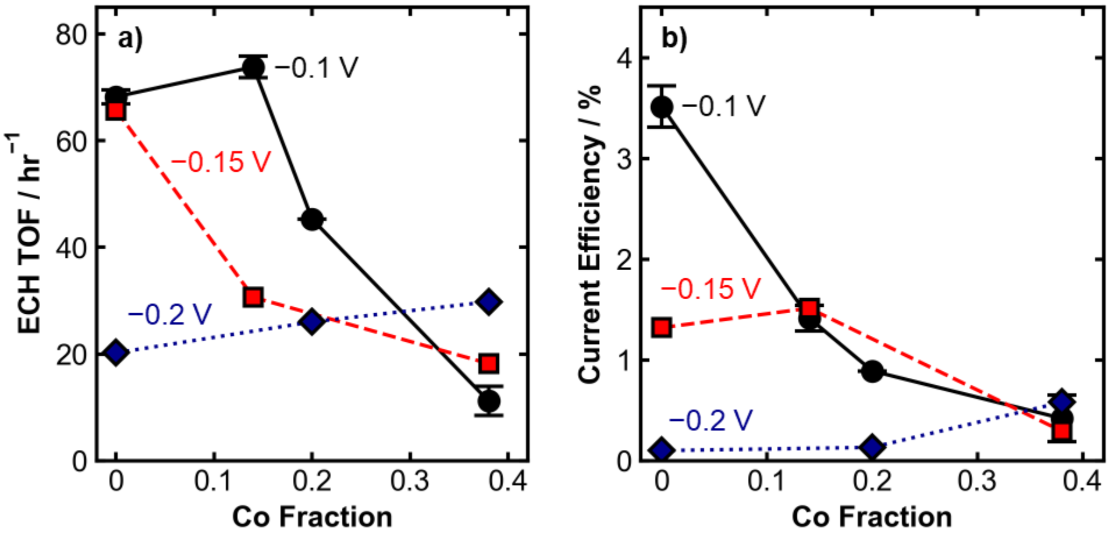

Figure 4-4 Experimental ECH turnover frequency and current efficiency on Pt_xCo_y/felt catalysts as a function of Co fraction for different applied potentials. **a)** ECH TOF in 20 mM phenol in 3 M acetate buffer supporting electrolyte (pH 5.2) at 23.3 °C and −0.1, −0.15 or −0.2 V vs. RHE. The applied potential was directly corrected for 85% of the series resistances using the potentiostat ZIR technique and the remaining 15% series resistance was further corrected manually to give ±0.01 V of target potential. The number of surface atoms of the catalysts used to calculate the TOF was estimated from the Pt H_{UPD} surface area. **b)** Current efficiency to ECH calculated from the moles of ECH products with respect to the amount of charge passed.

4.3.4 Effect of Co Alloying on Phenol Adsorption and Hydrogenation Barriers

In aqueous phase, we do not find a significant change in the experimental adsorption free energy of phenol with increasing Co fraction (**Figure 4-5**) despite the varying ECH TOF with Co fraction. We find the adsorption free energy of phenol to be −22.5 kJ mol^{-1}, −19.0 kJ mol^{-1}, and −20.5 kJ mol^{-1} kJ mol^{-1} on Pt/C, Pt_3Co/C, and PtCo/C, respectively. We find the adsorption energies are independent of phenol coverage. This constant aqueous phenol adsorption energy with Co fraction highlights that the phenol adsorption energy is also not a descriptor for ECH. To extract the free energy for phenol adsorption, we fit the coverage vs. concentration data to a Temkin isotherm shown in **Eq. 4-1**.

$$\frac{\theta_{\mathrm{P}}}{\theta_{sat}} = \frac{\exp\left(\frac{-(\Delta G^{aq}_{ad,\theta=0} + \alpha\theta_P)}{RT}\right) C_{\mathrm{P}}}{\left(1 + \exp\left(\frac{-(\Delta G^{aq}_{ad,\theta=0} + \alpha\theta_P)}{RT}\right) C_{\mathrm{P}}\right)} \qquad \textbf{Eq. 4-1}$$

Here θ_P is the phenol coverage, θ_{sat} is the saturation coverage, $\Delta G^{aq}_{ad,\theta=0}$ is the aqueous adsorption free energy in kJ mol^{-1} at a phenol coverage of zero, α is how adsorbate-adsorbate interactions influence the adsorption energy as a function of coverage in kJ mol^{-1}, C_{P} is the concentration of phenol, R is the ideal gas constant, and T is temperature in Kelvin. A caveat of these adsorption isotherms is that they probe the coverage of phenol as a function of bulk phenol concentration solely on the surface Pt atoms because the coverage of phenol on Co atoms cannot be probed using $\mathrm{H_{UPD}}$. We have previously shown that metals such as Pt and Rh which adsorb organic molecules (e.g., phenol) with very different energies in the gas phase have similar aqueous-phase adsorption energies.[35] We attributed this similar phenol adsorption between Pt and Rh to the energy penalty of displacing water molecules from the liquid/metal interface which offsets the energy difference observed in the gas phase (i.e., although Rh adsorbs phenol in the gas phase more strongly than Pt, it also adsorbs water more strongly, so the penalty for displacing water is larger on Rh than on Pt).[63,221]

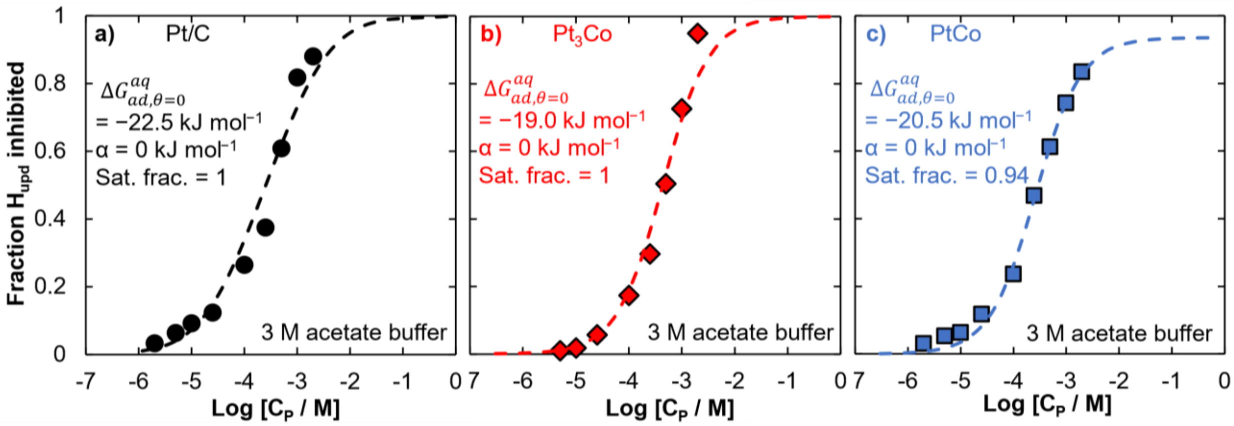

Figure 4-5 Phenol adsorption energies from adsorption experiments on Pt$_x$Co$_y$/C catalysts. Phenol adsorption isotherm on **a)** Pt/C, **b)** Pt$_3$Co/C, and **c)** PtCo/C from inhibition of hydrogen underpotential deposition with different

bulk phenol concentrations in 3 M acetate buffer and 23°C. The dashed lines in a), b), and c) are fits of the data to a Temkin adsorption model to extract the aqueous adsorption energy and its coverage dependence α.

Through DFT modeling, we demonstrate that the structure and composition of the alloy surface has a notable impact on the activation enthalpy of the first hydrogenation step. The DFT-predicted geometries for the first hydrogenation step of phenol on PtCo and Pt/PtCo are shown in **Figure 4-6a** as representative examples. In **Figure 4-6b** we show the computed activation enthalpy ($\Delta H_f^\ddagger$) as a function of Co fraction (y_{Co}) for $\mathrm{Pt_xCo_y}$ and $\mathrm{Pt/Pt_xCo_y}$. We calculate $\Delta H_f^\ddagger$ as the enthalpy of the transition state for the first hydrogenation step relative to the enthalpy of surface-adsorbed hydrogen and phenol. The activation enthalpy increases almost linearly with Co fraction on the $\mathrm{Pt_xCo_y}$ surfaces but decreases linearly with Co fraction for the $\mathrm{Pt/Pt_xCo_y}$ surfaces. The opposite trend in activation enthalpy with Co fraction on the two types of surfaces highlights the impact of having Co and Pt on the surface ($\mathrm{Pt_xCo_y}$) compared to only Pt on the surface ($\mathrm{Pt/Pt_xCo_y}$).

By comparing the activation enthalpy to the hydrogen adsorption enthalpy and hydrogenation reaction enthalpy, we observe why the $\mathrm{Pt_xCo_y}$ and $\mathrm{Pt/Pt_xCo_y}$ surfaces are predicted to have such different trends in hydrogenation rates with Co fraction. We show $\Delta H_f^\ddagger$ as a function of the computed hydrogen adsorption enthalpy (ΔH_{H}) on each respective surface in **Figure 4-6c**. On the $\mathrm{Pt/Pt_xCo_y}$ surface, $\Delta H_f^\ddagger$ decreases with weakening hydrogen adsorption. We previously hypothesized that weakening hydrogen adsorption on a pure Pt catalyst through controlling the pH can influence the hydrogenation barrier through Brønsted-Evans-Polanyi (BEP) relations.[222] Briefly, with all else being held constant, a weaker adsorbed hydrogen would result in a more favorable hydrogenation reaction energy and consequently a lowered hydrogenation barrier. Although ΔH_{H} seems to be a descriptor for the $\mathrm{Pt/Pt_xCo_y}$ surfaces, $\Delta H_f^\ddagger$ is not simply a function of ΔH_{H} for the $\mathrm{Pt_xCo_y}$ surfaces. By examining $\Delta H_f^\ddagger$ on $\mathrm{Pt_xCo_y}$ as a function of the hydrogenation reaction enthalpy (ΔH_{rxn}) in **Figure 4-6d**, we demonstrate that hydrogenation on Pt_xCo_y follows a BEP relationship, with a higher reaction enthalpy correlating with a higher activation enthalpy. The more endothermic ΔH_{rxn} on the Pt_xCo_y surfaces compared Pt/Pt_xCo_y surfaces indicate that the hydrogenated intermediate species (PH*) is less stable than the reactants (P* + H*) when there is Co in the surface catalyst layer. The slope near one implies a late transition state. For the Pt_xCo_y surfaces, the surface with the weakest hydrogen adsorption is not the surface with the least endothermic reaction enthalpy. Ultimately, despite adsorbed hydrogen being an important reactant, the hydrogen adsorption energy alone is not a suitable descriptor for phenol hydrogenation like it is for HER. Instead, the activation enthalpy more closely follows a BEP relationship, and the higher $\Delta H_f^{\ddagger}$ on Pt_xCo_y surfaces than on Pt or Pt/Pt_xCo_y surfaces is caused by the weaker interaction between the hydrogenated phenol intermediate and the Pt_xCo_y surface.

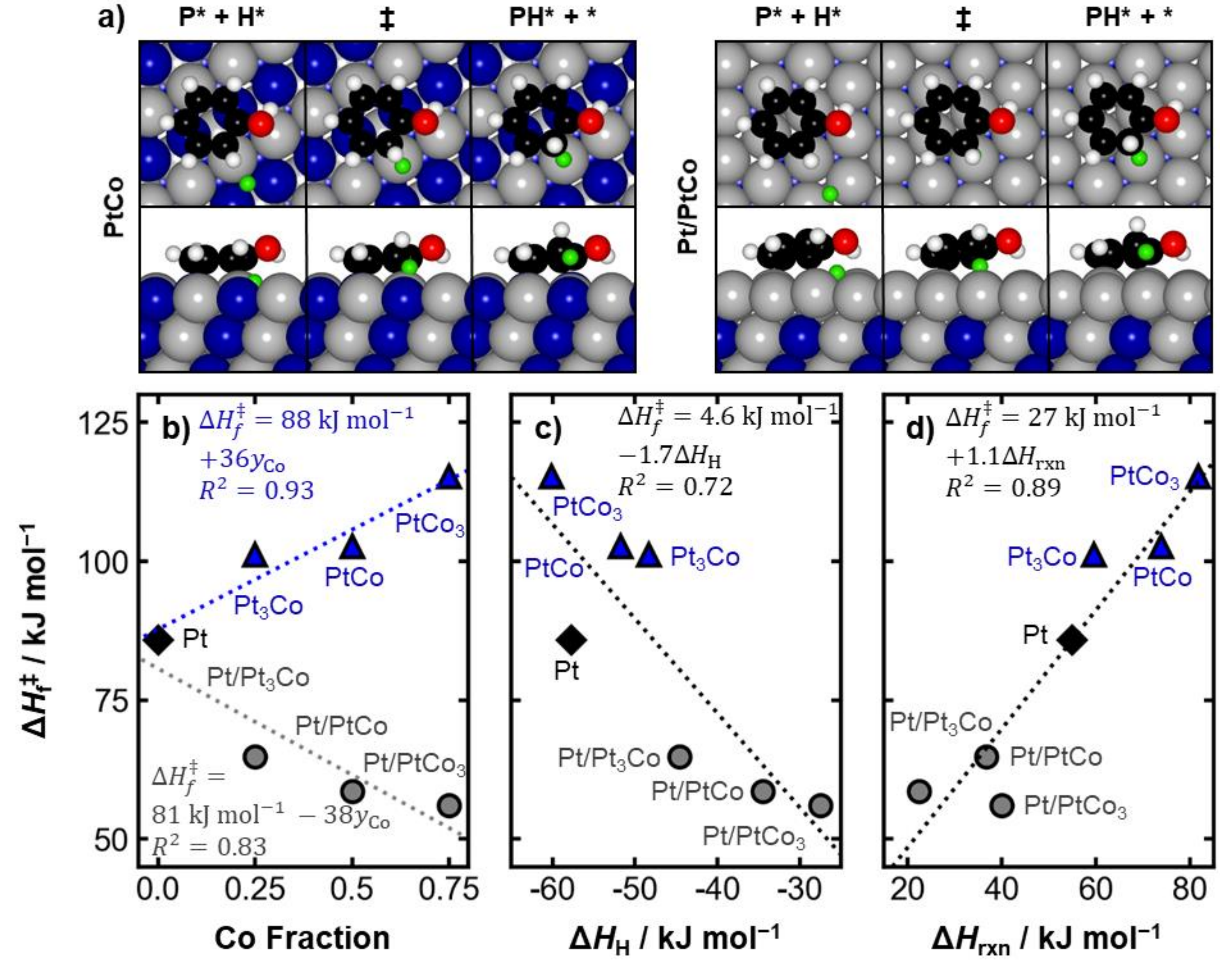

Figure 4-6 Activation enthalpy for the first hydrogenation step of phenol. **a)** Top and side views of DFT-predicted geometries corresponding to the initial, transition, and final states for the first hydrogenation of phenol on the (111) facet of both PtCo and Pt/PtCo. Color legend: Pt = gray, Co = blue, O = red, C = black, and H = white. The H* atom participating in the hydrogenation reaction is colored green. Activation enthalpy for the first hydrogenation of phenol on Pt$_x$Co$_y$ and Pt/Pt$_x$Co$_y$ as a function of **b)** Co fraction, **c)** the adsorption enthalpy of hydrogen (ΔH_H), and **d)** the reaction enthalpy for the first hydrogenation step of phenol at 300 K (ΔH_{rxn}). Blue triangles correspond to activation enthalpies calculated on Pt$_x$Co$_y$ and gray circles correspond to barriers calculated on Pt/Pt$_x$Co$_y$. Black diamonds correspond to pure Pt. Linear fits to the data are shown along with corresponding equations.

4.3.5 Explaining ECH Activity on Pt$_x$Co$_y$ Alloys Using a Langmuir-Hinshelwood Model

We are able to describe the trend in experimental TOF with Co fractions and applied potentials shown in **Figure 4-4** using a Langmuir-Hinshelwood model to capture the effects of Co alloying on hydrogen adsorption energy, phenol adsorption energy, and hydrogenation activation enthalpy. Assuming that the first hydrogenation step is rate determining,[12,21] we estimate the TOF as a function of potential and Co fraction using a simple microkinetic model. In **Eq. 4-2**, we show that the equilibrium adsorption coefficient for hydrogen (K_H) is a function of the applied electrochemical potential (E) and the hydrogen adsorption free energy on a given surface. F is Faraday's constant. We note that we assume the ΔG_H at 0 V vs. RHE here is the same as that computed for **Figure 4-1**, referenced to 1 bar H_2.

$$K_{\mathrm{H}}(E) = \exp\left(\frac{-\Delta G_{\mathrm{H}}(E = 0\ \mathrm{V\ vs.\ RHE})}{RT}\right)\exp\left(\frac{-FE}{RT}\right) \qquad \textbf{Eq. 4-2}$$

In **Eq. 4-3**, we assume that the phenol equilibrium adsorption coefficient (K_P) is independent of potential, although in reality there may be variations due to the impact of potential on the interfacial water layer.[119] The adsorption coefficient is dependent on the free energy of adsorption of phenol, $\Delta G_{\mathrm{ads,P}}$.

$$K_{\mathrm{P}} = \exp\left(\frac{-\Delta G_{\mathrm{ads,P}}}{RT}\right) \qquad \textbf{Eq. 4-3}$$

If the first hydrogenation step is rate determining, the TOF will be described by **Eq. 4-4**. The TOF depends on the rate constant, k_{ECH}, and the product of the hydrogen and phenol coverage, θ_{H} and θ_{P}.[21] The coverages are given by the equilibrium adsorption coefficients when adsorption is quasi-equilibrated. Here C_P is the concentration of phenol and C_H is an 'equivalent' chemical potential of hydrogen, as we have elaborated in previous work.[35]

$$TOF = k_{ECH}\theta_{\mathrm{H}}\theta_{\mathrm{P}} = k_{ECH}\frac{K_{\mathrm{H}}C_{\mathrm{H}}K_{\mathrm{P}}C_{\mathrm{P}}}{(1 + K_{\mathrm{H}}C_{\mathrm{H}} + K_{\mathrm{P}}C_{\mathrm{P}})^2} \qquad \textbf{Eq. 4-4}$$

The rate constant depends on the enthalpy of the first hydrogenation step's transition state relative to the reactant energy ($\Delta H_f^{\ddagger}$) as we show in **Eq. 4-5**. A is a preexponential factor, which we assume to be independent of the Co content of the catalyst surface, and we do not include any influence of the applied potential on the rate constant.

$$k_{ECH} = A\exp\left(\frac{-\Delta H_f^{\ddagger}}{RT}\right) \qquad \textbf{Eq. 4-5}$$

We predict the rate constant as a function of the Co fraction due to a dependence of the activation barrier on the Co fraction (**Figure 4-6b**). The linear trends in **Figure 4-6b** indicate that the rate constant would exponentially decrease with Co fraction on the mixed Co and Pt surface and exponentially increase with Co fraction on the Pt skin surface. As the hydrogen adsorption free energy is also a function of the Co fraction (**Figure 4-6b**), we can describe the TOF as a function of Co content and potential if the first hydrogenation step is rate determining. Here we assume K_P is constant with Co content, and we use a $\Delta G_{ads,P}$ value of -9 kJ mol^{-1} based on our previously obtained value for the adsorption energy of phenol on the active site of Pt for ECH.[21] We discuss additional details of the kinetic model in the Appendix.

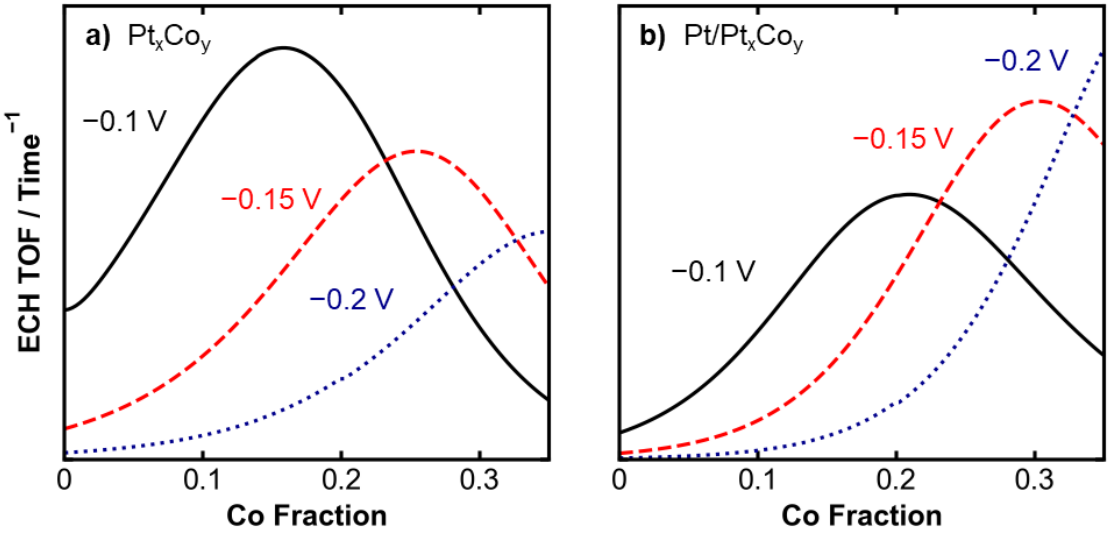

Figure 4-7 ECH turnover frequency on Pt$_x$Co$_y$/felt, as a function of Co fraction and potential using a Langmuir-Hinshelwood model. **a)** Calculated ECH TOF assuming the first hydrogenation step is rate determining, and the transition state barrier increases as a function of Co fraction, as found for the for the mixed surface Pt$_x$Co$_y$ structure (Pt$_x$Co$_y$) in **Figure 6**. **b)** Calculated ECH TOF assuming the first hydrogenation step is rate determining, and the transition state barrier is decreases as a function of Co fraction, as found for the Pt skin structure (Pt/Pt$_x$Co$_y$) in **Figure 6**. The temperature used is 300 K.

We show the prediction of the TOF as a function of potential and Co fraction in **Figure 4-7** for the two types of catalyst surfaces. The results on the mixed Co and Pt surface in **Figure 4-7a** qualitatively match our experimental results in **Figure 4-4a**. At more negative potentials the hydrogen coverage will increase on Pt$_x$Co$_y$, which for catalysts that adsorb hydrogen relatively strongly, will cause the phenol coverage to decrease and the TOF to go down. For higher Co fractions, where the hydrogen adsorption energy is weaker, the effect of more negative potential is less detrimental, as the phenol coverage remains high. In this way, the kinetic model captures why the maximum in ECH TOF with Co fraction varies as a function of applied potential. At comparable coverages of hydrogen and phenol for a pure Pt catalyst compared to a Pt_xCo_y alloy, the TOF is lower for the alloy due to the higher activation enthalpy (**Figure 4-6b**). The increase in TOF with Co fraction observed experimentally at −0.1 V vs. RHE in **Figure 4-4a** is explained by our model as weakening the hydrogen adsorption energy, which allows a higher coverage of phenol on the surface, thus increasing the rate. Although this higher coverage of phenol results in an increase in the ECH rate, the current efficiency for ECH at −0.1 V vs. RHE may be lower with Co fraction (**Figure 4-4b**) because of an increase in the HER activity.

The model for the TOF on a Pt skin with a Pt_xCo_y core (**Figure 4-7b**) does not match our experimental values, further corroborating the mixed Pt_xCo_y surface indicated from our HER measurements, characterization, and DFT calculations of the energetically preferred surface. The decrease in activity at sufficiently high Co fractions is due to a decrease in the hydrogen coverage, conceptually similar to that described for **Figure 4-7a**. In **Figure 4-7b**, due to the prediction that an increasing Co fraction will decrease the hydrogenation barrier for a Pt/Pt_xCo_y structure, the ECH TOF is predicted to increase under almost all conditions up to high Co fractions, which is not what we observe experimentally. We predict a catalyst with a stable Pt skin and a Pt_xCo_y core structure under ECH conditions would be a more active catalyst based on DFT-calculated activation energies and our kinetic modeling. Further study of Pt/Pt_xCo_y core-shell alloys is needed to test the stability of Pt/Pt_xCo_y catalysts under ECH conditions and to experimentally verify the enhanced activity for phenol ECH.

4.4 Conclusions

We find that Pt_xCo_y alloys at low Co fractions are more active toward ECH of phenol than pure Pt at −0.1 V vs. RHE, but the ECH current efficiency is lower than pure Pt due to their high HER activity. Pt_xCo_y preferentially forms structures with Co and Pt on the surface under our ECH and HER conditions, as opposed to a Pt skin. Although the HER activity correlates with computed hydrogen adsorption energies on Pt_xCo_y surfaces, with surfaces that adsorb hydrogen more weakly having higher HER activity, the hydrogen adsorption energy is an insufficient descriptor for ECH activity. Rather, the hydrogenation activation enthalpies follow a Brønsted-Evans-Polanyi relationship with respect to the reaction enthalpies, and the Pt_xCo_y surfaces have more endothermic reaction enthalpies and larger activation enthalpies than Pt despite adsorbing hydrogen more weakly. We qualitatively explain the experimental ECH TOF trends on the Pt_xCo_y surfaces with a Langmuir-Hinshelwood kinetic model. Our DFT and kinetic modeling predict that Pt/Pt_xCo_y alloys, i.e., a pure Pt surface layer with Pt_xCo_y core, would have enhanced ECH activity, although further work to synthesize and stabilize these structures under ECH conditions is needed.

Chapter 5 Conclusion & Outlook

5.1 Summary

Producing transportation fuels and chemicals through the valorization of biomass-derived molecules is a promising strategy to decrease our reliance on fossil fuels; however, the catalysts required for biomass conversion are insufficient to make the technology cost-competitive with fossil fuels. The goal of the research presented in this dissertation was to use a joint computational-experimental approach to elucidate the structure-property relationships that govern aqueous-phase hydrogenation of bio-oil compounds to aid in the development of active and selective catalysts to improve the viability of technologies for the sustainable production of fuels and chemicals.

In Chapter 2, we explored various approaches for estimating the aqueous-phase adsorption energies of model bio-oil compounds on catalytically relevant facets of Pt and Rh. We explained how gas-phase and implicit solvent modeling techniques, commonly used to approximate aqueous-phase behavior, fail to reproduce experimental adsorption trends, leading to inaccurate predictions of a metal's catalytic hydrogenation activity. Through direct comparison with experimentally determined aqueous-phase adsorption energies, we demonstrated that accounting for solvent displacement at the solvent/catalyst interface using a bond-additivity model based on first-principles calculations yields improved agreement with experimental measurements. Specifically we showed that DFT-computed adsorption energies of organics and water in addition to tabulated thermodynamic properties enable rapid and semi-quantitative predictions of aqueous-phase adsorption energies. These results highlight the necessity of accounting for solvent effects, particularly solvent displacement, at the metal interface when modeling adsorption of organic molecules relevant to condensed-phase catalytic reactions. The work in this chapter highlights a fast approach to quantify a solvent's effect on organic adsorption, which may help rationalize the selection of a solvent environment to tune condensed-phase catalytic rates.

In Chapter 3, we studied ECH and TCH of phenol on Pt and Rh nanoparticles supported on carbon (Pt/C and Rh/C) to identify the active site on Rh/C and explain the activity and structure sensitivity of Rh/C and Pt/C. We fit phenol TCH rate data on Rh/C to a Langmuir-Hinshelwood model and extracted the phenol adsorption energy on the active site to compare with adsorption energies measured on terraces and stepped facets. We modeled phenol hydrogenation on (111) terraces and (221) steps of Pt and Rh using density functional theory and microkinetic modeling and elucidated the relationship between intrinsic kinetics and phenol adsorption strength. We studied phenol ECH on Rh/C as a function of particle size and found that larger particles, which have a higher fraction of terrace sites compared to smaller particles, are more active. Ultimately, we found that the (111) terraces of Pt and Rh are active for phenol hydrogenation, which our computational results indicate is due to higher intrinsic activity and weaker phenol adsorption. By providing a better understanding of the active site of Pt/C and Rh/C for phenol hydrogenation, these findings may help inform the design of catalysts to preferentially expose and stabilize catalytically active sites.

In Chapter 4, we studied ECH of phenol on platinum-cobalt alloys to investigate whether the properties that cause an enhancement in the rate for electrochemical reactions like hydrogen evolution reaction (HER) and oxygen reduction reaction are similarly beneficial for ECH of phenol. We hypothesized that because adsorbed hydrogen is an important reactant for phenol ECH, the barrier for hydrogenation would be lower if the strength between adsorbed hydrogen and the catalyst surface was reduced. We tested a series of Pt_xCo_y alloys supported on carbon (Pt_xCo_y/C) for their HER activity, and found that Pt_3Co/C, which adsorbed hydrogen the weakest, had the highest HER activity. However, experimental measurements revealed that the activity of the Pt_xCo_y/C alloys toward ECH was not described by the hydrogen adsorption energy, and that alloys with weaker hydrogen adsorption energies were not necessarily more active for ECH. Characterization of the catalysts revealed that the surfaces consisted of both Pt and Co atoms. To explain these results, we constructed a series of model alloy systems with mixed platinum-cobalt surfaces (Pt_xCo_y) as well as systems where the top layer was replaced with pure Pt to emulate a core-shell alloy (Pt/Pt_xCo_y). Our DFT modeling revealed that the activation barriers for hydrogenation of phenol were not described by the hydrogen adsorption energy, but instead more closely followed a Brønsted-Evans-Polanyi relationship with respect to the reaction energies. Barriers on the Pt_xCo_y alloys were predicted to increase with Co fraction and barriers on Pt/Pt_xCo_y were predicted to decrease with Co fraction. Our DFT-predicted activation barriers combined with kinetic modeling rationalized the experimental findings on the Pt_xCo_y/C catalysts. Kinetic modeling predicted Pt/Pt_xCo_y alloys to have enhanced activity compared to Pt, and future synthesis and testing of platinum-cobalt core-shell alloys for phenol ECH is a promising future direction.

Together, these chapters explored various properties that govern aqueous-phase catalytic hydrogenation of biomass-derived compounds. These works helped disentangle the complicated relationship that exists between aqueous-phase adsorption, intrinsic reaction kinetics, and how they govern the overall rate of hydrogenation. Future effort toward furthering these aims will continue to advance the development of materials for efficient biomass conversion.

5.2 Extension of Current Research

5.2.1 Applying the Bond-Additivity Model to New Materials

The work presented in Chapter 2 shows that the bond-additivity model performs well for pure metals where solvent adsorption or adhesion is well understood, however, extending this approach to predict adsorption energies of organics on new materials is an ongoing challenge. The bond-additivity model relies upon an accurate understanding of solvent adsorption properties in order to make reliable predictions of aqueous-phase adsorption energies of organics. Adhesion energies of water and various organic solvents have been measured on the (111) facets of Pt and Ni,[66] which make up only a small portion of the catalyst design space. The lack of experimentally or computationally determined adsorption and adhesion energies hinders the extension of the bond-additivity model to new catalyst materials or solvent environments.

Preliminary results investigating phenol adsorption on platinum-cobalt alloys, based on the work in Chapter 4, highlight that while the bond-additivity model can reliably predict phenol adsorption on pure Pt, the model fails to match experimentally observed trends on the alloys. **Figure 5-1** shows the aqueous-phase phenol adsorption energies on Pt_xCo_y and Pt/Pt_xCo_y predicted using the bond-additivity model compared the adsorption energies measured experimentally through isotherm fitting. The experimental values and DFT-computed values of the adsorption energy agree well on Pt, but the adsorption energies on the alloys are predicted to be much weaker than what is seen experimentally. Although the discrepancies between the experimental and computational adsorption energies may stem from the limitations in the experimental method used to extract the adsorption energies on the alloys (see Chapter 4 for details), they may be due to an erroneous description of water adsorption on the platinum-cobalt alloy surfaces. A more detailed model of water adsorption on alloy surfaces may be necessary to make better predictions of aqueous-phase adsorption from a modeling perspective.

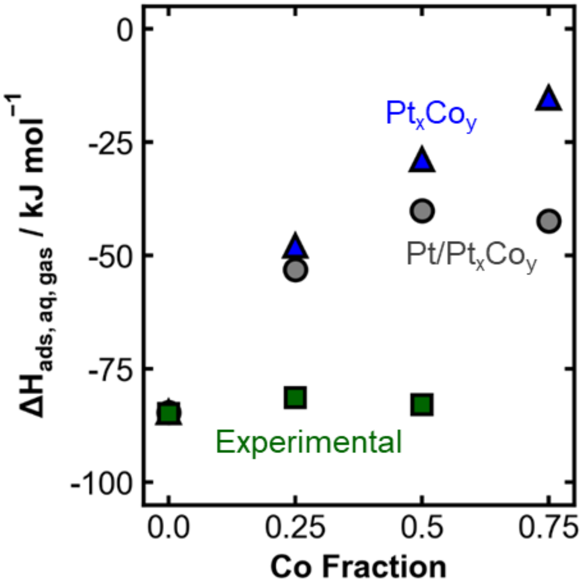

Figure 5-1 Aqueous-phase phenol adsorption on platinum-cobalt alloys. DFT-predicted aqueous-phase adsorption energies of phenol on the (111) facets of Pt_3Co, PtCo, and $PtCo_3$ where both Pt and Co are present in the catalyst surface are shown with blue triangles. DFT-predicted aqueous-phase adsorption energies on phenol on Pt/Pt_3Co, Pt/PtCo, and Pt/$PtCo_3$ are shown with gray circles. Experimentally measured aqueous-phase adsorption energies from isotherm fitting are shown in green squares.

Reliable computational approaches for predicting solvent adsorption behavior on metals and alloys would allow for the bond-additivity model to be applied to rapidly predict aqueous-phase adsorption behavior for a wide range of organic species and surfaces. Here, I highlight two approaches for estimating solvent adhesion energies from molecular dynamics simulations. Leroy *et al.* proposed a thermodynamic integration scheme for estimating adhesion energies at a liquid/solid interface referred to as the phantom-wall method.[223,224] A schematic of the phantom-wall method is shown in **Figure 5-2a**. In this approach, a phantom wall, which is an artificial potential that only interacts with the liquid, is moved from inside the solid surface outward in order to break the liquid/solid interactions, and the change in the free energy of the system is estimated. This method, however, is based on classical molecular dynamics and requires accurate force fields to describe the liquid/solid interactions at the interface. More recently, a hybrid QM/MM scheme was proposed for estimating adhesion energies referred to as density functional theory in classical explicit solvents (DFT-CES).[225,226] A schematic of this method is shown in **Figure 5-2b**. In this approach, the energetics of the solid are evaluated with DFT, but the dynamics of the liquid are treated with classical molecular dynamics, thus accelerating the computation compared to a purely quantum mechanical approach. The DFT-CES method does not rely on classical force fields to describe the liquid/solid interactions and was used to closely reproduce the experimental adhesion energy of water on Pt(111).[66,227]

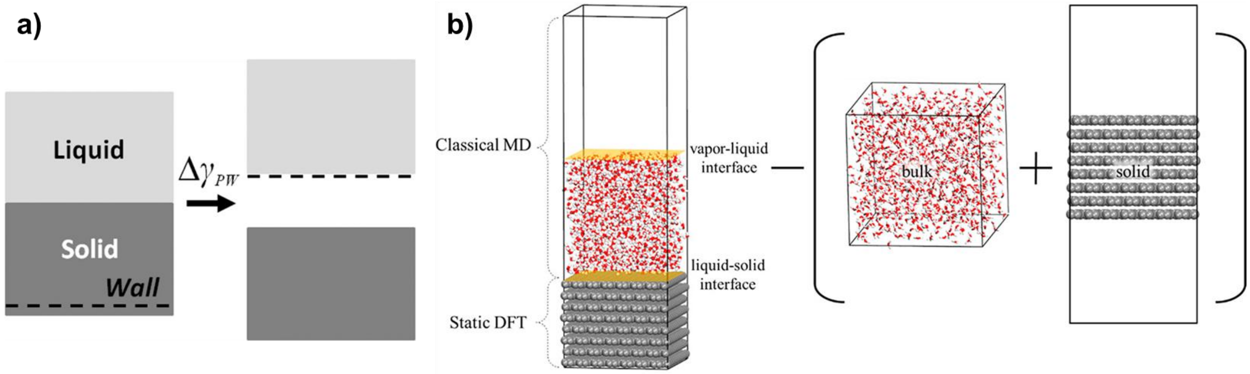

Figure 5-2 Computational approaches for computing solvent adhesion energies. **a)** Phantom wall method for calculation solvent adhesion energies from classical molecular dynamics. Adapted from ref [224]. **b)** DFT-CES method for calculating solvent adhesion energies from a QM/MM approach. Adapted from ref [226].

Computational approaches like the phantom-wall method and DFT-CES can be applied to evaluate solvent adhesion energies on materials relevant to aqueous-phase ECH and TCH such as metals and alloys. Furthermore, these methods can allow for the study of solvent adsorption behavior on materials that may not be easily studied experimentally, such as on specific surface facets or surfaces with defects. Ultimately, estimating solvent adhesion energies would allow for rapid prediction of aqueous-phase adsorption energies of molecules on catalytically relevant materials through the bond-additivity framework without each molecule needing to be simulated individually using a more computationally demanding solvent modeling technique.

5.2.2 Modeling the Electrochemical Environment

One of the challenges in computational electrocatalysis is accurately modeling the electrochemical environment. To model an electrochemical environment, it is necessary to account for effects of the applied electric potential and interactions between the electrode, the electrolyte, and the surface-adsorbed species. Together, these effects can alter adsorption thermodynamics and reaction kinetics. The computational hydrogen electrode (CHE) method is a popular approach for approximating the effect of the applied electric potential for processes that involve an electron transfer steps including adsorption processes and elementary reaction steps.[228,229] However, the CHE only approximates electrochemical behavior,[230,231] and a more rigorous approach is necessary to model electrochemical systems with higher accuracy.

Recently, there has been growing interest in performing density functional theory calculations within a grand-canonical ensemble where the number of electrons in the system is adjusted to achieve a desired electron chemical potential, which is related to an electrode potential, to mimic experimental electrochemical conditions.[230,232,233] I will refer to this approach of DFT modeling with a grand-canonical ensemble of electrons as grand canonical density functional theory (GC-DFT). One of the challenges of modeling electric charge is that periodic DFT systems must be charge-balanced.[233] However, pairing DFT with an implicit solvation model enables the modeling of charged electrode surfaces because the implicit solvent model provides a counter charge to maintain overall charge neutrality in the simulation cell.[232,234] Thus, GC-DFT calculations are performed by changing the number of electrons in the system to achieve a desired electrode potential while leveraging a polarizable continuum model of the solvent environment to balance the system charge.

GC-DFT calculations have been performed with various DFT codes such as VASP using the VASPsol implicit solvation model.[235–237] However, past implementations have often relied on iterative schemes to converge the number of electrons to achieve the desired electrode potential, which can be costly.[235,237] However, more recent codes have been introduced to make GC-DFT modeling more computationally efficient and user-friendly. GC-DFT calculations implemented in the JDFTx code adjust the number of electrons automatically to achieve a desired electron chemical potential.[238]

Figure 5-3 shows preliminary results of the hydrogen adsorption energy on Pt(111) modeled as a function of applied potential using the JDFTx software compared to the potential-dependence of the adsorption energies using the CHE method. The similarity of the slopes of the two methods show that the values calculated with JDFTx do not deviate far from expected behavior based on the CHE model. Although the two methods perform similarly for something simple such as hydrogen adsorption, GC-DFT modeling can be used to explore effects of the applied potential on processes not readily described by the CHE model. For example, the CHE method was shown to greatly overestimate the effect of the applied potential for the electrochemical reduction of CO_2, and GC-DFT modeling provided more accurate reaction energetics.[239] GC-DFT modeling has also been used to evaluate the effect of applied potential on reaction kinetics. Recently, the JDFTx code has been used to perform grand-canonical nudged elastic band calculations in order to find transition states of electrochemical reactions under an applied potential.[240,241]

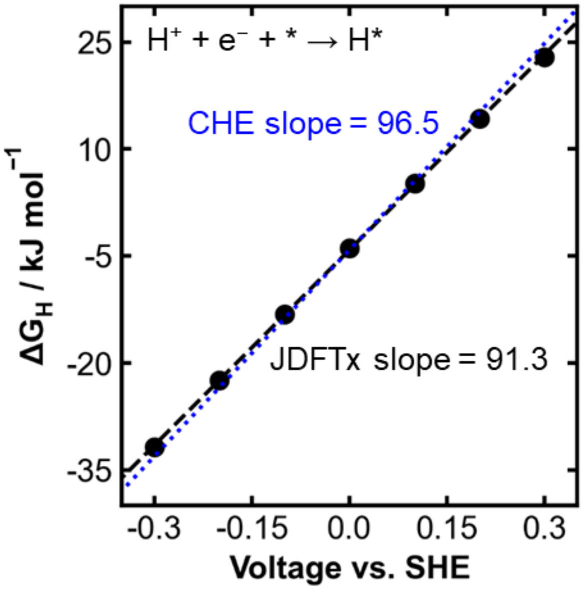

Figure 5-3 Hydrogen adsorption from GC-DFT and CHE. Potential-dependent adsorption energies of hydrogen on Pt(111) as a function of applied potential. Values computed using the JDFTx code are shown in black and values corresponding to the computational hydrogen electrode model are shown in blue.

Although JDFTx is a promising approach for modeling electrochemical processes, one of the major challenges to is efficient scaling with system size. Poor scaling with system size makes it challenging to model bio-oil hydrogenation with this approach. In my experience, the computational cost of simulating small supercells (i.e., 2 × 2 × 4 slabs) was comparable to VASP; however, simulating supercells with an adsorbed bio-oil molecule JDFTx (i.e., 4 × 4 × 4 slabs) was computationally intractable. Performing GC-DFT calculations using the current implementation of JDFTx (version 1.7.0) may incur additional computational cost compared to other DFT codes. However, careful parallelization of computing resources may be able to accelerate JDFTx performance.

Accurately modeling electrochemical environments and accounting for the effects of an applied potential are necessary in order to construct detailed atomistic models of electrocatalytic systems. While the CHE model is popular because of its simplicity, emerging implementations of GC-DFT in popular DFT codes allow for a more rigorous modeling of the applied electric potential on critical processes. Future work on the ECH of bio-oil compounds would benefit from these recent developments.

5.2.3 Experimental Verification of Platinum-Cobalt Core-Shell Alloys

Alloying highly active but expensive platinum-group metals with earth abundant materials is a strategy to reduce catalyst cost. In some cases, alloying simply improves the activity of the platinum-group metal on a mass basis by reducing the amount of the expensive material needed to produce the catalyst. However in a variety of applications, alloying platinum-group metals with earth abundant metals enhances both the mass activity and specific activity of the catalyst through enhancement of the catalysts electronic and structural properties.[242] Platinum-cobalt catalysts been shown to be promising electrocatalysts for a variety of applications like fuel cells.[201] In Chapter 4, we discussed the ECH of phenol on platinum-cobalt alloys. We found that catalyst with both Pt and Co atoms present on the catalyst surface did not significantly enhance ECH activity compared to Pt. However, our DFT calculations indicated that platinum-cobalt core-shell alloys with a pure Pt skin and a Pt_xCo_y shell may have enhanced performance for ECH of phenol. In the future, I hope to see the synthesis and testing of platinum-cobalt core-shell alloys for phenol ECH. Future experimental verification could provide additional confidence to our modeling and could drive further exploration of alloys as efficient and low-cost alternatives to platinum-group metals for aqueous-phase hydrogenation reactions.

5.3 Current Challenges & Limitations

The presence of solvent, ions, and the effect of an applied electric potential all influence the adsorption properties and reaction behavior of bio-oil compounds on metals and alloys in an electrochemical environment. Accurate description of adsorption and hydrogenation of bio-oils in an electrochemical environment requires a model that accounts for the effect of ions and an applied potential. **Figure 5-4** summarizes some of the effects that ions have on the solvent/surface interface including the blocking of sites, the restructuring of the interfacial solvent layer, and influence over transition state energies of certain processes.

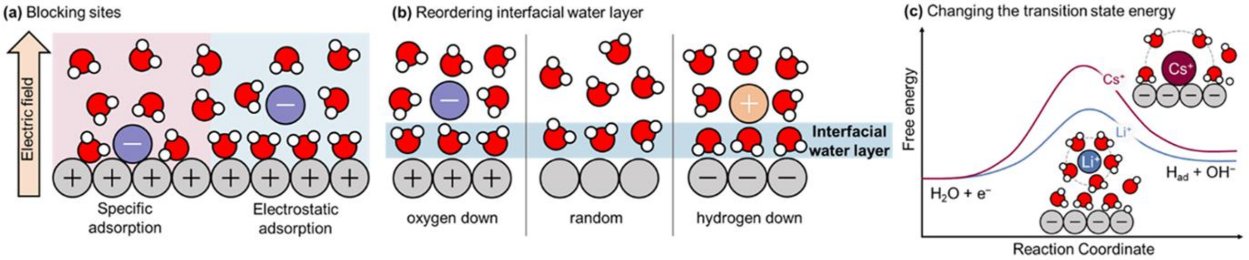

Figure 5-4 Summary of ion effects in an electrochemical environment. **a)** Blocking of adsorption sites by the presence of ions in an aqueous solution. **b)** Restructuring of interfacial water induced by the presence of anions and cations. **c)** Modification of transition state energies from the presence of different cations. Adapted from ref [243].

Although the current formulation of the bond-additivity model approximates the effects of pure solvents on the adsorption of bio-oil compounds, it is not currently well adapted to account for phenomena in a more complex electrochemical environment. While the bond-additivity model may still be a useful tool, modeling electrochemical adsorption should not rely on this method alone. Instead, more advanced methods, such as molecular dynamics simulations are needed to more accurately describe adsorption in more representative electrochemical environments.

In addition to aqueous-phase adsorption, modeling bio-oil hydrogenation in a fully solvated environment would advance our understanding of reactions in the condensed phase. In Chapter 3, we approximate aqueous-phase hydrogenation behavior using gas-phase hydrogenation kinetics. Although past studies have shown that the barriers for the hydrogenation of C=C bonds is not significantly affected by the presence of solvent,[73] solvation affects can still contribute to the overall free energy landscape of aqueous-phase bio-oil hydrogenation. The free energy diagrams presented in Chapter 3 assume that the solvent displaced upon phenol adsorption all returns to the surface as the product, cyclohexanone, desorbs. This approach, however, leads to an incorrect product desorption energy. In reality, solvent can restructure around the partially hydrogenated surface intermediates, which can change the energetics of the reaction in numerous ways. For example, the solvation energies of the surface intermediates likely differ from that of the reactant and product molecules. This contribution to the energy is likely small, however, since solvation energy of phenol and cyclohexanone differ by only 10 kJ mol^{-1} (Appendix B.3). The restructuring of solvent can affect the overall reaction energetics more significantly if a portion of the displaced solvent returns to the metal surface along the reaction coordinate. Because the return of solvent to the surface is an exothermic process, the relative energies of surface intermediates would be lower than what is predicted based on gas-phase calculations if solvent restructuring is accurately captured. Modeling differences in solvation along the reaction coordinate would lead to a more accurate treatment of product desorption in the aqueous phase and would allow for kinetic modeling to more accurately predict rate determining steps and apparent activation energies, both of which were found to be qualitatively and quantitatively incorrect compared to experiment in Chapter 3. More importantly, accurate treatment of solvation of intermediates and surfaces during hydrogenation would help models elucidate activity differences between surfaces that might have similar hydrogenation barriers but interact differently with the solvent environment.

Previous work has aimed to model explicit solvation effects for the hydrogenation of model bio-oil compounds, but the current approaches do not adequately sample the local solvent environment around the hydrogenated intermediates. For example, some works have used molecular dynamics simulations to generate solvent configurations around adsorbed reactants, and nudged elastic band (NEB)[152] calculations were used to find transition states for the subsequent hydrogenation reactions.[71,73,244] The solvent environment around the hydrogenated intermediates, however, was not re-optimized after each elementary step. Thus, these approaches fail to capture changes in the local solvent environment around the intermediates over the course of the reaction. Other approaches have used a combination of NEB calculations and molecular dynamics where the NEB replicas were minimized as the solvated system was quenched from finite temperature to 0 K over a time scale of 1−2 ps.[72] This approach allows for the restructuring of solvent around the transition state, however, the time scales considered are too short for solvent to restructure around the hydrogenated intermediate. Thus, critical phenomena such as the return of displaced solvent to the surface are still not properly described. Current approaches only approximate true aqueous-phase processes, and I believe adequate sampling along the reaction coordinate is essential in order to construct free energy diagrams for hydrogenation reactions that reflect what is happening in real systems. The major challenge hindering the accurate modeling of condensed phase hydrogenation reactions is that molecular dynamics simulations are computationally expensive. However, as computational resources improve and as new computational workflows for treating solvent environments are developed, more accurate simulations may be performed to explore electrochemical reactions.

5.4 Final Remarks

In this chapter, I have presented what I consider to be some of the promising future directions for the continuation of work in this research area. This is an exciting time to be in the field of computational electrochemistry because we are gaining access to more powerful and efficient computational resources, and novel methods for the evaluation of important electrochemical phenomena are being developed. My hope is that the work that this dissertation is based upon will serve as a useful contribution to the field, and that future research will be able to bring us closer to the ultimate goal of improved environmental sustainability.

Appendix A: Supporting Information for Adsorption of Organics on Pt and Rh

This appendix was adapted from Akinola, J.; Barth, I.; Goldsmith, B. R.; Singh, N. Adsorption Energies of Oxygenated Aromatics and Organics on Rhodium and Platinum in Aqueous Phase. *ACS Catal.* **2020**, *10* (9), 4929–4941. My contribution to this work is the density functional theory modeling. James Akinola performed the experimental work.

A.1 Reversibility of Hydrogen Underpotential Deposition in Acetate Buffer and in the Presence of Phenol

The current densities in the hydrogen underpotential deposition (H_{upd}) region on Rh in acetate buffer shown in **Appendix Figure A-1** are proportional to the scan rate. This is expected as the total charge (current integrated over time) should be independent of scan rate for an equilibrated process.

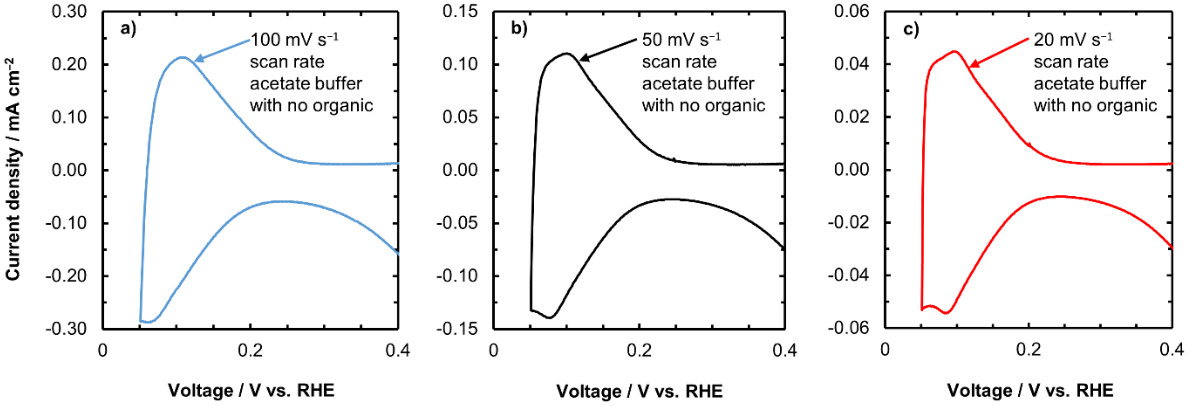

Appendix Figure A-1 Cyclic voltammograms on Rh wire. Cyclic voltamograms showing the H_{upd} on Rh wire in acetate buffer (100 mM acetic acid, 100 mM sodium acetate, pH = 5) at 298 K and scan rates of **a)** 100 mV s^{-1}, **b)** 50 mV s^{-1}, **c)** 20 mV s^{-1}.

The change in the H_{upd} desorption charge with scan rate (**Appendix Table A-1**) is approximately 7%. Partially this may be related to errors in determining the charge (e.g., where to select the background double layer charging current), and partially may be real differences in the amount of H_{upd} that is adsorbed and desorbed at slower scan rates. For our studies because we did not see any significant differences in the adsorption isotherms derived at the different scan rates, we selected the faster scan rates (100 mV s^{-1}) to minimize the total time required for the full set of CV experiments.

Appendix Table A-1 Desorption charges for H_{upd}. Desorption charges for H_{upd} (Q_{des}) of Rh wire in acetate buffer supporting electrolyte corresponding to data in **Figure 2-1** at 100, 50, or 20 mV s^{-1} scan rate.

Scan rate	**100 mV s^{-1} (Appendix Figure A-1a)**	**50 mV s^{-1} (Appendix Figure A-1b)**	**20 mV s^{-1} (Appendix Figure A-1c)**
Q_{des} (μC)	10.2	10.7	10.9

The data in **Appendix Figure A-1** shows that H adsorption and H* desorption on Pt and Rh are reversible with and without phenol. The difference in the charge from H adsorption (Q_{ads}) and H* desorption (Q_{des}) is nearly constant even with increasing concentration of phenol for both Pt and Rh wires. For Rh, the higher adsorption charge compared with the desorption charge is caused by the convolution of the Rh_2O_3 reduction peak with the H^+ reduction peak, causing the 'adsorption' charge (in actuality the reduction charge) to be larger than the desorption charge. Thus, we use Q_{des} to represent the H_{upd} charge unless stated otherwise (i.e., the fraction of H_{upd} charge inhibited refers to the effect of the organic on the desorption charge because of site blocking, see **A.5**). The constant ratio of Q_{ads} and Q_{des} at all phenol concentrations indicates that H* does not react with adsorbed phenol within this potential window at 100 mV s^{-1} scan rate, as otherwise the Q_{des} would decrease relative to Q_{ads} at higher phenol concentrations.

The Q_{ads} was obtained by integrating the area under the H adsorption region after converting the H_{upd} potential window to a time using the voltage scan rate and subtracting the baseline (double layer) charge from the CVs in **Figure 2-1**. The baseline current for Rh was chosen at 500 mM phenol because at this high concentration, the H^+ and the Rh_2O_3 reduction peaks were completely inhibited by phenol adsorption. The Q_{des} was obtained by integrating the area under the H* desorption peak in the positive oxidation scan and subtracting the double layer charge.

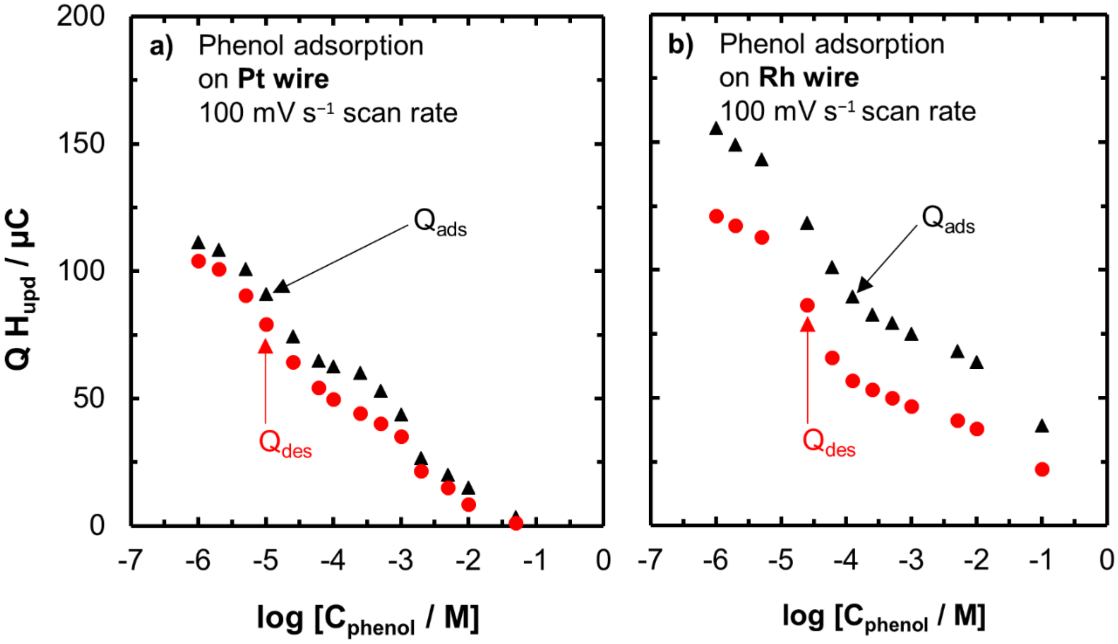

Appendix Figure A-2 H_{upd} adsorption charge. The H_{upd} adsorption charge (from reduction during the portion of the cyclic voltammogram where the voltage sweeps in the negative direction, Q_{ads}) and desorption charge (from oxidation, Q_{des}) on polycrystalline **a)** Pt and **b)** Rh wires as a function of phenol concentration. Charges are calculated from the cyclic voltammograms in **Figure 2-1**. The larger adsorption charge for Rh than desorption charge is because of the Rh oxide reduction peak overlapping with the H_{upd} reduction peak, causing an overprediction of the Q_{ads} charge. The reversibility of the H_{upd} charge is constant with phenol concentration for both metals.

A.2 Change in Bulk Phenol Concentration by Adsorption of Phenol on Rh Wire

It is important to know if there is an appreciable change in the bulk phenol concentration after phenol adsorbs on the Rh surface since an accurate isotherm fit depends on the actual bulk phenol concentration. Here we show there is not an appreciable change in the bulk phenol concentration upon phenol adsorption. We base this analysis on the maximum Rh surface area exposed in our experiments (0.661 cm^2 from **Appendix Figure A-3c**) and the lowest bulk phenol concentration used. The total volume of the electrolyte (130 mL) was kept the same in all measurements.

We assume the same number of Rh and Pt atoms per $cm^2 = 1.31 \times 10^{15}$ atoms from refs [245,246]. Thus, the number of Rh (or Pt) atoms covered by phenol at maximum coverage is:

$$Rh\ atoms = 1.31 \times 10^{15}\ atoms\ cm^{-2} \times max.phenol\ coverage \times ECSA$$

where ECSA is the electrochemical active surface area and we assume the max. phenol coverage is 1 monolayer. Using the maximum ECSA of our samples gives:

$$Rh\ atoms = 1.31 \times 10^{15}\ atoms\ cm^{-2} \times 1 \times 0.661\ cm^{2} = 8.66 \times 10^{14}\ atoms$$

Assuming that one phenol molecule adsorbing flat covers five Rh atoms, the number of moles of phenol to completely block the Rh wire (i.e., at adsorption saturation) is:

$$8.66 \times 10^{14}\ Rh\ atoms \times \frac{1\ phenol\ molecule}{5\ Rh\ atoms} \times \frac{1\ mol\ phenol}{6.02 \times 10^{23}\ phenol\ molecules}$$

$$= 2.874 \times 10^{-10}\ moles\ phenol$$

The volume of acetate buffer + phenol in solution is 130 mL. Therefore, the moles of phenol in 1 µM solution (the lowest phenol concentration we studied) is 1.3×10^{-7} moles. Even if an adsorption saturation coverage of phenol from the bulk concentration is reached, the amount of phenol remaining in bulk solution would be:

$$1.3 \times 10^{-7}\ moles\ phenol - 2.874 \times 10^{-10}\ moles\ phenol = 1.297 \times 10^{-7}\ moles\ phenol$$

The new concentration of solution after phenol adsorption would then be:

$$\frac{1.297 \times 10^{-7}\ moles\ phenol}{0.13\ L} = 9.977 \times 10^{-7}\ mol\ L^{-1} = 0.9977\ \mu M$$

Therefore, the bulk phenol concentration remains approximately constant even at the lowest bulk phenol concentration of 1 µM (0.2% loss in concentration at 1 µM). However, at these low bulk concentrations much less than a full monolayer of phenol is adsorbed based on the small decrease in H_{upd} charge shown in **Figure 2-1**, so in actuality the decrease in bulk phenol concentration would be even smaller. This analysis holds for all organics on Pt as well because a similar area of Pt or Rh was immersed in the supporting electrolyte.

A.3 Reproducibility of the Effect of Phenol Adsorption on H_{upd}

To determine the reproducibility of the H_{upd} method for quantifying phenol adsorption on Rh, we conducted several repetitions at the same bulk concentration of phenol. In **Appendix Figure A-3a**, 60 μM phenol was added after stepwise increments from five intermediate concentrations. However, in **Appendix Figure A-3b** and **Appendix Figure A-3c**, prepared in separate runs, 60 μM was added after a single increment in phenol concentration. For all three runs, a similar relative drop in H_{upd} charge was observed, showing that the fraction of H_{upd} inhibited was reproducible and independent of the surface areas exposed and the path taken to attain the desired concentration. That is, CV measurements performed at lower concentration ranges did not impact later measurements at higher concentrations. We also show in **A.4** that measurements at higher concentrations do not impact later measurements at lower concentrations.

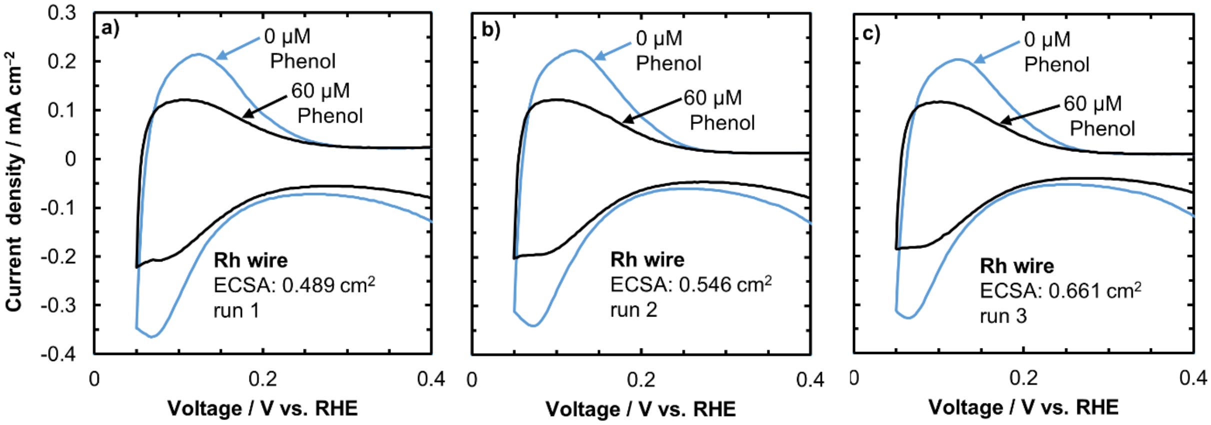

Appendix Figure A-3 Reproducibility of phenol adsorption on Rh. Cyclic voltamograms to test the reproducibility of phenol adsorption on rhodium wire from three different repetitions. In **a)**, the final 60 μM concentration was reached by adding five intermediate concentrations (1, 2, 5 10, 25 μM are shown in **Figure 2-1** of the main text) and taking CVs at each of those intermediate concentrations. In b) and c) the 60 μM concentration was directly reached in one addition, without CV measurements at intermediate concentrations. The supporting electrolyte was 100 mM acetate buffer at 298 K and the scan rate was 100 mV s^{-1}. The ECSA shown is of the run with no phenol, which is used to normalize the current. A value of 221 μC cm^{-2} was used to calculate the ECSA.[247,248]

In **Appendix Table A-2**, the fraction of H_{upd} inhibited at 60 μM phenol is listed for the three runs in **Appendix Figure A-3** and is in the range of 0.43 ± 0.01 even with different amounts of time in reaching the desired phenol concentration. This result indicates that no time effect is present in our estimations of the phenol coverage.

Appendix Table A-2 H_{upd} desorption charges with varying phenol concentration. H_{upd} desorption charge (Q_{des}) at 0 and 60 µM phenol and the fraction of H_{upd} inhibited on Rh wire at 60 µM phenol for the different measurements shown in **Appendix Figure A-3**.

	Repetition 1 (Appendix Figure A-3a)		**Repetition 2 (Appendix Figure A-3b)**		**Repetition 3 (Appendix Figure A-3c)**	
Phenol concentration (µM)	Q_{des} (µC)	Fraction of H_{upd} inhibited	Q_{des} (µC)	Fraction of H_{upd} inhibited	Q_{des} (µC)	Fraction of H_{upd} inhibited
0	108	--	120	--	147	--
60	60.4	0.439	66.8	0.444	84.7	0.427

A.4 Reversibility of Organic Adsorption on Rh and Pt

Adsorption of organics must be reversible in the H_{upd} potential window in order to extract accurate adsorption energies. The H_{upd} desorption charge after phenol replacement with new supporting electrolyte is close to the H_{upd} charge without phenol, with about 99% of the H_{upd} charge recovered on Rh and 97% of the H_{upd} charge recovered on Pt (**Appendix Table A-3**).

Appendix Table A-3 H_{upd} desorption charges on Pt and Rh. The H_{upd} desorption charge without phenol, with 60 µM phenol, and after replacing phenol solution with new supporting electrolyte on Pt wire (**Appendix Figure A-4a**) and Rh wire (**Appendix Figure A-4e**).

	Pt wire		**Rh wire**	
Phenol concentration (µM)	Q_{des} (µC)	Fraction of H_{upd} inhibited	Q_{des} (µC)	Fraction of H_{upd} inhibited
0	16.6	0	148	0
60	7.1	0.571	85.5	0.426
0*	16.1	0.0303	146	0.0143

Also listed is the fraction of H_{upd} inhibited, calculated from the exact desorption charge before rounding to three significant figures. * The concentration is in actuality >0 due to trace remaining phenol in the cell after replacing 60 µM phenol with new supporting electrolyte, as well as from any phenol desorbed from the electrode surface (see **A.2**).

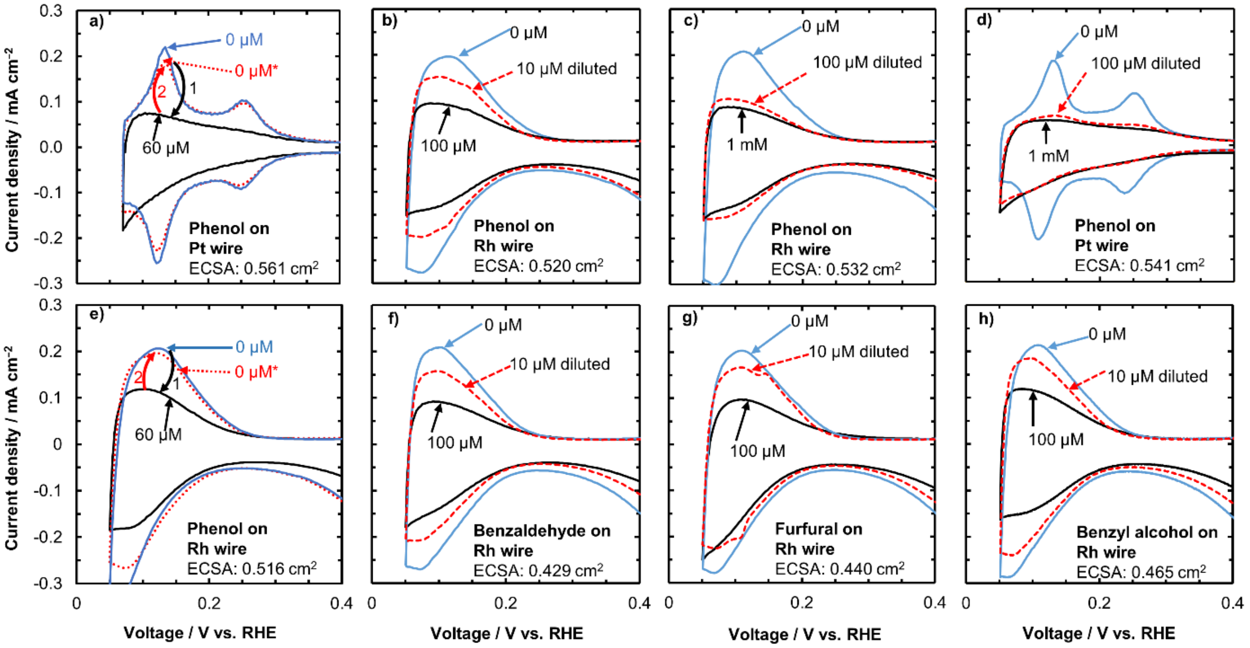

Appendix Figure A-4 Cyclic voltammograms showing reversibility. Cyclic voltammograms showing the reversibility of organic adsorption on rhodium and platinum after controlled dilution. **a)** Dilution from 60 µM phenol to 0 µM on Pt. **b)** Dilution from 100 µM phenol to 10 µM on Rh. **c)** Dilution from 1 mM phenol to 100 µM on Rh. **d)** Dilution from 1 mM phenol to 100 µM on Pt. **e)** Dilution from 60 µM phenol to 0 µM on Rh. **f)** Dilution from 100 µM benzaldehyde to 10 µM on Rh. **g)** Dilution from 100 µM furfural to 10 µM on Rh. **h)** Dilution from 100 µM benzyl alcohol to 10 µM on Rh. Supporting electrolyte is acetate buffer (pH 5), and the CV is obtained at 100 mV s^{-1} scan rate and 298 K. In **a** and **e**, step 1 (black arrow) represents phenol addition while step 2 (red arrow) represents dilution. 0 µM* the CV of the new solution is slightly different from 0 µM because of a small amount of phenol remaining in the cell after dilution.

In **Appendix Figure A-4**, the initial CV of the supporting electrolyte containing no organic is shown by a blue line, while CVs with 1 mM, 100 µM, or 60 µM organic in supporting electrolyte are indicated by a black line. The CV of the diluted organic(i.e., from 1 mM to 100 µM, 100 µM to 10 µM or 60 µM to 0 µM) is shown by a red dashed line. The phenol concentration in **Appendix Figure A-4a** and **Appendix Figure A-4e** was increased to 60 µM and the new cyclic voltammogram shows a drop in the H_{upd} charge compared to when no phenol is in the supporting electrolyte. When the 60 µM phenol solution is replaced with acetate buffer containing no phenol (without removing or recleaning the Pt or Rh wire), the H_{upd} charge is 97% and 99% recovered on Pt and Rh, respectively as adsorbed phenol desorbs reversibly from the metal (**Appendix Table A-3**). The reason the H_{upd} charge in **Appendix Figure A-4a** and **Appendix Figure A-4e** is incompletely recovered is because of small traces of phenol remaining in the electrochemical cell. For all cases, the CV of the diluted organic showed a higher H_{upd} charge compared to the initial concentration before dilution, and matched the CVs taken at the concentrations directly without diluting, as seen in the isotherms in **Figure 2-2** and **Figure 2-5**. This observation shows that organic adsorption/desorption is reversible in this potential window. The method of dilution is outlined in the main text.

A.5 Obtaining the Fraction of H_{upd} Inhibited and Organic Coverage from the Difference in H_{upd} Charge

The catalyst surface is covered by adsorbed hydrogen (H*) in acetate buffer electrolyte, whereas with an organic also present in solution there is competition with H* for adsorption sites, which manifests as a noticeable drop in measured H_{upd} charge. The fraction of H_{upd} inhibited because of organic adsorption is:

$$Fraction\ of\ H_{upd}\ inhibited = \frac{Q_{des}\ without\ organic - Q_{des}\ with\ organic}{Q_{des}\ without\ organic} \qquad \textbf{Eq. A-1}$$

Assuming this drop is only due to organic (e.g., phenol) adsorption, the fraction of H_{upd} inhibited is the coverage of organic $\theta_{organic}$ normalized to the fraction of H_{upd} inhibited at saturation. Thus $\theta_{organic} = 1$ is at complete saturation with organic and $\theta_{organic} = 0$ is when no organic is in solution.

$$\theta_{organic} = \frac{Q_{des}\ without\ organic - Q_{des}\ with\ organic}{Q_{des}\ without\ organic - Q_{des}\ with\ sat.organic} \qquad \textbf{Eq. A-2}$$

A.6 Fitting Experimental Adsorption Isotherm Data Using the Temkin Model

Here we describe the fitting of experimental adsorption isotherms for phenol, albeit this process is applicable to all the organics studied in this work. The adsorption of bulk phenol in solution ($Ph_{(aq)}$)

onto a free catalyst site available for phenol adsorption ($*$) to form an adsorbed phenol ($Ph\,*$) is shown by **Eq. A-3**:

$$Ph_{(aq)} + * \rightleftharpoons Ph\,* \qquad \textbf{Eq. A-3}$$

The equilibrium adsorption constant ($K^{aq}_{eq,ads,\theta}$) of **Eq. A-3** is shown in **Eq. A-4**:

$$K^{aq}_{eq,ads,\theta} = \frac{\theta_{Ph}}{C_{Ph}\theta_{*}} \qquad \textbf{Eq. A-4}$$

where C_{Ph} is the bulk concentration of phenol, θ_{Ph} is the coverage of phenol (we use *Ph* here for phenol, but could also represent other organics), and θ_{*} is the fraction of free sites. The bulk concentration of phenol is not changed upon adsorption in our experiments (**A.2**). In this H_{upd} method we assume that hydrogen can adsorb on the free sites, but not on the sites that phenol is adsorbed onto, therefore we can indirectly determine the phenol coverage using **Eq. A-5**:

$$\theta_{Ph} + \theta_{*} = 1 \qquad \textbf{Eq. A-5}$$

Combining **Eq. A-4** and **Eq. A-5** gives an adsorption isotherm (**Eq. A-6**), where the equilibrium adsorption constant is $K^{aq}_{eq,ads,\theta}$, with the subscript θ referring to the phenol coverage, included to indicate that the equilibrium adsorption constant may be dependent on phenol coverage because of adsorbate-adsorbate interactions.[93,94]

$$\frac{\theta_{Ph}}{\theta_{sat}} = \frac{K^{aq}_{eq,ads,\theta}\,C_{Ph}}{\left(1 + K^{aq}_{eq,ads,\theta}C_{Ph}\right)} \qquad \textbf{Eq. A-6}$$

where θ_{sat} is the saturation coverage. If we assume that the equilibrium adsorption constant follows a Temkin model, such that the free energy of adsorption changes linearly with coverage, then:

$$K^{aq}_{eq,ads,\theta} = \exp\left(\frac{-(\Delta G^{0}_{ads,aq,\theta=0} + \alpha\theta_{Ph})}{RT}\right) \qquad \textbf{Eq. A-7}$$

where α is a parameter with units of kJ mol^{-1} that represents the strength of adsorbate-adsorbate interactions, and $\Delta G^0_{ads,aq,\theta=0}$ is the adsorption free energy in kJ mol^{-1} at a phenol coverage of zero. **Eq. A-6** and **Eq. A-7** can be combined to give:

$$\theta_{Ph} = \frac{\exp\left(\frac{-(\Delta G^0_{ads,aq,\theta=0} + \alpha\theta_{Ph})}{RT}\right) C_{Ph}}{\left(1 + \exp\left(\frac{-\Delta G^0_{ads,aq,\theta=0} + \alpha\theta_{Ph})}{RT}\right) C_{Ph}\right)} \qquad \textbf{Eq. A-8}$$

Using the constructed adsorption isotherms of the coverage of phenol measured indirectly by the decrease in H$_{upd}$ charge as a function of the bulk phenol concentration, we can fit the data to **Eq. A-8** by varying the parameters of $\Delta G^0_{ads,aq,\theta=0}$ and α. For a two-site adsorption model, the saturation coverage for site 1 was chosen as the coverage where the isotherm first plateaus, whereas adsorption on site 2 begins at the organic concentration immediately above that which saturates site 1.

As discussed in the Experimental & Computational Methods section of the main text, our coverage measurements from the H$_{upd}$ technique are not at the potential of zero charge (PZC), or at a slightly cathodic potential where maximum coverage is achieved.[97] Nevertheless, coverages obtained here for phenol on Pt using the H$_{upd}$ method match closely to reported coverages obtained by radiotracer method at potentials close to the PZC,[119] corroborating the accuracy of H$_{upd}$ method.

A.7 Details on Free Energy Calculations and Adsorption Geometries of Organics on Several Model Facets of Pt and Rh

The gas-phase enthalpies and free energies of adsorption were calculated using ideal-gas statistical mechanics as implemented in the Atomic Simulation Environment Python library.[146] The enthalpies of gas-phase molecules ($H_{gas,R}$) were calculated at 298.15 K and consist of the electronic energy (*E*) at zero Kelvin, the zero point energy (E_{ZPE}), and the integral with temperature of the heat capacity at constant pressure (C_P).

$$H_{gas,R}(T) = E + E_{ZPE} + \int_0^T C_P dT$$

$$C_P = k_B + C_{V,trans} + C_{V,rot} + C_{V,vib} + C_{V,elec}$$

$$\int_0^T C_{V,vib} dT = \sum_i^{3N-6} \frac{\epsilon_i}{e^{\epsilon_i/k_B T} - 1}$$

$C_{V,trans}$ and $C_{V,rot}$ are both equal to $\frac{3}{2}k_B$ for a three-dimensional, nonlinear molecule. The ϵ_i represent energies of the $3N - 6$ vibrational modes of the molecules, where *N* is the number of atoms. The electronic contribution to the heat capacity, $C_{V,elec}$, is assumed to be zero. k_B is the Boltzmann constant.

The entropies of gas-phase molecules ($S_{gas,R}$) were calculated at *T* = 298.15 K and pressure (*P*) = 1 atm.

$$S_{gas,R}(T, P) = S_{trans} + S_{rot} + S_{vib} + S_{elec} - k_B \ln \frac{P}{P^\circ}$$

$$S_{trans} = k_B \left\{ \ln \left[\left(\frac{2\pi M k_B T}{h^2} \right)^{3/2} \frac{k_B T}{P^\circ} \right] + \frac{5}{2} \right\}$$

$$S_{rot} = k_B \left\{ \ln \left[\frac{\sqrt{\pi I_A I_B I_C}}{\sigma} \left(\frac{8\pi^2 k_B T}{h^2} \right)^{3/2} \right] + \frac{3}{2} \right\}$$

$$S_{vib} = k_B \sum_i^{3N-6} \left[\frac{\epsilon_i}{k_B T (e^{\epsilon_i/k_B T} - 1)} - \ln\left(1 - e^{-\epsilon_i/k_B T}\right) \right]$$

$$S_{elec} = k_B \ln[2 \times (total\ spin) + 1]$$

Here M is mass of the molecule, I_i are the moments of inertia, σ is the symmetry factor, h is Planck's constant, and $P°$ is the standard pressure (1 atm). $\sigma = 1$ is used for organics and $\sigma = 2$ is used for water.

The internal energies of adsorbed molecules were calculated in the harmonic limit by treating all *3N* degrees of freedom as vibrations. Internal energy and enthalpy are related by $H(T) = U(T) + PV$. The PV term was assumed to be small, therefore the enthalpies were assumed to be approximately equal to the calculated internal energies.

$$H_{gas,R/M}(T) \approx U(T) = E + E_{ZPE} + \sum_{i}^{3N} \frac{\epsilon_i}{e^{\epsilon_i/k_B T} - 1}$$

The enthalpies and Gibb's free energies of metal surfaces were assumed to be equal to the electronic energies at 0 K ($E_{gas,M}$) predicted by DFT. Therefore, the enthalpy of adsorption in the gas phase at 298.15 K was calculated as $\Delta H^0_{ads,gas,R/M} = H_{gas,R/M} - H_{gas,R} - E_{gas,M}$ where $H_{gas,R/M}$ is the enthalpy of gas-phase organic *R* on metal *M*. The Gibb's free energy of adsorption in the gas phase was calculated as $\Delta G^0_{ads,gas,R/M} = \Delta H^0_{ads,gas,R/M} - T\Delta S^0_{ads,gas,R/M}$. The standard change in entropy of the organics upon adsorption in gas phase ($\Delta S^0_{ads,gas,R/M}$) was calculated the same way as for our experimental measurements using the correlation described in **Eq. A-11** (see **A.9**). Here, we assume the entropies of adsorption in the aqueous phase ($\Delta S^0_{ads,aq,gas,R/M}$) are the same as in the gas phase and that the entropy associated with displacing water from the surface is zero.

The enthalpies of adsorbed molecules in the aqueous phase using implicit solvent were obtained using VASPsol ($E_{VASPsol}$) and thermodynamic corrections based on vibrational frequencies of the adsorbed molecule in the gas phase. The energy from VASPsol includes the free energy associated with solvating the organic molecule and the metal surface.

$$H_{aq,R/M}(T) \approx U(T) = E_{VASPsol} + E_{ZPE} + \sum_{i}^{3N} \frac{\epsilon_i}{e^{\epsilon_i/k_B T} - 1}$$

The enthalpy of adsorption in the aqueous phase relative to the gas-phase organic molecule was calculated as $\Delta H^0_{ads,aq,gas,R/M} = H_{aq,R/M} - H_{gas,R} - E_{aq,M}$, where $H_{aq,R/M}$ is the enthalpy of aqueous organic *R* on metal *M* and $E_{aq,M}$ is the electronic energy of the solvated metal surface at 0 K. The free energy of adsorption in the aqueous phase relative to the gas-phase organic was calculated as $\Delta G^0_{ads,aq,gas,R/M} = \Delta H^0_{ads,aq,gas,R/M} - T\Delta S^0_{ads,gas,R/M}$. As discussed in the main text, where it is clear what *R* and *M* refer to, the *R/M* term is omitted.

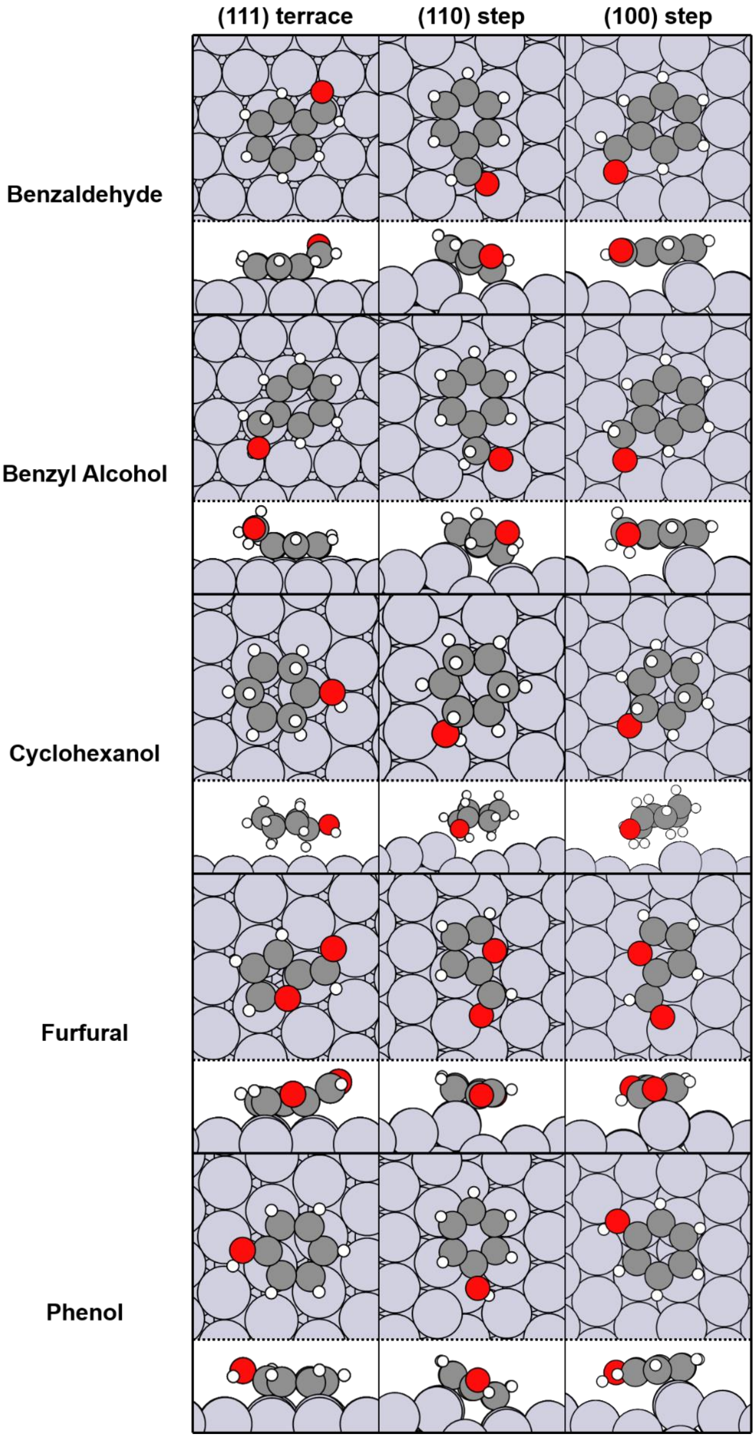

Appendix Figure A-5 DFT geometries of phenol, benzaldehyde, benzyl alcohol, furfural, and cyclohexanol on Pt. Top and side view geometries of adsorbed species studied here on the (111) terrace and the (110) and (100) steps of platinum in gas phase. The (110) and (100) steps were modeled using the (553) and (533) surfaces, respectively.

Appendix Figure A-5 shows the adsorption geometries of the organics on Pt facets. On the Pt(111) terrace, benzaldehyde and phenol adsorb with the centroid of the ring above the bridge site with 30° rotation (bridge30), which is consistent with previous studies.[26,29] Benzyl alcohol also adsorbs in the bridge30 configuration. Cyclohexanol adsorbs with both the alkane ring and the alcohol group above a three-fold hollow site. Furfural adsorbs with the ring above a three-fold hollow site with the ring oxygen above a bridge site, consistent with previous studies.[249] On the Pt(110) step, benzaldehyde, benzyl alcohol, and phenol adsorb with the aromatic ring above the four-fold hollow site of the step and the functional group at the step edge. Cyclohexanol adsorbs with the alcohol group at the step edge. Furfural adsorbs with the ring above the three-fold hollow site of the step and the aldehyde group at the step edge. On the Pt(100) step, benzaldehyde, benzyl alcohol, cyclohexanol, and phenol adsorb with the rings above the four-fold hollow site of the step and the functional groups above the three-fold hollow site of the terrace. Furfural adsorbs with the ring above the four-fold hollow site of the step and the aldehyde group at the step edge.

Appendix Figure A-6 shows that benzaldehyde and benzyl alcohol adsorb on Rh(111) in the same configurations as on Pt(111). Cyclohexanol, however, adsorbs with the center of the ring above the bridge site with the alcohol group above an atop site and furfural adsorbs above a three-fold hollow site with the oxygen of the ring above an atop site. Phenol adsorbs in the bridge30 configuration, consistent with what has been previously reported.[26] All organics adsorb on the Rh(110) step in the same configurations as on the Pt(110) step. On the Rh(100) step, benzaldehyde and phenol adsorb at the step edge. Benzyl alcohol adsorbs with the aromatic ring above the four-fold hollow site and the alcohol group above a three-fold hollow site on the terrace below the step. Cyclohexanol adsorbs with the alcohol at the step edge and the ring above an atop site on the terrace below the step. Furfural adsorbs with the ring above the four-fold hollow site and the aldehyde group at the step edge.

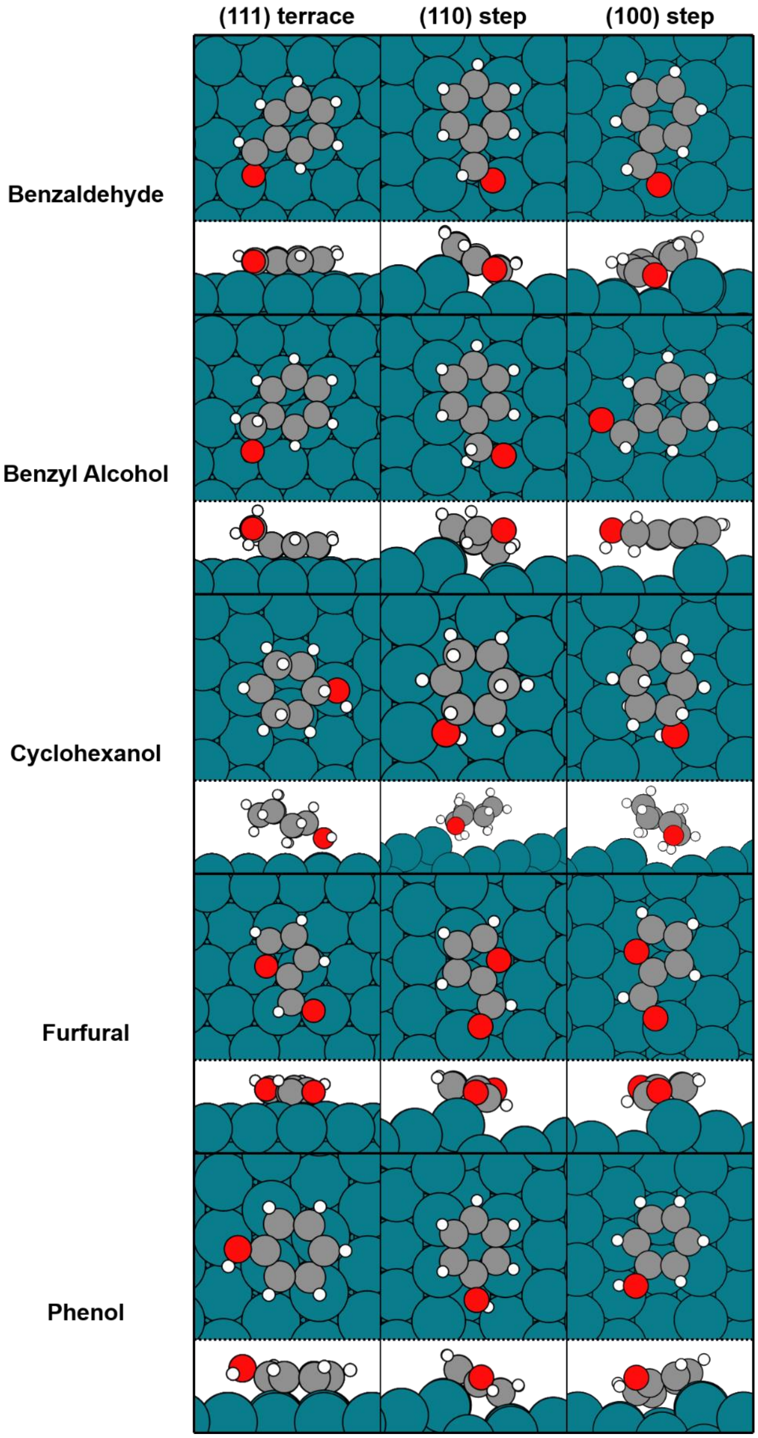

Appendix Figure A-6 DFT geometries of phenol, benzaldehyde, benzyl alcohol, furfural, and cyclohexanol on Rh. Top and side view geometries of adsorbed species studied here on the (111) terrace, (110) step, and (100) step of rhodium in gas phase. The (110) and (100) steps were modeled using the (553) and (533) surfaces, respectively.

A.8 Calculated Gas-Phase and Aqueous-Phase Adsorption Energies of Organics and Water

Adsorption energies from DFT using PBE-D3 for the organic molecules studied here as well as water are summarized in **Appendix Table A-4**. The ‘Gas Phase’ and ‘Implicit Solvent’ calculations were done as described in **A.7**, and the ‘Bond Additivity’ calculations were done using the gas phase values as described in **A.11**.

Appendix Table A-4 DFT-predicted adsorption energies. DFT-predicted electronic energy (ΔE), enthalpy (ΔH) and Gibb’s free energy (ΔG) of adsorption for benzaldehyde, benzyl alcohol, cyclohexanol, furfural, and phenol on the (111) terrace, (110) step, and (100) step facets of platinum and rhodium.

Benzaldehyde									
Metal	Facet	Gas Phase			Implicit Solvent			Bond Additivity	
		ΔE	ΔH	ΔG	ΔE	ΔH	ΔG	ΔH	ΔG
Platinum	(111) terrace	−225	−226	−188	−255	−256	−218	−94	−57
	(110) step	−281	−286	−248	−302	−307	−269	−121	−85
	(100) step	−257	−256	−218	−280	−279	−241	−40	−2
Rhodium	(111) terrace	−312	−317	−279	−326	−331	−293	−112	−75
	(110) step	−322	−333	−295	−333	−344	−306	−124	−88
	(100) step	−281	−292	−254	−288	−299	−261	40	80
Benzyl Alcohol									
Metal	Facet	Gas Phase			Implicit Solvent			Bond Additivity	
		ΔE	ΔH	ΔG	ΔE	ΔH	ΔG	ΔH	ΔG
Platinum	(111) terrace	−250	−253	−213	−274	−277	−238	−128	−89
	(110) step	−300	−310	−270	−319	−329	−289	−159	−119
	(100) step	−282	−283	−243	−300	−301	−262	−80	−40
Rhodium	(111) terrace	−288	−293	−254	−303	−309	−270	−104	−64
	(110) step	−296	−310	−271	−310	−323	−284	−114	−75
	(100) step	−274	−279	−240	−287	−292	−253	40	79
Cyclohexanol									
Metal	Facet	Gas Phase			Implicit Solvent			Bond Additivity	
		ΔE	ΔH	ΔG	ΔE	ΔH	ΔG	ΔH	ΔG
Platinum	(111) terrace	−121	−128	−90	−137	−144	−106	−24	15
	(110) step	−136	−146	−107	−147	−157	−119	3	33
	(100) step	−122	−129	−91	−137	−145	−106	72	110
Rhodium	(111) terrace	−122	−124	−85	−129	−136	−98	65	104
	(110) step	−157	−159	−121	−174	−177	−139	34	73
	(100) step	−126	−135	−97	−133	−142	−104	182	221

Furfural

Metal	Facet	Gas Phase			Implicit Solvent			Bond Additivity	
		ΔE	ΔH	ΔG	ΔE	ΔH	ΔG	ΔH	ΔG
Platinum	(111) terrace	−176	−170	−133	−202	−195	−159	−92	−56
	(110) step	−250	−251	−214	−271	−272	−235	−95	−59
	(100) step	−241	−242	−205	−264	−264	−228	−34	3
Rhodium	(111) terrace	−239	−244	−207	−256	−261	−224	−66	−29
	(110) step	−286	−288	−251	−302	−303	−267	−88	−51
	(100) step	−286	−287	−251	−299	−301	−264	36	73

Phenol

Metal	Facet	Gas Phase			Implicit Solvent			Bond Additivity	
		ΔE	ΔH	ΔG	ΔE	ΔH	ΔG	ΔH	ΔG
Platinum	(111) terrace	−215	−217	−181	−244	−246	−210	−76	−40
	(110) step	−286	−289	−253	−301	−304	−268	−130	−94
	(100) step	−262	−262	−226	−280	−280	−244	−51	−14
Rhodium	(111) terrace	−261	−267	−231	−277	−284	−247	−60	−24
	(110) step	−281	−290	−253	−290	−298	−262	−86	−49
	(100) step	−253	−261	−225	−262	−270	−233	67	103

Water

Metal	Facet	Gas Phase			Implicit Solvent			Bond Additivity	
		ΔE	ΔH	ΔG	ΔE	ΔH	ΔG	ΔH	ΔG
Platinum	(111) terrace	−44	−39	0	−78	−72	−47	N/A	N/A
	(110) step	−74	−69	−43	−109	−104	−78	N/A	N/A
	(100) step	−58	−52	−27	−106	−100	−74	N/A	N/A
Rhodium	(111) terrace	−55	−52	−27	−85	−82	−57	N/A	N/A
	(110) step	−80	−75	−50	−103	−98	−72	N/A	N/A
	(100) step	−76	−71	−45	−100	−95	−69	N/A	N/A

All adsorption energies in **Appendix Table A-4** are with respect to gas phase molecules (e.g. ΔH is $\Delta H^{0}_{ads,aq,gas,R/M}$). All enthalpies and free energies are calculated at 298.15 K and 1 atm. Entropy of adsorption is calculated using the correlation (**Eq. A-11**) described by Campbell and Sellers.[121]

A.9 Converting from Aqueous Free Energies of Adsorption to Aqueous Enthalpies of Adsorption

The process outlined in **Scheme A-1** is used to convert from aqueous-phase free energies of adsorption obtained from fits to the experimental isotherms in **Figure 2-2** and **Figure 2-5** to aqueous-phase enthalpies of adsorption is the same as that used in ref [28]. The process consists of three steps, i) converting the organic aqueous equilibrium adsorption constant ($K_{eq,ads,\theta}^{aq}$) to the free energy of adsorption of the gas-phase organic in aqueous phase ($\Delta G_{ads,aq,gas,\theta}^{0}$) using Henry's law constant, K_H , ii) converting to the enthalpy of adsorption of the gas-phase organic using an estimate of the adsorption entropy,[121] and iii) converting to the enthalpy of adsorption of the aqueous-phase organic by subtracting the organic enthalpy of solvation. The value of $\Delta H_{ads,aq,gas,\theta}^{0}$ determined through this method can be directly compared to the calculated values discussed in **A.7** and the value of $\Delta H_{ads,aq,\theta}^{0}$ can be directly compared to values from solution calorimetry.

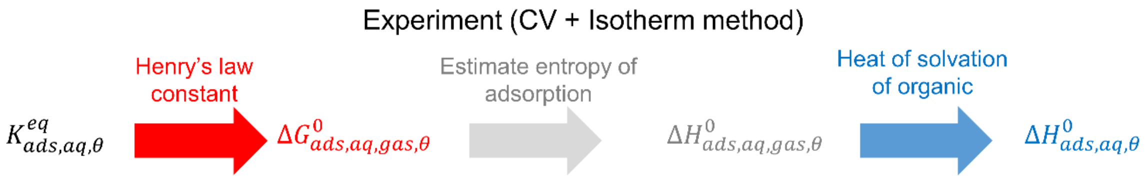

Scheme A-1 Estimating enthalpies from CV. Outlined procedure of estimating the aqueous phase adsorption enthalpies from CV method and isotherms.

The values used for the three steps outlined in **Scheme A-1** are shown in **Appendix Table A-5**. The Henry's law constant, K_H, at 298.15 K for each individual organic in water is used to convert the aqueous adsorption constant to the equilibrium constant and thus free energy of adsorption) of a gas-phase organic relative to the adsorbed organic in the aqueous phase according to **Eq. A-9**.

$$K_{eq,ads,aq,\theta}^{gas} = K_{eq,ads,\theta}^{aq}/K_H = e^{\frac{-\Delta G_{ads,aq,gas,\theta}^{0}}{RT}} = e^{\frac{-\Delta H_{ads,aq,gas,\theta}^{0}}{RT}} e^{\frac{\Delta S_{ads,aq,gas}^{0}}{R}} \qquad \textbf{Eq. A-9}$$

The enthalpy of adsorption of the gas-phase organic relative to the adsorbed organic in aqueous phase is estimated by assuming an entropy of adsorption from the correlation in ref [121]. This correlation uses gas-phase entropies to predict adsorption entropies. For molecules where the gas-phase entropies were not tabulated we used entropies calculated by ideal gas statistical mechanics.

Appendix Table A-5 Enthalpies of solvation. Henry's law constant (K_H) at 298.5 K, gas-phase entropy, and enthalpy of solvation (ΔH_{Solv}) for molecules studied in this work.

Molecule	Henry's law constant (bar M^{-1})	Gas phase entropy (J mol^{-1} K^{-1})	ΔH_{Solv} (kJ mol^{-1})
Phenol	5.0×10^{-4} from ref [250]	314.8 from ref [251] 313.5 *	−50.0 from ref [252]
Benzaldehyde	2.6×10^{-2} from ref [250]	334.1 *	−42.2 from ref [253]
Furfural	3.86×10^{-3} from ref [254]	318.4 *	−58.0 from refs [250,255]
Benzyl alcohol	1.1×10^{-4} from ref [250]	347.9 *	−66.9 from ref [256]
Cyclohexanol	5.9×10^{-3} from ref [250]	353.83 from ref [251] 339.7 *	−70.7 from ref [257]

* Values calculated in this work by ideal gas statistical mechanics.

The heat of solvation ($-\Delta H_{Solv}$) of a given organic was obtained either directly from references or by applying the van't Hoff equation (**Eq. A-10**) and using the reported temperature dependence of the Henry's law constant. ΔH_{Solv} was subtracted from the gas-phase adsorption enthalpy to obtain the adsorption enthalpy of the solvated organic.

$$\frac{d\ln K_H}{d\left(\frac{1}{T}\right)} = \frac{-\Delta H_{Solv}}{R} \qquad \textbf{Eq. A-10}$$

To clarify, we show an example of how the aqueous-phase adsorption enthalpies were estimated. The procedure is outlined in greater detail in the Appendix of ref [28]. From fitting the adsorption isotherm for Rh (**Figure 2-2**), the aqueous phase equilibrium constant for phenol on site 1 was $K_{eq,ads,\theta}^{aq} = 37{,}600$ (unitless), where the assumed standard state coverage is $\theta^0 = 0.5$. To obtain the adsorption equilibrium constant in aqueous phase relative to gas phase phenol, $K_{eq,ads,aq,\theta}^{gas}$, we used the Henry's law constant K_H:

$$K_{eq,ads,aq,\theta}^{gas} = \frac{K_{eq,ads,\theta}^{aq}}{K_H} = \frac{37{,}600}{5\times10^{-4}} = 7.52\times10^{7}$$

To be consistent with our previous work in ref [28] we next shift the standard state coverage to $\theta^0 = 0.054$ before making an approximation of the entropy of adsorption to determine enthalpies. We use a standard state coverage of $\theta^0 = 0.054$ for phenol on Pt(111), which is calculated as outlined in ref [258] using the atomic surface density of Pt(111) and the saturation coverage of phenol on Pt(111).[65] This value of θ^0 is thus specifically for Pt(111) with phenol based on previous experimental measurements, but we use it for all systems here (including Rh) despite the slight differences in the saturation coverage and number of metal atoms per cm^2.

$$K_{eq,ads,aq,\theta=0.054}^{gas} = \frac{K_{eq,ads,\theta}^{aq}}{\frac{\theta^0}{1-\theta^0}K_H} = \frac{37{,}600}{\frac{0.054}{1-0.054}5 \times 10^{-4}} = 1.32 \times 10^9$$

The entropy correlation from ref [121] is used to estimate the aqueous-phase adsorption entropy using gas-phase organic entropy. We assume that the adsorbed organic entropy is the same in the aqueous phase as it would be in the gas phase assuming there is no entropy change in displacement of the water adlayer. Our DFT-predicted adsorption entropies also use this correlation in **Eq. A-11**.

$$\Delta S_{ad,aq,gas}^0 = S_{ad}^0 - S_{gas}^0 = \left(0.70S_{gas}^0 - 3.3R\right) - S_{gas}^0 = -\left[0.30S_{gas}^0 + 3.3R\right] \qquad \textbf{Eq. A-11}$$

where R is the gas constant = 8.314 J mol^{-1} K^{-1}, S_{gas}^0 is the standard gas-phase entropy of the organic (phenol in this case), S_{ad}^0 is the standard adsorbate entropy, and $\Delta S_{ad,aq,gas}^0$ is the entropy of the adsorbed solvated organic relative to gas phase.

For phenol, S_{gas}^0 = 314.8 J mol^{-1} K^{-1} = (38 R) from ref [251]. Therefore, we can calculate the entropy of adsorption of gas-phase phenol onto Rh in the aqueous phase by:

$$\Delta S_{ad,aq,gas}^0 = -[0.30 \times 38R + 3.3R] = -14.7R$$

Using the estimated entropy of adsorption, we convert the equilibrium constant of adsorption for gas-phase phenol onto aqueous Rh into an enthalpy of adsorption. Note that the entropy of adsorption is calculated using $\theta^0 = 0.054$, and would be shifted by 2.5 R if instead we reported at $\theta^0 = 0.5$ as discussed in ref [28,258]. The resulting enthalpies at obtained using $\theta^0 = 0.054$ are those reported in **Table 2-1**.

$$\Delta H^0_{ads,aq,gas,\theta=0.054} = T\Delta S^0_{ads,aq,gas} - RT\ln K^{gas}_{eq,ads,aq,\theta=0.054}$$

$$= T(-14.7R) - RT\ln K^{gas}_{eq,ads,aq,\theta=0.054}$$

$$= RT[-14.7 - \ln K^{gas}_{eq,ads,aq,\theta=0.054}]$$

$$= 8.314\frac{J}{mol\,K} \times 298.15\,K \times [-14.7 - \ln[1.32 \times 10^9]]$$

$$\Delta H^0_{ads,aq,gas,\theta=0.054} = -88.6\,kJ\,mol^{-1}$$

To estimate the aqueous phase adsorption enthalpy of phenol, we subtract the enthalpy of solvation ΔH_{Solv} listed in **Appendix Table A-1**, which for phenol is −50 kJ mol^{-1}.

$$\Delta H^0_{ads,aq,\theta=0.054} = \Delta H^0_{ads,aq,gas,\theta=0.054} - \Delta H_{Solv}$$

$$\Delta H^0_{ads,aq,\theta=0.054} = -88.6\,kJ\,mol^{-1} - (-50)\,kJ\,mol^{-1} = -38.6\,kJ\,mol^{-1}$$

A.10 Reversibility of Hydrogen Underpotential Deposition in the Presence of Furfural

The H_{upd} adsorption/desorption region on Pt and Rh in acetate buffer with increasing furfural concentration was not reversible (**Figure 2-4b**) as opposed to the other organics tested here. The data in **Appendix Figure A-7** shows the adsorption (Q_{ads}) and desorption (Q_{des}) charges at different furfural concentrations. At low furfural concentrations, Q_{ads} is close to that of Q_{des} indicating H* is completely desorbed in the oxidative scan in the underpotential region (0.05 V to 0.35 V). However, at high furfural concentrations Q_{des} is lower than Q_{ads}, indicating that some H* is not desorbed in the oxidative scan. One possibility is that the H* reacts with a co-adsorbed species (such as furfural, or an adsorbed furfural fragment). If this reaction of H* with the adsorbed organic species is a catalytic reaction (i.e., one where multiple turnovers occur), the amount of H* that is reacted which would not be counted during desorption would increase proportionally with increasing time. That is, normalizing the amount of unrecovered charge to the time should result in a constant value (equivalent to a turnover frequency).

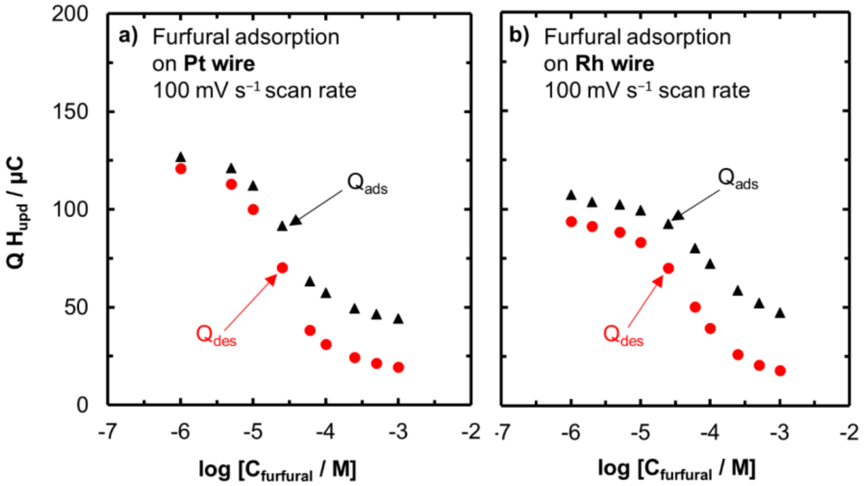

Appendix Figure A-7 Adsorption and desorption charge in the presence of furfural. The H_{upd} adsorption charge (Q_{ads}) and desorption charge (Q_{des}) on **a)** Pt and **b)** Rh as a function of furfural concentration. Charges are calculated from **Figure 2-4b** in the same way as described for **Appendix Figure A-2**. The initial higher adsorption charge Q_{ads} for Rh is because of the Rh oxide reduction peak being convoluted into the H_{upd} reduction peak. The lack of reversibility of the H_{upd} charge is seen for furfural on both metals.

We show that the irreversibility of H_{upd} in the presence of furfural is not due to a catalytic reaction with H* because at lower scan rates (i.e., at longer times spent in the H_{upd} potential) there is no proportional increase in the loss of H*. The data in **Appendix Figure A-8a** and **Appendix Figure A-8b** shows the fraction of total H_{upd} on Pt and Rh that is not recovered at different scan rates. For all the scan rates, the unrecovered charge increases with furfural concentration. In **Appendix Figure A-8c** and **Appendix Figure A-8d**, we normalize this fraction to the average time that a hydrogen adatom spends on the metal surface during the scan, estimated as half of the total time during the H_{upd} region ($t_{ave} = V_{H_{upd}}$ / scan rate), where $V_{H_{upd}}$ is the H_{upd} potential window (0.3 V, from the 0.05 V–0.35 V window in the CVs). If the unrecovered reduction charge was due to a catalytic reaction of furfural with adsorbed hydrogen, it would be proportional to the amount of time spent in the region where hydrogen and furfural are coadsorbed, i.e., at slower scan rates (longer times) the amount of unrecovered charge would be larger. If this were the case, normalizing to the reaction time would result in equal values at different scan rates. Because the results in **Appendix Figure A-8c** and **Appendix Figure A-8d** show that there is a large scan rate dependence on this term, it implies there is no turnover reaction occurring, but rather a set amount of charge is not recovered, essentially independent of the scan rate. Possible reasons for this irreversibility are that (i) furfural is partially being hydrogenated in the short scan time within the H adsorption region (0.05 V–0.35 V), but not turning over (i.e., furfural is partially hydrogenated, but remains adsorbed on the surface and does not go onto further products and desorb), (ii) the reaction time is insufficient for a turnover to occur, or (iii) furfural when adsorbed is decarbonylated,[128] to form a furyl intermediate and CO*, and then one of these species is irreversibly reduced/hydrogenated during the cathodic scan.

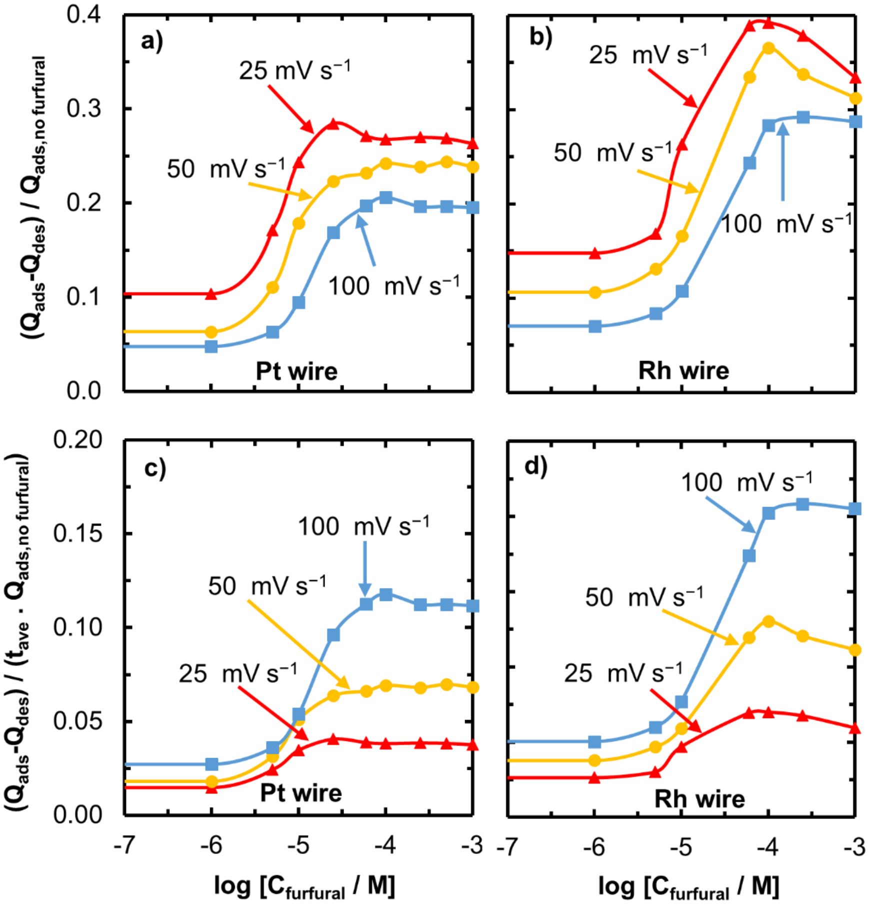

Appendix Figure A-8 Irreversibility of furfural adsorption. Fraction of unrecovered H* (or electrons) in the desorption region $(Q_{ads} - Q_{des})/Q_{ads,no\ furfural}$ as a function of furfural concentration at 25, 50 and 100 mV s^{-1} scan rates on **a)** a Pt wire and **b)** Rh wire. The data in **Appendix Figure A-7** is used for the 100 mV s^{-1} plots. The fraction of unrecovered H* from a) and b) normalized to the average scan time as a function of furfural concentration for 25, 50, and 100 mV s^{-1} on **c)** Pt wire and **d)** Rh wire. Here $t_{ave} = V_{H_{upd}}$/scan rate.

The adsorption information for furfural on Pt is shown in **Appendix Figure A-9**. As a note, although we report this as adsorption energies for furfural, recent reports indicate that furfural may not be adsorbed molecularly on Pt.[128] Although those studies were in more acidic conditions (pH = 1 rather than pH = 5 here) and higher furfural concentrations (100 mM vs. maximum of 1 mM here), there is evidence of low temperature furfural decarbonylation on Pt[259–261] that indicates the adsorbed species we are probing here may be a furfural fragment, rather than furfural itself.

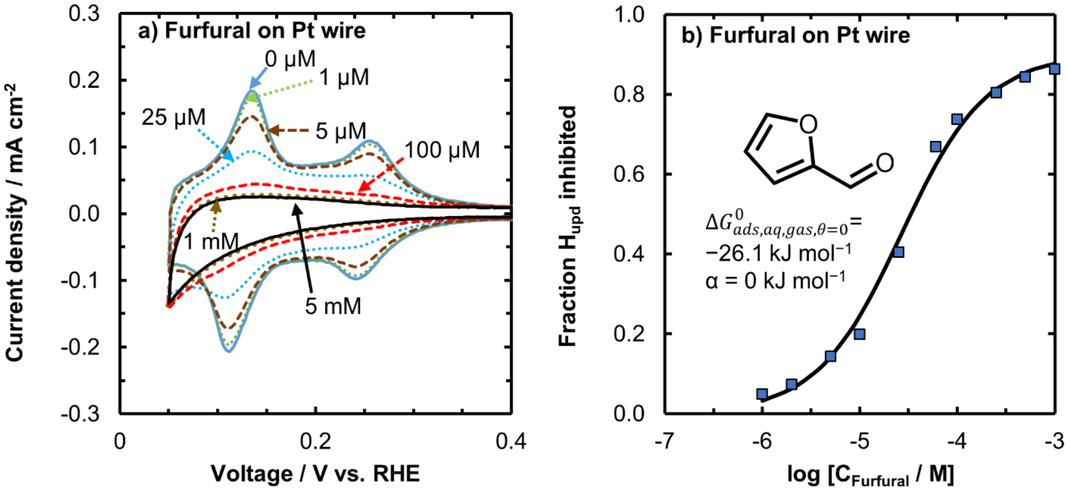

Appendix Figure A-9 Cyclic voltammograms in presence of furfural. **a)** Cyclic voltammograms showing the H_{upd} region at different bulk furfural concentrations on Pt wire. **b)** Fraction of H_{upd} inhibited by furfural from the cyclic voltammograms in a) as a function of furfural concentration to construct an adsorption isotherm of furfural on Pt wire. The isotherm fit using a Temkin adsorption model is indicated by the black line.

A.11 Saturation Coverage & Number of Displaced Waters in Bond-Additivity Model

In this section we discuss how to estimate the number of waters displaced upon adsorption of an organic molecule, *n*, onto a metal surface, which is integral to using the bond-additivity model[63] to correct between gas-phase and aqueous-phase adsorption energies. To do this, we assume that the number of water molecules displaced can be found by multiplying the inverse of the saturation coverage of the organic (the inverse being the number of atoms of surface metal per organic molecule) by the saturation coverage of water (number of water molecules per atom of surface metal). The saturation coverage of water on Pt(111) is assumed to be 0.72 monolayer (ML) based on previous work.[63,64] Water coverages are unknown on the other surfaces considered in this work, so we assume them to be the same as that of the Pt(111) terrace. As discussed in the methods of the main text, phenol on Pt(111) in the aqueous phase is thought to adsorb in regions where the local saturation is equal to the saturation coverage of 1/9 ML.[108] Thus, the value of n for phenol on Pt(111) is:

$$n = \frac{1}{\left(\frac{1\ molecule\ phenol}{9\ surface\ Pt\ atoms}\right)} \times \frac{0.72\ molecules\ water}{1\ surface\ Pt\ atoms} = \frac{6.5\ molecules\ water}{1\ molecule\ phenol}$$

To test whether we can computationally reproduce the experimental saturation coverage of phenol on Pt(111) in water, we study the aqueous-phase adsorption energies as a function of coverage using the bond-additivity model. The gas-phase adsorption energy of phenol was calculated at 1/16 ML, 1/9 ML, and 1/4 ML coverage, and each coverage was treated as saturation in the aqueous-phase. Specifically, 11.5, 6.5, and 2.9 water molecules were assumed to be displaced at each of the three coverages, respectively. The coverage corresponding to the maximum heat of adsorption was assumed to be the true saturation coverage and was used in subsequent applications of the bond-additivity model. The data in **Appendix Figure A-10a** for phenol agrees with the experimentally measured phenol coverage, with a maximum aqueous heat of adsorption occurring at 1/9 ML phenol. The local coverage of benzaldehyde and benzyl alcohol in the aqueous phase is unknown, but because phenol, benzaldehyde, and benzyl alcohol are similar in size and all have a phenyl group, the saturation coverage of benzaldehyde and benzyl alcohol is assumed to be the same as that of phenol. The coverage of cyclohexanol was also assumed to be the same as phenol. Furfural differs from the other aromatic molecules in that it does not have a phenyl group. Saturation coverage and water displacement were studied using the above approach for furfural on Pt(111). **Appendix Figure A-10b** shows furfural adsorbs the strongest in the aqueous phase at 3/16 ML coverage, displacing 3.8 water molecules upon adsorption.

The coverage of phenol and furfural on Pt(110) steps in the aqueous phase is unknown experimentally, so it was explored using the bond-additivity model. Because the size of the Pt(110) terrace is simpler to vary compared to the step, coverage dependence of phenol adsorption was explored on the terrace. Saturation coverage and number of displaced waters for phenol and furfural on the (110) terrace were assumed to be the same on the step. **Appendix Figure A-10c** and **Appendix Figure A-10d** show that heats of adsorption of phenol and furfural both reach maxima at 1/6 ML coverage. Therefore, 1/6 ML coverage and 4.3 displaced waters were chosen for the bond-additivity model for Pt(110).

As with the (110) step, the coverage of phenol and furfural is not known experimentally on the Pt(100) step. Saturation coverage and number of displaced waters were estimated on the step by modeling the Pt(100) terrace. **Appendix Figure A-10e** shows that the heat of adsorption of phenol in the aqueous phase reaches a maximum at 1/9 ML coverage. At this coverage, 6.5 water molecules are assumed to be displaced by the adsorbing organic. **Appendix Figure A-10f** shows that the heat of adsorption of furfural in the aqueous phase reaches a maximum at 3/16 ML, corresponding to 3.8 displaced water molecules.

The organic saturation coverages and number of water molecules displaced on the (111) terraces as well as the (110) and (100) steps of Pt and Rh are summarized in **Appendix Table A-6.** We find that all organics excluding furfural adsorb at 1/9 ML coverage on (111) terrace and (100) step surfaces and displace 6.5 water molecules. Furfural adsorbs at a higher coverage (3/16 ML) and therefore displaces fewer waters (3.8 molecules). On the (110) surfaces, all molecules are found to adsorb at 1/6 ML coverage and displace 4.3 water molecules.

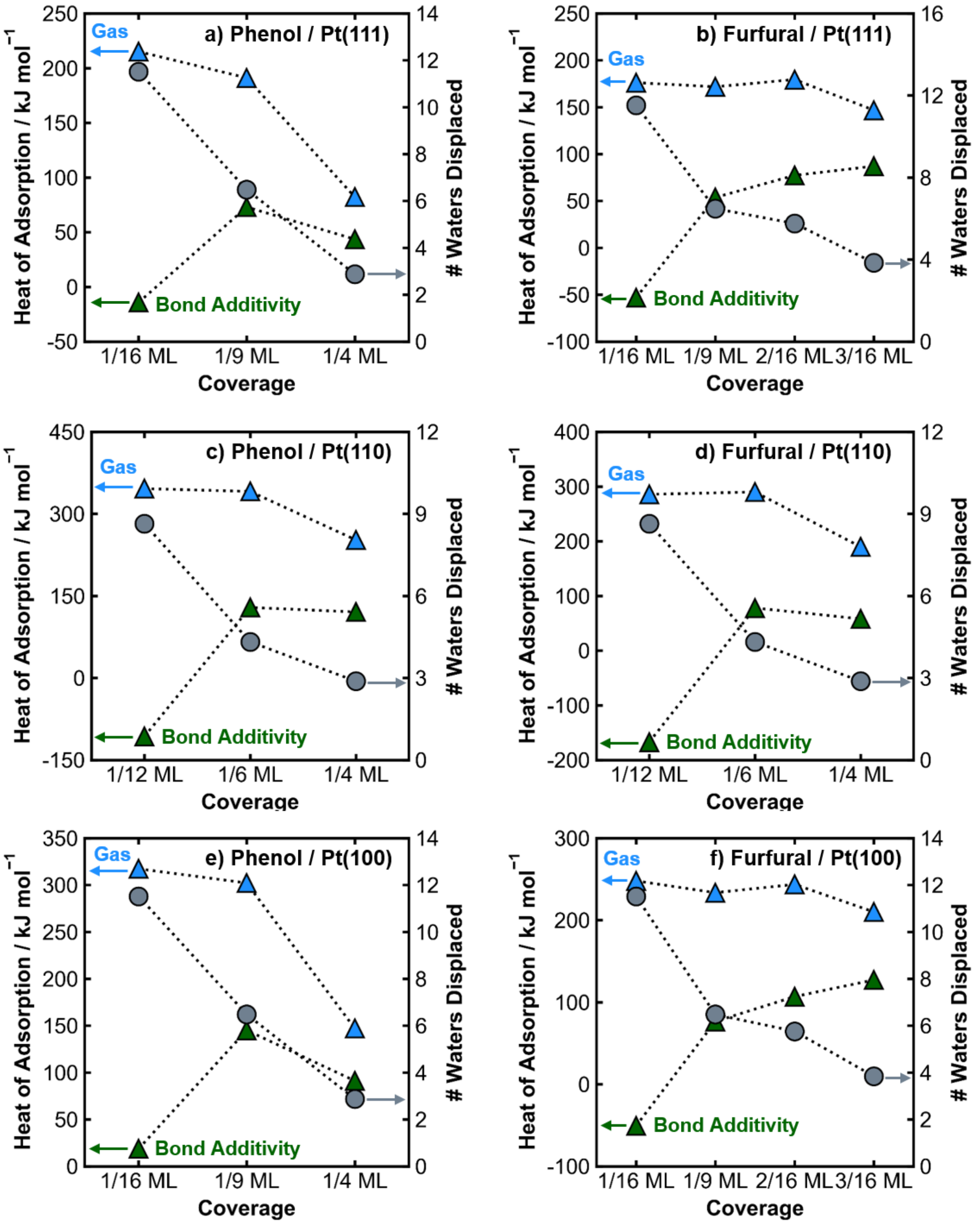

Appendix Figure A-10 Heats of adsorption as a function of organic coverage. **a)** Cyclic voltammograms showing the H_{upd} region at different bulk furfural concentrations on Pt wire. **b)** Fraction of H_{upd} inhibited by furfural from the cyclic voltammograms in a) as a function of furfural concentration to construct an adsorption isotherm of furfural on Pt wire. The isotherm fit using a Temkin adsorption model is indicated by the black line.

Saturation coverage is not known for either water or the organics on any of the rhodium surfaces. Here, we assume that the saturation coverages calculated for platinum are the same for rhodium. The gas phase adsorption enthalpies of all organics on Pt(111) and Rh(111) were calculated at saturation coverage for the bond-additivity model. A coverage of 1/9 ML on the (111) surface was achieved by modeling a 3×3 slab consisting of 9 surface atoms and 4 atomic layers. A coverage of 3/16 ML on the (111) surface was achieved by co-adsorbing three organics on a 4×4 slab consisting of 16 surface atoms and 4 atomic layers. A 5×5×1 Monkhorst-Pack *k*-point grid was used for 3×3 slabs, and a 3×3×1 Monkhorst-Pack *k*-point grid was used for 4×4 slabs.

The coverage dependence of adsorption on the steps is computationally demanding to explore due to the presence of both terrace and step features on the surfaces used to model the steps. Therefore, the adsorption enthalpy at 1/16 ML coverage was used in the bond-additivity model for all organics on the (110) and (100) steps. The number of water molecules displaced from the steps was estimated by calculating the saturation coverage of the organic on the corresponding terrace. A coverage of 1/6 ML on the (110) terrace was achieved by modeling a 2×3 slab consisting of 6 surface atoms and 5 atomic layers. A coverage of 1/9 ML on the (100) terrace was achieved by modeling a 3×3 slab consisting of 9 surface atoms and 4 atomic layers. A 5×5×1 Monkhorst-Pack *k*-point grid was used for 2×3 slabs and 3×3 slabs. A coverage of 3/16 ML was achieved on the (100) terrace by co-adsorbing 3 molecules onto a 4×4 surface consisting of 16 surface atoms and 4 atomic layers. A 3×3×1 Monkhorst-Pack *k*-point grid was used for 4×4 slabs. **Appendix Table A-6** summarizes the saturation coverages and numbers of displaced water molecules used in the bond additivity model.

Appendix Table A-6 Saturation coverages of organics. Saturation coverage (θ_{sat}) of organic and number of water molecules displaced used to calculate the aqueous heat of adsorption using the bond-additivity model.

Surface	Molecule	θ_{sat}	# Waters displaced, *n*
Pt(111) terrace	Benzaldehyde	1/9	6.5
	Benzyl Alcohol	1/9	6.5
	Cyclohexanol	1/9	6.5
	Furfural	3/16	3.8

	Phenol	1/9	6.5
Pt(110) step	Benzaldehyde	1/6	4.3
	Benzyl Alcohol	1/6	4.3
	Cyclohexanol	1/6	4.3
	Furfural	1/6	4.3
	Phenol	1/6	4.3
Pt(100) step	Benzaldehyde	1/9	6.5
	Benzyl Alcohol	1/9	6.5
	Cyclohexanol	1/9	6.5
	Furfural	3/16	3.8
	Phenol	1/9	6.5
Rh(111) terrace	Benzaldehyde	1/9	6.5
	Benzyl Alcohol	1/9	6.5
	Cyclohexanol	1/9	6.5
	Furfural	3/16	3.8
	Phenol	1/9	6.5
Rh(110) step	Benzaldehyde	1/6	4.3
	Benzyl Alcohol	1/6	4.3
	Cyclohexanol	1/6	4.3
	Furfural	1/6	4.3
	Phenol	1/6	4.3
Rh(100) step	Benzaldehyde	1/9	6.5
	Benzyl Alcohol	1/9	6.5
	Cyclohexanol	1/9	6.5
	Furfural	3/16	3.8
	Phenol	1/9	6.5

As a simple way to probe the validity of the assumption that organics displace the same number of water molecules on the steps and terraces, we compared phenol adsorption geometries on (110) and (100) steps and their corresponding terraces. Phenol adsorbed onto the (110) and (100) steps and terraces of platinum and rhodium is shown in **Appendix Figure A-11**. On both the (110) steps and the terraces of the two metals, phenol adsorbs with the ring and alcohol groups centered above four-fold hollow sites. Because the adsorbed structure is similar on the two surfaces, the number of water molecules displaced from the (110) step may be similar to the number of water molecules displaced from the terrace. This assumption appears to be reasonable, as bond additivity calculations for aromatics on the Pt(110) step agree qualitatively with experiment, and bond additivity calculations for aromatics on the Rh(110) step agree quantitatively with experiment.

The adsorption sites for phenol are distinct on the (100) steps compared to the terraces for Pt and Rh. Because the adsorption configuration of phenol is dissimilar on the steps and terraces, it is likely a different number of water molecules are displaced from the two surfaces upon adsorption of phenol. The number of waters displaced from the (100) step is assumed to be the same as on the terrace in this study for computational tractability. The poor agreement between bond additivity predictions and experimental measurements may be a result of this inaccurate treatment of water displacement on the (100) step. Accurately estimating the number of water molecules displaced from the step, however, requires more rigorous methods, such as ab-initio molecular dynamics simulations, which were not considered in the current work.

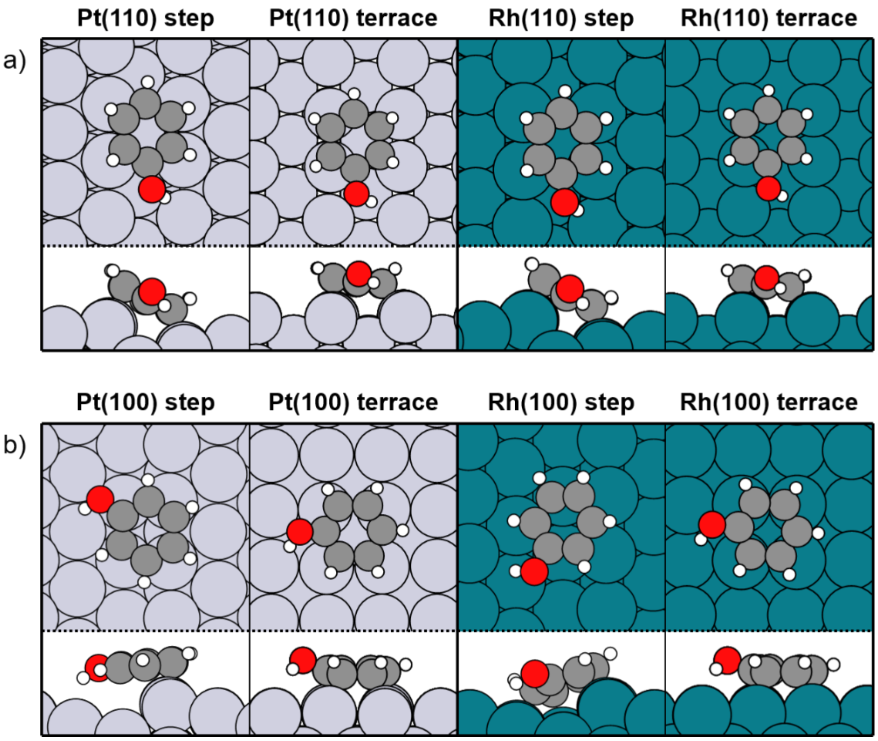

Appendix Figure A-11 Adsorption configurations of phenol on (100) terraces and (110) steps. Adsorption configurations of phenol on **a)** the (110) steps and terraces of platinum and rhodium and **b)** the (100) steps and terraces of platinum and rhodium.

The enthalpies of adsorption of gas-phase organics 'R' onto metal 'M' in the aqueous phase were calculated using **Eq. 2-2** as given in the main text, and reproduced here. The example below outlines the calculation of the adsorption enthalpy of phenol on Pt(111).

$$-\Delta H^0_{ads,aq,gas,R/M} = -\Delta H^0_{ads,gas,R/M} + n\left(\Delta H^0_{ads,gas\ water/M} + \Delta H^0_{vap}\right) - 2\gamma_{water(liq)}\sigma_R + (water\text{-}R) \quad \textbf{Eq. 2-2}$$

$\Delta H^0_{ads,gas,R/M}$, the gas-phase enthalpy of adsorption of phenol on Pt(111), is calculated to be −195 kJ mol^{-1} at 1/9 ML coverage. $\Delta H^0_{ads,gas,water/M}$ is the enthalpy of adsorption of water onto metal '*M*'. Modeling a single water molecule predicts water adsorption to be weaker than what is seen experimentally because the energy of the molecule is not stabilized by favorable water-water interactions.[262] However, modeling water as a hexagonal ice-like layer is also inaccurate as liquid water is less ordered at standard temperatures. Le *et al.* have found that water molecules at the solid/liquid interface form approximately three hydrogen bonds.[263] Here, the adsorption enthalpy of water is taken to be the adsorption enthalpy of an adsorbed water monomer plus the energetic contribution from three hydrogen bonds. To estimate the energy of a hydrogen bond, two water molecules were modeled in vacuum and the energy resulting from water-water interactions was calculated as $E_{w-w} = (E_{w,w} - 2 \cdot E_w)/2$ where $E_{w,w}$ is the energy of the two water molecules together in the simulation cell and E_w is the energy of an isolated water molecule. The strength of water-water interactions was calculated to be −7 kJ mol^{-1}. Therefore, the enthalpy of adsorption of each water molecule onto metal 'M' was calculated as the sum of the adsorption energy of a water monomer plus the energies of three hydrogen bonds. On Pt(111), $\Delta H^0_{ads,gas,water/M}$ is calculated to be −59 kJ mol^{-1} after accounting for hydrogen bonds that stabilize adsorbed water molecules. The enthalpy of vaporization ΔH^0_{vap} of water was taken as 41 kJ mol^{-1}.[264]

$2\gamma_{water(liq)}\sigma_R$ describes water-water interactions over the area of an adsorbed organic molecule. $\gamma_{water(liq)}$, the surface energy of liquid water, is known experimentally to be 73 kJ m^{-2}.[265] The area of each molecule on each surface is estimated using the area of the metal onto which the molecule is adsorbed. For phenol on Pt(111), phenol is known to adsorb at 1/9 ML coverage where each molecule adsorbs on nine platinum atoms corresponding to an area of 0.60 nm^2. The area of each molecule is calculated on each surface using the described approach. (*water-R*) describes the interactions between water and the organic and is defined as $-1/2\,\Delta H_{Solv,R} + \gamma_{water(liq)}\sigma_R$ where $\Delta H_{Solv,R}$ is the solvation enthalpy of the organic in water. The resulting aqueous heat of adsorption predicted for phenol on Pt(111) is within 5 kJ mol^{-1} of the heat of adsorption determined experimentally.

$$-\Delta H^{0}_{ads,aq,gas,R/M}$$

$$= 195\ kJ\ mol^{-1} + 6.5(-59\ kJ\ mol^{-1} + 41\ kJ\ mol^{-1}) - 52.7\ kJ\ mol^{-1} + 51.4\ kJ\ mol^{-1} = 76\ kJ\ mol^{-1}$$

The calculations and bond-additivity model here assume an uncharged metal surface. Because the PZC is different for different Pt or Rh facets, experimentally measuring at certain potentials would mean the different facets have different surface charges, which is known to influence the water adsorption energy.[95,96] However, the PZC of Pt(111) is not much different from Pt(100) (0.33 V and 0.38 V vs. RHE in 0.1 M H_2SO_4 at pH 1 respectively),[122,123] and Rh(111) and Rh(100) are also similar to one another (0.106 V and 0.154 V in 0.1 M H_2SO_4 at pH 1, respectively).[124] Although the PZC is sensitive to pH[266] and may be different at the pH 5 used in this work, we assume differences in the adsorption energies from differences in the charge of the Pt and Rh facets are minor.

A.12 Comparison of Experimental and Theoretical Heats of Adsorption Using the optB88-vdw Functional

All gas-phase and aqueous heats of adsorption of phenol, benzaldehyde, furfural, benzyl alcohol, and cyclohexanol reported in the main text were calculated with DFT using the PBE exchange-correlation functional with the D3 dispersion correction (PBE-D3). We compare the results obtained using PBE-D3 with those obtained using the optB88-vdw exchange-correlation functional, which has been shown to more closely reproduce gas-phase adsorption energies of phenol.[27,133] The heats of adsorption using optB88-vdw and PBE-D3 are compared in **Appendix Figure A-12**.

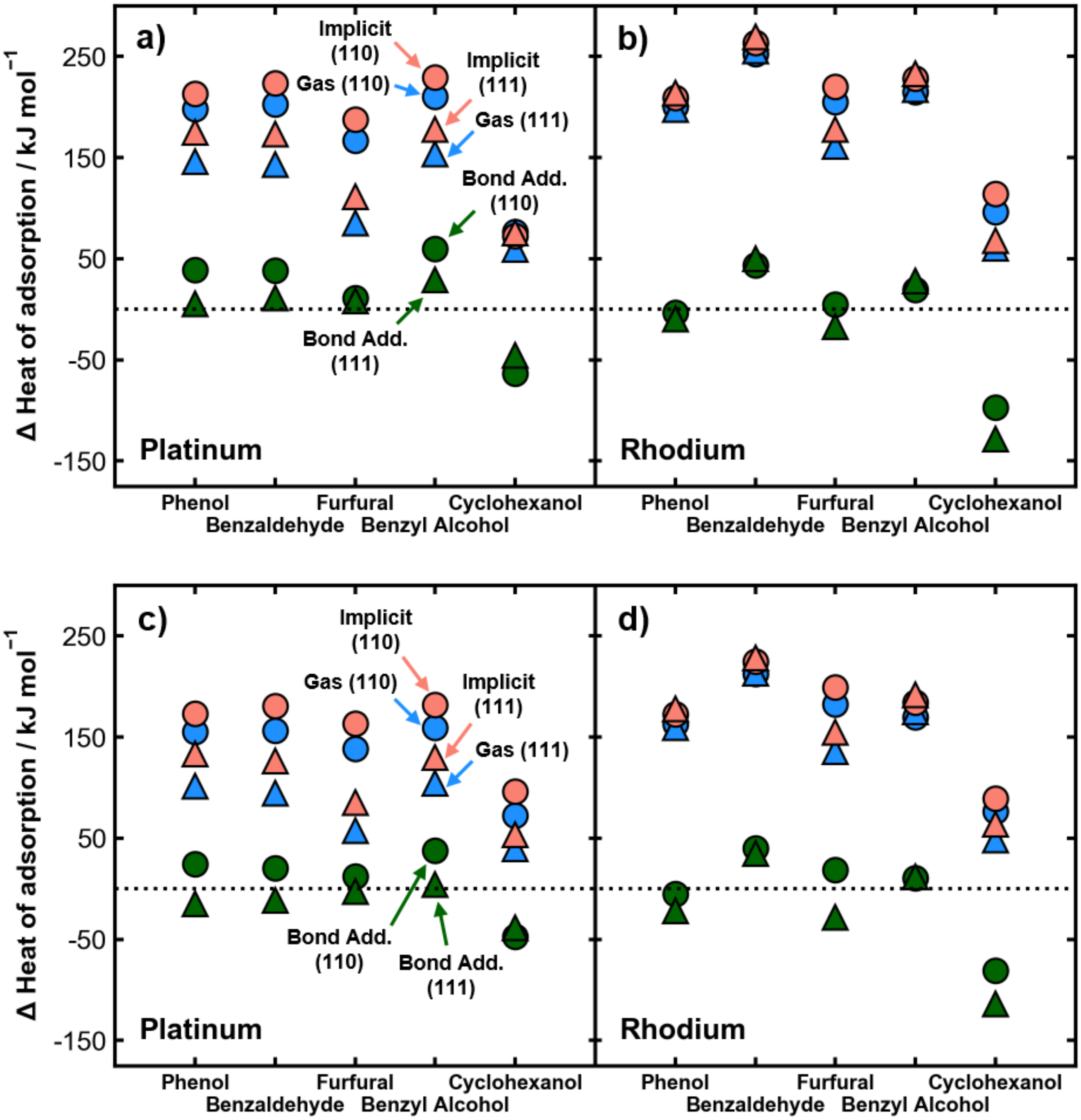

Appendix Figure A-12 Comparison of PBE-D3 and optB88-vdw functionals. Calculated heats of adsorption on **a)** platinum and **b)** rhodium using the PBE-D3 method referenced to experimental heats of adsorption. Values are the same as those from **Figure 2-6**, reproduced here for comparison. Calculated heats of adsorption on **c)** platinum and **d)** rhodium using the optB88-vdw functional referenced to experimental heats of adsorption. Calculations on (110) steps are compared to site 1 and (111) facets are compared to site 2. Heats of adsorption are calculated in the gas phase and in the aqueous phase using an implicit solvent model or a bond-additivity model (Bond Add.).

The qualitative trends in the heats of adsorption do not change when using either PBE-D3 or optB88-vdw. Heats of adsorption using the bond-additivity model are predicted to be on average 7 kJ mol^{-1} lower (12 kJ mol^{-1} if excluding cyclohexanol) using optB88-vdw compared to PBE-D3. The gas-phase and implicit aqueous-phase heats of adsorption from both methods are estimated to be ~50-250 kJ mol^{-1} too large compared with experiment. Regardless of the functional choice, the aqueous-phase heats of adsorption predicted using a bond-additivity model are in much closer quantitative agreement with experiment.

Appendix B: Supporting Information for Structure Sensitivity of Pt and Rh

This appendix was adapted from Barth, I.; Akinola, J.; Lee, J.; Gutiérrez, O. Y.; Sanyal, U.; Singh, N.; Goldsmith, B. R. Explaining the Structure Sensitivity of Pt and Rh for Aqueous-Phase Hydrogenation of Phenol. *J. Chem. Phys.* **2022**, *156* (10), 104703. My contribution to this work is the density functional theory modeling. James Akinola performed the experimental work.

B.1 Modeling Phenol Hydrogenation on Pt and Rh

Phenol and Hydrogen Co-Adsorption on Rh and Pt Facets

The Gibbs free energy of adsorbed phenol with hydrogen was studied as a function of hydrogen coverage (θ_H) on Pt(111), Rh(111), Pt(221), and Rh(221). On Pt(111) and Rh(111), two different adsorption configurations of phenol were considered. On bare Pt(111), phenol prefers to adsorb parallel to the surface with the centroid of the aromatic ring above a bridge site rotated 30° with respect to the unit cell (bridge-30). The second most stable adsorption configuration was phenol adsorbed parallel to the surface with the centroid of the aromatic ring above an HCP hollow site rotated 0° with respect to the unit cell (HCP-0).[27] We considered two adsorption configurations of phenol for Pt(111) and Rh(111) because the most stable adsorption motif may change once hydrogen is co-adsorbed to the surface. For example, the most stable adsorption motif of benzene on Pd(111) is bridge-30 at low θ_H and HCP-0 at high θ_H.[267] We only consider a single phenol adsorption configuration on Pt(221) and Rh(221).

The DFT-optimized geometries of phenol adsorbed on the clean metal surface and co-adsorbed with 1/9, 4/9, and 6/9 ML of hydrogen are shown for Pt(111) and Rh(111) in **Appendix**

Figure B-1 and **Appendix Figure B-2**. Hydrogen was placed in the same sites used previously to model the co-adsorption of benzene and hydrogen on Pd(111).[157] At 1/9 ML, a single hydrogen atom is adsorbed in an FCC hollow site. At 4/9 ML, four hydrogen atoms are adsorbed in a combination of FCC and HCP hollow sites. At 6/9 ML, six hydrogen atoms are adsorbed in the unoccupied FCC hollow sites. We predict the most stable adsorption configuration of phenol on Pt(221) and Rh(221) to be at the step edge. We consider adsorbed phenol with 1/9, 4/9, and 6/9 ML of hydrogen adsorbed in unoccupied hollow sites. The DFT-optimized geometries for Pt(221) and Rh(221) are shown in **Appendix Figure B-3** and **Appendix Figure B-4**.

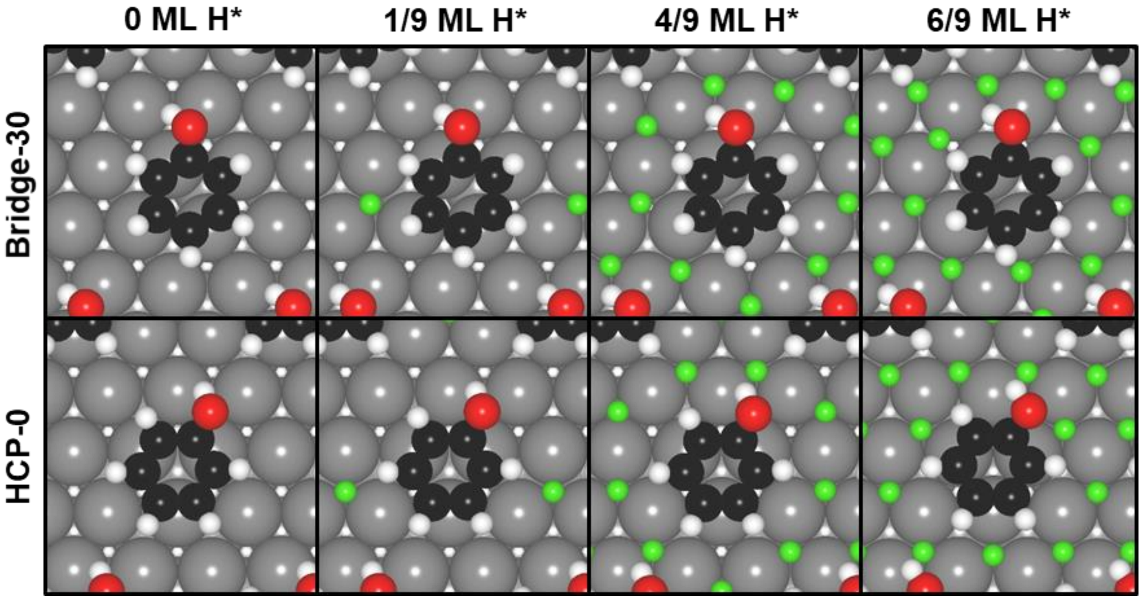

Appendix Figure B-1 Phenol with co-adsorbed hydrogen on Pt(111). DFT-optimized geometries of phenol in the bridge-30 and HCP-0 configurations on Pt(111) with 0, 1/9, 4/9, and 6/9 ML of co-adsorbed hydrogen. Geometries correspond to energetics reported in **Appendix Figure B-5a**. Color legend: Pt = grey; O = red; C = black; H (phenol) = white; H (surface) = green.

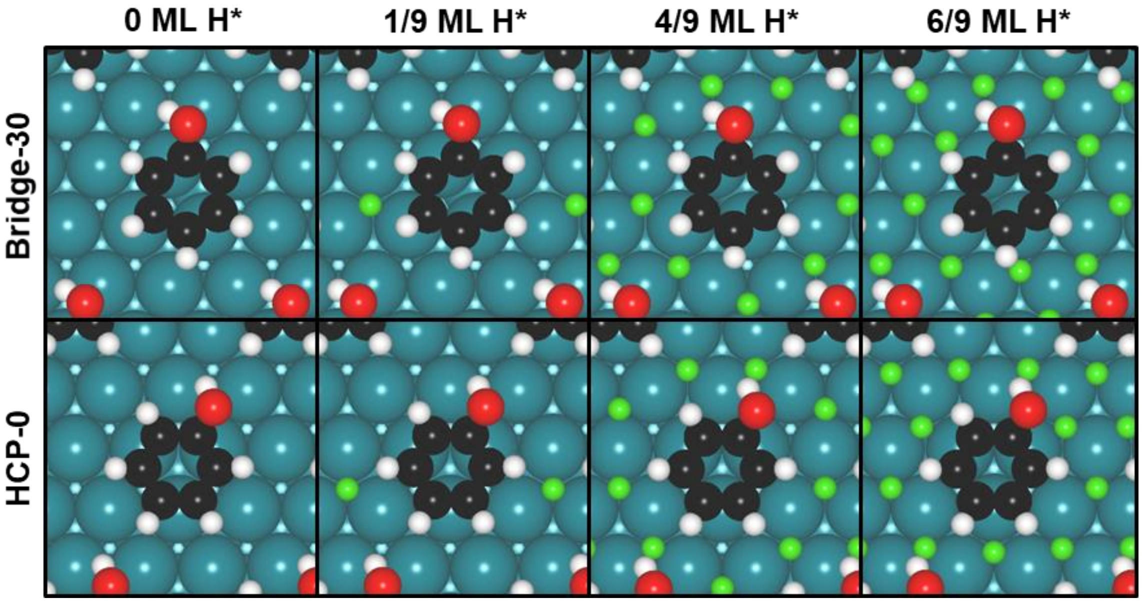

Appendix Figure B-2 Phenol with co-adsorbed hydrogen on Rh(111). DFT-optimized geometries of phenol in the bridge-30 and HCP-0 configurations on Rh(111) with 0, 1/9, 4/9, and 6/9 ML of co-adsorbed hydrogen. Geometries correspond to energetics reported in **Appendix Figure B-5c**. Color legend: Rh = teal; O = red; C = black; H (phenol) = white; H (surface) = green.

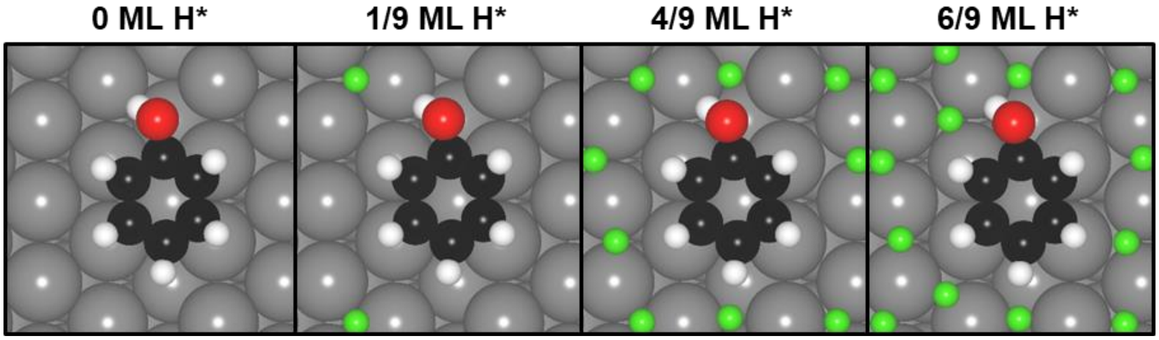

Appendix Figure B-3 Phenol with co-adsorbed hydrogen on Pt(221). DFT-optimized geometries of phenol adsorbed to the step edge of Pt(221) with 0, 1/9, 4/9, and 6/9 ML of co-adsorbed hydrogen. Geometries correspond to energetics reported in **Appendix Figure B-5b**. Color legend: Pt = grey; O = red; C = black; H (phenol) = white; H (surface) = green.

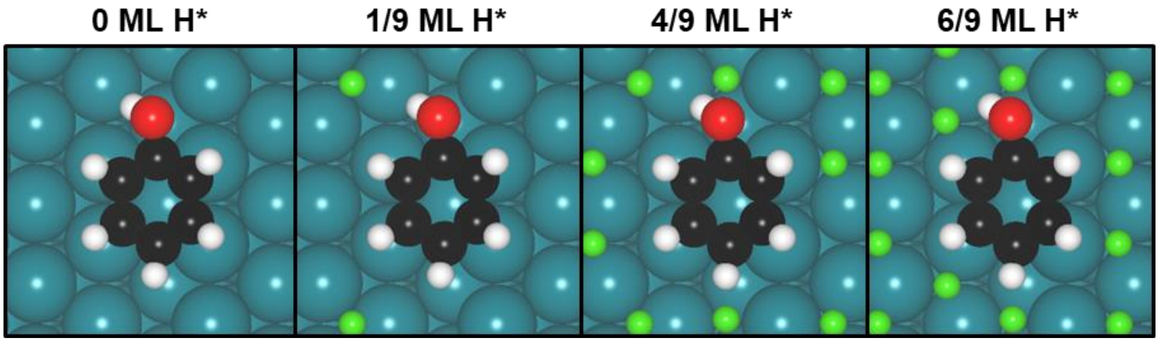

Appendix Figure B-4 Phenol with co-adsorbed hydrogen on Rh(221). DFT-optimized geometries of phenol adsorbed to the step edge of Rh(221) with 0, 1/9, 4/9, and 6/9 ML of co-adsorbed hydrogen. Geometries correspond to energetics reported in **Appendix Figure B-5d**. Color legend: Rh = teal; O = red; C = black; H (phenol) = white; H (surface) = green.

The relative Gibbs free energies of adsorbed phenol with co-adsorbed hydrogen on Pt(111), Pt(221), Rh(111), and Rh(221) at the different θ_H are shown in **Appendix Figure B-5**. The free energy of adsorbed phenol and hydrogen at each hydrogen coverage ($\Delta G_{\theta,ads}$) was calculated using **Eq. B-1**.

$$\Delta G_{\theta,ads} = G_{phenol*+nH*} + (A-n)\cdot G_{H^{+}+e^{-}} \qquad \textbf{Eq. B-1}$$

$G_{phenol*+nH*}$ denotes the free energy of adsorbed phenol with co-adsorbed hydrogen corresponding to the DFT-optimized structures in **Appendix Figure B-1** through **Appendix Figure B-4**. $G_{phenol*+nH*}$ was evaluated in the harmonic limit at 300 K. $(A-n)\cdot G_{H^{+}+e^{-}}$ is the free energy of the protons, which is equal to $\frac{1}{2}G_{H_2}$ at 0 V vs. RHE based on the computational hydrogen electrode model. The free energy of H_2 (G_{H_2}) was evaluated in the ideal gas limit at 300 K and 1 bar. *A* denotes the total number of hydrogen atoms considered in the system and *n* denotes the number of adsorbed hydrogens. The value of *A* is constant across the range of hydrogen coverages on each facet so that the total number of atoms in each system is constant at each coverage. For example, the free energy of adsorbed phenol on Pt(111) or Rh(111) with 1/9 ML of adsorbed hydrogen is calculated as $\Delta G_{\theta,ads} = G_{phenol*+H*} + (6-1)\cdot G_{H^{+}+e^{-}}$. In this example, *A* = 6 because only six hydrogen atoms are considered in the system. One of the hydrogen atoms is adsorbed, thus *n* = 1. The remaining hydrogen atoms are not adsorbed.

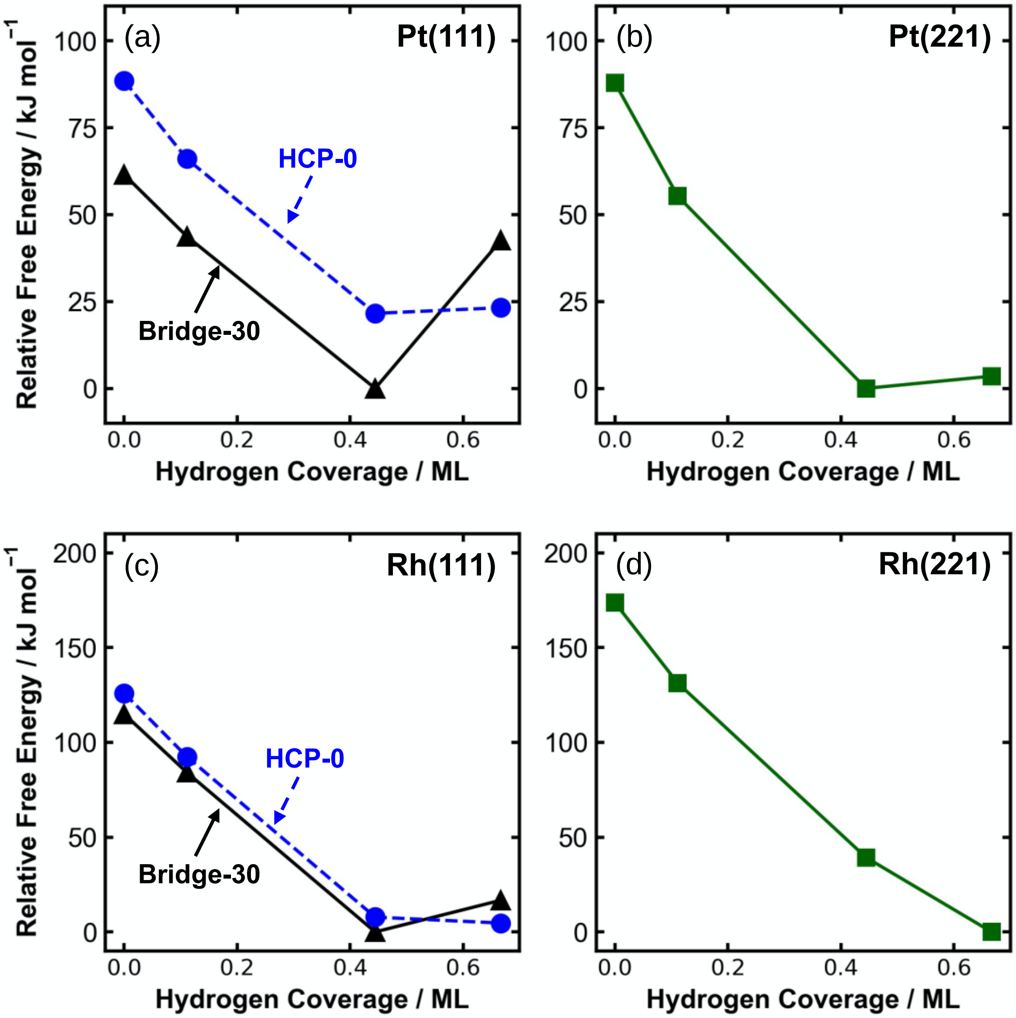

Appendix Figure B-5 Free energy of phenol with co-adsorbed hydrogen. Relative free energy of phenol and co-adsorbed hydrogen at 300 K and 1 bar H_2 on **(a)** Pt(111), **(b)** Pt(221), **(c)** Rh(111), and **(d)** Rh(221). Phenol is adsorbed in the bridge-30 and HCP-0 configurations on (111) terraces or on the step edge for (221) facets. Solvation effects are not included.

Evaluating Implicit Solvation for Phenol Hydrogenation on Rh(111)

The effect of implicit solvation was evaluated using VASPsol with the default parameters for water solvent.[40,41] Phenol hydrogenation to cyclohexanone was modeled on a 4×4×4 Rh(111) slab without co-adsorbed hydrogen. The phenol hydrogenation reaction mechanism modeled is shown in **Appendix Figure B-6a**, and the corresponding energetics of the reaction with and without implicit solvation are compared in **Appendix Figure B-6b**. All energies were referenced to adsorbed phenol. We find implicit solvation to have little effect on the reaction energetics. Therefore, we do not include implicit solvation for phenol hydrogenation on Pt and Rh.

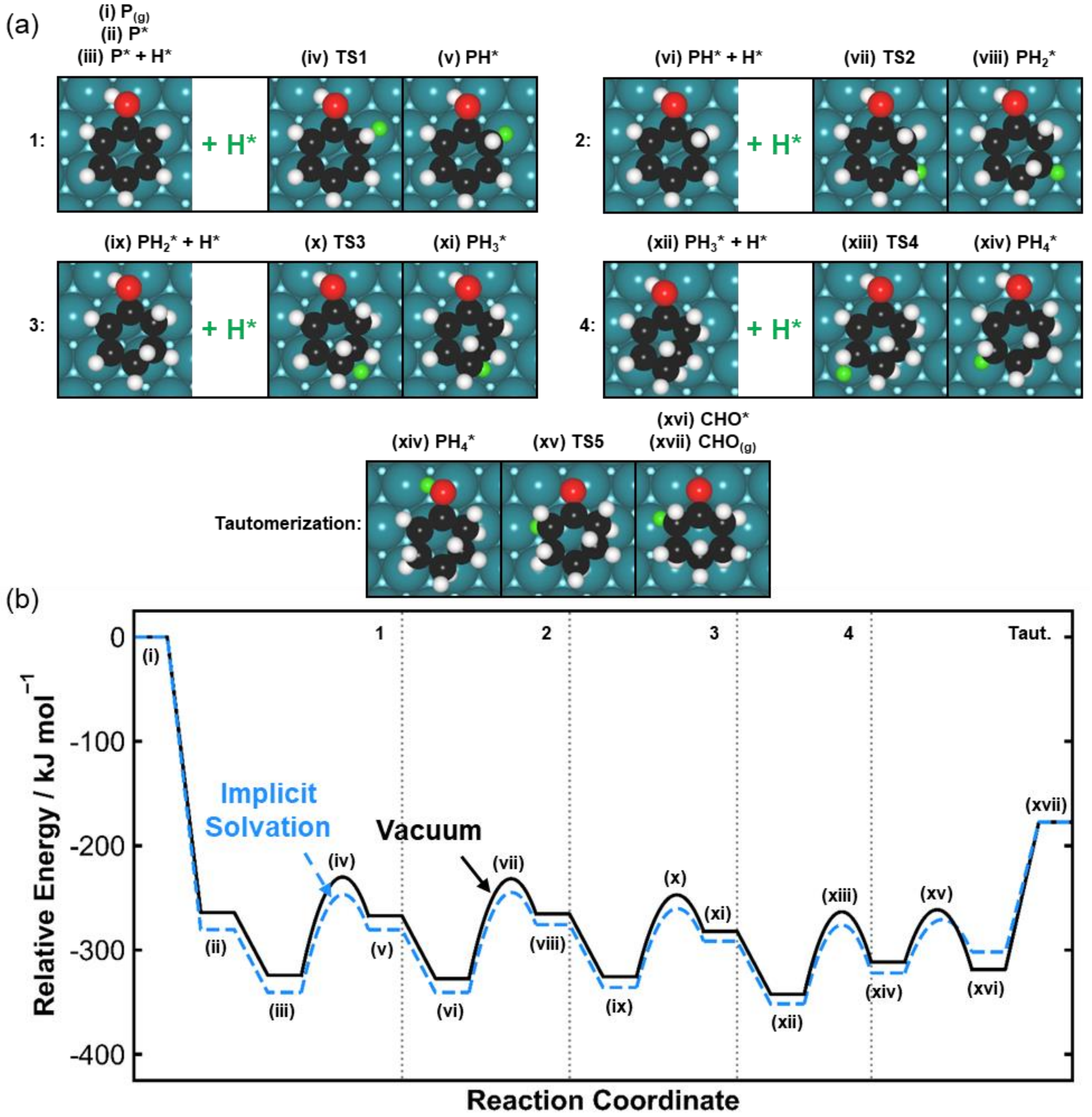

Appendix Figure B-6 Free energy diagram of phenol hydrogenation in vacuum and with implicit solvation. **(a)** DFT-predicted geometries corresponding to the initial, transition, and final states for the hydrogenation of phenol ($P_{(g)}$) to adsorbed cyclohexanone ($CHO_{(g)}$) on Rh(111) with and without implicit solvation. Products of the first, second, third, and fourth hydrogenation additions are denoted PH*, PH_2*, PH_3*, and PH_4*, respectively. TS1, TS2, TS3, and TS4 denote hydrogenation transition states and TS5 denotes the tautomerization transition state. Color legend: Rh = teal, O = red, C = black, and H = white. The H* atom participating in each elementary reaction step is colored green. **(b)** Reaction energy profile for the hydrogenation of phenol on Rh(111) with and without implicit solvation at 0 K. The black solid line corresponds to the reaction modeled in vacuum and the blue dashed line corresponds to the reaction modeled with implicit solvation.

B.2 Measuring Intrinsic Catalyst Activity

Calculating Turnover Frequency from Rate Measurements

The turnover frequency (TOF) for phenol hydrogenation is defined as the rate of formation of reaction products (cyclohexanone and cyclohexanol) per metal surface site calculated according to **Eq. B-2**:

$$\mathrm{TOF} = \frac{\text{moles of total product formed}}{\text{moles of surface metal } \times \text{ time}} = \frac{\text{rate of total product formed}}{\text{moles of surface metal}} \qquad \textbf{Eq. B-2}$$

The moles of total product formed were determined as described in the main text. For the particle size dependence studies, the moles of surface Rh per weight of catalyst for the Rh/C samples with weight loadings of 1, 3, 5, and 10 wt% was measured using H_2 chemisorption. The moles of surface Rh per catalyst weight was multiplied by the mass of electrocatalyst loaded into the carbon felt used as working electrode to determine the moles of surface Rh in the reactor.

For the TCH concentration dependence measurements, the moles of surface Rh was calculated using the dispersion of the catalyst. Assuming a cuboctahedron geometry for metal dispersions of 0.20–0.92, the dispersion (*D*) was calculated from **Eq. B-3** as described in ref. [172]:

$$D = \frac{\text{moles of surface Rh}}{\text{moles of total Rh}} = \left(\frac{d_{atom}}{d_p} \times 3.32\right)^{\frac{1}{1.23}}\mathrm{T} \qquad \textbf{Eq. B-3}$$

where d_p is the mean particle size extracted from XRD analysis and d_{atom} is the metal atomic diameter, which for Rh is 0.269 nm.[268] The value of d_p for 20 wt% Rh was 2.9 nm from XRD measurements in **Appendix Figure B-7**. Thus, for 10 mg of 20 wt% Rh supported on Vulcan carbon the moles of surface Rh is:

$$10\ \mathrm{mg\ Rh/C} \times \frac{20\ \mathrm{mg\ Rh}}{100\ \mathrm{mg\ Rh/C}} \times \frac{1\ \mathrm{g\ Rh}}{1000\ \mathrm{mg\ Rh}} \times \frac{1\ \text{mole total Rh}}{102.9055\ \mathrm{g\ Rh}} \times \left(\frac{0.269\ \mathrm{nm}}{2.9\ \mathrm{nm}} \times 3.32\right)^{\frac{1}{1.23}}$$
$$= 7.6\ \times 10^{-6}\ \text{moles of surface Rh}$$

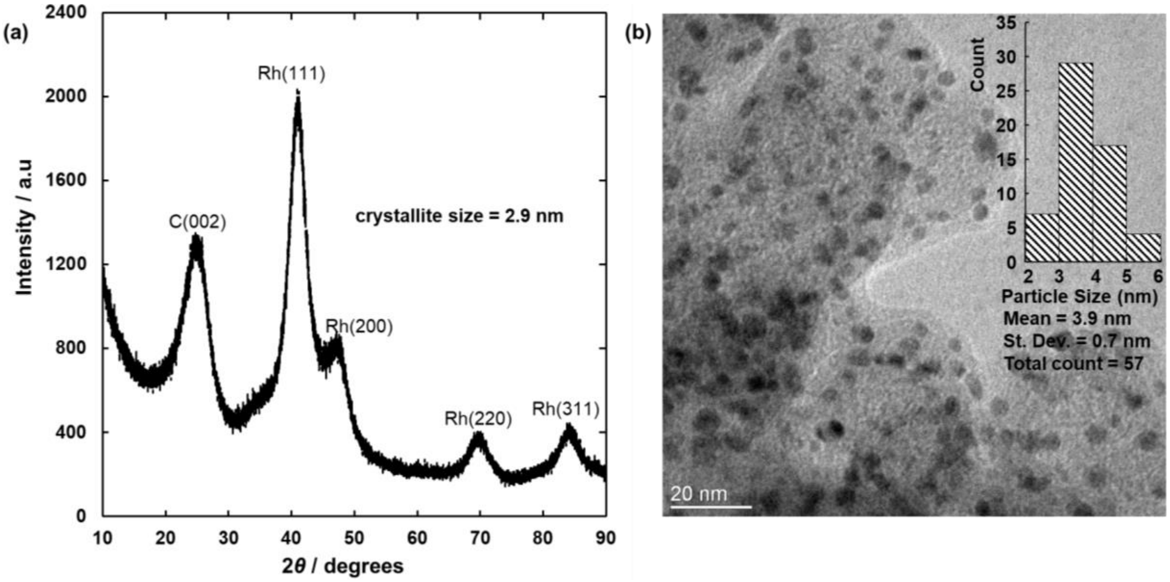

Appendix Figure B-7 X-ray diffraction for Rh/C. **(a)** X-ray diffraction pattern for 20 wt% Rh/C used for phenol concentration dependence studies in **Figure 3-1**. The Scherrer equation was used to calculate the average crystallite size using the full width at half maximum of each Rh(111), Rh(220), and Rh(311) peak. The Rh(200) peak was not used to evaluate the crystallite size because of the uncertain baseline of the peak. **(b)** TEM micrograph for the same 20 wt% Rh/C. Darker objects correspond to Rh metal, while the lighter areas are the Vulcan XC-72 carbon support. The Rh particle size distribution is shown in the inset.

Appendix Table B-1 Catalyst particle sizes. Weight loading of Rh supported on carbon, commercial source of the catalyst, reaction for which each catalyst was used, average particle sizes from TEM, XRD, and H_2 chemisorption and dispersion from H_2 chemisorption and XRD.

Catalyst	Source	Reaction	Particle size by TEM / nm	Crystallite size by XRD[a] / nm	Particle size by H_2 chemisorption[b] / nm	Dispersion by H_2 chemisorption	Dispersion by XRD
1 wt% Rh/C	Sigma-Aldrich	ECH	2	N/A	2.5	0.43	N/A
3 wt% Rh/C	Sigma-Aldrich	ECH	5	N/A	6.5	0.2	N/A
5 wt% Rh/C	Sigma-Aldrich	ECH	7	N/A	10	0.135	N/A
10 wt% Rh/C	Sigma-Aldrich	ECH	10	N/A	13.5	0.1	N/A
20 wt% Rh/C	Fuel Cell Store	TCH	3.9	2.9	N/A	N/A	0.38

a. Crystallite size estimated using the Scherrer equation. b. Particle sizes from H_2 chemisorption are estimated from the measured dispersion using a cube octahedron model.[15]

Appendix Table B-1 shows that for the 1, 3, 5, and 10 wt% catalysts, the particle sizes measured from TEM increase with increasing Rh weight loading. This trend matches with particle sizes estimated from H_2 chemisorption. However, H_2 chemisorption predicts particle sizes slightly larger than TEM, which could arise from the model used to estimate particle size for H_2 chemisorption (assuming the particles are cuboctahedron in shape). Particle sizes could not be estimated from XRD data for the 1, 3, 5, and 10 wt% Rh catalysts because the metal loadings were too low to accurately resolve the XRD peaks. XRD with Scherrer analysis performed for the 20 wt% Rh catalyst from Fuel Cell Store gave a crystallite size of 2.9 nm, which is 25% lower than the average particle size from TEM (3.9 nm). The higher particle size by TEM is possibly because at the TEM magnification used, particle sizes less than 2 nm cannot be detected (see histogram in **Appendix Figure B-7b**). From either TEM or XRD the 20 wt% Rh/C from Fuel Cell Store has smaller average particle size than expected compared to the lower Rh weight loadings. One possible reason is because the 20 wt% Rh/C was synthesized on Vulcan XC-72 carbon and the lower Rh loadings (from Sigma Aldrich) were synthesized on activated carbon.

Identifying Conditions where the Reaction is Kinetically Limited

We operated at conditions where both external and internal mass transfer limitations are eliminated to measure the intrinsic catalytic activity. For the ECH particle size dependence studies performed on Rh/C infiltrated in a porous carbon felt, we operated at conditions (felt thickness of 3.2 mm and a stir bar speed of 500 rpm) that we have previously reported to be devoid of both internal and external mass transfer limitations.[82] For the concentration dependence studies on the non-porous Rh/C nanoparticles, we are specifically concerned about external mass transfer of bulk phenol to the metal surface or removal of formed products from the surface. In **Appendix Figure B-8**, the TOFs are unchanging at stir bar speeds of 500 rpm and above indicating no external mass transfer limitations at these conditions. The same stir bar speed of 500 rpm was used for both ECH and

TCH studies. We use the lower bound phenol concentration of 10 mM to probe external mass transfer limitations because mass transfer will be slowest at the lowest phenol concentration.

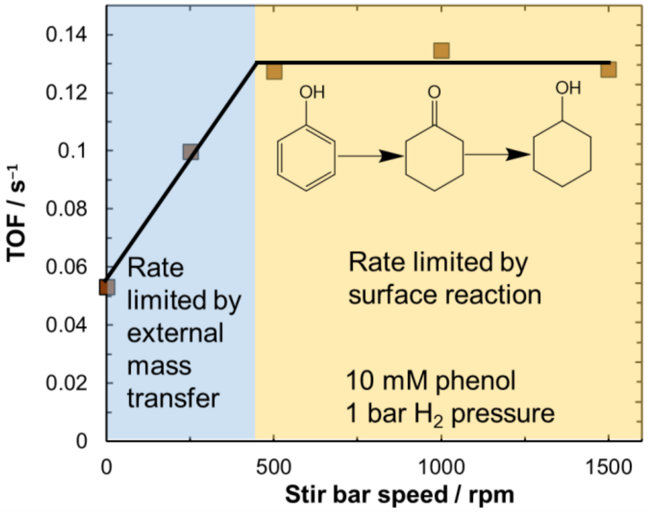

Appendix Figure B-8 Mass transfer limitations for phenol hydrogenation. Turnover frequency (TOF) as a function of stir bar speed for TCH of 10 mM phenol at 25 °C and 1 bar H_2. TOFs were normalized to the number of exposed Rh metal determined using XRD. The blue shaded region is limited by mass transfer whereas the orange shaded region is kinetically limited.

Appendix Table B-2 Experimental ECH kinetics on Rh/C. ECH TOF, Faradaic efficiency to ECH, and catalyst utilization for Rh/C catalysts.

Catalyst	**Particle size from TEM / nm**	**TOF / s^{-1}**	**Faradaic efficiency to ECH / %**	**Catalyst utilization / µmol s^{-1} g_{Rh}^{-1}**
1 wt% Rh/C	2	0.0033	4	14
3 wt% Rh/C	5	0.035	17	68
5 wt% Rh/C	7	0.086	29	110
10 wt% Rh/C	10	0.19	35	180

Catalyst utilization is calculated as thus: TOF $\times$ metal dispersion $\times \frac{\text{1 mol of total Rh}}{\text{102.9055 g Rh}}$. The catalyst dispersion $\left(\frac{\text{mol surface Rh}}{\text{mol of total Rh}}\right)$ is measured by H_2 chemisorption and reported in **Appendix Table B-1**.

B.3 Reaction Pathway Modeling for Phenol Hydrogenation on Pt and Rh Facets

Reaction Free Energies for Phenol Hydrogenation on Pt and Rh

For $P_{(g)} + 2H_{2(g)} \rightleftharpoons CHO_{(g)}$, the gas-phase reaction enthalpy and free energy were calculated to be -126 kJ mol^{-1} and -54 kJ mol^{-1}, respectively. The solvation energies of phenol and cyclohexanone are −27 kJ mol^{-1} and −17 kJ mol^{-1}, respectively, based on the Henry's law constants (20 mol m^{-3} Pa^{-1} and 0.38 mol m^{-3} Pa^{-1} for phenol and cyclohexanone, respectively).[161] The aqueous-phase reaction free energy for the reaction $P_{(aq)} + 2H_{2(g)} \rightleftharpoons CHO_{(aq)}$ was −44 kJ mol^{-1}.

Appendix Table B-3 DFT-calculated reaction energetics for microkinetic modeling on Pt. Reaction free energies and barriers on Pt(111) and Pt(221) for hydrogenation of phenol at the applied potential of $U = 0$ V vs. RHE (i.e., 300 K and 1 bar $H_{2(g)}$) on Pt surfaces. ΔG_{rxn} is the reaction free energy, $\Delta G^{\ddagger}_{F}$ is the activation barrier in the forward direction, and $\Delta G^{\ddagger}_{B}$ is the activation barrier in the backward direction. The energies correspond to **Figure 3-2** of the main text and were used in the microkinetic model. The adsorption free energies of phenol are experimental values from ref. [28].

Energies associated with phenol ECH on Pt(111) at 0 V vs. RHE.

Reaction	ΔG_{rxn} (kJ/mol)	$\Delta G^{\ddagger}_{F}$ (kJ/mol)	$\Delta G^{\ddagger}_{B}$ (kJ/mol)
(P adsorption) $P + * \rightleftharpoons P*$	−9	0	9
(H adsorption) $H^+ + e^- + * \rightleftharpoons H*$	−18	0	18
(1) $P* + H*_i \rightleftharpoons PH* + H*_{i-1}$	24	47	23
(2) $PH* + H*_i \rightleftharpoons PH_2* + H*_{i-1}$	−7	81	88
(3) $PH_2* + H*_i \rightleftharpoons PH_3* + H*_{i-1}$	25	85	61
(4) $PH_3* + H*_i \rightleftharpoons PH_4* + H*_{i-1}$	5	92	87
(Taut.) $PH_4* + H*_i \rightleftharpoons CHO* + H*_i$	−23	63	87
(CHO desorption) $CHO* \rightleftharpoons CHO + *$	−15	0	15

Energies associated with phenol ECH on Pt(221) at 0 V vs. RHE.

Reaction	ΔG_{rxn} (kJ/mol)	$\Delta G^{\ddagger}_{F}$ (kJ/mol)	$\Delta G^{\ddagger}_{B}$ (kJ/mol)
(P adsorption) $P + * \rightleftharpoons P*$	−29	0	29
(H adsorption) $H^+ + e^- + * \rightleftharpoons H*$	−25	0	25
(1) $P* + H*_i \rightleftharpoons PH* + H*_{i-1}$	61	92	31
(2) $PH* + H*_i \rightleftharpoons PH_2* + H*_{i-1}$	47	78	32
(3) $PH_2* + H*_i \rightleftharpoons PH_3* + H*_{i-1}$	33	64	31
(4) $PH_3* + H*_i \rightleftharpoons PH_4* + H*_{i-1}$	12	98	86
(Taut.) $PH_4* + H*_i \rightleftharpoons CHO* + H*_i$	5	85	86
(CHO desorption) $CHO* \rightleftharpoons CHO + *$	73		−73

Appendix Table B-4 DFT-calculated reaction energetics for microkinetic modeling on Rh. Reaction free energies and barriers on Rh(111) and Rh(221) facets for hydrogenation at the applied potential of $U = 0$ V vs. RHE (i.e., 300 K and 1 bar $H_{2(g)}$). ΔG_{rxn} is the reaction free energy, $\Delta G^{\ddagger}_{F}$ is the activation barrier in the forward direction, and $\Delta G^{\ddagger}_{B}$ is the activation barrier in the backward direction. The energies correspond to **Figure 3-4** of the main text and were used in the microkinetic model. The adsorption free energies of phenol are experimental values from ref. [35].

Energies associated with phenol ECH on Rh(111) at 0 V vs. RHE.

Reaction	ΔG_{rxn} (kJ/mol)	$\Delta G^{\ddagger}_{F}$ (kJ/mol)	$\Delta G^{\ddagger}_{B}$ (kJ/mol)
(P adsorption) $P + * \rightleftharpoons P*$	−7	0	7
(H adsorption) $H^{+} + e^{-} + * \rightleftharpoons H*$	−31	0	31
(1) $P* + H*_{i} \rightleftharpoons PH* + H*_{i-1}$	59	87	28
(2) $PH* + H*_{i} \rightleftharpoons PH_{2}* + H*_{i-1}$	41	80	39
(3) $PH_{2}* + H*_{i} \rightleftharpoons PH_{3}* + H*_{i-1}$	47	73	25
(4) $PH_{3}* + H*_{i} \rightleftharpoons PH_{4}* + H*_{i-1}$	27	63	36
(Taut.) $PH_{4}* + H*_{i} \rightleftharpoons CHO* + H*_{i}$	−23	40	62
(CHO desorption) $CHO* \rightleftharpoons CHO + *$	65.9	0	−65.9

Energies associated with phenol ECH on Rh(221) at 0 V vs. RHE .

Reaction	ΔG_{rxn} (kJ/mol)	$\Delta G^{\ddagger}_{F}$ (kJ/mol)	$\Delta G^{\ddagger}_{B}$ (kJ/mol)
(P adsorption) $P + * \rightleftharpoons P*$	−26	0	26
(H adsorption) $H^{+} + e^{-} + * \rightleftharpoons H*$	−15	0	15
(1) $P* + H*_{i} \rightleftharpoons PH* + H*_{i-1}$	71	72	0
(2) $PH* + H*_{i} \rightleftharpoons PH_{2}* + H*_{i-1}$	59	66	7
(3) $PH_{2}* + H*_{i} \rightleftharpoons PH_{3}* + H*_{i-1}$	20	65	60
(4) $PH_{3}* + H*_{i} \rightleftharpoons PH_{4}* + H*_{i-1}$	5	65	60
(Taut.) $PH_{4}* + H*_{i} \rightleftharpoons CHO* + H*_{i}$	−30	36	66
(CHO desorption) $CHO* \rightleftharpoons CHO + *$	82	0	−82

The gas-phase hydrogenation of phenol to cyclohexanone without co-adsorbed hydrogen was modeled on the (111), (100), and (553) facets of Pt and Rh. The reaction was modeled on 4×4×4 slabs of Pt and Rh, corresponding to 1/16 ML coverage of phenol. The (553) stepped surface was used instead of the (221) stepped surface to ensure that the slab was similar in size to the (111) and (100) slabs. The (553) and (221) stepped facets both contain a (110)-like step and only differ in the length of the terrace region of the slab. The DFT-predicted geometries of the initial, transition, and final states on Rh(111) are shown in **Appendix Figure B-9a**. Identical reaction mechanisms were considered on Pt(111), Pt(100), Pt(553), Rh(111), Rh(100), and Rh(553). The corresponding reaction free energy diagrams are shown in **Appendix Figure B-9b**. The reaction rates were predicted using mean-field microkinetic modeling with the DFT-computed free energies as input parameters. The Arrhenius plot in **Appendix Figure B-9c** compares the TOFs on the three facets of Pt and Rh. Pt(111) is predicted to be the most active facet for the gas-phase hydrogenation of phenol without co-adsorbed hydrogen present. Pt(111) is predicted to be over four of magnitude more active than Pt(100) and over seven orders of magnitude more active than the Pt(553) step. The Rh(553) step is predicted to be the most active facet for the gas-phase hydrogenation of phenol, although the TOFs on Rh(553) and R(111) are within two orders of magnitude. The Rh(100) terrace is over four orders of magnitude less active than the Rh(111) terrace. The (100) terraces of Pt and Rh were not considered further in this work because of the relative inactivity compared to the (111) terraces.

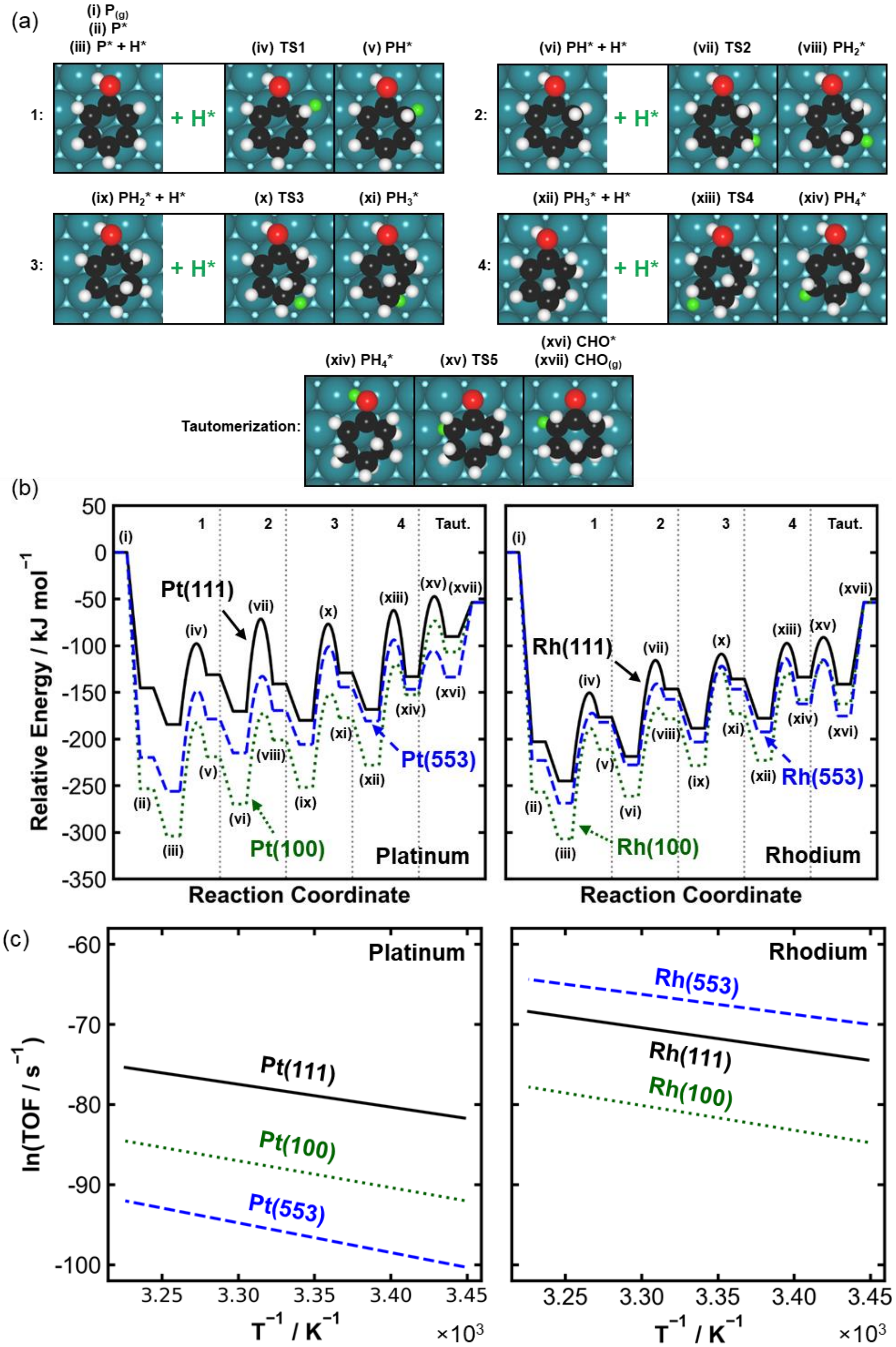

Appendix Figure B-9 Phenol hydrogenation on 4 × 4 × 4 slabs. **(a)** DFT-predicted geometries corresponding to the initial, transition, and final states for the hydrogenation of phenol ($P_{(g)}$) to cyclohexanone ($CHO_{(g)}$) on a 4 × 4 × 4 Rh(111) slab without co-adsorbed hydrogen. **(b)** Reaction energy profile for the gas-phase hydrogenation of phenol on Pt(111), Pt(100), and Pt(553) (left) and Rh(111), Rh(100), and Rh(553) (right). Adsorption, activation and reaction free energies are DFT-computed free energies at 300 K and 1 bar H_2. Color legend: Rh = teal, O = red, C = black, and H = white. The H* atom participating in each elementary reaction step is highlighted in green. **(c)** Arrhenius plot for the gas-phase hydrogenation of phenol on Pt(111), Pt(100), and Pt(553) (left) and Rh(111), Rh(100), and Rh(553) (right) between 290 K and 310 K based on microkinetic modeling.

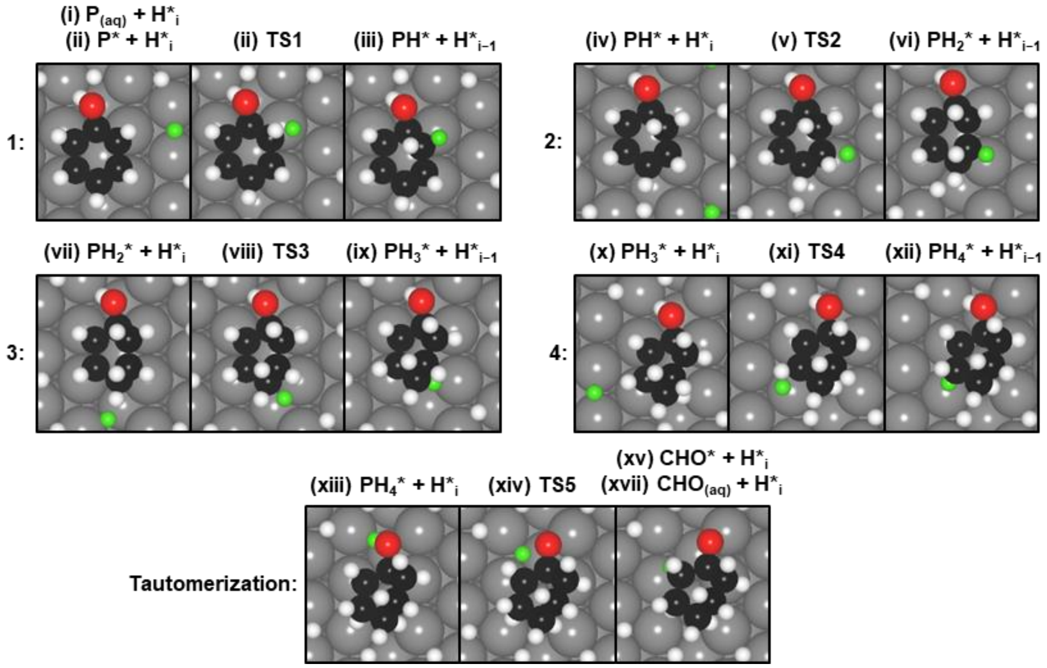

Appendix Figure B-10 DFT-predicted geometries for phenol hydrogenation on Pt(221). DFT-predicted geometries corresponding to the initial, transition, and final states for the hydrogenation of phenol ($P_{(aq)}$) to adsorbed cyclohexanone ($CHO_{(aq)}$) on Pt(221) with 4/9 ML of co-adsorbed hydrogen. Products of the first, second, third, and fourth hydrogenation additions are denoted PH*, PH_2*, PH_3*, and PH_4*, respectively. TS1, TS2, TS3, and TS4 denote hydrogenation transition states and TS5 denotes the tautomerization transition state. H^*_i corresponds to adsorbed hydrogen at 4/9 ML hydrogen coverage, and H^*_{i-1} corresponds to the surface after one adsorbed hydrogen has reacted. Color legend: Pt = grey, O = red, C = black, and H = white. The H* participating in each elementary reaction step is highlighted in green. The corresponding energetics are shown in **Figure 3-2b** of the main text.

The degree of rate control from microkinetic modeling is shown in **Appendix Figure B-11a** and the predicted surface coverages are shown in **Appendix Figure B-11b**. The fourth hydrogenation step is predicted to have the highest degree of rate control on Pt(111), Pt(221), Rh(111), and Rh(221). On Pt(111), the second hydrogenation step is predicted to have a negative degree of rate control, indicating that the product of the second hydrogenation step (PH_2) inhibits the formation of cyclohexanone. This is consistent with the predicted coverages on Pt(111) which show that PH_2 has a high surface coverage, inhibiting the adsorption of the reactants (i.e., phenol and hydrogen). The coverage of phenol is likely too low on Rh(111) because the calculated hydrogen adsorption energy, which does not include solvent effects, is strong relative to the experimental aqueous-phase phenol adsorption energy.

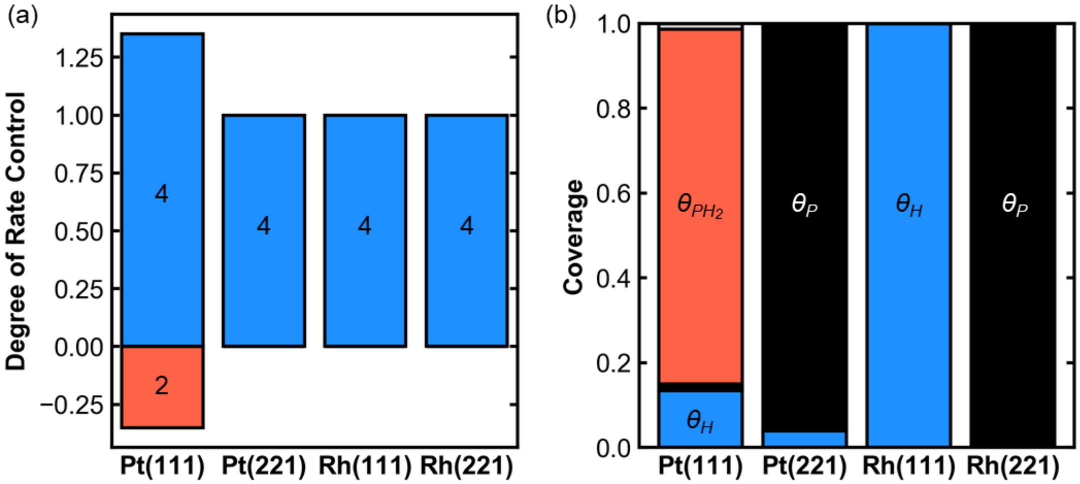

Appendix Figure B-11 Degree-of-rate-control and coverage analysis on Pt and Rh. **(a)** Degree-of-rate-control analysis from microkinetic modeling on Pt(111) ($\Delta G_{P,weak} = -9$ kJ mol^{-1}), Pt(221) ($\Delta G_{P,strong} = -29$ kJ mol^{-1}), Rh(111) ($\Delta G_{P,weak} = -7$ kJ mol^{-1}), and Rh(221) ($\Delta G_{P,strong} = -26$ kJ mol^{-1}). The fourth hydrogenation step (4) has the highest degree of rate control on all surfaces. **(b)** Equilibrium coverage of species on Pt(111), Pt(221), Rh(111), and Rh(221). θ_P denotes the coverage of phenol and is shown in black, θ_H denotes the coverage of hydrogen and is shown in blue, θ_{PH2} denotes the coverage of the twice hydrogenation phenol intermediate and is shown in red. All other adsorbed intermediates are shown in grey. $T = 300$ K and 20 mM phenol was used in the calculation.

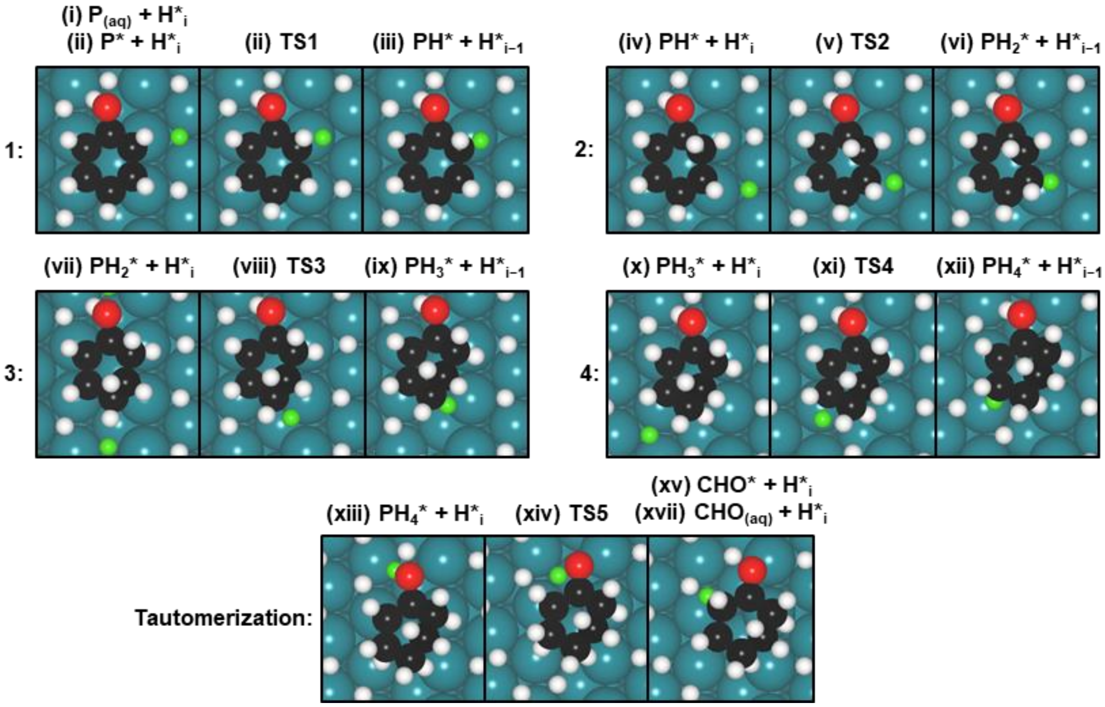

Appendix Figure B-12 DFT-predicted geometries for phenol hydrogenation on Rh(221). DFT-predicted geometries corresponding to the initial, transition, and final states for the hydrogenation of phenol ($P_{(aq)}$) to cyclohexanone ($CHO_{(aq)}$) on Rh(211) with 6/9 ML of co-adsorbed hydrogen. Products of the first, second, third, and fourth hydrogenation additions are denoted PH*, PH_2*, PH_3*, and PH_4*, respectively. TS1, TS2, TS3, and TS4 denote hydrogenation transition states and TS5 denotes the tautomerization transition state. H^*_i corresponds to adsorbed hydrogen at 6/9 ML hydrogen coverage, and H^*_{i-1} corresponds to the surface after one adsorbed hydrogen has reacted. Color legend: Rh = teal, O = red, C = black, and H = white. The H* participating in each elementary reaction step is highlighted in green. The corresponding energetics are shown in **Figure 3-4b** of the main text.

Determining Phenol Hydrogenation Mechanism on Rh(111)

Two plausible mechanisms for phenol hydrogenation on Rh(111) were evaluated. In Mechanism 1 (*M1*), phenol is hydrogenated to 1-cyclohexenol, which subsequently tautomerizes to form cyclohexanone. In Mechanism 2 (*M2*), phenol loses a hydrogen to form phenoxy and is sequentially hydrogenated to form cyclohexanone. *M1* and *M2* are summarized in **Scheme B-1**. The conversion of phenol to phenoxy has been studied on Pt(111) and Rh(111).[26] Conversion of phenol was found to be endothermic on Pt(111), but was exothermic on Rh(111). Phenol hydrogenation on Pt(111) has been predicted to proceed through *M1*.[68] Therefore, we model phenol hydrogenation using *M1* on Pt(111) and Pt(221). However, phenol hydrogenation on Rh(111) may proceed through *M2* due to the conversion of phenol to phenoxy being energetically favorable on Rh(111),[26] thus we consider both *M1* and *M2* for Rh.

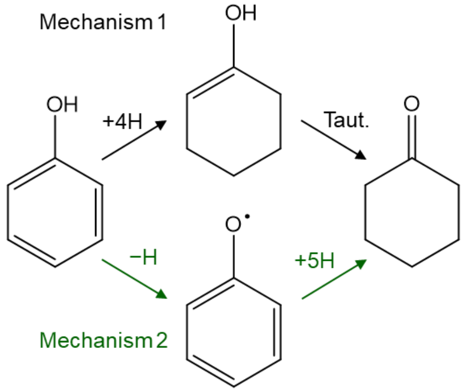

Scheme B-1 Comparison of phenol hydrogenation mechanisms. Phenol hydrogenation to 1-cyclohexenol followed by tautomerization to form cyclohexanone through Mechanism 1 (*M1*). Phenol loses a hydrogen to form phenoxy and is subsequently hydrogenated to form cyclohexanone in Mechanism 2 (*M*2).

We study both mechanisms on Rh(111) to identify the more favorable reaction pathway for phenol hydrogenation at 0 K on a 4×4×4 slab of Rh(111), corresponding to 1/16 ML coverage of phenol. The adsorption, activation, and reaction energies are shown in **Appendix Figure B-13**. M1 has a slightly lower effective barrier between (iii) and (iv) (91 kJ mol^{-1}) compared to the effective barrier between (iv) and (viii) in M2 (97 kJ mol^{-1}) indicating that the hydrogenation of phenol would occur faster through M1 than through M2. Therefore, M1, the same mechanism as on Pt, was chosen to model phenol hydrogenation on Rh.

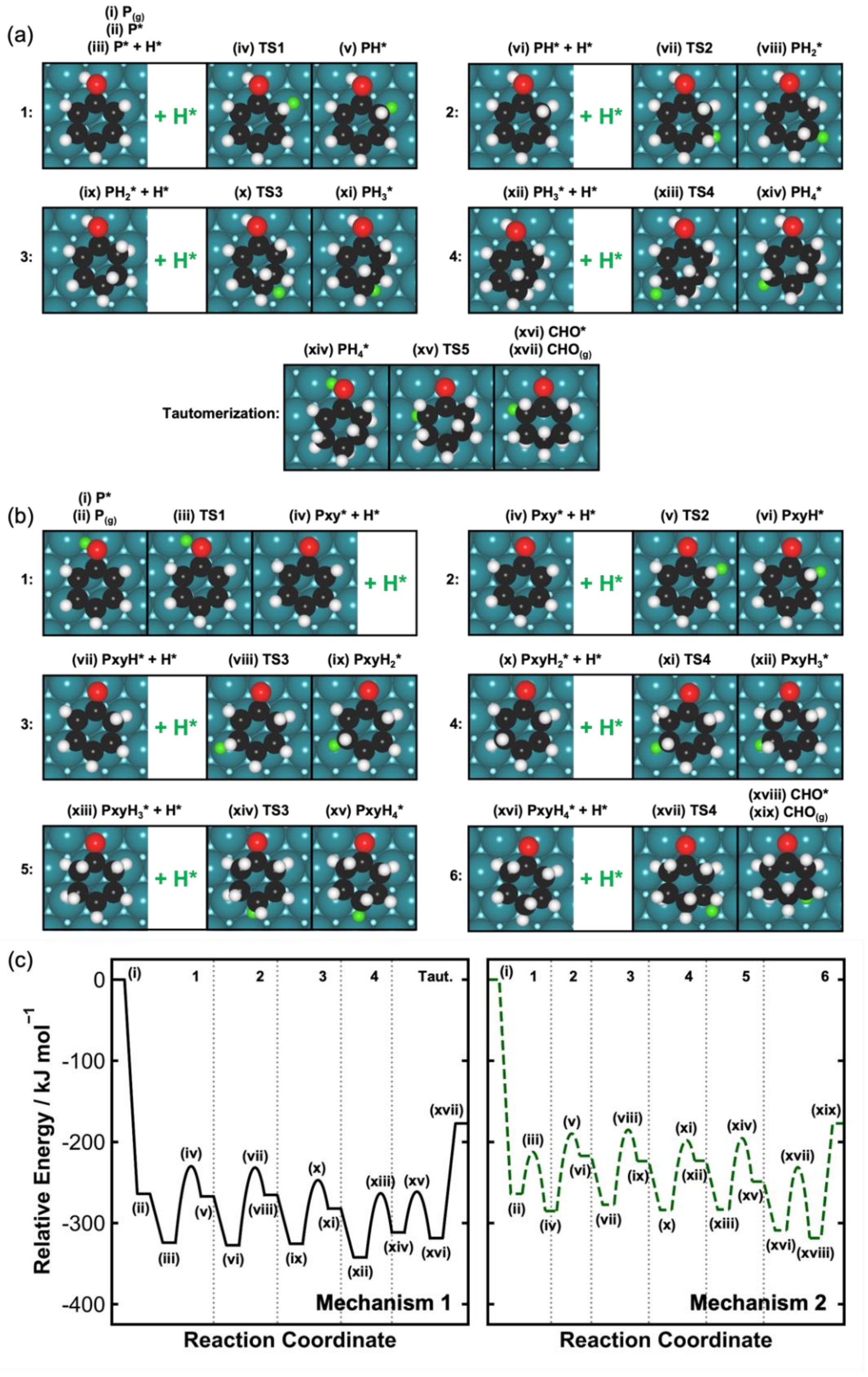

Appendix Figure B-13 Reaction energetics for mechanism comparison for phenol hydrogenation. DFT-predicted geometries corresponding to the initial, transition, and final states for the hydrogenation of phenol ($P_{(g)}$) to adsorbed cyclohexanone ($CHO_{(g)}$) on Rh(111) via **(a)** Mechanism 1 and **(b)** Mechanism 2. The phenoxy intermediate in Mechanism 2 is denoted as Pxy*. **(c)** Reaction energy profile for the electrocatalytic hydrogenation of phenol on Rh(111) via Mechanism 1 (left) and Mechanism 2 (right) at 0 K. Color legend: Pt = grey, O = red, C = black, and H = white. The H* atom participating in each elementary reaction step is highlighted in green (cases where more than one hydrogen is colored green are due to periodic boundary conditions).

Appendix C: Supporting Information for Phenol Hydrogenation on Platinum-Cobalt Alloys

This appendix was adapted from Barth, I.; Akinola, J.; Singh, N.; Goldsmith, B. R. Electrocatalytic Hydrogenation of Phenol on Platinum-Cobalt Alloys. *Submitted*, **2023**. My contribution to this work is the density functional theory modeling. James Akinola performed the experimental work.

C.1 HER Kinetics of Pt_xCo_y/C Catalysts

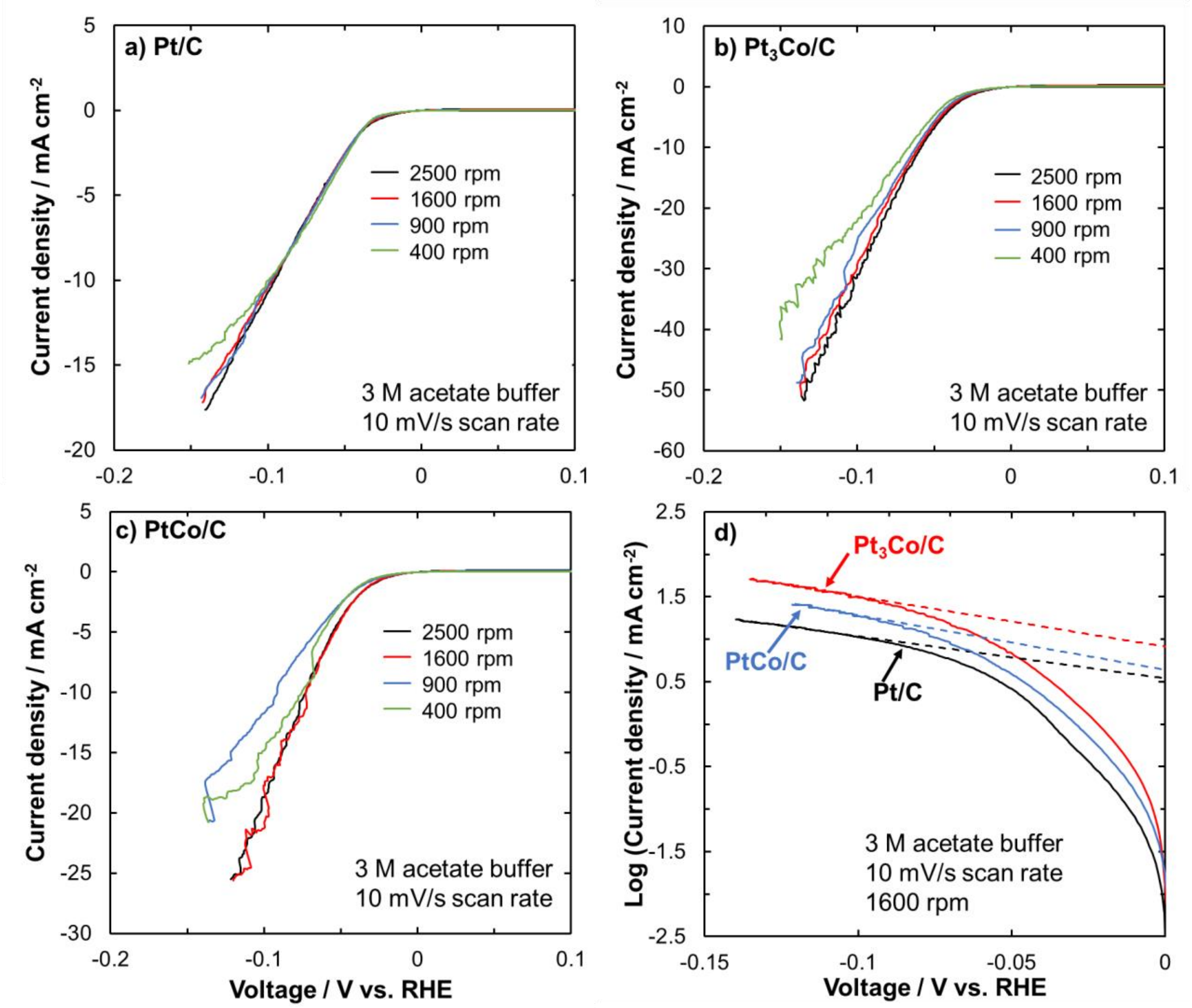

Appendix Figure C-1 Linear scan voltammograms and Tafel plots for Pt/C and Pt_xCo_y/C. LSVs were performed at 23.3°C in 3 M acetate buffer (pH 5.2) and a scan rate of 10 mV/s at rotation speeds of 400, 900, 1600, and 2500 rpm for **a)** Pt/C, **b)** Pt_3Co/C, and **c)** PtCo/C. **d)** Log(current density) vs. the HER overpotential for Pt/C, Pt_3Co/C, and PtCo/C for measurements at 1600 rpm. The Tafel lines (dashed lines) were obtained by fitting the data at potentials $\leq$ –0.1 V vs. RHE to the Tafel equation as described in the methods in the main text. The Tafel slopes for Pt/C, Pt_3Co/C and PtCo/C are 142 mV dec^{-1}, 170 mV dec^{-1} and 154 mV dec^{-1}, respectively.

C.2 Catalyst Lattice Constants

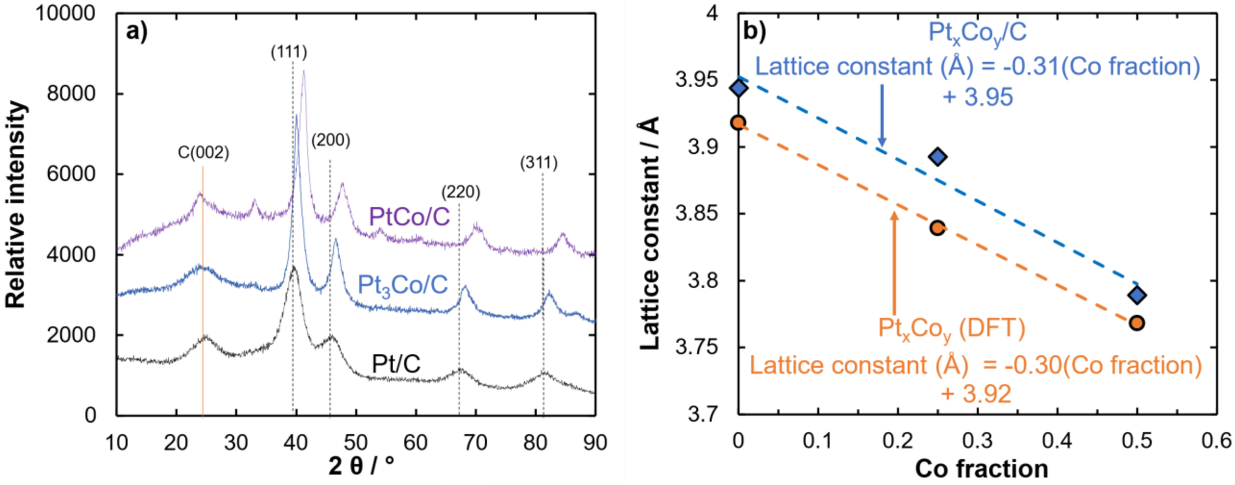

Appendix Figure C-2 X-ray diffraction (XRD) spectra and lattice constant as a function of Co fraction for Pt, Pt_3Co, and PtCo face-centered cubic structures. **a)** XRD spectra for Pt_xCo_y/C. The vertical lines in a) correspond to the 2θ peak locations for the Pt/C to observe the shift in peak location for Pt_xCo_y/C. **b)** Lattice constants from our DFT-modelled Pt_xCo_y slabs (orange) and lattice constants from Pt_xCo_y/C obtained using Bragg's law (blue).

A similar slope of the lattice constant with the Co fraction is observed in **Appendix Figure C-2b** for both the computed lattice constant and experimental data. The similar slope confirms that Pt_xCo_y/C forms an FCC alloy with the target Co fraction. The slope (0.3) from **Appendix Figure C-2b** was used to estimate the Co fraction for the Pt_xCo_y/felt samples shown in **Figure 4-2c** based on their lattice constant from their XRD data in **Figure 4-2b**.

C.3 Sublayer Segregation Energies

Sublayer segregation energies of Co in Pt_3Co, PtCo, and $PtCo_3$ core-shell alloys were calculated using the method described by Farsi & Deskins where Co atoms in the second layer are substituted with Pt atoms in the first layer, and the energy difference between the two slabs is taken.[269] Specifically, the segregation energies were calculated as $E_{seg} = E_{Co,first\ layer} - E_{Co,sublayer}$. Slabs were modeled using 2 × 2 × 4 supercells with the Pt/Pt_xCo_y structure. The settings for the calculations were the same as described in the Methods in the main text, except a 7 × 7 × 1 *k*-point grid was used to sample the Brillouin zone of the smaller supercells. One Co substitution was calculated for the Pt_3Co, up to two Co substitutions were calculated for PtCo, and up to three Co substitutions were calculated for $PtCo_3$. Each Co atom from the subsurface layer was substituted with each Pt atom from the surface layer, such that all possible substitutions were considered. Surface segregation energies were calculated under vacuum, with 0.25 monolayer (ML) of adsorbed hydrogen (H*), and with 1 ML H*.

Calculated segregation energies for the Pt/Pt_xCo_y alloys are shown in **Appendix Figure C-3**. Under vacuum conditions (**Appendix Figure C-3a**), all substitutions were positive in energy, indicating that it is energetically favorable for Pt to be in the surface and for Co to be in the subsurface, consistent with past work.[270] Although the energy is positive, the substitution of a single Co atom from the subsurface is lower in energy for slabs with higher Co fractions. Substituting more than one Co atom in Pt/PtCo and $Pt/PtCo_3$ is higher in energy than a single Co substitution. Calculated segregation energies with 0.25 ML of H* adsorbed on the slabs are shown in **Appendix Figure C-3b**. The segregation energies decreased in all instances compared to vacuum conditions. A single Co substitution is energetically unfavorable for Pt/Pt_3Co and Pt/PtCo, but is energetically favorable for $Pt/PtCo_3$. All predicted segregation energies of Co to the surface are exothermic when 1 ML of H* is modeled on the Pt/Pt_xCo_y slabs (**Appendix Figure C-3c**).

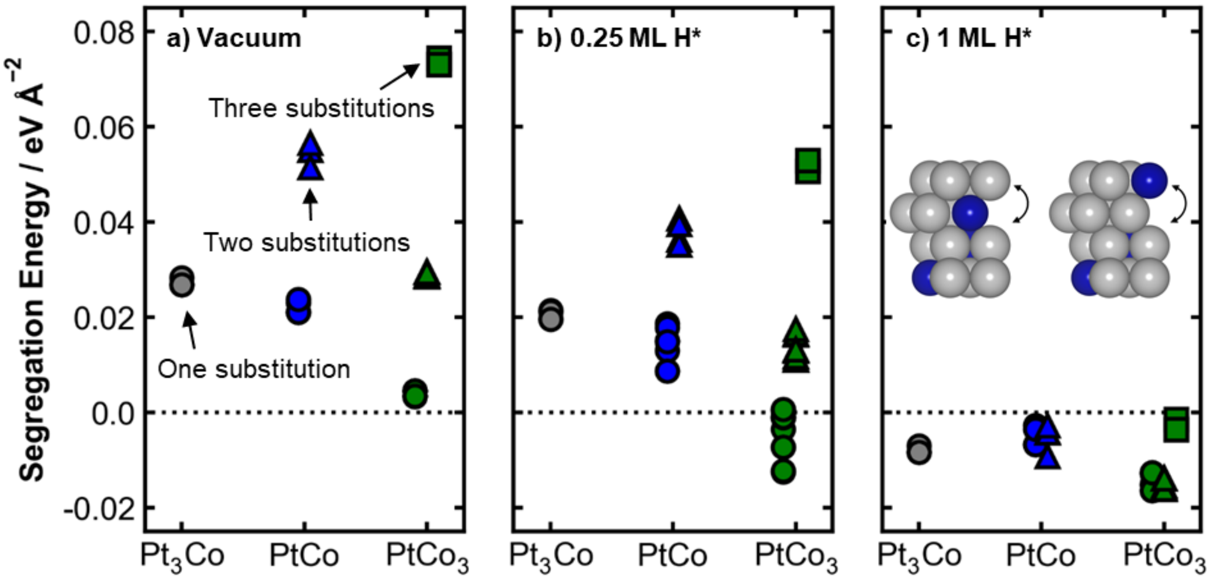

Appendix Figure C-3 Calculated surface segregation energies of Pt_xCo_y alloys. **a)** Segregation energies under vacuum conditions. **b)** Segregation energies with 0.25 ML H*. **c)** Segregation energies with 1 ML H*. An inset illustrating how substitutions of Co and Pt were modelled is in **c)**. Gray points correspond to the energies of Pt_3Co, blue points correspond to the energies of PtCo, and green points correspond to the energies of $PtCo_3$. Circles are for a single Pt-Co substitution, triangles are for two Pt-Co substitutions, and squares are for three Pt-Co substitutions.

C.4 Cyclic Voltammetry, X-ray Absorption, and Microscopy

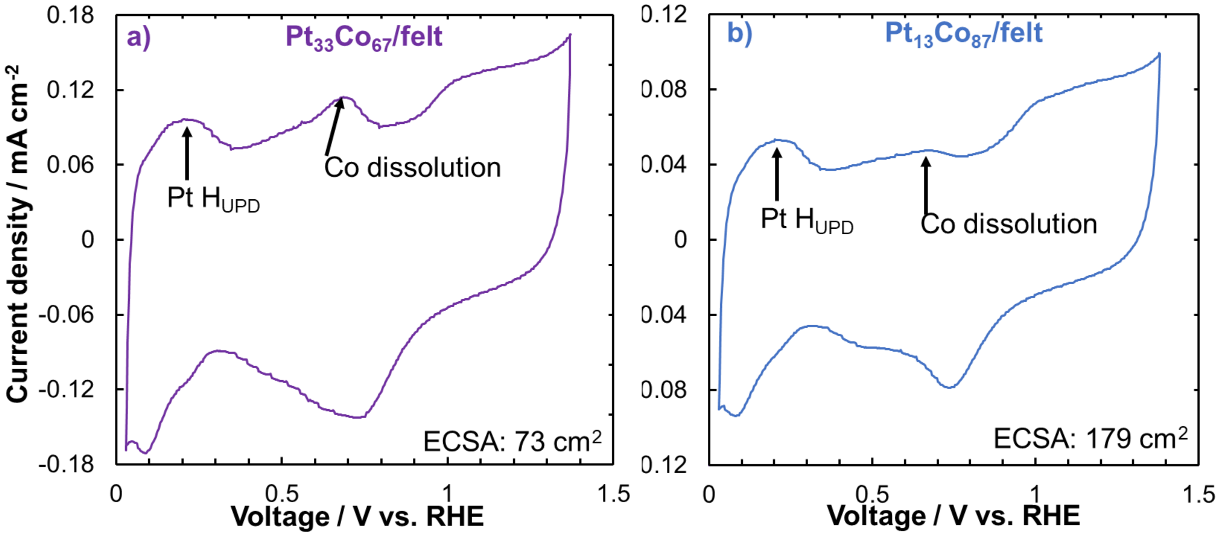

Appendix Figure C-4 Cyclic voltammograms of as prepared Pt_xCo_y/felt catalysts. **a)** Cycle #2 of the as prepared $Pt_{33}Co_{67}$/felt sample that became $Pt_{80}Co_{20}$/felt after pretreatment. **b)** Cycle #2 of the as prepared $Pt_{13}Co_{87}$/felt that became $Pt_{62}Co_{38}$/felt after pretreatment. CVs were performed in 3 M acetate buffer supporting electrolyte at 23.3°C and a scan rate of 20 mV/s.

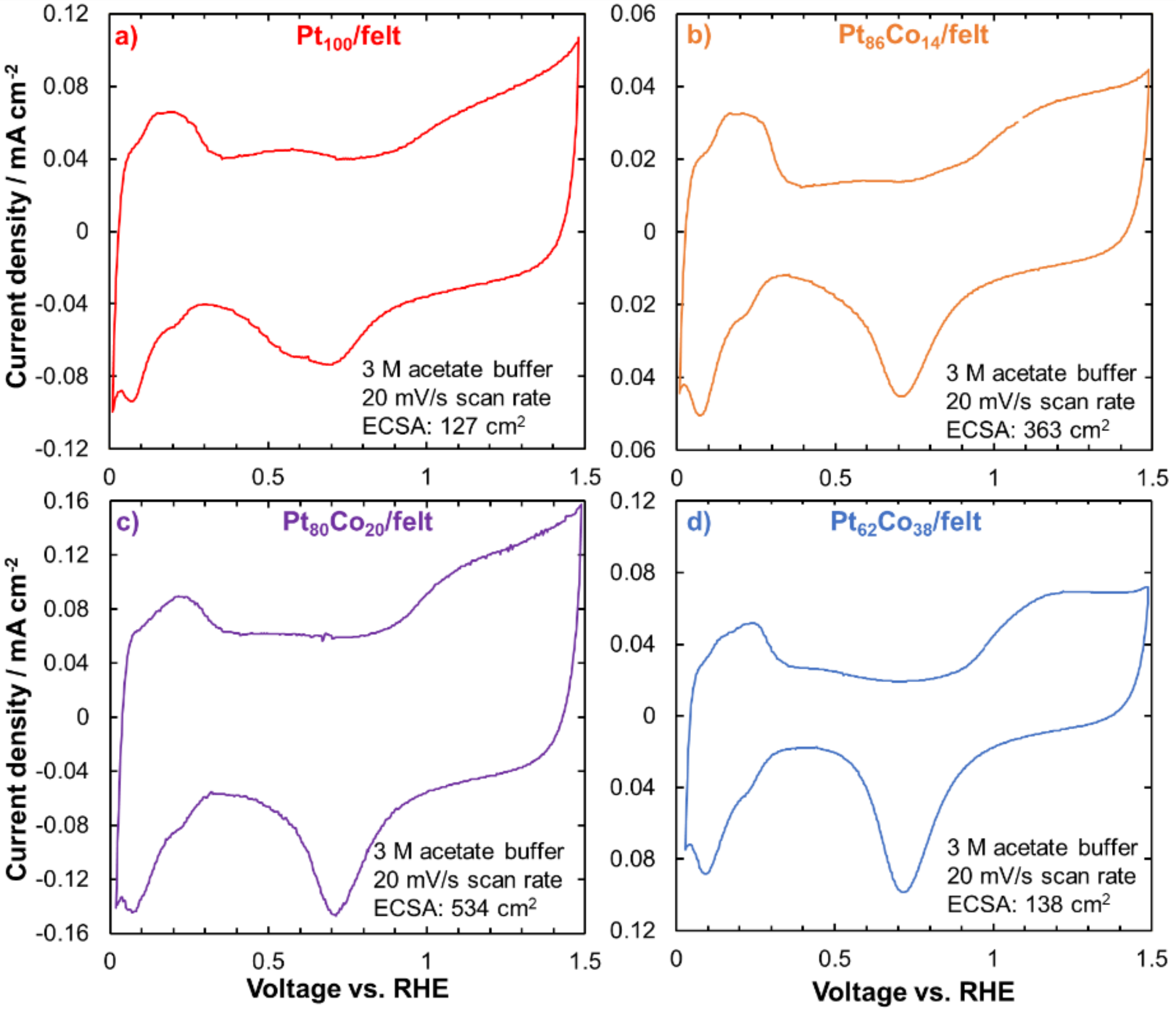

Appendix Figure C-5 Cyclic voltammograms of the pretreated catalysts synthesized on carbon felt support. **a)** Pt_{100}/felt, **b)** $Pt_{80}Co_{20}$/felt, **c)** $Pt_{86}Co_{14}$/felt, and **d)** $Pt_{62}Co_{38}$/felt. The CVs were performed in 3 M acetate buffer supporting electrolyte at 23.3 °C and at a scan rate of 20 mV/s.

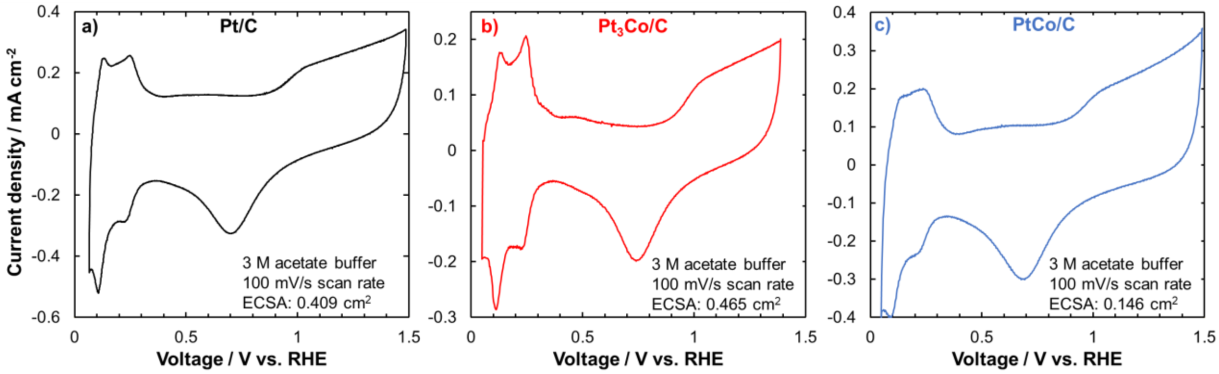

Appendix Figure C-6 Cyclic voltammograms of the pretreated catalysts supported on Vulcan carbon. **a)** Pt/C, **b)** Pt_3Co/C, and **c)** PtCo/C. The CVs were performed at 23.3°C in 3 M acetate buffer supporting electrolyte and at a scan rate of 100 mV/s. Cyclic voltammetry for the Vulcan carbon supported catalysts were performed in a rotating disk electrode set up. The much lower loading is the reason for the smaller ECSA compared to the catalysts supported on carbon felt in **Appendix Figure C-5**.

Cyclic voltammograms of the as-prepared catalyst, prior to cyclic voltammetry pretreatment, indicate dissolution of Co (**Appendix Figure C-4**). Following the pretreatment protocol, the oxidation peak corresponding to Co dissolution at −0.7 V vs. RHE no longer appears (**Appendix Figure C-5** & **Appendix Figure C-6**). The reduction peak at approximately −0.7 V vs. RHE corresponds to reduction of platinum oxide.

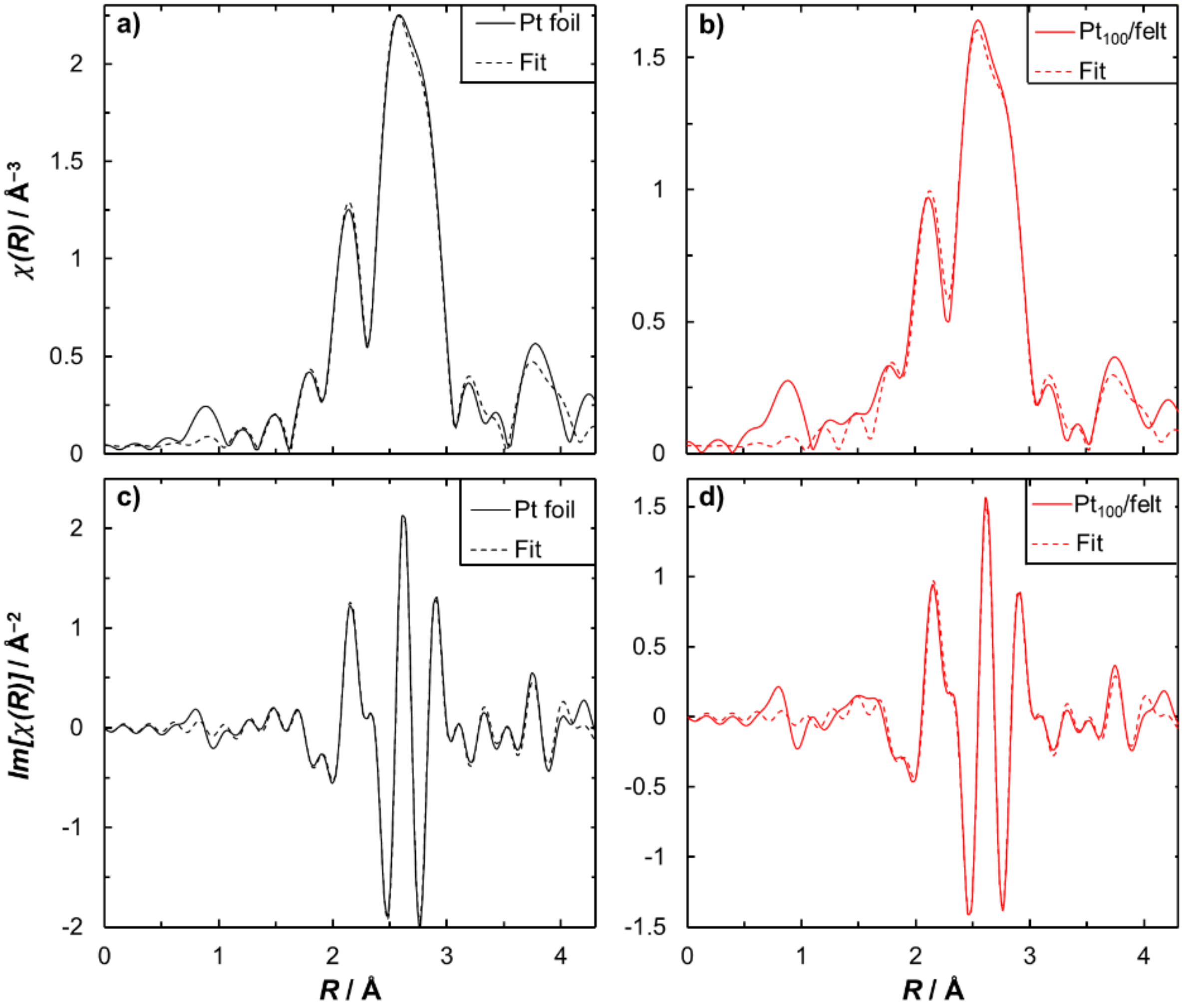

Appendix Figure C-7 Extended X-ray absorption fine structure (EXAFS) spectra of Pt foil and Pt_{100}/felt catalysts performed at the Pt L_3-edge and their fit. The magnitude of the *R*-space spectra (solid lines) and their fits (dashed lines) using a Pt-Pt first and second shell for **a)** Pt foil and **b)** Pt_{100}/felt. The imaginary *R*-space spectra (solid lines) and their Artemis fits (dashed lines) for **c)** Pt foil and **d)** Pt_{100}/felt.

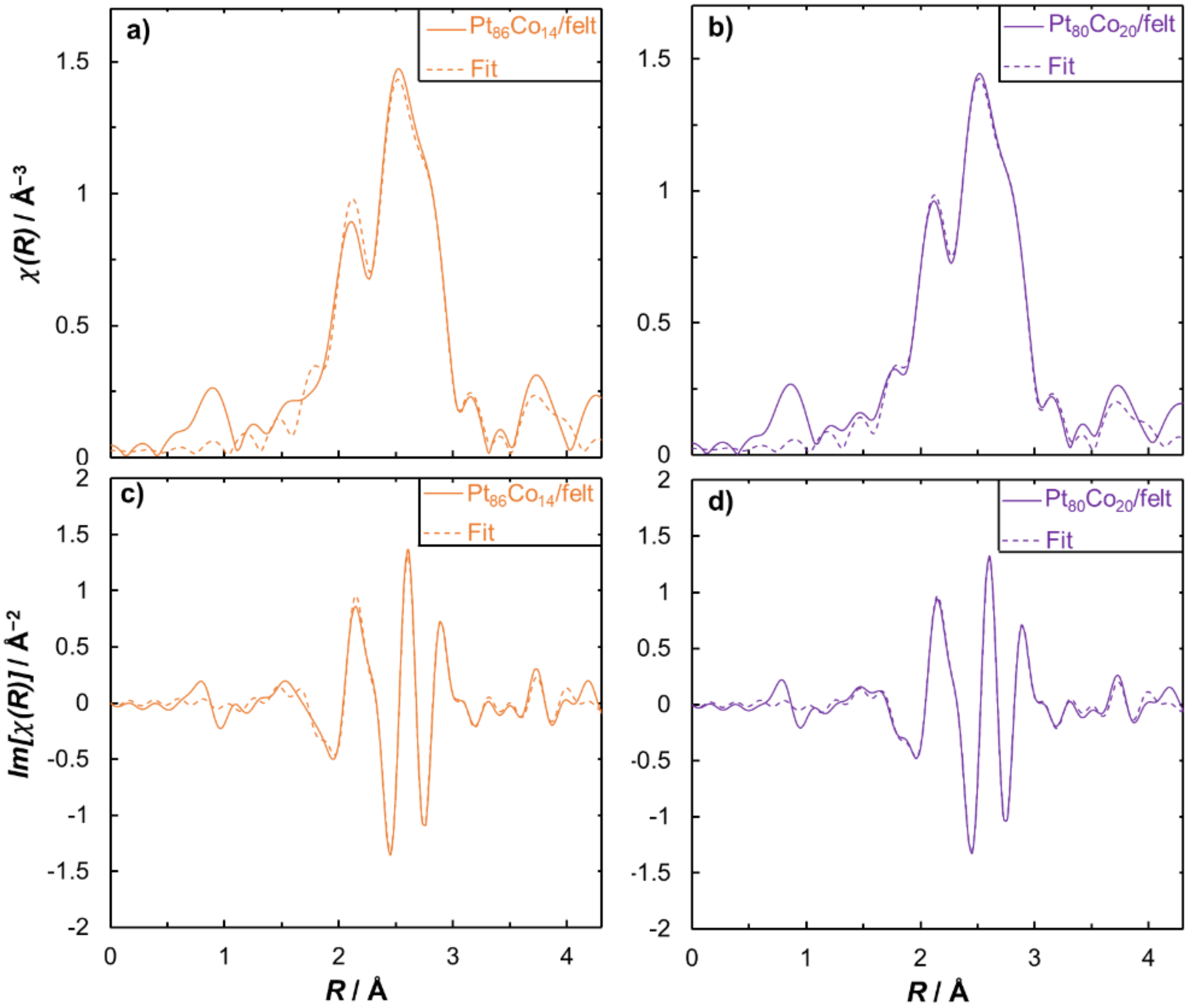

Appendix Figure C-8 EXAFS spectra of $Pt_{86}Co_{14}$/felt and $Pt_{80}Co_{20}$/felt catalysts performed at the Pt L_3-edge and their fit. The magnitude of the *R*-space spectra (solid lines) and their fits (dashed lines) to a Pt-Pt first and second shell and a Pt-Co first shell for **a)** $Pt_{86}Co_{14}$/felt and **b)** $Pt_{80}Co_{20}$/felt. The imaginary *R*-space spectra (solid lines) and their fits (dashed lines) for **c)** $Pt_{86}Co_{14}$/felt and **d)** $Pt_{80}Co_{20}$/felt.

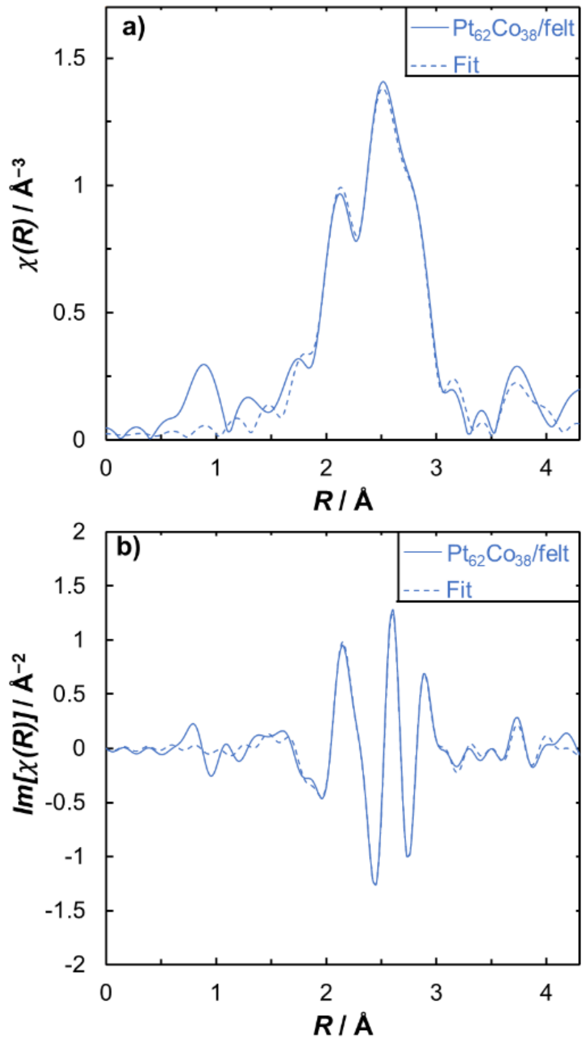

Appendix Figure C-9 EXAFS spectra of Pt$_{62}$Co$_{38}$/felt at the Pt L$_3$-edge and fit. **a)** The magnitude of the *R*-space spectrum (solid line) and its fit (dashed line) to a Pt-Pt first and second shell and a Pt-Co first shell. **b)** The imaginary *R*-space spectra (solid line) and its fit (dashed line).

Appendix Table C-1 Tabulated EXAFS fitting results. Tabulated fitting results for EXAFS of the Pt foil and pretreated Pt$_x$Co$_y$/felt catalysts at the Pt L$_3$-edge. When fitting the Pt foil, the Pt coordination numbers for the 1st and 2nd shell was set to 12 and 6 (bolded), respectively to obtain the amplitude factor $S_0^2 = 0.852 \pm 0.035$ that is used to fit the Pt$_x$Co$_y$/felt spectra. The results of the fittings and errors for *R*, CN, σ^2, and ΔE_0 are given in the table.

	Material	Pt foil	Pt$_{100}$/felt	Pt$_{86}$Co$_{14}$/felt	Pt$_{80}$Co$_{20}$/felt	Pt$_{62}$Co$_{38}$/felt
Pt-Pt	*R* (Å)	2.765 ± 0.002	2.758 ± 0.003	2.744 ± 0.004	2.744 ± 0.0029	2.743 ± 0.004
	CN	**12**	10.70 ± 0.64	9.77 ± 1.13	9.63 ± 0.86	9.59 ± 1.04
	σ^2 (Å^2)	0.005 ± 0.0002	0.006 ± 0.0003	0.006 ± 0.0005	0.006 ± 0.0004	0.007 ± 0.0005
	ΔE_0 (eV)	8.35 ± 0.36	7.54 ± 0.52	7.26 ± 0.47	6.67 ± 0.68	6.71 ± 0.54
Pt-Co	*R* (Å)	N/A	N/A	2.663 ± 0.041	2.663 ± 0.023	2.663 ± 0.023
	CN	N/A	N/A	1.06 ± 1.17	1.09 ± 0.72	1.15 ± 0.79
	σ^2 (Å^2)	N/A	N/A	0.013± 0.0106	0.010± 0.0055	0.009± 0.0054
	ΔE_0 (eV)	8.35 ± 0.36	7.54 ± 0.52	7.26 ± 0.47	6.67 ± 0.68	6.71 ± 0.54
Pt-Pt (2n	*R* (Å)	3.909 ± 0.008	3.901 ± 0.014	3.879 ± 0.019	3.879 ± 0.017	3.885 ± 0.019

	CN	**6**	3.83 ± 2.03	2.54 ± 1.86	2.87 ± 1.65	2.53 ± 1.74
	σ^2 (Å^2)	0.006 ± 0.0008	0.007 ± 0.0028	0.006± 0.0036	0.007± 0.0032	0.006± 0.0035
	ΔE_0 (eV)	8.35 ± 0.36	7.54 ± 0.52	7.26 ± 0.47	6.67 ± 0.68	6.71 ± 0.54

Appendix Table C-2 Tabulated XANES fitting results. Tabulated linear combination fitting results of XANES for Pt_xCo_y/felt catalysts at the Pt L_3-edge using Pt foil and PtO_2 as standards. Fitting was performed at −20 eV below the edge and 30 eV post edge.

Material	**% Pt**	**% PtO_2**
Pt_{100}/felt	97.7	2.3
$Pt_{86}Co_{14}$/felt	99.7	0.3
$Pt_{80}Co_{20}$/felt	99.4	0.6
$Pt_{62}Co_{38}$/felt	98.6	1.4

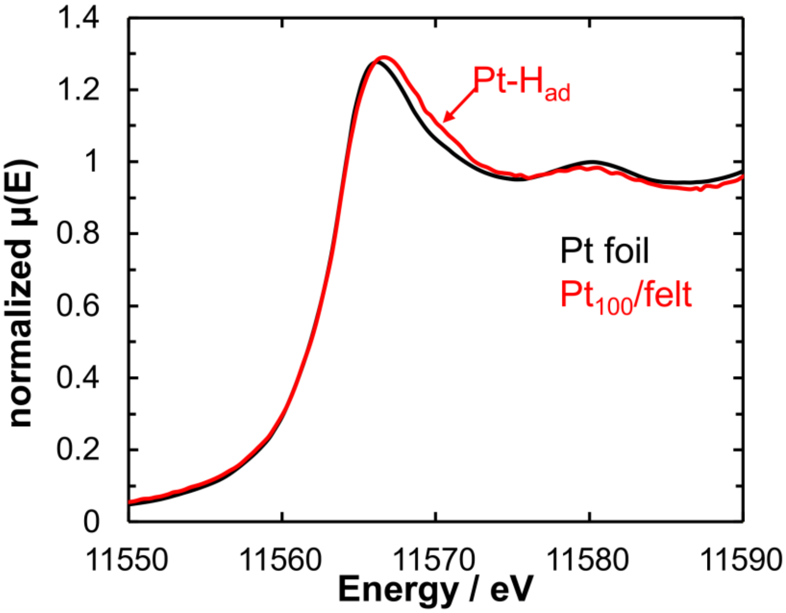

Appendix Figure C-10 XANES of Pt_{100}/felt at the Pt L_3-edge at −0.05 V vs. RHE and Pt foil. Supporting electrolyte is 3 M acetate buffer with graphite rod as counter and a leak-free Ag/AgCl as reference electrode. Reference electrode was calibrated to RHE before using it for experiments.

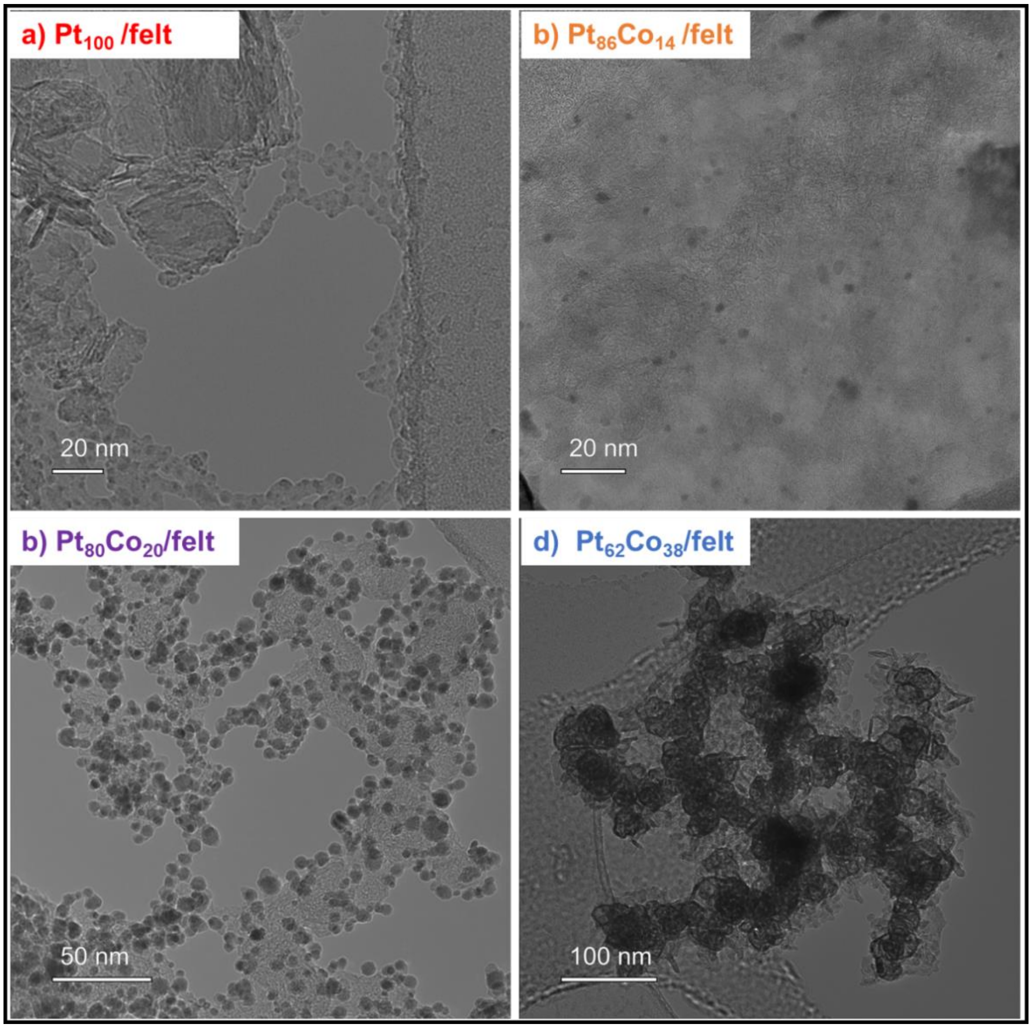

Appendix Figure C-11 Representative transmission electron microscopy (TEM) micrographs of the Pt_xCo_y/felt catalysts. **a)** Pt_{100}/felt, **b)** $Pt_{86}Co_{14}$/felt, **c)** $Pt_{80}Co_{20}$/felt, **d)** $Pt_{62}Co_{38}$/felt. All images are taken after pretreatment to remove unalloyed Co, but before use for ECH.

Appendix Table C-3 Pt_xCo_y particle sizes. Particle sizes from TEM and XRD using the Scherrer equation for the pretreated Pt_xCo_y on felts and on Vulcan carbon. The first shell Pt-metal coordination number from EXAFS and particle size from the correlation in ref. [271] is shown.

Catalyst	TEM particle size / nm	XRD crystallite size / nm	EXAFS total 1st shell coordination number	Particle size range based on EXAFS coordination / nm
Pt_{100}/felt	5.8 ± 1.3	9.7	10.7 ± 0.6	2.3−4.3
$Pt_{86}Co_{14}$/felt	5.8 ± 1.8	8.0	10.8 ± 1.2	2.0–8.5
$Pt_{80}Co_{20}$/felt	5.5 ± 1.2	8.0	10.7 ± 0.9	2.1–5.5
$Pt_{62}Co_{38}$/felt	13.6 ± 3.3	7.9	10.7 ± 1.0	2.0–6.0
Pt/C	4.2 ± 0.7	2.5	7.2 ± 1.2	0.9−1.4
Pt_3Co/C	5.3 ± 1.2	4.6	9.4 ± 0.9	1.4–2.5
PtCo/C	5.1 ± 1.1	4.4	8.5 ± 1.0	1.2–1.9

C.5 Kinetic Model

We use a Langmuir-Hinshelwood kinetic model to understand the ECH TOF behavior on the Pt_xCo_y/felt catalysts as described in the main text (**Eq. 4-2** through **Eq. 4-5**). In addition to the assumptions described in the main text (i.e., phenol adsorption is independent of applied potential, hydrogen adsorption is a function of applied potential, surface reaction is the rate-determining step, the rate constant is independent of potential), to describe the TOF as a function of Co fraction we make the following assumptions:

1. The H adsorption energy weakens with Co fraction for both the Pt_xCo_y and Pt/Pt_xCo_y structures provided the Co fraction is less than 0.5. Although at Co fraction = 0.5 the Pt_xCo_y structures shows stronger H adsorption, we model Co fractions < 0.5 for simplicity. Evidence for this assumption is shown in **Figure 4-1b** of the main text.
2. The phenol adsorption energy is unaffected by Co fraction. Evidence for this is shown by the experimental values in **Figure 4-5** in the main text.
3. The first hydrogenation barrier increases linearly with Co fraction for the Pt_xCo_y structure and reduces with Co fraction for the Pt/Pt_xCo_y structure. Evidence for this assumption is shown in **Figure 4-6** of the main text.

In **Eq. C-1** we show our model for the TOF of phenol ECH as a function of both Co fraction in the catalyst (y_{Co}) and applied electrochemical potential (E). This equation and the variables are the same as combining **Eq. 4-4** and **Eq. 4-5** in the main text, except here we indicate the explicit dependence of certain terms on y_{Co} and E. For example, $K_{\mathrm{H}}(y_{\mathrm{Co}}, E)$ is the equilibrium adsorption coefficient of H as a function of Co content in the catalyst and applied potential.

$$TOF(y_{\mathrm{Co}}, E) = A \exp^{\left(\frac{-\Delta H_f^{\ddagger}(y_{\mathrm{Co}})}{RT}\right)} \frac{K_{\mathrm{H}}(y_{\mathrm{Co}}, E) C_{\mathrm{H}} K_{\mathrm{P}} C_{\mathrm{P}}}{(1 + K_{\mathrm{H}}(y_{\mathrm{Co}}, E) C_{\mathrm{H}} + K_{\mathrm{P}} C_{\mathrm{P}})^2} \quad \textbf{Eq. C-1}$$

We use a value of 10^8 sec^{-1} for the pre-exponential factor (A). The activation enthalpy for the first hydrogenation step ($\Delta H_f^\ddagger$) as a function of Co fraction is given by **Eq. C-2**:

$$\Delta H_f^\ddagger(y_{\mathrm{Co}}) = \Delta H_f^\ddagger(y_{\mathrm{Co}} = 0) + \beta_1 y_{\mathrm{Co}} \qquad \textbf{Eq. C-2}$$

where $\Delta H_f^\ddagger(y_{\mathrm{Co}} = 0)$ is the activation enthalpy for pure Pt, R is the ideal gas constant = 8.314 kJ mol^{-1} and T is the temperature = 300 K. As we show in **Figure 4-6b**, the computed first hydrogenation activation enthalpy linearly scales with Co fraction, where it increases for the Pt_xCo_y structure and decreases for the Pt/Pt_xCo_y structure. To capture this qualitatively in our kinetic model we use a value of β_1 = 8 kJ mol^{-1} for the Pt_xCo_y structures and β_1 = −8 kJ mol^{-1} for the Pt/Pt_xCo_y structures. We note that directly including the computed activation enthalpies into the model does not give quantitative agreement with our experimental rates, so we look instead for qualitative trends.

We assume the phenol adsorption equilibrium constant K_P is independent of the Co fraction and potential as discussed in the main text. In reality, the potential may affect $\Delta G_{\mathrm{ads,P}}$ by strengthening the water-metal bond at potentials far away from the potential of zero charge of the metal in the system.[119] The adsorption energies from the isotherms fits on the Pt_xCo_y alloy in **Figure 4-5** are also almost independent of the Co fraction. The fitted value is an average value of both the active (111) facet and inactive (100) and (110) steps. We use the $\Delta G_{\mathrm{ads,P}}$ = −9 kJ mol^{-1} for the (111) facet of Pt, which we have previously shown is the active facet for phenol ECH on Pt.[21] The concentration of phenol used in our experiments was 20 mM, so we set C_{P} = 0.02 M in the model.

We show the dependence of the energy of adsorption of hydrogen onto the catalyst by **Eq. C-3**. We use a value of $\Delta G_{\mathrm{H}}(y_{\mathrm{Co}} = 0, E = 0\text{ V vs. RHE})$ = −1 kJ mol^{-1} calculated in the aqueous-phase for Pt.[272] We use a value of β_2 = 40.4 kJ mol^{-1} in the model which represents how ΔG_{H} is weakened with increasing Co fraction from the trend in **Figure 4-1b** in the main text.

$$\Delta G_{\mathrm{H}}(y_{\mathrm{Co}}, E = 0\ \mathrm{V\ vs.\ RHE}) = \Delta G_{\mathrm{H}}(y_{\mathrm{Co}} = 0, E = 0\ \mathrm{V\ vs.\ RHE}) + \beta_2 y_{\mathrm{Co}} \qquad \textbf{Eq. C-3}$$

Combining **Eq. C-3** with **Eq. 4-2** in the main text we describe the hydrogen adsorption coefficient as a function of Co fraction and potential in **Eq. C-4**.

$$K_{\mathrm{H}}(y_{\mathrm{Co}}, E) = \exp\left(\frac{-[\Delta G_{\mathrm{H}}(y_{\mathrm{Co}} = 0, E = 0\ \mathrm{V\ vs.\ RHE}) + \beta_2 y_{\mathrm{Co}}]}{RT}\right)\exp\left(\frac{-FE}{RT}\right) \qquad \textbf{Eq. C-4}$$

Coupling **Eq. C-1**, **Eq. C-2**, and **Eq. C-4** and specified constants, we obtain the equation that we use to predict the ECH TOF shown in **Figure 4-7**.

References

(1) Tursi, A. A Review on Biomass: Importance, Chemistry, Classification, and Conversion. *Biofuel Res. J.* **2019**, *6* (2), 962–979. https://doi.org/10.18331/BRJ2019.6.2.3.

(2) Akhade, S. A.; Singh, N.; Gutiérrez, O. Y.; Lopez-Ruiz, J.; Wang, H.; Holladay, J. D.; Liu, Y.; Karkamkar, A.; Weber, R. S.; Padmaperuma, A. B.; et al. Electrocatalytic Hydrogenation of Biomass-Derived Organics: A Review. *Chem. Rev.* **2020**, *120* (20), 11370–11419. https://doi.org/10.1021/acs.chemrev.0c00158.

(3) Dhyani, V.; Bhaskar, T. A Comprehensive Review on the Pyrolysis of Lignocellulosic Biomass. *Renew. Energy* **2018**, *129*, 695–716. https://doi.org/10.1016/j.renene.2017.04.035.

(4) Gollakota, A. R. K.; Kishore, N.; Gu, S. A Review on Hydrothermal Liquefaction of Biomass. *Renew. Sustain. Energy Rev.* **2018**, *81* (April 2017), 1378–1392. https://doi.org/10.1016/j.rser.2017.05.178.

(5) Zhang, Q.; Chang, J.; Wang, T.; Xu, Y. Review of Biomass Pyrolysis Oil Properties and Upgrading Research. *Energy Convers. Manag.* **2007**, *48* (1), 87–92. https://doi.org/10.1016/j.enconman.2006.05.010.

(6) Zhang, X.-S.; Yang, G.-X.; Jiang, H.; Liu, W.-J.; Ding, H.-S. Mass Production of Chemicals from Biomass-Derived Oil by Directly Atmospheric Distillation Coupled with Co-Pyrolysis. *Sci. Rep.* **2013**, *3* (1), 1120. https://doi.org/10.1038/srep01120.

(7) Mullen, C. A.; Boateng, A. A. Chemical Composition of Bio-Oils Produced by Fast Pyrolysis of Two Energy Crops. *Energy and Fuels* **2008**, *22* (3), 2104–2109. https://doi.org/10.1021/ef700776w.

(8) Bagnato, G.; Sanna, A.; Paone, E.; Catizzone, E. Recent Catalytic Advances in Hydrotreatment Processes of Pyrolysis Bio-Oil. *Catalysts* **2021**, *11* (2), 157. https://doi.org/10.3390/catal11020157.

(9) Chen, D.; Zhou, J.; Zhang, Q.; Zhu, X. Evaluation Methods and Research Progresses in Bio-Oil Storage Stability. *Renew. Sustain. Energy Rev.* **2014**, *40*, 69–79. https://doi.org/10.1016/j.rser.2014.07.159.

(10) Bulushev, D. A.; Ross, J. R. H. Catalysis for Conversion of Biomass to Fuels via Pyrolysis and Gasification: A Review. *Catal. Today* **2011**, *171* (1), 1–13. https://doi.org/10.1016/j.cattod.2011.02.005.

(11) Song, Y.; Sanyal, U.; Pangotra, D.; Holladay, J. D.; Camaioni, D. M.; Gutiérrez, O. Y.; Lercher, J. A. Hydrogenation of Benzaldehyde via Electrocatalysis and Thermal Catalysis on Carbon-Supported Metals. *J. Catal.* **2018**, *359*, 68–75. https://doi.org/10.1016/j.jcat.2017.12.026.

(12) Song, Y.; Gutiérrez, O. Y.; Herranz, J.; Lercher, J. A. Aqueous Phase Electrocatalysis and Thermal Catalysis for the Hydrogenation of Phenol at Mild Conditions. *Appl. Catal. B Environ.* **2016**, *182*, 236–246. https://doi.org/10.1016/j.apcatb.2015.09.027.

(13) Garedew, M.; Young-Farhat, D.; Jackson, J. E.; Saffron, C. M. Electrocatalytic Upgrading

of Phenolic Compounds Observed after Lignin Pyrolysis. *ACS Sustain. Chem. Eng.* **2019**, *7* (9), 8375–8386. https://doi.org/10.1021/acssuschemeng.9b00019.

(14) Zhu, Y.; Biddy, M. J.; Jones, S. B.; Elliott, D. C.; Schmidt, A. J. Techno-Economic Analysis of Liquid Fuel Production from Woody Biomass via Hydrothermal Liquefaction (HTL) and Upgrading. *Appl. Energy* **2014**, *129*, 384–394. https://doi.org/10.1016/j.apenergy.2014.03.053.

(15) Brown, T. R.; Zhang, Y.; Hu, G.; Brown, R. C. Techno-Economic Analysis of Biobased Chemicals Production via Integrated Catalytic Processing. *Biofuels, Bioprod. Biorefining* **2012**, *6* (1), 73–87. https://doi.org/10.1002/bbb.344.

(16) Meyer, P. A.; Snowden-Swan, L. J.; Rappé, K. G.; Jones, S. B.; Westover, T. L.; Cafferty, K. G. Field-to-Fuel Performance Testing of Lignocellulosic Feedstocks for Fast Pyrolysis and Upgrading: Techno-Economic Analysis and Greenhouse Gas Life Cycle Analysis. *Energy & Fuels* **2016**, *30* (11), 9427–9439. https://doi.org/10.1021/acs.energyfuels.6b01643.

(17) Werpy, T.; Petersen, G. *Top Value Added Chemicals from Biomass: Volume I -- Results of Screening for Potential Candidates from Sugars and Synthesis Gas*; Golden, CO (United States), 2004. https://doi.org/10.2172/15008859.

(18) Holladay, J. E.; White, J. F.; Bozell, J. J.; Johnson, D. *Top Value-Added Chemicals from Biomass - Volume II—Results of Screening for Potential Candidates from Biorefinery Lignin*; Richland, WA (United States), 2007; Vol. II. https://doi.org/10.2172/921839.

(19) Sanyal, U.; Lopez-Ruiz, J.; Padmaperuma, A. B.; Holladay, J.; Gutiérrez, O. Y. Electrocatalytic Hydrogenation of Oxygenated Compounds in Aqueous Phase. *Org. Process Res. Dev.* **2018**, *22* (12), 1590–1598. https://doi.org/10.1021/acs.oprd.8b00236.

(20) Yu, W.; Porosoff, M. D.; Chen, J. G. Review of Pt-Based Bimetallic Catalysis: From Model Surfaces to Supported Catalysts. *Chem. Rev.* **2012**, *112* (11), 5780–5817. https://doi.org/10.1021/cr300096b.

(21) Singh, N.; Sanyal, U.; Ruehl, G.; Stoerzinger, K. A.; Gutiérrez, O. Y.; Camaioni, D. M.; Fulton, J. L.; Lercher, J. A.; Campbell, C. T. Aqueous Phase Catalytic and Electrocatalytic Hydrogenation of Phenol and Benzaldehyde over Platinum Group Metals. *J. Catal.* **2020**, *382*, 372–384. https://doi.org/10.1016/j.jcat.2019.12.034.

(22) Song, Y.; Chia, S. H.; Sanyal, U.; Gutiérrez, O. Y.; Lercher, J. A. Integrated Catalytic and Electrocatalytic Conversion of Substituted Phenols and Diaryl Ethers. *J. Catal.* **2016**, *344*, 263–272. https://doi.org/10.1016/j.jcat.2016.09.030.

(23) Singh, N.; Song, Y.; Gutiérrez, O. Y.; Camaioni, D. M.; Campbell, C. T.; Lercher, J. A. Electrocatalytic Hydrogenation of Phenol over Platinum and Rhodium: Unexpected Temperature Effects Resolved. *ACS Catal.* **2016**, *6* (11), 7466–7470. https://doi.org/10.1021/acscatal.6b02296.

(24) Singh, N.; Nguyen, M.-T.; Cantu, D. C.; Mehdi, B. L.; Browning, N. D.; Fulton, J. L.; Zheng, J.; Balasubramanian, M.; Gutiérrez, O. Y.; Glezakou, V.-A.; et al. Carbon-Supported Pt during Aqueous Phenol Hydrogenation with and without Applied Electrical Potential: X-Ray Absorption and Theoretical Studies of Structure and Adsorbates. *J. Catal.* **2018**, *368*, 8–19. https://doi.org/10.1016/j.jcat.2018.09.021.

(25) Yang, G.; Maliekkal, V.; Chen, X.; Eckstein, S.; Shi, H.; Camaioni, D. M.; Baráth, E.; Haller, G. L.; Liu, Y.; Neurock, M.; et al. Rate Enhancement of Phenol Hydrogenation on Pt by Hydronium Ions in the Aqueous Phase. *J. Catal.* **2021**, *404*, 579–593. https://doi.org/10.1016/j.jcat.2021.11.003.

(26) Honkela, M. L.; Björk, J.; Persson, M. Computational Study of the Adsorption and Dissociation of Phenol on Pt and Rh Surfaces. *Phys. Chem. Chem. Phys.* **2012**, *14* (16), 5849–5854. https://doi.org/10.1039/c2cp24064e.

(27) Chaudhary, N.; Hensley, A.; Collinge, G.; Wang, Y.; McEwen, J.-S. Coverage-Dependent Adsorption of Phenol on Pt(111) from First Principles. *J. Phys. Chem. C* **2020**, *124* (1), 356–362. https://doi.org/10.1021/acs.jpcc.9b07517.

(28) Singh, N.; Sanyal, U.; Fulton, J. L.; Gutiérrez, O. Y.; Lercher, J. A.; Campbell, C. T. Quantifying Adsorption of Organic Molecules on Platinum in Aqueous Phase by Hydrogen Site Blocking and in Situ X-Ray Absorption Spectroscopy. *ACS Catal.* **2019**, *9* (8), 6869–6881. https://doi.org/10.1021/acscatal.9b01415.

(29) Rasmussen, A. M. H.; Hammer, B. Adsorption, Mobility, and Dimerization of Benzaldehyde on Pt(111). *J. Chem. Phys.* **2012**, *136* (17), 174706. https://doi.org/10.1063/1.4707952.

(30) Sievers, C.; Noda, Y.; Qi, L.; Albuquerque, E. M.; Rioux, R. M.; Scott, S. L. Phenomena Affecting Catalytic Reactions at Solid–Liquid Interfaces. *ACS Catal.* **2016**, *6* (12), 8286–8307. https://doi.org/10.1021/acscatal.6b02532.

(31) Li, G.; Wang, B.; Resasco, D. E. Water-Mediated Heterogeneously Catalyzed Reactions. *ACS Catal.* **2020**, *10* (2), 1294–1309. https://doi.org/10.1021/acscatal.9b04637.

(32) Li, G.; Zhao, Z.; Mou, T.; Tan, Q.; Wang, B.; Resasco, D. Experimental and Computational Kinetics Study of the Liquid-Phase Hydrogenation of C=C and C=O Bonds. *J. Catal.* **2021**, *404* (xxxx), 771–785. https://doi.org/10.1016/j.jcat.2021.09.002.

(33) Li, G.; Wang, B.; Resasco, D. E. Solvent Effects on Catalytic Reactions and Related Phenomena at Liquid-Solid Interfaces. *Surf. Sci. Rep.* **2021**, *76* (4), 100541. https://doi.org/10.1016/j.surfrep.2021.100541.

(34) Saleheen, M.; Heyden, A. Liquid-Phase Modeling in Heterogeneous Catalysis. *ACS Catal.* **2018**, *8* (3), 2188–2194. https://doi.org/10.1021/acscatal.7b04367.

(35) Akinola, J.; Barth, I.; Goldsmith, B. R.; Singh, N. Adsorption Energies of Oxygenated Aromatics and Organics on Rhodium and Platinum in Aqueous Phase. *ACS Catal.* **2020**, *10* (9), 4929–4941. https://doi.org/10.1021/acscatal.0c00803.

(36) Basdogan, Y.; Maldonado, A. M.; Keith, J. A. Advances and Challenges in Modeling Solvated Reaction Mechanisms for Renewable Fuels and Chemicals. *WIREs Comput. Mol. Sci.* **2020**, *10* (2), 1–19. https://doi.org/10.1002/wcms.1446.

(37) Steinmann, S. N.; Sautet, P.; Michel, C. Solvation Free Energies for Periodic Surfaces: Comparison of Implicit and Explicit Solvation Models. *Phys. Chem. Chem. Phys.* **2016**, *18* (46), 31850–31861. https://doi.org/10.1039/C6CP04094B.

(38) Steinmann, S. N.; Michel, C. How to Gain Atomistic Insights on Reactions at the Water/Solid Interface? *ACS Catal.* **2022**, *12* (11), 6294–6301. https://doi.org/10.1021/acscatal.2c00594.

(39) Oğuz, I. C.; Vassetti, D.; Labat, F. Assessing the Performances of Different Continuum Solvation Models for the Calculation of Hydration Energies of Molecules, Polymers and Surfaces: A Comparison between the SMD, VASPsol and FDPB Models. *Theor. Chem. Acc.* **2021**, *140* (8), 1–13. https://doi.org/10.1007/s00214-021-02799-w.

(40) Mathew, K.; Sundararaman, R.; Letchworth-Weaver, K.; Arias, T. A.; Hennig, R. G. Implicit Solvation Model for Density-Functional Study of Nanocrystal Surfaces and Reaction Pathways. *J. Chem. Phys.* **2014**, *140* (8), 084106. https://doi.org/10.1063/1.4865107.

(41) Mathew, K.; Kolluru, V. S. C.; Mula, S.; Steinmann, S. N.; Hennig, R. G. Implicit Self-Consistent Electrolyte Model in Plane-Wave Density-Functional Theory. *J. Chem. Phys.* **2019**, *151* (23), 234101. https://doi.org/10.1063/1.5132354.

(42) Kresse, G.; Furthmüller, J. Efficiency of Ab-Initio Total Energy Calculations for Metals and Semiconductors Using a Plane-Wave Basis Set. *Comput. Mater. Sci.* **1996**, *6* (1), 15–50. https://doi.org/10.1016/0927-0256(96)00008-0.

(43) Kresse, G.; Furthmüller, J. Efficient Iterative Schemes for Ab Initio Total-Energy Calculations Using a Plane-Wave Basis Set. *Phys. Rev. B* **1996**, *54* (16), 11169–11186. https://doi.org/10.1103/PhysRevB.54.11169.

(44) Iyemperumal, S. K.; Deskins, N. A. Evaluating Solvent Effects at the Aqueous/Pt(111) Interface. *ChemPhysChem* **2017**, *18* (16), 2171–2190. https://doi.org/10.1002/cphc.201700162.

(45) Bramley, G. A.; Nguyen, M.-T.; Glezakou, V.-A.; Rousseau, R.; Skylaris, C.-K. Understanding Adsorption of Organics on Pt(111) in the Aqueous Phase: Insights from DFT Based Implicit Solvent and Statistical Thermodynamics Models. *J. Chem. Theory Comput.* **2022**, *18* (3), 1849–1861. https://doi.org/10.1021/acs.jctc.1c00894.

(46) Valleau, J. P.; J.M., T. Nonphysical Sampling Distributions in Monte Carlo Free-Energy Estimation: Umbrella Sampling. *J. Comput. Phys.* **1977**, *23* (2), 187–199.

(47) Torrie, G. M.; Valleau, J. P. Monte Carlo Free Energy Estimates Using Non-Boltzmann Sampling: Application to the Sub-Critical Lennard-Jones Fluid. *Chem. Phys. Lett.* **1974**, *28* (4), 578–581. https://doi.org/10.1016/0009-2614(74)80109-0.

(48) Kästner, J. Umbrella Sampling. *Wiley Interdiscip. Rev. Comput. Mol. Sci.* **2011**, *1* (6), 932–942. https://doi.org/10.1002/wcms.66.

(49) Martins, S. A.; Sousa, S. F.; Ramos, M. J.; Fernandes, P. A. Prediction of Solvation Free Energies with Thermodynamic Integration Using the General Amber Force Field. *J. Chem. Theory Comput.* **2014**, *10* (8), 3570–3577. https://doi.org/10.1021/ct500346y.

(50) Straatsma, T. P.; Berendsen, H. J. C. Free Energy of Ionic Hydration: Analysis of a Thermodynamic Integration Technique to Evaluate Free Energy Differences by Molecular Dynamics Simulations. *J. Chem. Phys.* **1988**, *89* (9), 5876–5886. https://doi.org/10.1063/1.455539.

(51) Laio, A.; Parrinello, M. Escaping Free-Energy Minima. *Proc. Natl. Acad. Sci. U. S. A.* **2002**, *99* (20), 12562–12566. https://doi.org/10.1073/pnas.202427399.

(52) Laio, A.; Gervasio, F. L. Metadynamics: A Method to Simulate Rare Events and Reconstruct the Free Energy in Biophysics, Chemistry and Material Science. *Reports Prog. Phys.* **2008**, *71* (12). https://doi.org/10.1088/0034-4885/71/12/126601.

(53) Piccini, G.; Lee, M.-S.; Yuk, S. F.; Zhang, D.; Collinge, G.; Kollias, L.; Nguyen, M.-T.; Glezakou, V.-A.; Rousseau, R. Ab Initio Molecular Dynamics with Enhanced Sampling in Heterogeneous Catalysis. *Catal. Sci. Technol.* **2022**, *12* (1), 12–37. https://doi.org/10.1039/D1CY01329G.

(54) Faheem, M.; Heyden, A. Hybrid Quantum Mechanics/Molecular Mechanics Solvation Scheme for Computing Free Energies of Reactions at Metal-Water Interfaces. *J. Chem. Theory Comput.* **2014**, *10* (8), 3354–3368. https://doi.org/10.1021/ct500211w.

(55) Clabaut, P.; Schweitzer, B.; Götz, A. W.; Michel, C.; Steinmann, S. N. Solvation Free Energies and Adsorption Energies at the Metal/Water Interface from Hybrid Quantum-Mechanical/Molecular Mechanics Simulations. *J. Chem. Theory Comput.* **2020**, *16* (10), 6539–6549. https://doi.org/10.1021/acs.jctc.0c00632.

(56) Zare, M.; Saleheen, M. S.; Singh, N.; Uline, M. J.; Faheem, M.; Heyden, A. Liquid-Phase Effects on Adsorption Processes in Heterogeneous Catalysis. *JACS Au* **2022**, *2* (9), 2119–2134. https://doi.org/10.1021/jacsau.2c00389.

(57) Saleheen, M.; Zare, M.; Faheem, M.; Heyden, A. Computational Investigation of Aqueous Phase Effects on the Dehydrogenation and Dehydroxylation of Polyols over Pt(111). *J. Phys. Chem. C* **2019**, *123* (31), 19052–19065. https://doi.org/10.1021/acs.jpcc.9b04994.

(58) Spohr, E.; Heinzinger, K. Molecular Dynamics Simulation of a Water/Metal Interface. *Chem. Phys. Lett.* **1986**, *123* (3), 218–221. https://doi.org/10.1016/0009-2614(86)80016-1.

(59) Sun, L.; Deng, W.-Q. Recent Developments of First-Principles Force Fields. *Wiley Interdiscip. Rev. Comput. Mol. Sci.* **2017**, *7* (1), e1282. https://doi.org/10.1002/wcms.1282.

(60) Heinz, H.; Vaia, R. A.; Farmer, B. L.; Naik, R. R. Accurate Simulation of Surfaces and Interfaces of Face-Centered Cubic Metals Using 12−6 and 9−6 Lennard-Jones Potentials. *J. Phys. Chem. C* **2008**, *112* (44), 17281–17290. https://doi.org/10.1021/jp801931d.

(61) Clabaut, P.; Fleurat-Lessard, P.; Michel, C.; Steinmann, S. N. Ten Facets, One Force Field: The GAL19 Force Field for Water–Noble Metal Interfaces. *J. Chem. Theory Comput.* **2020**, *16* (7), 4565–4578. https://doi.org/10.1021/acs.jctc.0c00091.

(62) Steinmann, S. N.; Ferreira De Morais, R.; Götz, A. W.; Fleurat-Lessard, P.; Iannuzzi, M.; Sautet, P.; Michel, C. Force Field for Water over Pt(111): Development, Assessment, and Comparison. *J. Chem. Theory Comput.* **2018**, *14* (6), 3238–3251. https://doi.org/10.1021/acs.jctc.7b01177.

(63) Singh, N.; Campbell, C. T. A Simple Bond-Additivity Model Explains Large Decreases in Heats of Adsorption in Solvents Versus Gas Phase: A Case Study with Phenol on Pt(111) in Water. *ACS Catal.* **2019**, *9* (9), 8116–8127. https://doi.org/10.1021/acscatal.9b01870.

(64) Lew, W.; Crowe, M. C.; Karp, E.; Campbell, C. T. Energy of Molecularly Adsorbed Water on Clean Pt(111) and Pt(111) with Coadsorbed Oxygen by Calorimetry. *J. Phys. Chem. C* **2011**, *115* (18), 9164–9170. https://doi.org/10.1021/jp201608x.

(65) Carey, S. J.; Zhao, W.; Mao, Z.; Campbell, C. T. Energetics of Adsorbed Phenol on Ni(111) and Pt(111) by Calorimetry. *J. Phys. Chem. C* **2019**, *123* (13), 7627–7632. https://doi.org/10.1021/acs.jpcc.8b03155.

(66) Rumptz, J. R.; Campbell, C. T. Adhesion Energies of Solvent Films to Pt(111) and Ni(111) Surfaces by Adsorption Calorimetry. *ACS Catal.* **2019**, *submitted* (111), acscatal.9b03591. https://doi.org/10.1021/acscatal.9b03591.

(67) Liu, D.; Li, G.; Yang, F.; Wang, H.; Han, J.; Zhu, X.; Ge, Q. Competition and Cooperation of Hydrogenation and Deoxygenation Reactions during Hydrodeoxygenation of Phenol on Pt(111). *J. Phys. Chem. C* **2017**, *121* (22), 12249–12260. https://doi.org/10.1021/acs.jpcc.7b03042.

(68) Li, G.; Han, J.; Wang, H.; Zhu, X.; Ge, Q. Role of Dissociation of Phenol in Its Selective Hydrogenation on Pt(111) and Pd(111). *ACS Catal.* **2015**, *5* (3), 2009–2016. https://doi.org/10.1021/cs501805y.

(69) Zhong, J.; Chen, J.; Chen, L. Selective Hydrogenation of Phenol and Related Derivatives. *Catal. Sci. Technol.* **2014**, *4* (10), 3555–3569. https://doi.org/10.1039/c4cy00583j.

(70) Smith, H. A.; Stump, B. L. A Study of the Catalytic Hydrogenation of Hydroxybenzenes over Platinum and Rhodium Catalysts. *J. Am. Chem. Soc.* **1961**, *83* (12), 2739–2743. https://doi.org/10.1021/ja01473a032.

(71) Hensley, A. J. R.; Wang, Y.; Mei, D.; McEwen, J.-S. Mechanistic Effects of Water on the

Fe-Catalyzed Hydrodeoxygenation of Phenol. The Role of Brønsted Acid Sites. *ACS Catal.* **2018**, *8* (3), 2200–2208. https://doi.org/10.1021/acscatal.7b02576.
(72) Yoon, Y.; Rousseau, R.; Weber, R. S.; Mei, D.; Lercher, J. A. First-Principles Study of Phenol Hydrogenation on Pt and Ni Catalysts in Aqueous Phase. *J. Am. Chem. Soc.* **2014**, *136* (29), 10287–10298. https://doi.org/10.1021/ja501592y.
(73) Zhao, Z.; Bababrik, R.; Xue, W.; Li, Y.; Briggs, N. M.; Nguyen, D.-T.; Nguyen, U.; Crossley, S. P.; Wang, S.; Wang, B.; et al. Solvent-Mediated Charge Separation Drives Alternative Hydrogenation Path of Furanics in Liquid Water. *Nat. Catal.* **2019**, *2* (5), 431–436. https://doi.org/10.1038/s41929-019-0257-z.
(74) Bodenschatz, C. J.; Xie, T.; Zhang, X.; Getman, R. B. Insights into How the Aqueous Environment Influences the Kinetics and Mechanisms of Heterogeneously-Catalyzed COH* and CH 3 OH* Dehydrogenation Reactions on Pt(111). *Phys. Chem. Chem. Phys.* **2019**, *21* (19), 9895–9904. https://doi.org/10.1039/C9CP00824A.
(75) Sasaki, K.; Kunai, A.; Harada, J.; Nakabori, S. Electrolytic Hydrogenation of Phenols in Aqueous Acid Solutions. *Electrochim. Acta* **1983**, *28* (5), 671–674. https://doi.org/10.1016/0013-4686(83)85062-2.
(76) Amouzegar, K.; Savadogo, O. Electrocatalytic Hydrogenation of Phenol on Dispersed Pt: Reaction Mechanism and Support Effect. *Electrochim. Acta* **1998**, *43* (5–6), 503–508. https://doi.org/10.1016/S0013-4686(97)00131-X.
(77) U.S. Energy Information Institution. *Annual Energy Outlook 2018 with Projections to 2050*; 2018; Vol. 44. https://doi.org/DOE/EIA-0383(2012) U.S.
(78) Czernik, S.; Bridgwater, A. V. Overview of Applications of Biomass Fast Pyrolysis Oil. *Energy & Fuels* **2004**, *18* (2), 590–598. https://doi.org/10.1021/ef034067u.
(79) Scott, D. S.; Plskorz, J.; Radleln, D. Liquid Products from the Continuous Flash Pyrolysis of Biomass. *Ind. Eng. Chem. Process Des. Dev.* **1985**, *24* (3), 581–588. https://doi.org/10.1021/i200030a011.
(80) Carneiro, J.; Nikolla, E. Electrochemical Conversion of Biomass-Based Oxygenated Compounds. *Annu. Rev. Chem. Biomol. Eng.* **2019**, *10* (1), 85–104. https://doi.org/10.1146/annurev-chembioeng-060718-030148.
(81) Furimsky, E. Catalytic Hydrodeoxygenation. *Appl. Catal. A Gen.* **2000**, *199* (2), 147–190. https://doi.org/10.1016/S0926-860X(99)00555-4.
(82) Sanyal, U.; Song, Y.; Singh, N.; Fulton, J. L.; Herranz, J.; Jentys, A.; Gutiérrez, O. Y.; Lercher, J. A. Structure Sensitivity in Hydrogenation Reactions on Pt/C in Aqueous-phase. *ChemCatChem* **2019**, *11* (1), 575–582. https://doi.org/10.1002/cctc.201801344.
(83) Singh, N.; Lee, M.-S.; Akhade, S. A.; Cheng, G.; Camaioni, D. M.; Gutiérrez, O. Y.; Glezakou, V.-A.; Rousseau, R.; Lercher, J. A.; Campbell, C. T. Impact of PH on Aqueous-Phase Phenol Hydrogenation Catalyzed by Carbon-Supported Pt and Rh. *ACS Catal.* **2019**, *9* (2), 1120–1128. https://doi.org/10.1021/acscatal.8b04039.
(84) Kristoffersen, H. H.; Shea, J. E.; Metiu, H. Catechol and HCl Adsorption on TiO2(110) in Vacuum and at the Water-TiO2 Interface. *J. Phys. Chem. Lett.* **2015**, *6* (12), 2277–2281. https://doi.org/10.1021/acs.jpclett.5b00958.
(85) Łosiewicz, B.; Jurczakowski, R.; Lasia, A. Kinetics of Hydrogen Underpotential Deposition at Polycrystalline Rhodium in Acidic Solutions. *Electrochim. Acta* **2017**, *225*, 160–167. https://doi.org/10.1016/j.electacta.2016.12.116.
(86) Zolfaghari, A. Hydrogen Adsorption on Pt and Rh Electrodes and Bloclung of Adsorption Sites. *Knowl. Creat. Diffus. Util.* **1997**, *254*, 481–487.

(87) Jerkiewicz, G. Comparison of Hydrogen Electroadsorption from the Electrolyte with Hydrogen Adsorption from the Gas Phase. *J. Electrochem. Soc.* **1996**, *143* (4), 1240. https://doi.org/10.1149/1.1836623.

(88) Deblois, M.; Lessard, J.; Jerkiewicz, G. Influence of Benzene on the HUPD and Anion Adsorption on Pt(1 1 0), Pt(1 0 0) and Pt(1 1 1) Electrodes in Aqueous H2SO4. *Electrochim. Acta* **2005**, *50* (16–17), 3517–3523. https://doi.org/10.1016/j.electacta.2004.12.029.

(89) Obradović, M. D.; Lessard, J.; Jerkiewicz, G. Cyclic-Voltammetry Behavior of Pt(1 1 1) in Aqueous HClO4 + C6H6: Influence of C6H6 Concentration, Scan Rate and Temperature. *J. Electroanal. Chem.* **2010**, *649* (1–2), 248–256. https://doi.org/10.1016/j.jelechem.2010.04.022.

(90) Gasparotto, L. H. S.; Gomes, J. F.; Tremiliosi-Filho, G. Cyclic-Voltammetry Characteristics of Poly(Vinyl Pyrrolidone) (PVP) on Single-Crystal Pt Surfaces in Aqueous H2SO4. *J. Electroanal. Chem.* **2011**, *663* (1), 48–51. https://doi.org/10.1016/j.jelechem.2011.09.025.

(91) Lam, C. H. C. H.; Das, S.; Erickson, N. C.; Hyzer, C. D.; Garedew, M.; Anderson, J. E.; Wallington, T. J.; Tamor, M. A.; Jackson, J. E.; Saffron, C. M.; et al. Towards Sustainable Hydrocarbon Fuels with Biomass Fast Pyrolysis Oil and Electrocatalytic Upgrading. *Sustain. Energy Fuels* **2017**, *1* (2), 258–266. https://doi.org/10.1039/C6SE00080K.

(92) Wieckowski, A.; Sobrowski, J.; Zelenay, P.; Franaszczuk, K. Adsorption of Acetic Acid on Platinum, Gold and Rhodium Electrodes. *Electrochim. Acta* **1981**, *26* (8), 1111–1119. https://doi.org/10.1016/0013-4686(81)85086-4.

(93) Garrone, E.; Bolis, V.; Fubini, B.; Morterra, C. Thermodynamic and Spectroscopic Characterization of Heterogeneity among Adsorption Sites: CO on Anatase at Ambient Temperature. *Langmuir* **1989**, *5* (4), 892–899. https://doi.org/10.1021/la00088a002.

(94) Vassiliev, Y. B.; Bagotzky, V. S.; Khazova, O. A.; Cherny, V. V.; Meretsky, A. M. Mechanism of Adsorption, Electroreduction and Hydrogenation of Compounds with Ethylenic Bonds on Platinum and Rhodium. Part I. Kinetics of Adsorption and Electroreduction. *J. Electroanal. Chem.* **1979**, *98* (2), 253–272. https://doi.org/10.1016/S0022-0728(79)80265-X.

(95) Bard, A. J.; Faulkner, L. R. *Electrochemical Methods: Fundamentals and Applications (Vol. 2)*; Wiley: New York, 1980.

(96) Gileadi, E. (Editor). *Electrosorption*; Springer Science & Business Media, 2012.

(97) Bockris, J. O. M.; Green, A.; Swinkels, D. A. J. Adsorption of Naphthalene on Solid Metal Electrodes. *J. Electrochem. Soc.* **1964**, *111* (6), 743–748. https://doi.org/10.1149/1.2426222.

(98) Goerigk, L.; Grimme, S. A Thorough Benchmark of Density Functional Methods for General Main Group Thermochemistry, Kinetics, and Noncovalent Interactions. *Phys. Chem. Chem. Phys.* **2011**, *13* (14), 6670–6688. https://doi.org/10.1039/c0cp02984j.

(99) Gautier, S.; Steinmann, S. N.; Michel, C.; Fleurat-Lessard, P.; Sautet, P. Molecular Adsorption at Pt(111). How Accurate Are DFT Functionals? *Phys. Chem. Chem. Phys.* **2015**, *17* (43), 28921–28930. https://doi.org/10.1039/c5cp04534g.

(100) Grimme, S.; Antony, J.; Ehrlich, S.; Krieg, H. A Consistent and Accurate Ab Initio Parametrization of Density Functional Dispersion Correction (DFT-D) for the 94 Elements H-Pu. *J. Chem. Phys.* **2010**, *132* (15), 154104. https://doi.org/10.1063/1.3382344.

(101) Perdew, J. P.; Burke, K.; Ernzerhof, M. Generalized Gradient Approximation Made Simple. *Phys. Rev. Lett.* **1996**, *77* (18), 3865–3868. https://doi.org/10.1103/PhysRevLett.77.3865.

(102) Han, F. Projector-Augmented Plane-Wave Method. In *Problems in Solid State Physics with Solutions*; WORLD SCIENTIFIC, 2011; Vol. 50, pp 391–396. https://doi.org/10.1142/9789814365031_0023.

(103) Haas, P.; Tran, F.; Blaha, P. Calculation of the Lattice Constant of Solids with Semilocal Functionals. *Phys. Rev. B* **2009**, *79* (8), 085104. https://doi.org/10.1103/PhysRevB.79.085104.

(104) Kittel, C. *Introduction to Solid State Physics*, 7th ed.; Wiley: New York, 1996.

(105) Bodenschatz, C. J.; Sarupria, S.; Getman, R. B. Molecular-Level Details about Liquid H 2 O Interactions with CO and Sugar Alcohol Adsorbates on Pt(111) Calculated Using Density Functional Theory and Molecular Dynamics. *J. Phys. Chem. C* **2015**, *119* (24), 13642–13651. https://doi.org/10.1021/acs.jpcc.5b02333.

(106) Saleheen, M.; Verma, A. M.; Mamun, O.; Lu, J.; Heyden, A. Investigation of Solvent Effects on the Hydrodeoxygenation of Guaiacol over Ru Catalysts. *Catal. Sci. Technol.* **2019**, *9* (22), 6253–6273. https://doi.org/10.1039/C9CY01763A.

(107) Mathew, K.; Hennig, R. G. Implicit Self-Consistent Description of Electrolyte in Plane-Wave Density-Functional Theory. **2016**, 1–6.

(108) Lu, F.; Salaita, G. N.; Laguren-Davidson, L.; Stern, D. A.; Wellner, E.; Frank, D. G.; Batina, N.; Zapien, D. C.; Walton, N.; Hubbard, A. T. Characterization of Hydroquinone and Related Compounds Adsorbed at Pt(111) from Aqueous Solutions: Electron Energy-Loss Spectroscopy, Auger Spectroscopy, LEED, and Cyclic Voltammetry. *Langmuir* **1988**, *4* (3), 637–646. https://doi.org/10.1021/la00081a024.

(109) Farias, M. J. S.; Camara, G. A.; Feliu, J. M. Understanding the CO Preoxidation and the Intrinsic Catalytic Activity of Step Sites in Stepped Pt Surfaces in Acidic Medium. *J. Phys. Chem. C* **2015**, *119* (35), 20272–20282. https://doi.org/10.1021/acs.jpcc.5b05386.

(110) Souza-Garcia, J.; Climent, V.; Feliu, J. M. Voltammetric Characterization of Stepped Platinum Single Crystal Surfaces Vicinal to the (1 1 0) Pole. *Electrochem. commun.* **2009**, *11* (7), 1515–1518. https://doi.org/10.1016/j.elecom.2009.05.044.

(111) Domke, K.; Herrero, E.; Rodes, A.; Feliu, J. M. Determination of the Potentials of Zero Total Charge of Pt(100) Stepped Surfaces in the $[01\bar{1}]$ Zone. Effect of the Step Density and Anion Adsorption. *J. Electroanal. Chem.* **2003**, *552* (SUPPL.), 115–128. https://doi.org/10.1016/S0022-0728(02)01471-7.

(112) Arán-Ais, R. M.; Figueiredo, M. C.; Vidal-Iglesias, F. J.; Climent, V.; Herrero, E.; Feliu, J. M. On the Behavior of the Pt(1 0 0) and Vicinal Surfaces in Alkaline Media. *Electrochim. Acta* **2011**, *58* (1), 184–192. https://doi.org/10.1016/j.electacta.2011.09.029.

(113) Souza-Garcia, J.; Angelucci, C. A.; Climent, V.; Feliu, J. M. Electrochemical Features of Pt(S)[n(110) × (100)] Surfaces in Acidic Media. *Electrochem. commun.* **2013**, *34*, 291–294. https://doi.org/10.1016/j.elecom.2013.07.007.

(114) Molodkina, E. B.; Danilov, A. I.; Feliu, J. M. Cu UPD at Pt(100) and Stepped Faces Pt(610), Pt(410) of Platinum Single Crystal Electrodes. *Russ. J. Electrochem.* **2016**, *52* (9), 890–900. https://doi.org/10.1134/S1023193515110117.

(115) Sasahara, A.; Tamura, H.; Tanaka, K. I. Catalytic Activity of Pt-Deposited Rh(110) Bimetallic Surface for NO + H2reaction. *J. Phys. Chem. B* **1997**, *101* (7), 1186–1189. https://doi.org/10.1021/jp962829z.

(116) Wasberg, M.; Hourani, M.; Wieckowski, A. Comparison of Voltammetry of Vacuum-Prepared Rh (100) and Rh (111) Electrodes. *J. Electroanal. Chem.* **1990**, *278* (1–2), 425–432. https://doi.org/10.1016/0022-0728(90)85155-X.

(117) Clavilier, J.; Wasberg, M.; Petit, M.; Klein, L. H. Detailed Analysis of the Voltammetry of Rh(111) in Perchloric Acid Solution. *J. Electroanal. Chem.* **1994**, *374* (1–2), 123–131. https://doi.org/10.1016/0022-0728(94)03363-3.

(118) Hourani, M.; Wieckowski, A. Single Crystal Electrochemistry of Rhodium. *J. Electroanal. Chem. Interfacial Electrochem.* **1988**, *244* (1–2), 147–161. https://doi.org/10.1016/0022-0728(88)80102-5.

(119) Bockris, J. O. M.; Jeng, K. T. In-Situ Studies of Adsorption of Organic Compounds on Platinum Electrodes. *J. Electroanal. Chem.* **1992**, *330* (1–2), 541–581. https://doi.org/10.1016/0022-0728(92)80330-7.

(120) McCrum, I. T.; Hickner, M. A.; Janik, M. J. First-Principles Calculation of Pt Surface Energies in an Electrochemical Environment: Thermodynamic Driving Forces for Surface Faceting and Nanoparticle Reconstruction. *Langmuir* **2017**, *33* (28), 7043–7052. https://doi.org/10.1021/acs.langmuir.7b01530.

(121) Campbell, C. T.; Sellers, J. R. V. The Entropies of Adsorbed Molecules. *J. Am. Chem. Soc.* **2012**, *134* (43), 18109–18115. https://doi.org/10.1021/ja3080117.

(122) Weaver, M. J. Potentials of Zero Charge for Platinum(111)-Aqueous Interfaces: A Combined Assessment from in-Situ and Ultrahigh-Vacuum Measurements. *Langmuir* **1998**, *14* (14), 3932–3936. https://doi.org/10.1021/la9801054.

(123) Gómez, R.; Feliu, J. M.; Aldaz, A.; Weaver, M. J. Validity of Double-Layer Charge-Corrected Voltammetry for Assaying Carbon Monoxide Coverages on Ordered Transition Metals: Comparisons with Adlayer Structures in Electrochemical and Ultrahigh Vacuum Environments. *Surf. Sci.* **1998**, *410* (1), 48–61. https://doi.org/10.1016/S0039-6028(98)00295-7.

(124) Xu, Q.; Linke, U.; Bujak, R.; Wandlowski, T. Preparation and Electrochemical Characterization of Low-Index Rhodium Single Crystal Electrodes in Sulfuric Acid. *Electrochim. Acta* **2009**, *54* (23), 5509–5521. https://doi.org/10.1016/j.electacta.2009.04.061.

(125) Gileadi, E. Electrosorption of Uncharged Molecules on Solid Electrodes. *J. Electroanal. Chem.* **1966**, *11* (2), 137–151. https://doi.org/10.1016/0022-0728(66)80073-6.

(126) Meng, S.; Wang, E. G.; Gao, S. Water Adsorption on Metal Surfaces: A General Picture from Density Functional Theory Studies. *Phys. Rev. B - Condens. Matter Mater. Phys.* **2004**, *69* (19), 1–13. https://doi.org/10.1103/PhysRevB.69.195404.

(127) Wagner, F. T.; Moylan, T. E. A Comparison between Water Adsorbed on Rh(111) and Pt(111), with and without Predosed Oxygen. *Surf. Sci.* **1987**, *191* (1–2), 121–146. https://doi.org/10.1016/S0039-6028(87)81052-X.

(128) Román, A. M.; Hasse, J. C.; Medlin, J. W.; Holewinski, A. Elucidating Acidic Electro-Oxidation Pathways of Furfural on Platinum. *ACS Catal.* **2019**, *9* (11), 10305–10316. https://doi.org/10.1021/acscatal.9b02656.

(129) Gong, L.; Agrawal, N.; Roman, A.; Holewinski, A.; Janik, M. J. Density Functional Theory Study of Furfural Electrochemical Oxidation on the Pt (1 1 1) Surface. *J. Catal.* **2019**, *373*, 322–335. https://doi.org/10.1016/j.jcat.2019.04.012.

(130) Jing, Z.; Whitten, J. L. The Adsorption of Benzene on Ni(111). *Surf. Sci.* **1991**, *250* (1–3), 147–158. https://doi.org/10.1016/0039-6028(91)90717-7.

(131) Klimeš, J.; Bowler, D. R.; Michaelides, A. Chemical Accuracy for the van Der Waals Density Functional. *J. Phys. Condens. Matter* **2010**, *22* (2), 022201. https://doi.org/10.1088/0953-8984/22/2/022201.

(132) Klimeš, J.; Bowler, D. R.; Michaelides, A. Van Der Waals Density Functionals Applied to Solids. *Phys. Rev. B* **2011**, *83* (19), 195131. https://doi.org/10.1103/PhysRevB.83.195131.

(133) Jia, X.; An, W. Adsorption of Monocyclic Aromatics on Transition Metal Surfaces: Insight into Variation of Binding Strength from First-Principles. *J. Phys. Chem. C* **2018**, *122* (38), 21897–21909. https://doi.org/10.1021/acs.jpcc.8b06321.

(134) Gorodetskii, V. V.; Nieuwenhuys, B. E.; Sachtler, W. M. H.; Boreskov, G. K. Adsorption of Hydrogen on Rhodium; Comparison with Hydrogen Adsorption on Platinum and Iridium. *Surf. Sci.* **1981**, *108* (2), 225–234. https://doi.org/10.1016/0039-6028(81)90446-5.

(135) Aguilar, F. X.; Saunders, A. Policy Instruments Promoting Wood-to-Energy Uses in the Continental United States. *J. For.* **2010**, *108* (3), 132–140.

(136) Biddinger, E. J.; Gutierrez, O. Y.; Holladay, J. Electrochemical Routes for Biomass Conversion. *J. Appl. Electrochem.* **2021**, *51* (1), 1–3. https://doi.org/10.1007/s10800-020-01525-x.

(137) Garedew, M.; Lam, C. H.; Petitjean, L.; Huang, S.; Song, B.; Lin, F.; Jackson, J. E.; Saffron, C. M.; Anastas, P. T. Electrochemical Upgrading of Depolymerized Lignin: A Review of Model Compound Studies. *Green Chem.* **2021**, *23* (8), 2868–2899. https://doi.org/10.1039/D0GC04127K.

(138) Lucas, F. W. S.; Grim, R. G.; Tacey, S. A.; Downes, C. A.; Hasse, J.; Roman, A. M.; Farberow, C. A.; Schaidle, J. A.; Holewinski, A. Electrochemical Routes for the Valorization of Biomass-Derived Feedstocks: From Chemistry to Application. *ACS Energy Lett.* **2021**, *6* (4), 1205–1270. https://doi.org/10.1021/acsenergylett.0c02692.

(139) Wang, H.; Lee, S.-J.; Olarte, M. V.; Zacher, A. H. Bio-Oil Stabilization by Hydrogenation over Reduced Metal Catalysts at Low Temperatures. *ACS Sustain. Chem. Eng.* **2016**, *4* (10), 5533–5545. https://doi.org/10.1021/acssuschemeng.6b01270.

(140) Sanyal, U.; Koh, K.; Meyer, L. C.; Karkamkar, A.; Gutiérrez, O. Y. Simultaneous Electrocatalytic Hydrogenation of Aldehydes and Phenol over Carbon-Supported Metals. *J. Appl. Electrochem.* **2021**, *51* (1), 27–36. https://doi.org/10.1007/s10800-020-01464-7.

(141) Sabatier, P. Hydrogénations et Déshydrogénations Par Catalyse. *Berichte der Dtsch. Chem. Gesellschaft* **1911**, *44* (3), 1984–2001. https://doi.org/10.1002/cber.19110440303.

(142) Huber, G. W.; Iborra, S.; Corma, A. Synthesis of Transportation Fuels from Biomass: Chemistry, Catalysts, and Engineering. *Chem. Rev.* **2006**, *106* (9), 4044–4098. https://doi.org/10.1021/cr068360d.

(143) Schweitzer, B.; Steinmann, S. N.; Michel, C. Can Microsolvation Effects Be Estimated from Vacuum Computations? A Case-Study of Alcohol Decomposition at the H2O/Pt(111) Interface. *Phys. Chem. Chem. Phys.* **2019**, *21* (10), 5368–5377. https://doi.org/10.1039/c8cp06331a.

(144) Kresse, G.; Hafner, J. Ab Initio Molecular Dynamcis for Liquid Metals. *Phys. Rev. B* **1993**, *47* (1), 558.

(145) Kresse, G.; Hafner, J. Ab Initio Molecular-Dynamics Simulation of the Liquid-Metalamorphous- Semiconductor Transition in Germanium. *Phys. Rev. B* **1994**, *49* (20), 14251–14269. https://doi.org/10.1103/PhysRevB.49.14251.

(146) Hjorth Larsen, A.; Jørgen Mortensen, J.; Blomqvist, J.; Castelli, I. E.; Christensen, R.; Dułak, M.; Friis, J.; Groves, M. N.; Hammer, B.; Hargus, C.; et al. The Atomic Simulation

Environment—a Python Library for Working with Atoms. *J. Phys. Condens. Matter* **2017**, *29* (27), 273002. https://doi.org/10.1088/1361-648X/aa680e.

(147) Klimeš, J.; Michaelides, A. Perspective: Advances and Challenges in Treating van Der Waals Dispersion Forces in Density Functional Theory. *J. Chem. Phys.* **2012**, *137* (12), 120901. https://doi.org/10.1063/1.4754130.

(148) Blöchl, P. E. Projector Augmented-Wave Method. *Phys. Rev. B* **1994**, *50* (24), 17953–17979. https://doi.org/10.1103/PhysRevB.50.17953.

(149) Kresse, G.; Joubert, D. From Ultrasoft Pseudopotentials to the Projector Augmented-Wave Method. *Phys. Rev. B* **1999**, *59* (3), 1758–1775. https://doi.org/10.1103/PhysRevB.59.1758.

(150) Methfessel, M.; Paxton, A. T. High-Precision Sampling for Brillouin-Zone Integration in Metals. *Phys. Rev. B* **1989**, *40* (6), 3616–3621. https://doi.org/10.1103/PhysRevB.40.3616.

(151) Monkhorst, H. J.; Pack, J. D. Special Points for Brillouin-Zone Integrations. *Phys. Rev. B* **1976**, *13* (12), 5188–5192. https://doi.org/10.1103/PhysRevB.13.5188.

(152) Henkelman, G.; Uberuaga, B. P.; Jónsson, H. A Climbing Image Nudged Elastic Band Method for Finding Saddle Points and Minimum Energy Paths. *J. Chem. Phys.* **2000**, *113* (22), 9901–9904. https://doi.org/10.1063/1.1329672.

(153) Abghoui, Y.; Skúlason, E. Hydrogen Evolution Reaction Catalyzed by Transition-Metal Nitrides. *J. Phys. Chem. C* **2017**, *121* (43), 24036–24045. https://doi.org/10.1021/acs.jpcc.7b06811.

(154) Conway, B. E.; Jerkiewicz, G. Relation of Energies and Coverages of Underpotential and Overpotential Deposited H at Pt and Other Metals to the 'Volcano Curve' for Cathodic H2 Evolution Kinetics. *Electrochim. Acta* **2000**, *45* (25–26), 4075–4083. https://doi.org/10.1016/S0013-4686(00)00523-5.

(155) Li, C.; Gao, H.; Wan, W.; Mueller, T. Mechanisms for Hydrogen Evolution on Transition Metal Phosphide Catalysts and a Comparison to Pt(111). *Phys. Chem. Chem. Phys.* **2019**, *21* (44), 24489–24498. https://doi.org/10.1039/C9CP05094A.

(156) Skúlason, E.; Karlberg, G. S.; Rossmeisl, J.; Bligaard, T.; Greeley, J.; Jónsson, H.; Nørskov, J. K. Density Functional Theory Calculations for the Hydrogen Evolution Reaction in an Electrochemical Double Layer on the Pt(111) Electrode. *Phys. Chem. Chem. Phys.* **2007**, *9* (25), 3241–3250. https://doi.org/10.1039/B700099E.

(157) Sabbe, M. K.; Canduela-Rodriguez, G.; Joly, J.-F.; Reyniers, M.-F.; Marin, G. B. Ab Initio Coverage-Dependent Microkinetic Modeling of Benzene Hydrogenation on Pd(111). *Catal. Sci. Technol.* **2017**, *7* (22), 5267–5283. https://doi.org/10.1039/C7CY00962C.

(158) Filot, I. A. W. W.; van Santen, R. A.; Hensen, E. J. M. M. The Optimally Performing Fischer-Tropsch Catalyst. *Angew. Chemie Int. Ed.* **2014**, *53* (47), 12746–12750. https://doi.org/10.1002/anie.201406521.

(159) Faheem, M.; Saleheen, M.; Lu, J.; Heyden, A. Ethylene Glycol Reforming on Pt(111): First-Principles Microkinetic Modeling in Vapor and Aqueous Phases. *Catal. Sci. Technol.* **2016**, *6* (23), 8242–8256. https://doi.org/10.1039/C6CY02111E.

(160) Xie, T.; Bodenschatz, C. J.; Getman, R. B. Insights into the Roles of Water on the Aqueous Phase Reforming of Glycerol. *React. Chem. Eng.* **2019**, *4* (2), 383–392. https://doi.org/10.1039/C8RE00267C.

(161) Sander, R. Compilation of Henry's Law Constants (Version 4.0) for Water as Solvent.

Atmos. Chem. Phys. **2015**, *15* (8), 4399–4981. https://doi.org/10.5194/acp-15-4399-2015.

(162) Bard, A. J.; Faulkner, L. R. Electronic Compensation of Resistance. In *Electrochemical Methods: Fundamentals and Applications*; John Wiley & Sons, Inc: New York, 2001.

(163) Efron, B.; Gong, G. A Leisurely Look at the Bootstrap, the Jackknife, and Cross-Validation. *Am. Stat.* **1983**, *37* (1), 36–48. https://doi.org/10.1080/00031305.1983.10483087.

(164) Caceci, M. S. Estimating Error Limits in Parametric Curve Fitting. *Anal. Chem.* **1989**, *61* (20), 2324–2327. https://doi.org/10.1021/ac00195a023.

(165) Li, H.; Ding, Z. Hydrogen Coverage Dependent C C Hydrogenation Activity on Rh(111). *Chem. Phys. Lett.* **2020**, *746* (February), 137287. https://doi.org/10.1016/j.cplett.2020.137287.

(166) Li, Y.; Liu, Z.; Crossley, S. P.; Jentoft, F. C.; Wang, S. Effect of Hydrogen Coverage on Hydrogenation of O-Cresol on Pt(111). *Appl. Surf. Sci.* **2018**, *443*, 575–580. https://doi.org/10.1016/j.apsusc.2018.02.288.

(167) Campbell, C. T. The Degree of Rate Control: A Powerful Tool for Catalysis Research. *ACS Catal.* **2017**, *7* (4), 2770–2779. https://doi.org/10.1021/acscatal.7b00115.

(168) Le Valant, A.; Comminges, C.; Can, F.; Thomas, K.; Houalla, M.; Epron, F. Platinum Supported Catalysts: Predictive CO and H2 Chemisorption by a Statistical Cuboctahedron Cluster Model. *J. Phys. Chem. C* **2016**, *120* (46), 26374–26385. https://doi.org/10.1021/acs.jpcc.6b09241.

(169) Van Hardeveld, R.; Hartog, F. The Statistics of Surface Atoms and Surface Sites on Metal Crystals. *Surf. Sci.* **1969**, *15* (2), 189–230. https://doi.org/10.1016/0039-6028(69)90148-4.

(170) Lundwall, M. J.; McClure, S. M.; Goodman, D. W. Probing Terrace and Step Sites on Pt Nanoparticles Using CO and Ethylene. *J. Phys. Chem. C* **2010**, *114* (17), 7904–7912. https://doi.org/10.1021/jp9119292.

(171) Jones, G.; Jakobsen, J. G.; Shim, S. S.; Kleis, J.; Andersson, M. P.; Rossmeisl, J.; Abild-Pedersen, F.; Bligaard, T.; Helveg, S.; Hinnemann, B.; et al. First Principles Calculations and Experimental Insight into Methane Steam Reforming over Transition Metal Catalysts. *J. Catal.* **2008**, *259* (1), 147–160. https://doi.org/10.1016/j.jcat.2008.08.003.

(172) Borodziński, A.; Bonarowska, M. Relation between Crystallite Size and Dispersion on Supported Metal Catalysts. *Langmuir* **1997**, *13* (21), 5613–5620. https://doi.org/10.1021/la962103u.

(173) Urchaga, P.; Baranton, S.; Napporn, T. W.; Coutanceau, C. Selective Syntheses and Electrochemical Characterization of Platinum Nanocubes and Nanotetrahedrons/Octahedrons. *Electrocatalysis* **2010**, *1* (1), 3–6. https://doi.org/10.1007/s12678-009-0002-5.

(174) Huang, M. H.; Lin, P. H. Shape-Controlled Synthesis of Polyhedral Nanocrystals and Their Facet-Dependent Properties. *Adv. Funct. Mater.* **2012**, *22* (1), 14–24. https://doi.org/10.1002/adfm.201101784.

(175) Bu, L.; Feng, Y.; Yao, J.; Guo, S.; Guo, J.; Huang, X. Facet and Dimensionality Control of Pt Nanostructures for Efficient Oxygen Reduction and Methanol Oxidation Electrocatalysts. *Nano Res.* **2016**, *9* (9), 2811–2821. https://doi.org/10.1007/s12274-016-1170-2.

(176) Cyr, A.; Chiltz, F.; Jeanson, P.; Martel, A.; Brossard, L.; Lessard, J.; Ménard, H. Electrocatalytic Hydrogenation of Lignin Models at Raney Nickel and Palladium-Based Electrodes. *Can. J. Chem.* **2000**, *78* (3), 307–315. https://doi.org/10.1139/v00-009.

(177) Li, Z.; Garedew, M.; Lam, C. H.; Jackson, J. E.; Miller, D. J.; Saffron, C. M. Mild Electrocatalytic Hydrogenation and Hydrodeoxygenation of Bio-Oil Derived Phenolic Compounds Using Ruthenium Supported on Activated Carbon Cloth. *Green Chem.* **2012**, *14* (9), 2540. https://doi.org/10.1039/c2gc35552c.

(178) Lam, C. H.; Lowe, C. B.; Li, Z.; Longe, K. N.; Rayburn, J. T.; Caldwell, M. A.; Houdek, C. E.; Maguire, J. B.; Saffron, C. M.; Miller, D. J.; et al. Electrocatalytic Upgrading of Model Lignin Monomers with Earth Abundant Metal Electrodes. *Green Chem.* **2015**, *17* (1), 601–609. https://doi.org/10.1039/C4GC01632G.

(179) Kleinert, M.; Barth, T. Phenols from Lignin. **2008**, No. 5, 736–745. https://doi.org/10.1002/ceat.200800073.

(180) Lu, S.; Menning, C. A.; Zhu, Y.; Chen, J. G. Correlating Benzene Hydrogenation Activity with Binding Energies of Hydrogen and Benzene on Co-Based Bimetallic Catalysts. *ChemPhysChem* **2009**, *10* (11), 1763–1765. https://doi.org/10.1002/cphc.200900139.

(181) Do, P. T. M.; Foster, A. J.; Chen, J.; Lobo, R. F. Bimetallic Effects in the Hydrodeoxygenation of Meta-Cresol on γ-Al2O3 Supported Pt–Ni and Pt–Co Catalysts. *Green Chem.* **2012**, *14* (5), 1388. https://doi.org/10.1039/c2gc16544a.

(182) Lonergan, W. W.; Vlachos, D. G.; Chen, J. G. Correlating Extent of Pt-Ni Bond Formation with Low-Temperature Hydrogenation of Benzene and 1,3-Butadiene over Supported Pt/Ni Bimetallic Catalysts. *J. Catal.* **2010**, *271* (2), 239–250. https://doi.org/10.1016/j.jcat.2010.01.019.

(183) Cheney, B. A.; Lauterbach, J. A.; Chen, J. G. Reverse Micelle Synthesis and Characterization of Supported Pt/Ni Bimetallic Catalysts on γ-Al2O3. *Appl. Catal. A Gen.* **2011**, *394* (1–2), 41–47. https://doi.org/10.1016/j.apcata.2010.12.021.

(184) Resende, K. A.; Hori, C. E.; Noronha, F. B.; Shi, H.; Gutierrez, O. Y.; Camaioni, D. M.; Lercher, J. A. Aqueous Phase Hydrogenation of Phenol Catalyzed by Pd and PdAg on ZrO2. *Appl. Catal. A Gen.* **2017**, *548* (July), 128–135. https://doi.org/10.1016/j.apcata.2017.08.005.

(185) Santori, G. F.; Casella, M. L.; Siri, G. J.; Adúriz, H. R.; Ferretti, O. A. Effect of Particle Size in the Hydrogenation of Crotonaldehyde on Supported Pt and Pt-Sn Catalysts. *React. Kinet. Mech. Catal.* **2002**, *75* (2), 225–230.

(186) Meyer, R. J.; Zhang, Q.; Kryczka, A.; Gomez, C.; Todorovic, R. Perturbation of Reactivity with Geometry: How Far Can We Go? *ACS Catal.* **2018**, *8* (1), 566–570. https://doi.org/10.1021/acscatal.7b03228.

(187) Humbert, M. P.; Chen, J. G. Correlating Hydrogenation Activity with Binding Energies of Hydrogen and Cyclohexene on M/Pt(111) (M = Fe, Co, Ni, Cu) Bimetallic Surfaces. *J. Catal.* **2008**, *257* (2), 297–306. https://doi.org/10.1016/j.jcat.2008.05.013.

(188) Liu, B.; Xiao, D.; Wang, Y.; Jia, P.; Huang, N.; Lan, X.; Wang, T. Correlating C═C, C═O, and C═N Hydrogenation Activity with Hydrogen Binding Energies on Ni–Fe Bimetallic Catalysts. *J. Phys. Chem. C* **2020**, *124* (34), 18595–18603. https://doi.org/10.1021/acs.jpcc.0c04302.

(189) Greeley, J.; Jaramillo, T. F.; Bonde, J.; Chorkendorff, I.; Nørskov, J. K. Computational High-Throughput Screening of Electrocatalytic Materials for Hydrogen Evolution. *Nat. Mater.* **2006**, *5* (11), 909–913. https://doi.org/10.1038/nmat1752.

(190) Zheng, J.; Sheng, W.; Zhuang, Z.; Xu, B.; Yan, Y. Universal Dependence of Hydrogen Oxidation and Evolution Reaction Activity of Platinum-Group Metals on PH and Hydrogen Binding Energy. *Sci. Adv.* **2016**, *2* (3), 1–9.

https://doi.org/10.1126/sciadv.1501602.

(191) Nørskov, J. K.; Bligaard, T.; Logadottir, A.; Kitchin, J. R.; Chen, J. G.; Pandelov, S.; Stimming, U. Trends in the Exchange Current for Hydrogen Evolution. *J. Electrochem. Soc.* **2005**, *152* (3), J23. https://doi.org/10.1149/1.1856988.

(192) Trasatti, S. Work Function, Electronegativity, and Electrochemical Behaviour of Metals. III. Electrolytic Hydrogen Evolution in Acid Solutions. *J. Electroanal. Chem.* **1972**, *39* (1), 163–184. https://doi.org/10.1016/S0022-0728(72)80485-6.

(193) Savadogo, O.; Piron, D. L. New Hydrogen Cathodes in Acid Medium: Case of Nickel Electrodeposited with Heteropolyacids (HPAs). *Int. J. Hydrogen Energy* **1990**, *15* (10), 715–721. https://doi.org/10.1016/0360-3199(90)90002-G.

(194) Skúlason, E.; Tripkovic, V.; Björketun, M. E.; Gudmundsdóttir, S.; Karlberg, G.; Rossmeisl, J.; Bligaard, T.; Jónsson, H.; Nørskov, J. K. Modeling the Electrochemical Hydrogen Oxidation and Evolution Reactions on the Basis of Density Functional Theory Calculations. *J. Phys. Chem. C* **2010**, *114* (42), 18182–18197. https://doi.org/10.1021/jp1048887.

(195) Greeley, J.; Nørskov, J. K. Large-Scale, Density Functional Theory-Based Screening of Alloys for Hydrogen Evolution. *Surf. Sci.* **2007**, *601* (6), 1590–1598. https://doi.org/10.1016/j.susc.2007.01.037.

(196) Pintauro, P. N.; Gil, M. P.; Warner, K.; List, G.; Neff, W. Electrochemical Hydrogenation of Soybean Oil with Hydrogen Gas. *Ind. Eng. Chem. Res.* **2005**, *44* (16), 6188–6195. https://doi.org/10.1021/ie0490738.

(197) Wang, Z.; Majima, T.; Zhao, G. Role of Ni in PtNi Alloy for Modulating the Proton − Electron Transfer of Electrocatalytic Hydrogenation Revealed by The. **2022**. https://doi.org/10.1021/acscatal.2c03551.

(198) Du, Y.; Chen, X.; Liang, C. Selective Electrocatalytic Hydrogenation of Phenols over Ternary Pt3RuSn Alloy. *Mol. Catal.* **2023**, *535* (December 2022), 112831. https://doi.org/10.1016/j.mcat.2022.112831.

(199) Mavrikakis, M.; Hammer, B.; Nørskov, J. K. Effect of Strain on the Reactivity of Metal Surfaces. *Phys. Rev. Lett.* **1998**, *81* (13), 2819–2822. https://doi.org/10.1103/PhysRevLett.81.2819.

(200) Wang, X.; Zhu, Y.; Vasileff, A.; Jiao, Y.; Chen, S.; Song, L.; Zheng, B.; Zheng, Y.; Qiao, S. Z. Strain Effect in Bimetallic Electrocatalysts in the Hydrogen Evolution Reaction. *ACS Energy Lett.* **2018**, *3* (5), 1198–1204. https://doi.org/10.1021/acsenergylett.8b00454.

(201) Pan, Y.-T.; Li, D.; Sharma, S.; Wang, C.; Zachman, M. J.; Wegener, E. C.; Kropf, A. J.; Kim, Y. S.; Myers, D. J.; Peterson, A. A.; et al. Ordered CoPt Oxygen Reduction Catalyst with High Performance and Durability. *Chem Catal.* **2022**, *2* (12), 3559–3572. https://doi.org/10.1016/j.checat.2022.10.030.

(202) Kitchin, J. R.; Nørskov, J. K.; Barteau, M. A.; Chen, J. G. Role of Strain and Ligand Effects in the Modification of the Electronic and Chemical Properties of Bimetallic Surfaces. *Phys. Rev. Lett.* **2004**, *93* (15), 4–7. https://doi.org/10.1103/physrevlett.93.156801.

(203) Wei, C.; Sun, Y.; Scherer, G. G.; Fisher, A. C.; Sherburne, M.; Ager, J. W.; Xu, Z. J. Surface Composition Dependent Ligand Effect in Tuning the Activity of Nickel-Copper Bimetallic Electrocatalysts toward Hydrogen Evolution in Alkaline. *J. Am. Chem. Soc.* **2020**, *142* (17), 7765–7775. https://doi.org/10.1021/jacs.9b12005.

(204) Wang, Y.; Cao, L.; Libretto, N. J.; Li, X.; Li, C.; Wan, Y.; He, C.; Lee, J.; Gregg, J.;

Zong, H.; et al. Ensemble Effect in Bimetallic Electrocatalysts for CO2 Reduction. *J. Am. Chem. Soc.* **2019**, *141* (42), 16635–16642. https://doi.org/10.1021/jacs.9b05766.

(205) Sachtler, W. M. H.; van Santen, R. A. Surface Composition and Selectivity of Alloy Catalysts. *Adv. Catal.* **1977**, *26* (C), 69–119. https://doi.org/10.1016/S0360-0564(08)60070-X.

(206) Long, N. V.; Yang, Y.; Minh Thi, C.; Minh, N. Van; Cao, Y.; Nogami, M. The Development of Mixture, Alloy, and Core-Shell Nanocatalysts with Nanomaterial Supports for Energy Conversion in Low-Temperature Fuel Cells. *Nano Energy* **2013**, *2* (5), 636–676. https://doi.org/10.1016/j.nanoen.2013.06.001.

(207) Oezaslan, M.; Hasché, F.; Strasser, P. Pt-Based Core-Shell Catalyst Architectures for Oxygen Fuel Cell Electrodes. *J. Phys. Chem. Lett.* **2013**, *4* (19), 3273–3291. https://doi.org/10.1021/jz4014135.

(208) Oezaslan, M.; Hasché, F.; Strasser, P. Oxygen Electroreduction on PtCo 3 , PtCo and Pt 3 Co Alloy Nanoparticles for Alkaline and Acidic PEM Fuel Cells. *J. Electrochem. Soc.* **2012**, *159* (4), B394–B405. https://doi.org/10.1149/2.075204jes.

(209) Oezaslan, M.; Strasser, P. Activity of Dealloyed PtCo3 and PtCu3 Nanoparticle Electrocatalyst for Oxygen Reduction Reaction in Polymer Electrolyte Membrane Fuel Cell. *J. Power Sources* **2011**, *196* (12), 5240–5249. https://doi.org/10.1016/j.jpowsour.2010.11.016.

(210) Saquib, M.; Halder, A. Dealloyed Pt3Co Nanoparticles with Higher Geometric Strain for Superior Hydrogen Evolution Reaction. *J. Solid State Chem.* **2018**, *262* (March), 229–236. https://doi.org/10.1016/j.jssc.2018.03.030.

(211) Leontyev, I. N.; Chernyshov, D. Y.; Guterman, V. E.; Pakhomova, E. V.; Guterman, A. V. Particle Size Effect in Carbon Supported Pt-Co Alloy Electrocatalysts Prepared by the Borohydride Method: XRD Characterization. *Appl. Catal. A Gen.* **2009**, *357* (1), 1–4. https://doi.org/10.1016/j.apcata.2008.12.023.

(212) Ravel, B.; Newville, M. ATHENA , ARTEMIS , HEPHAESTUS : Data Analysis for X-Ray Absorption Spectroscopy Using IFEFFIT. *J. Synchrotron Radiat.* **2005**, *12* (4), 537–541. https://doi.org/10.1107/S0909049505012719.

(213) Barth, I.; Akinola, J.; Lee, J.; Gutiérrez, O. Y.; Sanyal, U.; Singh, N.; Goldsmith, B. R. Explaining the Structure Sensitivity of Pt and Rh for Aqueous-Phase Hydrogenation of Phenol. *J. Chem. Phys.* **2022**, *156* (10), 104703. https://doi.org/10.1063/5.0085298.

(214) Kobayashi, S.; Tryk, D. A.; Uchida, H. Enhancement of Hydrogen Evolution Activity on Pt-Skin/Pt3Co [(111), (100), and (110)] Single Crystal Electrodes. *Electrochem. commun.* **2020**, *110* (November 2019), 106615. https://doi.org/10.1016/j.elecom.2019.106615.

(215) Guo, F.; Zou, Z.; Zhang, Z.; Zeng, T.; Tan, Y.; Chen, R.; Wu, W.; Cheng, N.; Sun, X. Confined Sub-Nanometer PtCo Clusters as a Highly Efficient and Robust Electrocatalyst for the Hydrogen Evolution Reaction. *J. Mater. Chem. A* **2021**, *9* (9), 5468–5474. https://doi.org/10.1039/d0ta10500g.

(216) Anniyev, T.; Kaya, S.; Rajasekaran, S.; Ogasawara, H.; Nordlund, D.; Nilsson, A. Tuning the Metal-Adsorbate Chemical Bond through the Ligand Effect on Platinum Subsurface Alloys. *Angew. Chemie Int. Ed.* **2012**, *51* (31), 7724–7728. https://doi.org/10.1002/anie.201201068.

(217) Zhang, X.; Wang, H.; Key, J.; Linkov, V.; Ji, S.; Wang, X.; Lei, Z.; Wang, R. Strain Effect of Core-Shell Co@Pt/C Nanoparticle Catalyst with Enhanced Electrocatalytic Activity for Methanol Oxidation. *J. Electrochem. Soc.* **2012**, *159* (3), B270–B276.

https://doi.org/10.1149/2.015203jes.
(218) Hyman, M. P.; Medlin, J. W. Effects of Electronic Structure Modifications on the Adsorption of Oxygen Reduction Reaction Intermediates on Model Pt(111)-Alloy Surfaces. *J. Phys. Chem. C* **2007**, *111* (45), 17052–17060. https://doi.org/10.1021/jp075108g.
(219) Luo, H.; Yukuhiro, V. Y.; Fernández, P. S.; Feng, J.; Thompson, P.; Rao, R. R.; Cai, R.; Favero, S.; Haigh, S. J.; Durrant, J. R.; et al. Role of Ni in PtNi Bimetallic Electrocatalysts for Hydrogen and Value-Added Chemicals Coproduction via Glycerol Electrooxidation. *ACS Catal.* **2022**, *12* (23), 14492–14506. https://doi.org/10.1021/acscatal.2c03907.
(220) Jia, Q.; Zhao, Z.; Cao, L.; Li, J.; Ghoshal, S.; Davies, V.; Stavitski, E.; Attenkofer, K.; Liu, Z.; Li, M.; et al. Roles of Mo Surface Dopants in Enhancing the ORR Performance of Octahedral PtNi Nanoparticles. *Nano Lett.* **2018**, *18* (2), 798–804. https://doi.org/10.1021/acs.nanolett.7b04007.
(221) Akinola, J.; Campbell, C. T.; Singh, N. Effects of Solvents on Adsorption Energies: A General Bond-Additivity Model. *J. Phys. Chem. C* **2021**, *125* (44), 24371–24380. https://doi.org/10.1021/acs.jpcc.1c06781.
(222) Singh, N.; Lee, M.-S.; Akhade, S. A.; Cheng, G.; Camaioni, D. M.; Gutiérrez, O. Y.; Glezakou, V.-A.; Rousseau, R.; Lercher, J. A.; Campbell, C. T. Impact of PH on Aqueous-Phase Phenol Hydrogenation Catalyzed by Carbon-Supported Pt and Rh. *ACS Catal.* **2019**, *9* (2), 1120–1128. https://doi.org/10.1021/acscatal.8b04039.
(223) Leroy, F.; Dos Santos, D. J. V. A.; Müller-Plathe, F. Interfacial Excess Free Energies of Solid-Liquid Interfaces by Molecular Dynamics Simulation and Thermodynamic Integration. *Macromol. Rapid Commun.* **2009**, *30* (9–10), 864–870. https://doi.org/10.1002/marc.200800746.
(224) Leroy, F.; Müller-Plathe, F. Dry-Surface Simulation Method for the Determination of the Work of Adhesion of Solid–Liquid Interfaces. *Langmuir* **2015**, *31* (30), 8335–8345. https://doi.org/10.1021/acs.langmuir.5b01394.
(225) Lim, H. K.; Lee, H.; Kim, H. A Seamless Grid-Based Interface for Mean-Field QM/MM Coupled with Efficient Solvation Free Energy Calculations. *J. Chem. Theory Comput.* **2016**, *12* (10), 5088–5099. https://doi.org/10.1021/acs.jctc.6b00469.
(226) Gim, S.; Lim, H.-K.; Kim, H. Multiscale Simulation Method for Quantitative Prediction of Surface Wettability at the Atomistic Level. *J. Phys. Chem. Lett.* **2018**, *9* (7), 1750–1758. https://doi.org/10.1021/acs.jpclett.8b00466.
(227) Gim, S.; Cho, K. J.; Lim, H.-K.; Kim, H. Structure, Dynamics, and Wettability of Water at Metal Interfaces. *Sci. Rep.* **2019**, *9* (1), 14805. https://doi.org/10.1038/s41598-019-51323-5.
(228) Nørskov, J. K.; Rossmeisl, J.; Logadottir, A.; Lindqvist, L.; Kitchin, J. R.; Bligaard, T.; Jónsson, H. Origin of the Overpotential for Oxygen Reduction at a Fuel-Cell Cathode. *J. Phys. Chem. B* **2004**, *108* (46), 17886–17892. https://doi.org/10.1021/jp047349j.
(229) Akhade, S. A.; Bernstein, N. J.; Esopi, M. R.; Regula, M. J.; Janik, M. J. A Simple Method to Approximate Electrode Potential-Dependent Activation Energies Using Density Functional Theory. *Catal. Today* **2017**, *288*, 63–73. https://doi.org/10.1016/j.cattod.2017.01.050.
(230) Hörmann, N. G.; Andreussi, O.; Marzari, N. Grand Canonical Simulations of Electrochemical Interfaces in Implicit Solvation Models. *J. Chem. Phys.* **2019**, *150* (4). https://doi.org/10.1063/1.5054580.

(231) Hörmann, N. G.; Marzari, N.; Reuter, K. Electrosorption at Metal Surfaces from First Principles. *npj Comput. Mater.* **2020**, *6* (1), 136. https://doi.org/10.1038/s41524-020-00394-4.
(232) Sundararaman, R.; Goddard, W. A.; Arias, T. A. Grand Canonical Electronic Density-Functional Theory: Algorithms and Applications to Electrochemistry. *J. Chem. Phys.* **2017**, *146* (11). https://doi.org/10.1063/1.4978411.
(233) Melander, M. M.; Kuisma, M. J.; Christensen, T. E. K.; Honkala, K. Grand-Canonical Approach to Density Functional Theory of Electrocatalytic Systems: Thermodynamics of Solid-Liquid Interfaces at Constant Ion and Electrode Potentials. *J. Chem. Phys.* **2019**, *150* (4), 041706. https://doi.org/10.1063/1.5047829.
(234) Petrosyan, S. A.; Briere, J.-F.; Roundy, D.; Arias, T. A. Joint Density-Functional Theory for Electronic Structure of Solvated Systems. *Phys. Rev. B* **2007**, *75* (20), 205105. https://doi.org/10.1103/PhysRevB.75.205105.
(235) Goodpaster, J. D.; Bell, A. T.; Head-Gordon, M. Identification of Possible Pathways for C-C Bond Formation during Electrochemical Reduction of CO2: New Theoretical Insights from an Improved Electrochemical Model. *J. Phys. Chem. Lett.* **2016**, *7* (8), 1471–1477. https://doi.org/10.1021/acs.jpclett.6b00358.
(236) Gao, Q.; Pillai, H. S.; Huang, Y.; Liu, S.; Mu, Q.; Han, X.; Yan, Z.; Zhou, H.; He, Q.; Xin, H.; et al. Breaking Adsorption-Energy Scaling Limitations of Electrocatalytic Nitrate Reduction on Intermetallic CuPd Nanocubes by Machine-Learned Insights. *Nat. Commun.* **2022**, *13* (1), 2338. https://doi.org/10.1038/s41467-022-29926-w.
(237) Pillai, H. S.; Xin, H. New Insights into Electrochemical Ammonia Oxidation on Pt(100) from First Principles. *Ind. Eng. Chem. Res.* **2019**, *58* (25), 10819–10828. https://doi.org/10.1021/acs.iecr.9b01471.
(238) Sundararaman, R.; Letchworth-Weaver, K.; Schwarz, K. A.; Gunceler, D.; Ozhabes, Y.; Arias, T. A. JDFTx: Software for Joint Density-Functional Theory. *SoftwareX* **2017**, *6*, 278–284. https://doi.org/10.1016/j.softx.2017.10.006.
(239) Alsunni, Y. A.; Alherz, A. W.; Musgrave, C. B. Electrocatalytic Reduction of CO2 to CO over Ag(110) and Cu(211) Modeled by Grand-Canonical Density Functional Theory. *J. Phys. Chem. C* **2021**, *125* (43), 23773–23783. https://doi.org/10.1021/acs.jpcc.1c07484.
(240) Singstock, N. R.; Musgrave, C. B. How the Bioinspired Fe 2 Mo 6 S 8 Chevrel Breaks Electrocatalytic Nitrogen Reduction Scaling Relations. *J. Am. Chem. Soc.* **2022**, *144* (28), 12800–12806. https://doi.org/10.1021/jacs.2c03661.
(241) Henkelman, G.; Jónsson, H. Improved Tangent Estimate in the Nudged Elastic Band Method for Finding Minimum Energy Paths and Saddle Points. *J. Chem. Phys.* **2000**, *113* (22), 9978–9985. https://doi.org/10.1063/1.1323224.
(242) Yu, P.; Pemberton, M.; Plasse, P. PtCo/C Cathode Catalyst for Improved Durability in PEMFCs. *J. Power Sources* **2005**, *144* (1), 11–20. https://doi.org/10.1016/j.jpowsour.2004.11.067.
(243) Mathanker, A.; Yu, W.; Singh, N.; Goldsmith, B. R. Effects of Ions on Electrocatalytic Hydrogenation and Oxidation of Organics in Aqueous Phase. *Curr. Opin. Electrochem.* **2023**, *40*, 101347. https://doi.org/10.1016/j.coelec.2023.101347.
(244) Li, Y.; Liu, Z.; Liu, Y.; Crossley, S. P.; Jentoft, F. C.; Wang, S. Hydrogenation of o - Cresol at the Water/Pt(111) Interface. *J. Phys. Chem. C* **2019**, *123* (9), 5378–5384. https://doi.org/10.1021/acs.jpcc.8b10546.
(245) Biegler, T.; Rand, D. A. J.; Woods, R. Limiting Oxygen Coverage on Platinized Platinum;

Relevance to Determination of Real Platinum Area by Hydrogen Adsorption. *J. Electroanal. Chem.* **1971**, *29* (2), 269–277. https://doi.org/10.1016/S0022-0728(71)80089-X.

(246) Bett, J.; Kinoshita, K.; Routsis, K.; Stonehart, P. A Comparison of Gas-Phase and Electrochemical Measurements for Chemisorbed Carbon Monoxide and Hydrogen on Platinum Crystallites. *J. Catal.* **1973**, *29* (1), 160–168.

(247) Woods, R. *Electroanalytical Chemistry: A Series of Advances*; Marcel Dekker: New York, 1976; Vol. 9.

(248) Rand, D. A. J.; Woods, R. The Nature of Adsorbed Oxygen on Rhodium, Palladium and Gold Electrodes. *J. Electroanal. Chem.* **1971**, *31* (1), 29–38. https://doi.org/10.1016/S0022-0728(71)80039-6.

(249) Cai, Q.-X.; Wang, J.-G.; Wang, Y.-G.; Mei, D. Mechanistic Insights into the Structure-Dependent Selectivity of Catalytic Furfural Conversion on Platinum Catalysts. *AIChE J.* **2015**, *61* (11), 3812–3824. https://doi.org/10.1002/aic.14902.

(250) Sander, R. *NIST Chemistry WebBook, NIST Standard Reference Database Number 69*; P.J.Linstrom, W.G.Mallard, Eds.; National Institute of Standards and Technology: Gaithersburg MD, 20899, 2018.

(251) Kudchadker, S. A.; Kudchadker, A. P.; Wilhoit, R. C.; Zwolinski, B. J. Ideal Gas Thermodynamic Properties of Phenol and Cresols. *J. Phys. Chem. Ref. Data* **1978**, *7* (2), 417–423. https://doi.org/10.1063/1.555573.

(252) Guedes, R. C.; Coutinho, K.; Costa Cabral, B. J.; Canuto, S. Differential Hydration of Phenol and Phenoxy Radical and the Energetics of the Phenol O−H Bond in Solution. *J. Phys. Chem. B* **2003**, *107* (18), 4304–4310. https://doi.org/10.1021/jp0219449.

(253) Kühne, R.; Ebert, R. U.; Schüürmann, G. Prediction of the Temperature Dependency of Henry's Law Constant from Chemical Structure. *Environ. Sci. Technol.* **2005**, *39* (17), 6705–6711. https://doi.org/10.1021/es050527h.

(254) Howard, P. H.; Meylan, W. The Physical Properties Database (PHYSPROP). Syracuse Research Corp: Syracuse, NY 2006.

(255) Grote, F.; Ermilova, I.; Lyubartsev, A. P. Molecular Dynamics Simulations of Furfural and 5-Hydroxymethylfurfural at Ambient and Hydrothermal Conditions. *J. Phys. Chem. B* **2018**, *122* (35), 8416–8428. https://doi.org/10.1021/acs.jpcb.8b03350.

(256) Abraham, M. H.; Whiting, G. S.; Fuchs, R.; Chambers, E. J. Thermodynamics of Solute Transfer from Water to Hexadecane. *J. Chem. Soc. Perkin Trans. 2* **2004**, No. 2, 291. https://doi.org/10.1039/p29900000291.

(257) Costa, F. S.; Eusébio, M. E.; Redinha, J. S.; Leitão, M. L. P. Enthalpies of Solvation of Hydroxyl Cyclohexane Derivatives in Different Solvents. *J. Chem. Thermodyn.* **1999**, *31* (7), 895–903. https://doi.org/10.1006/jcht.1999.0495.

(258) Campbell, C. T.; Sprowl, L. H.; Árnadóttir, L. Equilibrium Constants and Rate Constants for Adsorbates: Two-Dimensional (2D) Ideal Gas, 2D Ideal Lattice Gas, and Ideal Hindered Translator Models. *J. Phys. Chem. C* **2016**, *120* (19), 10283–10297. https://doi.org/10.1021/acs.jpcc.6b00975.

(259) Mark, L. O.; Jenkins, A. H.; Heinz, H.; Medlin, J. W. Furfuryl Alcohol Deoxygenation, Decarbonylation, and Ring-Opening on Pt(111). *Surf. Sci.* **2018**, *677* (May), 333–340. https://doi.org/10.1016/j.susc.2018.07.001.

(260) Shi, D.; Vohs, J. M. Deoxygenation of Biomass-Derived Oxygenates: Reaction of Furfural on Zn-Modified Pt(111). *ACS Catal.* **2015**, *5* (4), 2177–2183.

https://doi.org/10.1021/acscatal.5b00038.

(261) Taylor, M. J.; Jiang, L.; Reichert, J.; Papageorgiou, A. C.; Beaumont, S. K.; Wilson, K.; Lee, A. F.; Barth, J. V.; Kyriakou, G. Catalytic Hydrogenation and Hydrodeoxygenation of Furfural over Pt(111): A Model System for the Rational Design and Operation of Practical Biomass Conversion Catalysts. *J. Phys. Chem. C* **2017**, *121* (15), 8490–8497. https://doi.org/10.1021/acs.jpcc.7b01744.

(262) Michaelides, A. Density Functional Theory Simulations of Water–Metal Interfaces: Waltzing Waters, a Novel 2D Ice Phase, and More. *Appl. Phys. A* **2006**, *85* (4), 415–425. https://doi.org/10.1007/s00339-006-3695-9.

(263) Le, J.; Cuesta, A.; Cheng, J. The Structure of Metal-Water Interface at the Potential of Zero Charge from Density Functional Theory-Based Molecular Dynamics. *J. Electroanal. Chem.* **2018**, *819*, 87–94. https://doi.org/10.1016/j.jelechem.2017.09.002.

(264) Osborne, N. S.; Stimson, H. F.; Ginnings, D. C. Measurements of Heat Capacity and Heat of Vaporization of Water in the Range 0 Degrees to 100 Degrees C. *J. Res. Natl. Bur. Stand. (1934).* **1939**, *23* (2), 197–260. https://doi.org/10.6028/jres.023.008.

(265) Israelachvili, J. *Intermolecular and Surface Forces*; Academic Press, Ed.; Elsevier, 2011. https://doi.org/10.1016/C2009-0-21560-1.

(266) Gileadi, E.; Argade, S. D.; Bockris, J. O. M. The Potential of Zero Charge of Platinum and Its PH Dependence. *J. Phys. Chem.* **1966**, *70* (6), 2044–2046. https://doi.org/10.1021/j100878a501.

(267) Canduela-Rodriguez, G.; Sabbe, M. K.; Reyniers, M. F.; Joly, J. F.; Marin, G. B. Thermodynamic Study of Benzene and Hydrogen Coadsorption on Pd(111). *Phys. Chem. Chem. Phys.* **2014**, *16* (43), 23754–23768. https://doi.org/10.1039/c4cp02991g.

(268) Dhepe, P. L.; Fukuoka, A.; Ichikawa, M. Catalyst Preparation Using Supercritical Carbon Dioxide: Preparation of Rh/FSM-16 Catalysts and Their Catalytic Performances in Butane Hydrogenolysis Reaction. *Catal. Letters* **2002**, *81* (1–2), 69–75. https://doi.org/10.1023/A:1016060022914.

(269) Farsi, L.; Deskins, N. A. First Principles Analysis of Surface Dependent Segregation in Bimetallic Alloys. *Phys. Chem. Chem. Phys.* **2019**, *21* (42), 23626–23637. https://doi.org/10.1039/C9CP03984H.

(270) Su, H. Y.; Gu, X. K.; Ma, X.; Zhao, Y. H.; Bao, X. H.; Li, W. X. Structure Evolution of Pt-3d Transition Metal Alloys under Reductive and Oxidizing Conditions and Effect on the CO Oxidation: A First-Principles Study. *Catal. Today* **2011**, *165* (1), 89–95. https://doi.org/10.1016/j.cattod.2010.10.069.

(271) Jentys, A. Estimation of Mean Size and Shape of Small Metal Particles by EXAFS. *Phys. Chem. Chem. Phys.* **1999**, *1* (17), 4059–4063. https://doi.org/10.1039/a904654b.

(272) Yang, G.; Akhade, S. A.; Chen, X.; Liu, Y.; Lee, M.-S.; Glezakou, V.-A.; Rousseau, R.; Lercher, J. A. The Nature of Hydrogen Adsorption on Platinum in the Aqueous Phase. *Angew. Chemie Int. Ed.* **2019**, *58* (11), 3527–3532. https://doi.org/10.1002/anie.201813958.